PACIFIC EARTHQUAKE ENGINEERING RESEARCH CENTER

Simulation and Performance-Based Earthquake Engineering Assessment of Self-Centering Post-Tensioned Concrete Bridge Systems

Won K. Lee

and

Sarah L. Billington

Stanford University

PEER 2009/109
DECEMBER 2009

Simulation and Performance-Based Earthquake Engineering Assessment of Self-Centering Post-Tensioned Concrete Bridge Systems

Won K. Lee
Department of Civil and Environmental Engineering
Stanford University

Sarah L. Billington
Department of Civil and Environmental Engineering
Stanford University

PEER Report 2009/109
Pacific Earthquake Engineering Research Center
College of Engineering
University of California, Berkeley

December 2009

ABSTRACT

The focus of this research is on conducting a performance-based earthquake engineering assessment of self-centering bridge columns for structural concrete bridges. Standard highway bridges in highly seismic regions are typically designed for columns to undergo large inelastic deformations during severe earthquakes, which can result in residual displacements. These residual displacements are a measure of post-earthquake functionality in bridges, and can determine whether a bridge remains usable following an earthquake. To mitigate the effects of residual displacements, a number of self-centering systems for bridge columns using unbonded post-tensioned (UBPT) reinforcing steel are proposed and investigated. The research reported herein had three objectives: (1) to assess and develop simulation methods and models that can accurately capture key performance attributes of reinforced concrete and unbonded post-tensioned concrete bridge piers, to facilitate their comparison; (2) to provide a systematic assessment of various self-centering bridge column systems in terms of engineering performance, as well as expected repair costs and downtime, including a quantitative comparison to current code-conforming reinforced concrete bridge designs using the performance-based earthquake engineering methodology developed by the Pacific Earthquake Engineering Research Center; and (3) to evaluate the performance-based earthquake engineering methodology itself. The unbonded post-tensioned systems were found to perform comparably to the conventional reinforced concrete system in terms of peak drifts. Reductions to column damage in the case of some of the systems were found not to justify their higher initial costs. However, the unbonded post-tensioned columns sustained considerably lower residual drifts than the reinforced concrete columns, leading to significant reductions in expected bridge downtime following large earthquakes. These significant reductions in downtime make the unbonded post-tensioned systems desirable for important bridges that must remain operational following an earthquake.

ACKNOWLEDGMENTS

This work was supported primarily by the Earthquake Engineering Research Centers Program of the National Science Foundation, under award number EEC-9701568 through the Pacific Earthquake Engineering Research (PEER) Center. Any opinions, findings, and conclusions or recommendations expressed in this material are those of the authors and do not necessarily reflect those of the National Science Foundation.

The authors would like to acknowledge their fellow collaborators in bridge research on this project for their insights and participation: Professors Stephen Mahin, Boza Stojadinovic, John Stanton, Kevin Mackie, and Dr. Junichi Sakai. The assistance of Dr. Polsak Tothong with ground motion selection and probabilistic seismic hazard analysis is gratefully acknowledged.

CONTENTS

LIST OF FIGURES

LIST OF TABLES

1 Introduction

1.1 MOTIVATION

In recent years, the earthquake engineering community has been focusing attention on performance-based design in order to predict and better manage the post-earthquake functionality and condition of structures. Excessive direct and indirect monetary losses due to both structural and nonstructural damage that were sustained in recent earthquakes (e.g., Kobe 1995, Northridge 1995, Loma Prieta 1989) revealed that the then-current philosophy of designing for life safety (i.e., collapse prevention) was not sufficient in meeting the diverse needs of structure owners and of society as a whole. The goal of performance-based design is to incorporate a pre-defined level of post-earthquake performance into the design or retrofit of a structure such that the damage is kept to “acceptable” levels, with the definition of acceptable varying with both the type and use of a structure, as well as the owners’ needs.

The focus of this report is on bridge structures and, in particular, bridge columns. Bridges are a key component in the transportation network, which provides emergency services immediately following an earthquake. In addition, the uninterrupted function of the transportation network is crucial to maintaining normal societal function. Standard highway bridges in highly seismic regions such as California are typically designed such that plastic behavior will concentrate in the columns during earthquakes. The columns are expected to undergo large inelastic deformations during severe earthquakes, which can result in permanent, or residual, displacements. These residual displacements are an important measure of post-earthquake functionality in bridges, and can determine whether or not a bridge remains usable following an earthquake. For example, following the Kobe earthquake, over 100 reinforced concrete columns with a residual drift ratio (displacement normalized by column height) of over

1.75 percent were demolished even though they did not collapse (Kawashima et al. 1998). Finally, residual displacements have been shown to be an important parameter in determining the post-earthquake ability of bridges (Mackie and Stojadinovic 2004) and buildings (Bazzurro et al. 2004; Luco et al. 2004) to sustain aftershocks.

With the increased awareness of the importance of residual displacements, a number of novel systems have been under investigation recently with the goal of mitigating the effects of residual displacements. The primary method of dealing with large, expected inelastic deformations is to provide a restoring force to bring the structure back to its original position, i.e., to provide self-centering to the structure. The self-centering is typically provided in a passive fashion using gravity or unbonded post-tensioned (UBPT) steel. Several systems have been under investigation for both bridge and building systems making use of a number of novel methods and technologies. Experimental and analytical research on these systems has shown promise for their use in seismic applications.

To facilitate the timely adoption of these new technologies by practicing structural engineers, several issues must be investigated. An assessment of the seismic performance of the new systems, both with respect to residual displacements and to overall structural performance, must be made. Additionally, the performance of conventional systems with respect to residual displacements, which is typically unknown, must be evaluated. Finally, a systematic assessment to compare the performance of the two systems is needed. Such an assessment can be performed using a formalized framework for performance-based earthquake engineering (PBEE) such as the one developed by the Pacific Earthquake Engineering Research Center (PEER).

1.2 OBJECTIVES

The objectives of this research are three-fold. The first objective is to assess and develop simulation methods and models where needed that can accurately capture key performance attributes of reinforced concrete and unbonded post-tensioned concrete bridge piers, to facilitate their comparison.

The second objective is to provide a systematic assessment of various self-centering systems using unbonded post-tensioning for concrete highway bridge columns in highly seismic regions. The assessment will be performed by quantitatively comparing the seismic performance of the new systems to current code-conforming, conventional RC highway bridges both in terms of engineering response as well as more readily understood metrics such as expected repair costs and downtime. In this way, the performance of code-conforming highway bridges can also be benchmarked. The assessment is performed using PEER's PBEE methodology. The assessment requires detailed validation of analytical tools used to simulate the behavior of these systems under cyclic and dynamic loading, as well as extensive nonlinear time-history analyses.

The third objective is to evaluate the performance-based assessment methodology itself. As of the outset of this research, much of the research within PEER has focused only on improving or assessing one or two components of the methodology. While such detail is necessary for providing the best possible tools for the assessment, focus on the methodology as a whole can provide much insight into its robustness. When viewing the methodology in its entirety, the relative importance or sensitivity of the various components can be readily assessed, and thus point to where additional research may be needed. In addition, while investigating this new system using unbonded post-tensioning and new materials, several assumptions are made to use PEER’s assessment methodology because enough data do not exist. To evaluate the methodology, the sensitivity of the final results to various assumptions made throughout the analyses will be investigated.

1.3 ORGANIZATION

Chapter 2 presents a review of background information and concepts that are used throughout this report. First, a summary of PEER's PBEE assessment methodology is presented. Next, the design of current highway bridges in seismic regions and their expected response are presented, followed by a review of recent research on self-centering systems. Finally, a review of high-performance fiber-reinforced cementitious composite (HPFRCC) materials proposed for improved structural performance of self-centering systems is given.

In Chapter 3, a self-centering system for rectangular concrete columns using pre-cast, segmental construction with multiple, eccentric UBPT tendons is studied. The system also has the option of using HPFRCC materials for damage reduction. Detailed continuum finite element analysis of experimental tests on the system with the goal of accurately simulating and understanding the observed failure behavior are presented. The use of simulation to assess the cyclic behavior of the systems and to assess possible design improvements is also presented.

In Chapter 4, a self-centering system for circular concrete columns using a single, concentric UBPT tendon is studied. The ability of fiber element models to predict the peak and residual dynamic response of RC and UBPT columns is studied by simulating a set of experimental shaking table tests. The inability of fiber element models to capture residual displacements in RC columns is investigated, and a modified constitutive model for providing improved residual displacement response is presented.

Chapter 5 continues with the UBPT system studied in Chapter 4, and considers its use in a realistic highway bridge structure. A comparison is made between the use of conventional RC columns and UBPT columns using PEER's PBEE assessment methodology. Specifically, expected damage from peak and residual drifts in the columns is assessed. The improvement to the performance of the bridge with UBPT columns is evaluated, and the performance of code-conforming RC columns is evaluated. Finally, sensitivity to the assumptions made in the assessment is evaluated.

In Chapter 6, additional methods for providing further improvements to post-earthquake performance of UBPT bridge columns are investigated. Namely, the use of damage-tolerant HPFRCC materials and steel jacketing are considered. A performance assessment using PEER's PBEE methodology is again carried out considering two additional candidate bridges making use of the aforementioned technologies. Their performance is compared against the bridges with conventional RC columns and ordinary UBPT column of Chapter 5.

Chapter 7 concludes the report with a summary of the research and important results. The primary conclusions of the research are given, and possible areas of future research are discussed.

2 Background and Literature Review

2.1 INTRODUCTION

In this chapter, a review of background information and recent research important to this report are given. A summary of PEER's PBEE assessment methodology is presented first. Next, the current design of highway bridges in seismic regions and their expected response is presented followed by a review of recent research on self-centering systems. Finally, a review of high-performance fiber-reinforced cementitious composite (HPFRCC) is given. HPFRCCs are discussed in detail because of their unique properties, which provide a number of structural improvements but also present modeling challenges.

2.2 PEER’S PBEE METHODOLOGY

In a broad sense, performance-based engineering is “based on the premise that performance can be predicted and evaluated with confidence in order to make, together with the client, intelligent and informed tradeoffs based on life-cycle considerations rather than construction costs alone (Krawinkler REF).” This idea can of course be extended to earthquake engineering, and stands as the fundamental basis of the methodology for performance-based earthquake engineering developed by the Pacific Earthquake Engineering (PEER) Center as part of a ten-year, multi-disciplinary effort sponsored by the Earthquake Engineering Centers program of the National Science Foundation. The methodology developed by PEER stands as the state of the art at the current time, and will be the basis of the assessment used in this research. Several descriptions of the methodology have been presented in recent work (Porter 2003; Moehle and Deierlein 2004).

Early forms of PBEE design and assessment, such as ATC-32, ATC-40, FEMA 273, FEMA 356 and SEAOC’s Vision 2000 (ATC 1996a, 1996b; FEMA 1997, 2000; SEAOC 1995), made great advances in the name of performance-based design by explicitly considering the post-earthquake condition of structures. Common to all of these is the description of a set of performance-states of a structure following an earthquake (e.g., immediately operational, life safety, and near collapse) that are performance objectives to be met for various seismic events and to be decided upon by the owner and engineer. One of the primary limitations of these preliminary guidelines for PBEE was that many of the portions were based on simplified techniques (e.g., prediction and definition of seismic hazard, methods of structural analysis, prediction of component and structure performance) and did not take into account the wealth of new scientific information and advances available from the many disciplines involved. The methodology for PBEE as developed by PEER seeks to examine more rigorously the individual components involved in earthquake engineering and to combine them in a formalized framework for the seismic design and assessment of structures, using the most recent scientific and engineering information and related technologies and that produces quantifiable decision metrics. The entire procedure is conducted in a probabilistic manner, such that the inherent and often large uncertainties present in the individual disciplines involved can be incorporated in the analysis.

The PEER PBEE methodology is broken into four individual steps: (1) hazard analysis, (2) structural analysis, (3) damage analysis, and (4) loss analysis. The results of each of these steps represented as generalized variables are, respectively, intensity measure (IM), engineering demand parameter (EDP), damage measure (DM), and decision variable (DV). These generalized variables will be discussed in more detail in following sections. The relationship between the four steps can be represented schematically as shown in Figure 2.1. A Markovian independence is assumed in that the conditional probabilities of each step are assumed to be dependent on only the previous step and no others.

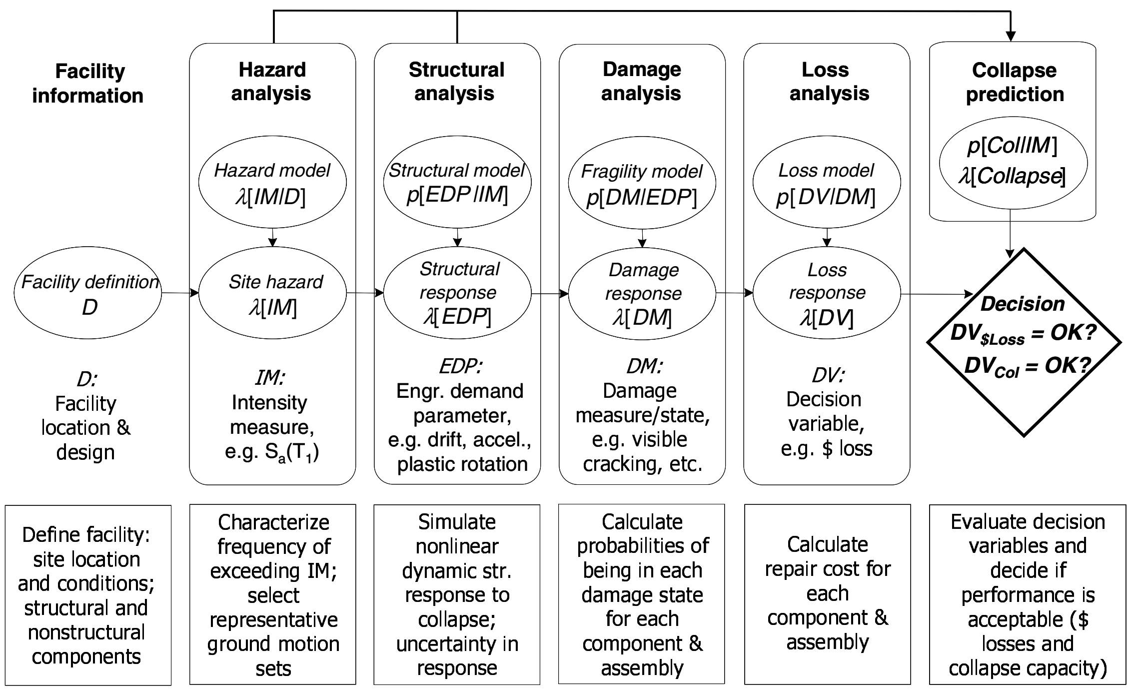

Fig. 2.1 Framework of performance-based earthquake engineering by PEER (after Haselton et al. 2005).

Using the Total Probability Theorem, the framework can be described mathematically using the following equation:

$$v(DV) = \iiint G(DV \mid DM) \cdot \left|dG(DM \mid EDP)\right| \cdot \left|dG(EDP \mid IM)\right| \cdot \left|d\lambda(IM)\right| \qquad (2.1)$$

In this equation, $d\lambda(IM)$ is the derivative of the mean annual frequency of exceeding a given IM value. The absolute value signs are required where the values are negative. $G(X|Y)$ is shorthand notation for the complementary cumulative probability distribution function for X given Y, as shown in Equation 2.2:

$$G(X \mid Y) = P[X \geq x \mid Y = y] \qquad (2.2)$$

In the remaining terms, $dG(Y|Z)$, is shorthand notation for the conditional probability distribution function for Y times dy, as shown in Equation 2.3:

$$dG(Y \mid Z) = f_{Y|Z}(y,z) \cdot dy \qquad (2.3)$$

The result of this equation, $v(DV)$ is the mean annual frequency of exceeding a given value of DV. In this equation, it is easily seen how the individual steps are related.

The advantage of this framework is that each of the four intermediate steps can be considered individually without consideration of the other steps. Therefore, scientists and engineers can focus their attention on their respective areas of specialty, while still contributing to the overall goal of analysis or assessment of a structure. For example, a structural engineer can perform advanced nonlinear dynamic analysis on a detailed structural model, without requiring in-depth knowledge of seismology, as the hazard curve can be obtained from seismologists or geotechnical engineers.

2.2.1 Hazard Analysis

The first step is the hazard analysis, which produces one or more intensity measures, or IMs. The IM is used to represent the intensity or strength of an earthquake, and is typically represented by such values as spectral acceleration or peak ground acceleration. However, recent research on a number of improved scalar (e.g., inelastic spectral displacement) and vector (e.g., elastic spectral acceleration with epsilon) IMs has also shown promise (Tothong and Cornell 2006a; Baker and Cornell 2005). The rate of exceedance of a given value of IM is typically given as the mean annual frequency of exceedance, and is represented with a hazard curve, which can be generated using a conventional probabilistic seismic hazard analysis (PSHA). Background on hazard curves and PSHA can be found in, for example, Kramer (1995). A typical hazard curve, as shown in Figure 2.2, plots the mean annual frequency of exceedance of an IM, such as spectral acceleration, versus the IM.

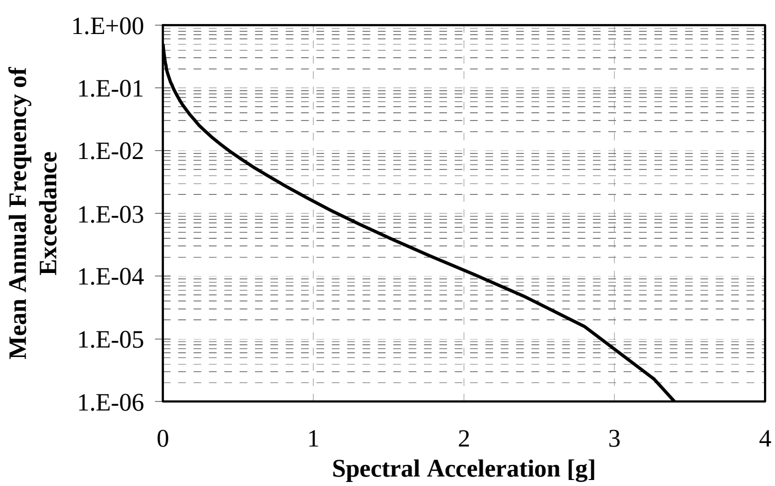

Fig. 2.2 Example hazard curve for spectral acceleration.

2.2.2 Structural Analysis

The second step is the structural analysis, in which a numerical model of the structure of interest in generated and subjected to analysis in order to predict engineering demand parameters (EDPs) given an IM. Models can be either linear or nonlinear, and analysis methods can be static or dynamic. These EDPs attempt to characterize the response of the structure under earthquake loading, and are represented with such values as drift or acceleration. A number of techniques have been developed to generate relationships between the IM and EDP. Perhaps the most commonly used of these is the incremental dynamic analysis procedure, often referred to simply as IDA (Vamvatsikos and Cornell 2002). IDA can be thought of as the dynamic equivalent of the nonlinear static pushover procedure. Given a structural model and an earthquake ground motion record, a series of nonlinear dynamic analyses are performed with the ground motion record scaled to increasing levels of an IM. The EDP of interest is then plotted against the IM to produce a "dynamic pushover curve." This is typically done with a suite of ground motions such that a sample of EDP values can be generated for each IM value. Alternative techniques include *stripe* analysis, which is similar to IDA except that the ground motions are not necessarily identical at the different scaling levels, and *cloud* analysis, in which no scaling of records is performed and records are chosen to capture a wide range of intensities.

An example IDA curve for a reinforced concrete building structure with an IM of spectral acceleration at the first mode period and an EDP of maximum interstory drift ratio is shown in Figure 2.3 (Deierlein and Haselton 2005). The plot is useful in that it shows both a range of values for an EDP given an IM level, as well as the IM level at which the structures reach a point of dynamic instability, or collapse (identifiable by the level at which the IDA curve begins to "flatline"). Note that contrary to conventional plotting methods, the IM, which is considered to be the independent variable, lies on the ordinate, while the EDP, which is considered to be the dependent variable, lies on the abscissa. This method of plotting is chosen to give the more familiar appearance of a pushover curve, which has base shear (force) on the ordinate and displacement on the abscissa.

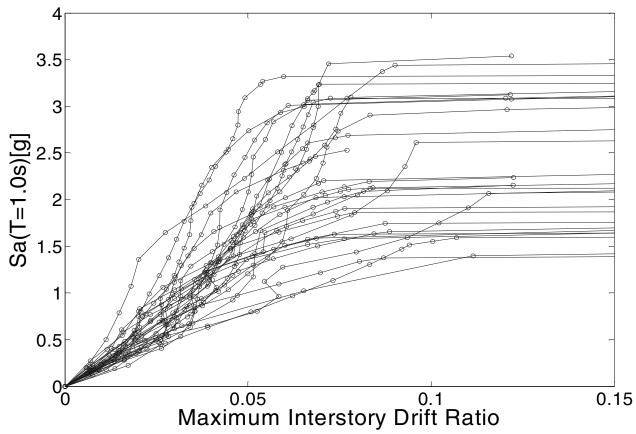

Fig. 2.3 Example IDA plot (Deierlein and Haselton 2005).

2.2.3 Damage Analysis

The third step is the damage analysis, in which damage in structural or nonstructural components is predicted based on EDP values. Damage measures (DMs) are typically represented by physically observable states of damage in a component that can be related to required courses of action such as repair or replacement. Examples include cracking in partition walls or spalling of cover concrete in columns. The relationship between EDP and DM is represented with a fragility curve, which gives the probability of being in or exceeding a DM given a value of EDP. The fragility curve is therefore a cumulative distribution function (CDF) of the probability of damage given an EDP. The development of EDP-DM relationships is typically based on available data from experimental testing or observed damage from previous earthquakes. For example, relationships between drift and certain damage states were developed based on statistical analyses of a database of experimental results for reinforced concrete columns (Berry and Eberhard 2003) and slab-column connections (Aslani and Miranda 2005). In cases where experimental data are limited or do not exist, judgment or “expert opinion” can be used, or reliability analysis can be used in conjunction with computer simulation to generate these relationships.

Example fragility curves for reinforced concrete slab column-connections with four damage states (light cracking, severe cracking, punching shear failure, and loss of vertical carrying capacity) are shown in Figure 2.4 (Aslani and Miranda 2005). Figure 2.4a shows the fitting of a fragility function to data assuming a lognormal distribution. Figure 2.4b shows the fragility curves for all four damage states. The EDP, or interstory drift ratio (IDR) in this case, is on the abscissa, while the probability of being in one of the four damage states is on the ordinate. To interpret the fragility curve, consider Damage State 3 (DS3) on Figure 2.4b, which is the occurrence of punching shear failure. At an IDR of 0.050, there is an approximately 70 percent probability that the slab-column connection will experience a punching shear failure.

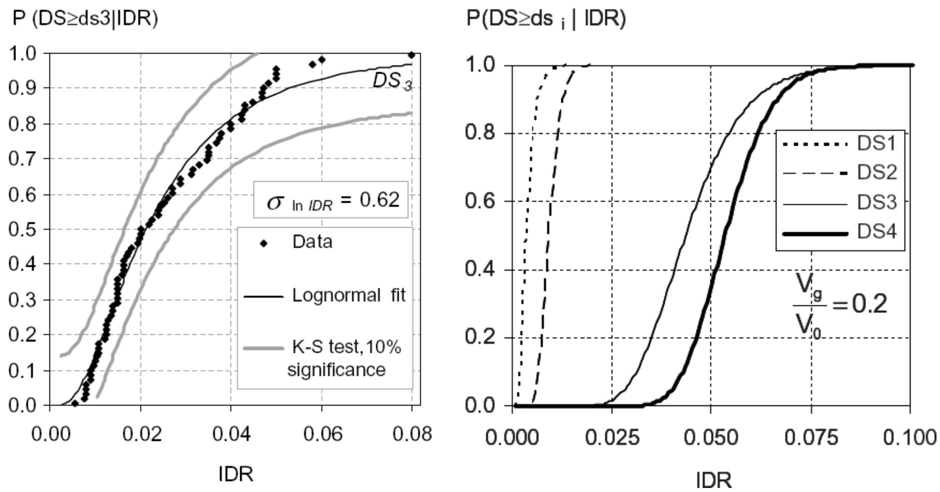

(a) (b)

Fig. 2.4 Fragility curves for slab column connections (from Aslani and Miranda 2005).

2.2.4 Loss Analysis

The final step is the loss analysis, in which losses are predicted based on damage sustained by the structure. The losses are typically represented by values that are meaningful to an owner or decision maker of a structure, such as direct monetary losses, downtime, and casualties. Far less research has been performed in this area as opposed to the other three steps. Direct repair costs for certain components can be estimated from construction cost estimation references such as R.S. Means (R.S. Means 2007), while the likely more significant indirect losses due to downtime of facilities can not be estimated as readily.

2.2.5 Summary of PEER PBEE Methodology

The development of the PBEE methodology by PEER provides a powerful tool for quantitatively assessing the behavior of new or existing structures in terms of both structural and nonstructural (but perhaps equally important) performance objectives, which in turn allows owners and decision-makers to make informed choices on design or retrofit options for structures. In addition, the methodology provides a means of quantitatively assessing structures that utilize new materials and/or technologies, something that is not possible with current design codes and guidelines. Such an assessment of using new materials and technologies in structures can provide information on the possible benefits of their use compared to that of conventional systems. This can help to speed the implementation of such materials or technologies in current design. For these reasons, the PEER PBEE methodology will be employed to assess the enhanced-performance column system for structural concrete bridges by comparing its performance to that of a traditional column system.

2.3 POST-EARTHQUAKE FUNCTIONALITY OF REINFORCED CONCRETE BRIDGES

A major goal of this research is to assess the possible improvements that can be brought to conventional reinforced concrete highway bridges through use of enhanced-performance materials and technologies. Reinforced concrete bridges have seen extensive damage in recent earthquakes, which directly affects the transportation network. To properly assess the performance behavior of RC highway bridges, it is important to first understand current design of these bridges, as well as their observed performance in earthquakes.

In current practice, the design of bridges in highly seismic regions such as California takes into consideration performance criteria following a seismic event. The seismic performance criteria for the design of bridges according to the California Department of Transportation's (Caltrans) Bridge Design Specifications and Seismic Design Criteria are summarized as follows (Caltrans 2001). Ordinary bridges should meet the following performance criteria: (1) Under the Functional-Evaluation ground motion, a bridge should maintain *immediate* service level and sustain only *repairable* damage, and (2) Under the Safety-Evaluation ground motion, a bridge should be in the *limited* service level or better, and can sustain *significant* damage. The *immediate* service level is achieved when "full access to normal traffic is available almost immediately following the earthquake," while the *limited* service level is achieved when "limited access (e.g., reduced lanes, light emergency traffic) is possible within days of the earthquake; full service is restorable within months." The repairable damage level is defined as "damage that can be repaired with a minimum risk of losing functionality," while significant damage is defined as having "a minimum risk of collapse, but damage that would require closure and repair."

As current codes produce designs that ensure *immediate* service levels following the functional-evaluation ground motion, the question arises as to why the performance of code-conforming bridges should be evaluated for post-earthquake functionality. The answer lies in the fact that a number of specified components of a bridge are expected to undergo significant inelastic deformations under the functional- and safety- evaluation ground motions. These large inelastic deformations, specifically in the columns, may therefore be expected to lead to substantial residual displacements, thereby preventing a bridge from being in the immediate service level. Residual displacements are not taken into consideration in current design.

The importance of residual displacements on post-earthquake functionality of bridge structures was highlighted following the 1995 Hyogo-Ken Nanbu (Kobe) earthquake in Japan. Following that earthquake, a large number of reinforced concrete bridge columns sustained severe damage, including large residual displacements (Ito et al. 1997; Kawashima and Unjoh 1997; Shiramama et al. 1998). Approximately 100 reinforced concrete columns had to be demolished and removed due to residual displacements exceeding 1.75 percent drift (a tilt angle of 1 degree) even though they had not collapsed (Kawashima et al. 1998). Residual displacements can make repair difficult and also lead to misalignment of the superstructure, making repair and use of the bridge expensive and difficult, or even impossible. Finally, residual displacements have been shown to be an important parameter in determining the post-earthquake capacity of bridges (Mackie and Stojadinovic 2004) and buildings (Bazzurro *et al.* 2004, Luco *et al.* 2004) to sustain aftershocks.

Given the importance of residual displacements, a number of studies have been performed for prediction of residual displacement demands following an earthquake (discussed in Chapter 4). In addition, limits on residual displacements have been incorporated into some codes, such as the seismic design criteria of the Japan Road Association's Design Specifications for Highway Bridges (Japan Road Association 2006). In the United States, however, the attention paid to residual displacements has been more limited, with no requirements for residual displacements in codes, and only mention of them in recommended provisions (Federal Emergency Management Agency 2000). The likelihood of significant loss of function of bridges due to excessive residual displacements should therefore be assessed for code-conforming bridges.

2.4 SELF-CENTERING SYSTEMS

To mitigate the problem of residual displacements, several innovative systems with the goal of providing self-centering have been developed and been a focus of study in the earthquake engineering community in recent years. One type of self-centering system for bridges involves allowing for controlled rocking of the piers under lateral loading, with the motion controlled by post-tensioning or other passive energy-dissipating devices. Mander and Cheng (1997a) performed experimental studies on a concrete bridge pier system in which the piers would act as rigid bodies and rock under lateral loading, with lateral displacement controlled with unbonded post-tensioning. The restoring force arises from the gravity force of the structure itself. Pollino and Bruneau (2005) performed numerical studies on the seismic design and behavior of a similar system for steel truss bridge piers. Again, rocking of a pier as a rigid body is expected, with the rocking controlled by the use of buckling-restrained braces acting as passive energy-dissipating devices.

The second type of system uses unbonded post-tensioning (UBPT) as the primary means of providing lateral resistance to concrete structures. The fact that the post-tensioning is unbonded rather than bonded means that strains in the member will not localize in the post-tensioning tendons at cracking locations. The even distribution of member strains to the entire length of the tendons leads to significantly lower strains in the tendons. The member can then be designed such that the post-tensioning strands will be expected to stay elastic even under conditions approaching failure. The cyclic behavior of the member will therefore be expected to be origin oriented with some energy dissipation. Additional energy dissipation can be provided through use of bonded reinforcing or through other means. The origin-oriented behavior is expected to minimize residual displacements that would be expected from bonded post-tensioned or traditional reinforced concrete systems. The behavior of the unbonded post-tensioned system as compared to a system with bonded reinforcement (mild or post-tensioned steel) is schematically shown below in Figure 2.5.

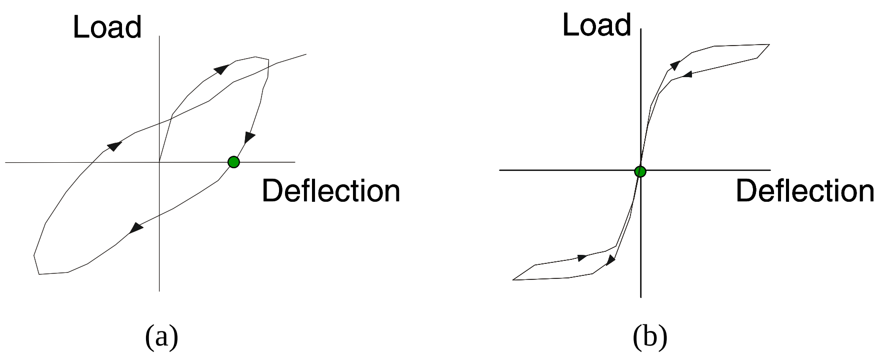

Fig. 2.5 Typical load deflection between behavior for (a) bonded steel and (b) unbonded post-tensioned steel systems.

The first study on such a system for seismic application is attributed to the precast seismic structural systems (PRESS) research program (Priestley et al. 1999). In this large-scale experimental study, a number of new seismic structural systems were investigated for precast concrete frame buildings. One of these systems was the use of UBPT as the only means of connecting the precast beams and columns, with no bonded reinforcing between them. Similarly to the rocking systems described above, the beams and columns are expected to act as rigid bodies, with nonlinear behavior concentrated at the interface between the two members, as the gap will open and close under cyclic loading.

Several analytical studies on modeling the cyclic and seismic behavior of these UBPT beam-column joints, as well as frames utilizing these types of joints, have been performed by a number of researchers. Priestley and Tao (1993) performed time-history analysis on simplified SDOF models of UBPT systems to assess displacement response under seismic loading. El-Sheikh et al. (2000) performed cyclic modeling and validation of the same UBPT beam-column connections with more advanced fiber element models. Time-history analyses were also performed on frame structures with the UBPT connections to evaluate seismic response using simplified models (Cheok et al. 1998) and using fiber element models (El-Sheikh et al. 1999).

A UBPT system has also been proposed for concrete walls in which precast wall segments that do not contain continuous, bonded reinforcing across the horizontal joints are connected with vertical UBPT. The lack of continuous bonded reinforcing across the joints means that lateral deformations in the walls will be manifested in the form of gap opening between the precast segments. Kurama et al. (1999, 2002) performed numerical studies on the cyclic and dynamic behavior using fiber element models to assess the dynamic behavior of the system and to develop seismic design guidelines. Kurama (2001) performed numerical studies using fiber element models on the same system but with the addition of supplemental friction dampers to provide energy dissipation. Perez et al. (2004a, 2004b) performed similar studies, again with fiber element models, on a related UBPT wall system, except with vertical rather than horizontal joints.

The use of UBPT to provide self-centering to concrete bridge columns has also been considered in much research. The idea of using vertical prestressing in columns to reduce residual displacements has been in existence for several years. Zatar and Mutsuyoshi (2000) performed small-scale cyclic experimental tests on partially prestressed concrete columns to quantify reductions in residual displacements based on initial work on vertically prestressed columns by Ikeda (1998).

Kwan and Billington (2003a, 2003b) evaluated the behavior of UBPT columns in single-bent and multiple-bent configurations with varying ratios of the amount of bonded mild steel reinforcing to unbonded post-tensioning using detailed continuum models as well as simplified equivalent SDOF models for dynamic analyses. Cyclic analyses on detailed continuum models showed that increases in the proportion of UBPT to bonded reinforcing resulted in reduced energy dissipation, but also resulted in reduced residual displacements. Time-history analyses using a suite of ground motions on equivalent SDOF models calibrated to the continuum models showed that increases in the proportion of UBPT to bonded reinforcing resulted in larger peak displacements (attributed to the lower energy dissipation), while again resulting in lower residual displacements.

Billington and Yoon (2004) performed small-scale quasi-static cyclic tests on precast, segmental UBPT columns. The hinge segments of the columns were made of either concrete or a fiber-reinforced cement composite material intended to provide energy dissipation to the system, for a type of system illustrated in Figure 2.6. The HPFRCC material was found to add energy dissipation to the system at low drift levels, and also sustained much lower damage than the concrete segments, and overall the columns sustained low residual displacements. A large-scale experimental program based on these small-scale tests was performed by Rouse and Billington (2005). The experimental program consisted of the quasi-static, cyclic testing of precast, segmental UBPT columns in double-curvature with either concrete or fiber-reinforced cement-composite material in the expected hinge segments. Again, low residual displacements were observed in the columns, and the columns with concrete hinges had lower energy dissipation and more damage than their fiber-reinforced counterparts.

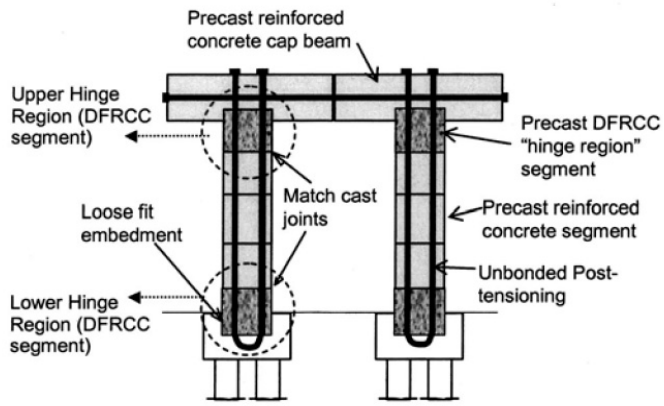

Fig. 2.6 Unbonded post-tensioned concrete bridge pier system with HPFRCC hinges (after Billington and Yoon 2004).

Finally, a series of numerical and experimental studies on the dynamic behavior of UBPT bridge columns has recently been completed by Sakai et al. (Sakai and Mahin 2004; Sakai et al. 2005). Recommendations for design of circular UBPT concrete columns, consisting of the replacement of bonded longitudinal reinforcing with a single concentric strand of unbonded post-tensioning, were developed based on cyclic analyses using fiber element models. Time-history analyses of the same fiber element models using a suite of ground motions showed that the peak displacements for the UBPT columns were similar to those of conventional RC columns, but with significant reductions in residual displacements. Large-scale specimens that were designed based on the guidelines obtained from the numerical studies were constructed and tested dynamically on a bi-directional shaking table with varying levels of ground motion intensity. The experimental results verified the results from the simulations, with similar peak displacements demands seen in both types of columns, but with the UBPT column having much lower residual displacements. Under repeated subjection to high-intensity shaking, the UBPT column continued to retain low residual displacement but eventually failed in a brittle manner. Further tests on additional specimens with modification to the hinge region of the column to improve performance (such as the use of steel jacketing) met all performance objectives, maintaining low residual displacements and not having brittle failure modes.

2.5 HIGH-PERFORMANCE FIBER-REINFORCED CEMENT COMPOSITES

In addition to providing self-centering to bridge columns, a second method for improving the performance of bridges subjected to earthquake loading is considered which consists of attempting to reduce the damage sustained in the columns by using advanced materials. Under cyclic lateral loads, reinforced concrete columns will have spalling of concrete cover which requires patching. In addition, the loss of cover can lead to buckling of longitudinal reinforcing. The use of recently-developed enhanced-performance fiber-reinforced cement-based materials as a replacement for easily damaged concrete in bridge columns has been proposed and is considered in this research.

2.5.1 Introduction to HPFRCC

Ordinary, unreinforced cement-based materials such as mortar and concrete possess poor tensile characteristics, displaying brittle behavior with low strengths and strain capacities. The addition of fibers to concrete has been shown to improve the mechanical properties of concrete in many ways. The most common reason for adding fibers is to improve the tensile properties of concrete, in terms of strength, ductility and toughness. Traditional fiber-reinforced concretes (FRCs) are characterized by quasi-brittle, or strain softening, behavior in tension, with first cracking followed by immediate crack localization. This behavior limits the FRCs primarily to nonstructural applications. FRCs are created by simply adding metallic or polymeric fibers to the concrete mix in relatively low volume fractions (typically less than 2 percent).

A superior class of materials, known as high-performance fiber-reinforced cement composites (HPFRCCs), are defined to possess better mechanical properties than traditional FRCs, most notably with several types displaying pseudo-strain-hardening behavior. The term *pseudo-strain hardening* (Li 1998) refers to the fact that after first cracking, the material will continue to gain strength with increasing strain, appearing similar to the strain-hardening behavior of many metals. Many HPFRCCs typically contain steel fibers at large volume fractions, often greater than 5 percent. Such large volume fractions of fibers make mixing and placing of these HPFRCCs difficult.

HPFRCCs are referred to as cement composites rather than concretes simply because many of the materials in this class do not use coarse aggregate. One example is the engineered cementitious composites (ECCs). ECCs possess strain-hardening behavior because the mix constituents are specifically proportioned and designed to achieve such behavior based on micromechanics principles (discussed in Section 2.5.2), hence the name *engineered* cementitious composite.

The improved tensile properties of ECC and other HPFRCC materials have made their use attractive to engineers in many applications where their properties can be beneficial, such as in earthquake engineering. The material proposed for use in this research is an ECC material; therefore detail will be given in following sections on the composition and behavior of this unique material.

2.5.2 ECC Material Behavior and Composition

The pseudo-strain-hardening behavior of ECCs is dependent on the ability of the composite material to undergo steady-state cracking (Li and Leung 1992). A simplified view of the steady-state cracking phenomenon will described as follows. A more detailed description can be found in Marshall et al. (1985), Li and Leung (1992), Li and Wu (1992), and Li (1993). After first cracking of the matrix occurs in a fiber composite material, the extension of the crack is resisted partly by the matrix material but primarily by the fibers bridging across the crack flanks. As the crack opens and extends through the matrix, the fiber bridging stress increases as the bridging zone increases and the fibers begin to debond and pull out. The crack begins to flatten as the bridging stress approaches the applied stress. When the bridging stress reaches the applied stress, the crack will continue to extend without an increase in applied stress; at this point the steady-state cracking stress has been reached. As the stress at the crack can be sustained by the bridging of the fibers, the applied load can be increased, allowing for the formation of additional cracks within the matrix. The presence of such distributed cracking is characteristic of ECC materials. This behavior is in sharp contrast to traditional FRCs, where the first crack localizes immediately and a decrease in load occurs with crack further opening.

To achieve this steady-state cracking behavior in a fiber composite material is not a straight-forward procedure, and can not be achieved without careful selection and proportioning of the materials with the desired properties. The matrix, fibers, and interfacial bond between the two must be carefully tailored to achieve the desired behavior. For example, to ensure that the fibers will pull out from the matrix rather than rupture is dependent on both the length of the fibers as well as the interfacial bond. If the combination of the interfacial bond and fiber length leads to a condition where the fibers will rupture rather than pull out, steady-state cracking can not be achieved. Fiber length can be easily changed, while interfacial bond can be modified with the use of chemical surface treatments to the fibers. As another example, the toughness of the matrix material must be selected such that the cracking strength is lower than the maximum bridging strength of the fibers. The matrix toughness can be controlled by selection of the water-to-cement ratio, aggregate size, etc. A more detailed description of the tailoring of mix constituents and proportions for pseudo-strain-hardening materials with steady-state cracking can be found in Li and Leung (1992), Li et al. (1995), and Li (1998).

Considering the requirements to achieve steady-state cracking, as well as the limits based on practical constraints (such as cost and workability) leads to an optimization problem of sorts to select the constituent proportions. The design of mix proportions will not be discussed here. The reader is referred to (Li and Leung (1992) and Li et al. (1995) for more detail on this subject. However, typical materials used and typical proportions of ECC will be presented here.

Typical ECCs contain Type I or Type I/II Portland cement, water, fine sand, fly ash, and roughly 2 percent or less by volume of high aspect ratio, typically polymeric fibers. In addition, chemical admixtures are typically added, such as viscosity-modifying admixtures (e.g., methyl cellulose) to improve dispersion of the fibers during mixing and high-range water-reducing admixtures (superplasticizers) to improve workability. The use of fine cementitious materials (fly ash or in early mix designs, silica fume) is to improve matrix-fiber bond. A number of materials for fibers have been successfully employed in ECCs, including polyvinyl alcohol (PVA) and ultra-high molecular weight polyethylene (UHMWPE). PVA fibers in particular have been developed with tailored surface properties to achieve necessary interfacial bond properties when mixed with the cement-based material. The price of fibers plays a large role in their selection in addition to chemical and mechanical properties. As stated previously, ECCs do not contain coarse aggregates.

2.5.3 Mechanical Behavior

As mentioned previously, the mechanical behavior of ECCs is different from concrete or traditional FRCs. The behavior differs in both monotonic tension and compression, as well as under cyclic loading. While the difference in behavior in tension is the distinguishing feature of

ECCs, the compressive behavior is also noteworthy. These differences will be discussed in the following sections.

2.5.3.1 Monotonic Tensile Behavior

As stated in Section 2.5.2, ECCs are defined to possess pseudo-strain-hardening behavior in tension due to their inclusion in the class of HFRC materials. Typical behavior consists of linear behavior to first cracking, followed by pseudo-strain hardening to strains between 0.5–6 percent (Li 1998), which corresponds to the steady-state cracking of the material. The peak stress is reached, corresponding to the point at which the crack localization finally occurs, after which softening will occur either rapidly or more gradually. As expected, the stress and strain at first cracking and at peak varies depending on the fiber type and mixing proportions. The difference in behavior between ECC (and other HPFRCCs) and traditional cement-based materials such as mortar and ordinary fiber-reinforced concrete can be seen in Figure 2.7. Again, mortar displays brittle behavior, while traditional fiber-reinforced concretes display quasi-brittle, or strain-softening, behavior.

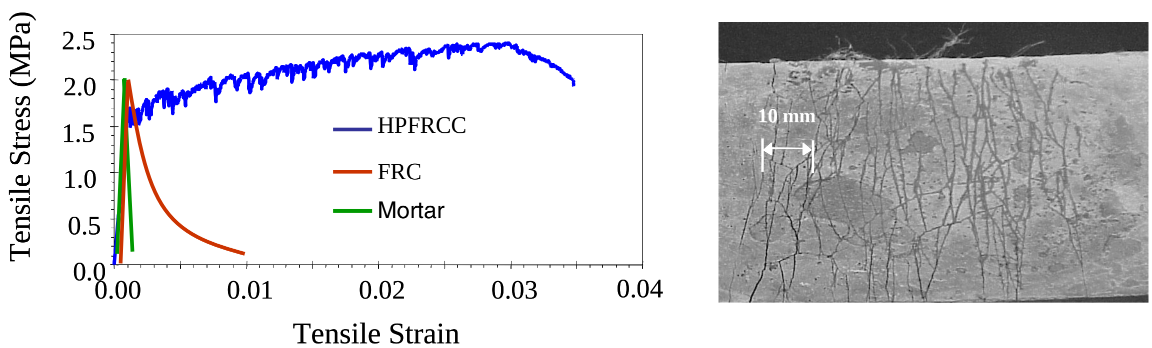

Fig. 2.7 Tensile stress-strain behavior of HPFRCC as compared to traditional cement-based materials; multiple, fine cracking behavior of tensile specimen (adapted from Kesner et al. 2003).

The occurrence of steady-state cracking in the ECC leads to the development of multiple, fine cracks in the matrix during loading rather than the formation of a single, large crack. These cracks are about only 100 μm in width (Li and Leung 1992). The multiple, fine cracking behavior as seen in a tensile specimen can be seen in Figure 2.7. In terms of damage tolerance of the material, which is an important factor in the context of performance-based engineering, the much finer cracking of the ECC makes it superior to that of ordinary concrete. When used in structural applications with steel reinforcing, this fine cracking can reduce the ingress of damaging chemicals and moisture. In addition, there are aesthetic benefits to fine cracking as opposed to having larger cracks.

While high-strain capacities have been obtained from uniaxial tensile tests for many ECCs, their magnitudes have been found to be highly dependent on specimen size and geometry (e.g., Kesner and Billington 2004; Kanakubo et al. 2005). Many results on early ECC research are based on the testing of thin, plate-like specimens (Li 1998, Li et al. 2001). The low thickness of the specimens relative to the size of the fibers leads to orienting of the fibers in the direction of loading. In a larger specimen that would be more representative of a structural member, such preferential orienting of the fibers would not occur, leading to lower strain capacities. Tests on identical mix designs of PE (Kesner and Billington 2004) and PVA (Kanakubo et al. 2005) ECCs with varying specimen geometries (e.g., cylinders, dog-bones, plates) have shown significantly different behavior depending on the specimen geometry. For example, for the PVA-ECC specimens tested by Kanakubo et al. (2005), the average strain at peak stress for a set of 13-mm-thick plate specimens was 2.26 percent, while the average strain at peak stress for the same material used in 100-mm-diameter cylinders was only 0.32 percent.

*2.5.3.2 **Monotonic Compressive Behavior***

Much like ordinary concrete, the compressive strength of ECC is highly variable, and depends strongly on the mixing proportions. The water-to-cement ratio and use of additional cementitious or pozzolanic materials are two primary factors in determining the compressive strength. Typical strength values are similar to that of ordinary concrete, ranging from around 35 to 70 MPa (Kesner et al. 2003). However, as the stiffness of concrete is largely determined by the aggregate, so too is that of ECC. The absence of coarse aggregate, which is typically the stiffest component of concrete, leads to an elastic modulus of ECC that is considerably lower than that of concrete. Again, the difference in modulus of ECC varies depending on the mixing proportions, but is generally about half of that of a concrete with a similar compressive strength (Kesner et al. 2003).

In terms of strain capacity, the strain at peak stress is generally larger than that of ordinary concrete (Fig. 2.8a). The higher strain is due to the lower compressive stiffness of the ECC. After the peak load is reached, the load begins to drop rapidly; however, this softening is much less brittle than that of ordinary concrete. While ordinary concrete will break apart immediately after reaching its compressive strength, the ECC is able to hold itself together (Fig.

2.8b). The more ductile behavior of the ECC arises from the presence of the fibers and because they are able to hold the matrix together, albeit loosely, after the peak strength has been reached. In this way the ECC is a self-confining material, and is much more damage tolerant than ordinary concrete, which again is a key consideration in the context of performance-based engineering.

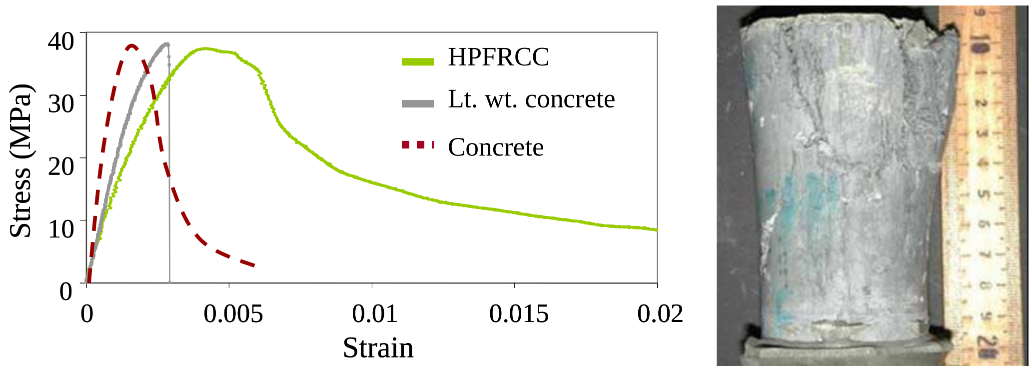

(a) (b)

Fig. 2.8 (a) Compressive stress-strain response of HPFRCC compared to traditional cement-based materials, and (b) absence of spalling in compression cylinder (scale in cm) (Kesner et al. 2003)

Little research has been conducted at this point in time on the compressive behavior of confined ECC. As with ordinary concrete, lateral confinement in the form of spiral or tie reinforcing may be expected to increase the compressive strength and ductility of ECC. Small-scale studies on 5-cm-diameter ECC cylinders with and without spiral reinforcing showed these two trends to hold for ECC, with increases in compressive strength and ductility being observed for the cylinders with spiral reinforcing (Olsen and Sulc 2004). Further research and testing on a larger scale is required to produce more reliable data and to develop predictive equations for confinement effects with ECC.

2.5.3.3 ***Cyclic Behavior***

For use in such applications as earthquake engineering, the cyclic behavior of ECC must be considered. The behavior of ECC under cyclic compression and cyclic tension-compression has been investigated by Kesner and Billington (2004). ECC was found to possess cyclic loading and unloading behavior that was notably different from that of ordinary concrete and other cement-based materials. Several types of ECC were tested, and similar behavior was observed for all types. Under cyclic compression, the ECC was found to unload and reload essentially elastically when loaded to levels before the peak stress. Unloading in the post-peak region was found to occur parabolically. Reloading also occurred parabolically, but with a greater stiffness than the unloading. The results from a typical cyclic compression tests for ECC with PVA fibers can be seen below in Figure 2.9a. The cyclic loading was not found to affect the peak strength and strain of the ECC, and the monotonic loading curve was found to provide a reasonable approximation of the cyclic loading envelope. This is an important finding, in that it is shown that results from monotonic tests can be used in cyclic constitutive models for ECC materials.

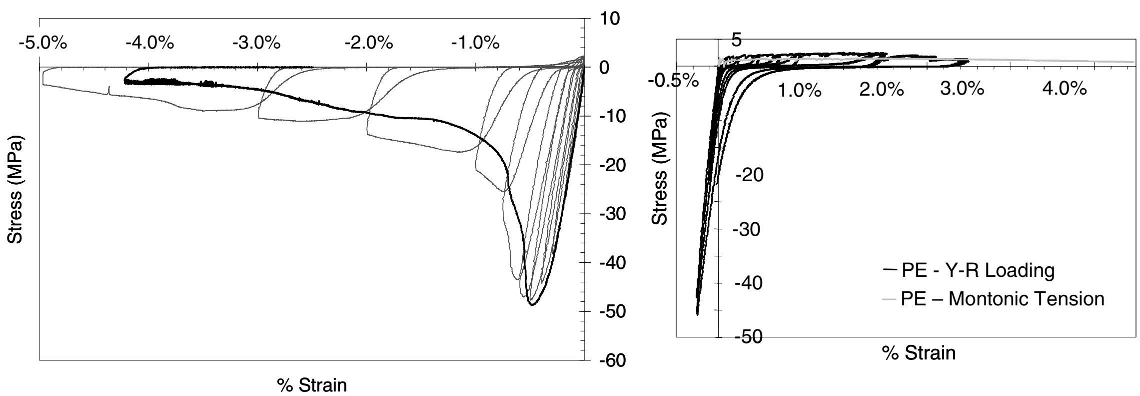

(a) (b)

Fig. 2.9 (a) Typical cyclic compressive behavior of HPFRCC with monotonic response superimposed and (b) typical cyclic tension-compression behavior of HPFRCC (Kesner et al. 2003)

In cyclic tension-compression, the ECC mixes were again found to display similar behavior. The primary finding from the cyclic tension-compression testing was that the tensile strain capacity was unaffected by compressive loading if the peak compressive stress of the ECC was not reached. However, if at some point in the cyclic loading the peak compressive stress was reached, the peak tensile strain that could be achieved was reduced. Aside from this, the cyclic loading envelopes could again be reasonably well approximated by the monotonic loading curves. The results from a typical cyclic tension-compression test for ECC can be seen in Figure 2.9b.

2.5.3.4 ***Load Rate Effect***

Another important consideration for the use of ECC is earthquake engineering applications is the effect of loading rate on the mechanical properties. Unlike many loads experienced by civil engineering structures, earthquake loading is dynamic and the inertial loads generated from earthquake shaking result in extremely high loading rates on structures and their components. The mechanical properties of many structural engineering materials, such as steel and concrete, are highly dependent on loading rate. For example, large increases in loading rate (by around 3 orders of magnitude, a reasonable increase in the realm of earthquake loading) has been shown to increase the compressive strength of concrete by approximately 30 percent (Neville 1996). The stiffness is also increased significantly.

The behavior of ECC under variable load rates was investigated by Douglas and Billington (2006). A set of ECC cylinder specimens was tested under several loading rates, including a rate intended to represent that of earthquake loading. The cylinders were found to have increases in both tensile and compressive strength and stiffness of about 15 to 35 percent. The tensile strain capacity, however, was reduced by approximately 50 percent. In addition, the strain at peak compressive strain was also reduced by roughly 10 percent. These factors should be considered in simulations of structures under dynamic earthquake loading.

2.5.3.5 ***Test Specimen Shape and Other Effects***

Many ECC tension specimens are thin, plate-like specimens. This leads to orienting of the fibers in the direction of loading, which gives higher values than larger specimens, which would have more random fiber orientations. Another effect is the fact that ECC is generally cast in relatively small quantities in table-top mixers, where greater control over actual quantities of the components exists, which is an important factor for engineered materials such as ECC. For the ECC cast here, a large mortar mixer was used, which led to poorer control of mixing quantities, in addition to providing less energy for mixing and distributing the fibers than is seen from the more powerful table-top mixers (Douglas 2005).

2.5.4 Structural Applications

The improved tensile properties and damage-tolerant characteristics of ECC make its use appealing for many structural applications. ECCs have been proposed to add strength, ductility, and energy dissipation to a number of systems through replacement of concrete with ECC, or in the same way to minimize or eliminate the need for heavy reinforcing details that can cause congestion in members and joints while maintaining similar performance. Examples include RC coupling beams (Canbolat et al. 2005; Yun et al. 2005) and in beam-column connections (Parra-Montesinos et al. 2005). In terms of utilizing the energy-dissipation characteristics of ECCs, their use has been proposed to provide energy dissipation to systems that do not possess such characteristics, such as frames or members reinforced with FRP bars that do not yield (Fischer and Li 2003a, 2003b), and for retrofit applications for seismically deficient structures (Kesner and Billington 2005).

ECCs have been proposed for uses where their damage-tolerant characteristics make them appealing in the view of performance-based engineering. For example, their use has been proposed in the plastic hinging regions of bridge columns (Rouse and Billington 2003; Billington and Yoon 2004). This is partially to provide energy dissipation, but also to improve the damage tolerance, as ECC does not spall in compression, which minimizes repair costs and can help to prevent buckling of longitudinal reinforcing bars. Finally, ECCs have been proposed for use in members where crack-width control is critical, for both protecting reinforcing and maintaining impermeability, such as in bridge decks and water containment vessels. Other benefits of using ECCs in structural applications include their improved tension-stiffening characteristics.

While the lack of experience, minimal design guidelines, and relatively high initial costs of using ECC have limited their use in structural applications, continued research along with the adoption of performance-based guidelines, is helping to speed the process of their implementation. In fact, two large-scale structural applications of ECC have recently been completed in Japan. The first is the Bihara bridge in Hokkaido, Japan, where the entire bridge deck is composed of cast-in-place PVA-ECC (Li 2006). The second is the use of precast ECC coupling beams in high-rise residential buildings, also in Japan (Li 2006). More structural applications of ECC can be expected with future research and the success of the existing, previously mentioned applications.

2.5.5 Summary of HPFRCC Material Literature Review

The development of a fiber-reinforced cement-based material with low fiber volume fractions, tensile pseudo-strain-hardening behavior, and excellent damage tolerance has opened the door to a large number of promising structural applications. Through material development and testing, and finally through structural testing, the ECC material has been shown to perform exceptionally well under its intended loading. The damage-tolerant behavior makes the ECC especially appealing for performance-based earthquake engineering. ECC is therefore considered a promising material for use in the enhanced-performance bridge system under investigation in this research.

3 Simulation of Precast Segmental UBPT Columns

3.1 INTRODUCTION

A key to using PEER's PBEE methodology successfully is the availability of analytical tools capable of accurately predicting the response of structural components and systems under static and dynamic loads. A number of analytical methods and software packages, incorporating nonlinear and dynamic behavior, exist for modeling the behavior of structures. To validate the adequacy of some of the currently available analytical tools in modeling the structural behavior of the enhanced-performance systems of interest, simulations are performed on a number of recently completed experimental tests that incorporate the use of UBPT as well as HPFRCC materials. The purpose of the simulations is to investigate the behavior of several enhanced-performance self-centering systems, as well as to select appropriate analytical methods to incorporate in the performance-based assessment.

Section 3.2 of the chapter contains simulations performed on a set of large-scale precast UBPT columns made using concrete and HPFRCC. Detailed continuum analyses are performed to determine the ability of the models to predict the behavior of precast, segmental systems with UBPT, as their behavior is fundamentally different than that of monolithic, continuous RC structures. The simulations are also used to examine the failure modes that were observed in the testing, as well as to investigate possible design improvements to both the HPFRCC and concrete UBPT systems.

The second section of the chapter contains simulations performed on a set of large-scale HPFRCC coupling beams specimens. Continuum analyses are again performed to assess the ability of constitutive models developed for HPFRCC materials in predicting the response of components with shear-dominated behavior. Parameter studies are then performed to determine the influence of the HPFRCC properties on the structural behavior of such shear-dominated components.

3.2 SIMULATION OF UBPT BRIDGE COLUMNS WITH HPFRCC AND CONCRETE HINGES

3.2.1 Objectives

The comparison of numerical simulations to experimental data is key to validating the use of PEER's PBEE methodology. The UBPT columns tested by Rouse and Billington (2004) were selected to be modeled with several goals in mind. The first objective was to use finite element analysis as an investigative tool to determine the possible reasons for the observed failure of the specimens, as the location of failure was somewhat unexpected. The second was to assess the ability of the modeling methods to predict the overall behavior of precast, segmental UBPT columns, both in terms of global load-drift response, as well as local damage response. The third was to use the analytical models to assess alternate designs for the system that would provide improved behavior to the original specimens. The final goal was to assess the validity of the HPFRCC constitutive model of Han et al. (2003) on large-scale specimens by comparing the simulation results to the experimental data. Additionally, a parameter study was also performed to determine the effect of the HPFRCC material properties on global behavior, and design recommendations are proposed for improved behavior of segmental UBPT columns.

3.2.2 Background on Experiments

The experimental program consisted of the testing of a set of six large-scale UBPT bridge columns. Full details of the experiments can be found in Rouse (2004). The column specimens had a height of 3.7 m and a 460-mm-square cross section. The specimens consisted of precast segments with cap and foundation blocks. The column comprised four precast segments, each 1.067 m in length, with the two end segments embedded into the cap and foundation blocks. The precast segments were connected with a flowable epoxy mortar, and had no continuous bonded reinforcing across the segmental joints. The segments were post-tensioned together with six 15.2-mm-diameter low-relaxation strands stressed to 690 MPa (roughly $0.4f_{pu}$). The post-tensioning tendons had anchorages at the top of the cap block and the bottom of the foundation block.

The specimens were tested in double curvature in order to represent the behavior of a column in a multiple-column bent configuration subjected to lateral loading. To achieve this deformation behavior, two specimens were tested simultaneously, as shown in Figure 3.1. Specimens were oriented horizontally (longitudinal axis parallel to the floor) with their foundation blocks connected to a steel reaction frame and cap blocks connected to one another to provide rotational restraint. The specimens were subjected to quasi-static cyclic lateral loads while under a constant axial load of 720 kN (applied with a hydraulic actuator), representing dead load from a bridge superstructure.

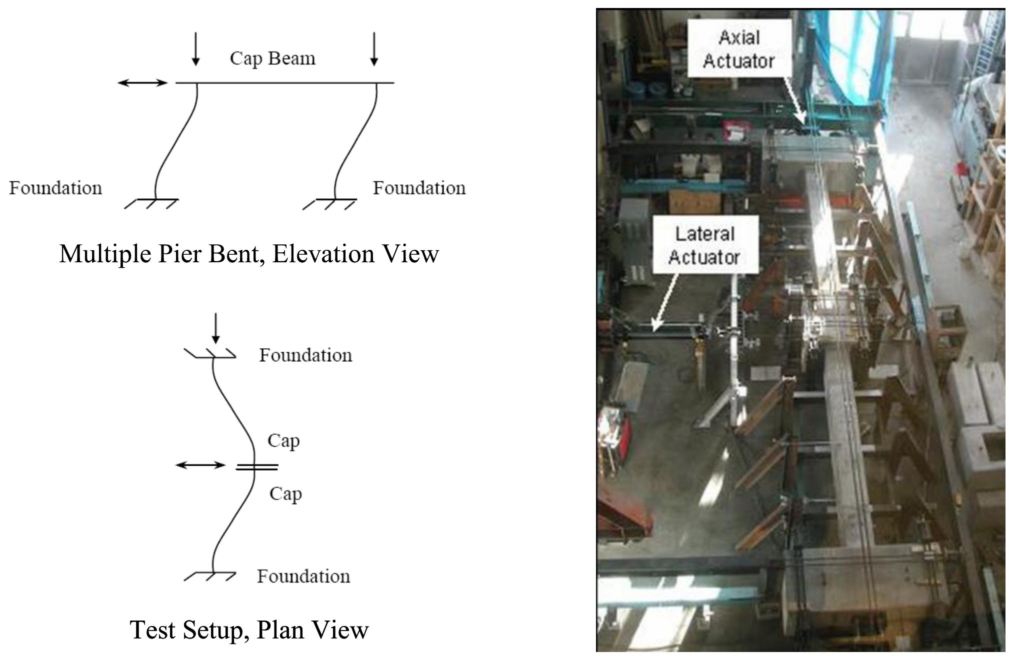

Fig. 3.1 Comparison of load-drift response for experiment and simulation for Specimen 3 - PVA hinge (image from Rouse 2004).

One of the variables in the experiments was the material in the hinging regions of the column. The three hinge region materials used were concrete and two ECC materials. One ECC used polyvinyl alcohol (PVA) fibers and the second mix used ultra-high molecular weight polyethylene (UHMWPE) fibers. Both types of ECC contained fibers at a volume fraction of 2 percent and had compressive strengths of roughly 35–45 MPa. Typical uniaxial tensile stress-strain curves for the two types of ECC obtained from tension tests are shown in Figure 3.2. The two ECC mixes each strain harden to less than 1 percent, which is significantly lower than the values of 3–6 percent typically reported for ECC (Li et al. 1995, 2001; Li 1998, Li 2002). This lower value is likely due to a number of effects, as discussed in Chapter 2. The concrete was a lightweight concrete and had a nominal compressive strength of 55 MPa at the time of testing as determined by cylinder tests.

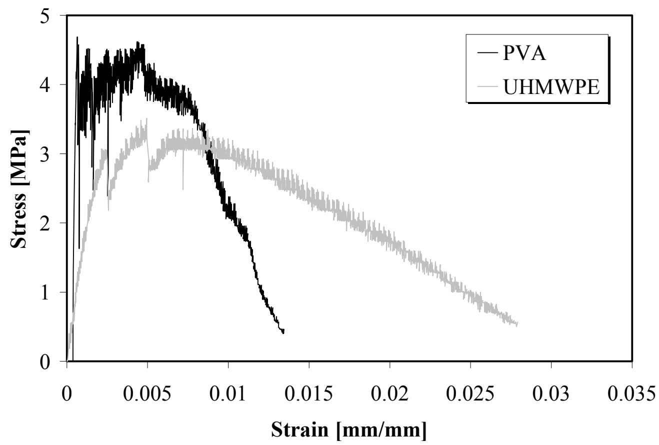

Fig. 3.2 Typical uniaxial tensile stress-strain behavior of ECC mixes (data from Rouse 2004).

The other two variables in the experimental program were the amount of reinforcing (both longitudinal and transverse) in the hinge segment and the length of the hinge segment. Two levels of reinforcing were used, the first was a heavier cage detailed to meet the 1983 AASHTO seismic bridge design code (AASHTO 1983), and the other was a lighter cage meeting only shear and shrinkage requirements of the 1996 AASHTO standard specifications (AASHTO 1996). The reinforcing details of the two hinge segments can be seen in Figure 3.3. The rectangular shapes seen in the cross sections are match-cast shear keys. The two hinge segments lengths used were 1.067 m and a shorter length of 0.864 m. The details of the six specimens tested are presented in Table 3.1.

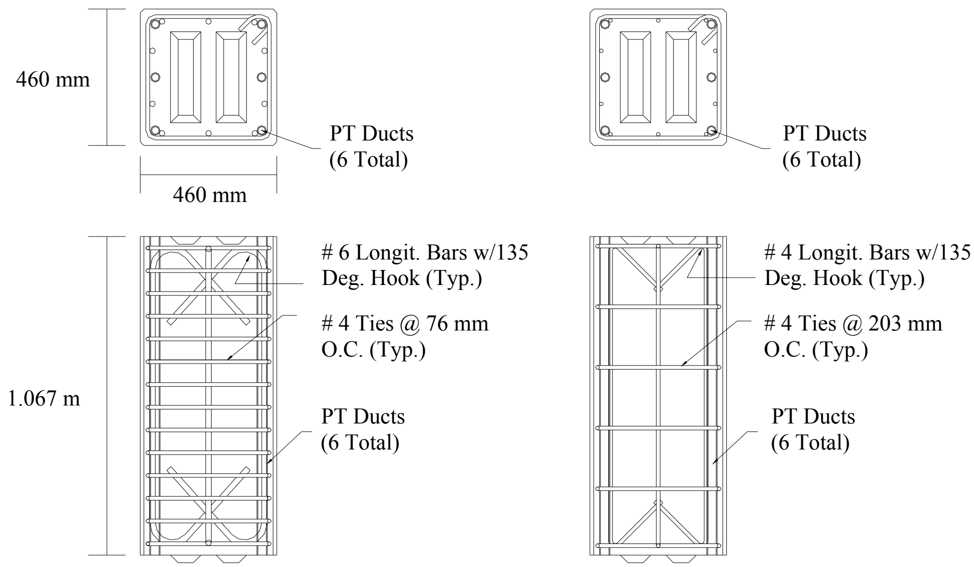

Fig. 3.3 Hinge segment reinforcing details (after Rouse 2004).

Table 3.1 Experimental specimen details.

Spec. No.	Hinge Segment Material	Hinge Segment Reinforcement	Hinge Segment Length
1	Concrete	Shear and Shrinkage	1.067 m
2	Concrete	Seismic	1.067 m
3	PVA-ECC	Shear and Shrinkage	1.067 m
4	UHMWPE-ECC	Shear and Shrinkage	1.067 m
5	PVA-ECC	Seismic	1.067 m
6	PVA-ECC	Shear and Shrinkage	0.864 m

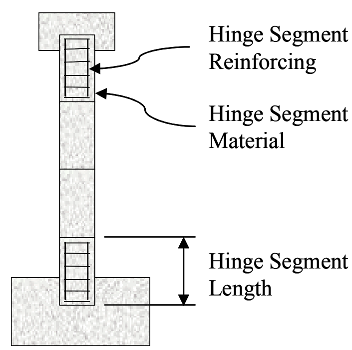

A final important note regarding the construction of the column segments is as follows: the ducts for the post-tensioning in the column segments were 2.54-cm-outer diameter, 0.28-cm-thick steel electrical tubing, rather than thin plastic ducts typically used for prestressed concrete. Rouse (2004) theorized that the ducts were a possible cause of the premature failure of the column specimens, and this is investigated through simulation in Section 3.2.6.

Prior to failure, the behavior of the UBPT column specimens as observed in the testing was as expected for precast segmental systems without continuous bonded reinforcing. Large cracks opened at the interfaces between segments at higher drift levels, as the separation of adjacent segments was unrestrained by any reinforcing after the compression from the prestressing and dead load was overcome. In addition, relatively low residual displacements (as compared to conventional RC members) were observed in the columns due to the presence of the unbonded post-tensioning.

The columns were expected to fail in the hinge segments, and close to the cap and foundation blocks, where the moments were the highest. However, the failures occurred closer to the joints closest to the cap and foundation block. The drift levels at failure were quite low (roughly 2–3 percent), and such low drift capacity is undesirable in seismic regions, for which this system is proposed. Therefore in addition to modeling the pre-failure behavior, it is necessary to identify the cause of the premature failure through analysis and simulation, and to make the appropriate design changes to prevent its future occurrence.

3.2.3 Finite Element Model

The continuum modeling performed herein was carried out using the DIANA (v. 8.1.2) finite element platform developed by TNO Software. A plane stress model was used in the majority of the analyses, as out-of-plane stresses were assumed to be negligible for the testing configuration. The finite element model is shown in Figure 3.4. The concrete and ECC were modeled using nine-noded quadrilateral isoparametric plane stress elements with a 3 x 3 Gauss integration scheme. Out-of-plane thicknesses of the plane stress elements were defined as 457 mm (18 in.) for the elements in the column, and 813 mm (32 in.) for the elements in the cap and foundation. All longitudinal and transverse bonded mild steel reinforcing bars were modeled with three-noded embedded reinforcing elements that are assumed to have perfect bond with the surrounding plane stress elements. Thus the bond-slip effect in the mild reinforcing was not included in these simulations.

The unbonded post-tensioning tendons were modeled with two-noded truss elements that were constrained at their end nodes to the concrete element nodes at the anchorage locations. This allowed the strains to be distributed evenly along the length of the post-tensioned tendons. However, curvature in the tendons could not be modeled using this method. An initial stress of 690 MPa, equal to the prestress in the tendons, was applied to the truss elements. The joints between the precast segments were not explicitly modeled using interface elements; therefore, cracking at the unreinforced joint regions was represented by smeared cracking in the plane stress elements (discussed further in Section 3.2.6.3).

(a)

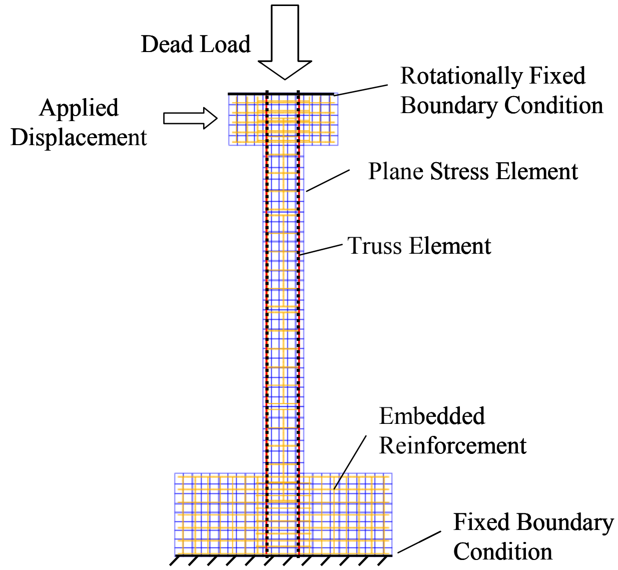

(b)

Fig. 3.4 (a) Photograph of concrete specimen and (b) finite element model.

The foundation block was modeled as fixed by providing pin supports at all nodes along the bottom of the model. The top nodes of the specimen (at the top of the cap block) were modeled as being rotationally fixed to represent the fixity provided by the connection to the cap of the other specimen. Because rotational degrees of freedom do not exist for the quadrilateral elements, rigid three-noded beam elements were added along the top of the cap, and their rotational degrees of freedom were constrained to provide the appropriate fixity. Point loads with a total magnitude equal to the magnitude of the axial load were applied to the top nodes of the cap block. Lateral loading was applied through applied displacements at two control nodes in the cap. Geometric nonlinearity was included in all analyses.

3.2.4 Constitutive Models

The concrete elements in the footing and the cap were modeled as linear elastic because nonlinear behavior (manifested by cracking or crushing) in those regions was neither expected nor observed during testing. The elastic modulus for the concrete in these and all other concrete segments was assumed to be 24.8 GPa (3600 ksi) based on the ACI equation for lightweight concrete (ACI 2005), shown in Equation 3.1.

$$E_c = w_c^{1.5} 33\sqrt{f'_c} \tag{3.1}$$

In this equation, E_c is the modulus of elasticity of concrete, w_c is the unit weight in lb/ft^3, and f'_c is the compressive strength in psi.

The concrete in the segments with the light reinforcing details was assumed to be unconfined due to the wide spacing of the transverse reinforcing. A fracture energy-based parabolic model was used to describe the compressive behavior of the concrete. A fracture energy-based model allows only a certain amount of energy to be released by a given element that undergoes compressive softening by modifying the post-peak curve based on the element size. This improves the mesh objectivity if rapid compressive softening occurs, as was expected for unconfined concrete. The model is defined with two parameters, the compressive strength and elastic modulus. A range of compressive fracture energy values as determined through experimentation has been reported as 10–25 N-mm/mm^2 (57–143 lb-in./in.^{2}) by Feenstra (1993). A value of 12 N-mm/mm^2 (65 lb-in./in.^{2}) was assumed, and the sensitivity of the analysis results to this value was investigated. The cyclic unloading and reloading behavior for all concrete models is secant, meaning that the stress path passes linearly through the origin upon unloading and reloading (see Fig. 3.5).

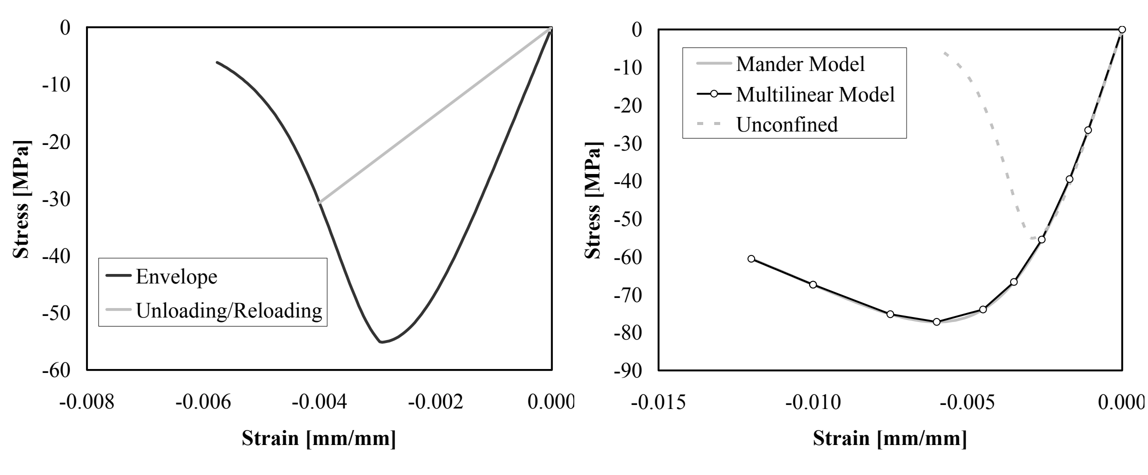

Fig. 3.5 Constitutive compressive behavior of (a) unconfined and (b) confined concrete.

For the concrete in the segments with the heavy reinforcing details, the compressive behavior was assumed to follow the Mander model for confined concrete (Mander et al. 1983), based on an unconfined compressive strength of 55 MPa (8 ksi). A multi-linear model was used to model the confined concrete. A fracture energy-based model was not used because rapid-compressive softening was not expected with the confined concrete. With the multi-linear model, stress-strain pairs are input to define the envelope stress-strain curve. According to the Mander model, for members with a rectangular cross section and confinement by rectangular hoops, the confined compressive strength can be found using the effective lateral confining stresses in the two transverse directions and the multi-axial failure surface of Willam and Warnke (1975). The solution of the multi-axial failure criterion in terms of the lateral confining stresses in graphical form can be seen in Figure 3.6. The effective lateral confining stress can be found from Equations 3.2 and 3.3.

$$f'_{lx} = k_e \rho_x f_{yh} \tag{3.2}$$

$$f'_{ly} = k_e \rho_y f_{yh} \tag{3.3}$$

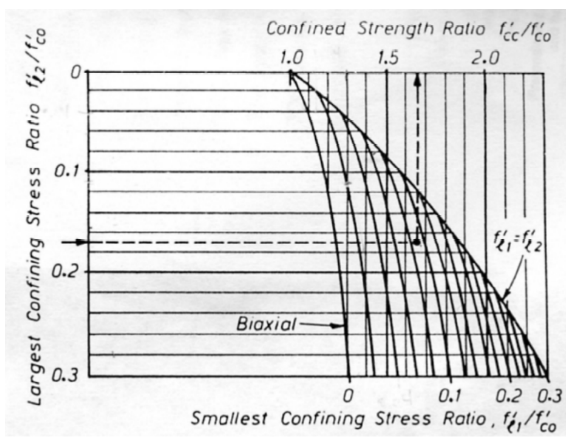

Fig. 3.6 Determination of confined compressive strength ratio from lateral confining stresses (from Mander et al. 1988).

In these equations, f'_{lx} and f'_{ly} are the effective lateral confining stress in the x and y directions, respectively, k_e is the confinement effectiveness coefficient, ρ_x and ρ_y are the transverse reinforcing ratios in the x and y directions, respectively, and f_{yh} is the yield strength of the transverse reinforcing. The confinement effectiveness coefficient is computed based on the areas of effectively confined versus unconfined concrete between hoops, and can be computed as shown in Equation 3.4:

$$k_e = \frac{\left(1 - \sum_{i=1}^{n} \frac{(w'_i)^2}{6 b_c d_c}\right)\left(1 - \frac{s'}{2b_c}\right)\left(1 - \frac{s'}{2d_c}\right)}{(1 - \rho_{cc})} \tag{3.4}$$

where w'_i is ith clear distance between adjacent longitudinal bars, b_c and d_c are the core dimensions to the centerlines of the perimeter hoop in the x and y directions, respectively, s' is the clear vertical spacing between hoops, and ρ_{cc} is the ratio of the area of longitudinal reinforcing to the area of the core of the section. After computing f'_{lx} are f'_{ly}, Figure 3.6 can be entered to find the confined strength ratio, f'_{cc}/f'_{co}, where f'_{cc} is the peak confined compressive strength and f'_{co} is the peak unconfined compressive strength. The peak confined compressive strength can then be computed from the confined strength ratio and the unconfined compressive strength. The peak compressive strain is computed using the equation proposed by Richart et al. (1928), shown in Equation 3.5.

$$\varepsilon'_{cc} = \varepsilon_{co}\left[1 + 5\left(\frac{f'_{cc}}{f'_{co}} - 1\right)\right] \tag{3.5}$$

Here, ε'_{cc} is the peak confined compressive strain and ε_{co} is the peak unconfined compressive strain, assumed to be 0.002 mm/mm.

Once the peak confined compressive strength and strain have been computed, these two values can be used along with the elastic modulus to describe the stress-strain relationship, which is assumed to follow the form originally proposed by Popovics (1973), shown in Equation 3.6,

$$f_c = \frac{f'_{cc} \frac{\varepsilon_c}{\varepsilon_{cc}} r}{r - 1 + \left(\frac{\varepsilon_c}{\varepsilon_{cc}}\right)^r} \tag{3.6}$$

where ε_c is the compressive strain in the concrete, f_c is the compressive stress in the concrete, and r is a shape factor defined by:

$$r = \frac{E_c}{E_c - \frac{f'_{cc}}{\varepsilon_{cc}}} \tag{3.7}$$

The behavior of the concrete following the Mander model is shown in Figure 3.5. Again, the loading and unloading behavior is assumed to be secant.

To model the tensile behavior of concrete, a smeared cracking model based on a total strain formulation (Feenstra et al. 1998) was used. In the total strain formulation, stresses are computed as a function of the strains. Within the total-strain formulation, two models for cracking are available: the fixed crack model and the rotating cracking model. In the case of the fixed cracking model, the crack direction becomes fixed upon first cracking and does not change with the change in principle stress directions. In the rotating crack model, the principal stress directions are constantly changing with the principal strain directions during cracking. While the fixed cracking model is more representative of the physical behavior of concrete, the rotating crack model has been shown to provide superior usability in terms of simplicity, numerical stability, and similarity with experimental results (Kwan and Billington 2001), and was therefore chosen for this research.

The model for the tensile behavior of concrete is shown in Figure 3.7. The cracking behavior was assumed to be linear until first cracking with a stiffness equal to the compressive modulus. The post-cracking behavior was defined to be fracture energy-based with linear tension softening. Again, a fracture energy-based model allows for improved mesh objectivity when softening occurs, as the post-peak branch of the tensile model varies depending on the element size and the fracture energy.

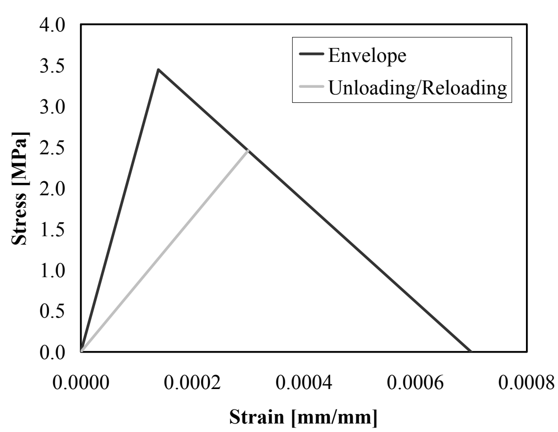

Fig. 3.7 Constitutive model for concrete in tension.

The tensile strength was computed from the ACI equation (American Concrete Institute 2005) for modulus of rupture of "all lightweight concretes," shown in Equation 3.8 in U.S. units:

$$f_r = 5.6\sqrt{f'_c} \tag{3.8}$$

where f_r is the modulus of rupture and f'_c is the compressive strength. The tensile fracture energy was calculated from the following equation from the CEB-FIP model code (1990),

$$G_f = 10^{-3}\alpha_F f_{cm}^{0.7} \qquad [N \cdot mm / mm^2] \tag{3.9}$$

where G_f is the tensile fracture energy, α_F is a coefficient based on the maximum aggregate size, and f_{cm} is the compressive strength. The α_F values are tabulated in the CEB-FIP code for various maximum aggregate sizes. The maximum aggregate size was taken to be 12.5 mm (0.5 in.) based on Rouse (2004), giving a value of 5 for α_F.

A bilinear model was used for the bonded mild steel reinforcing (Fig. 3.8). The assumed yield strength for the bonded reinforcing steel was 460 MPa (66.8 ksi), which is a mean actual value of yield strength for Grade 60 steel as determined through experimental testing (Melchers 1999). The initial stiffness (elastic modulus) was set as 200 GPa (29,000 ksi), and the post-yield (hardening) slope was set assumed to be 2 percent of the initial stiffness. The post-tensioning strands were modeled as linear elastic, as designed and as observed throughout the testing, with an elastic modulus of 186 GPa (26,977 ksi). An initial prestress of 690 MPa (100 ksi) was applied to the truss elements modeling the PT tendons.

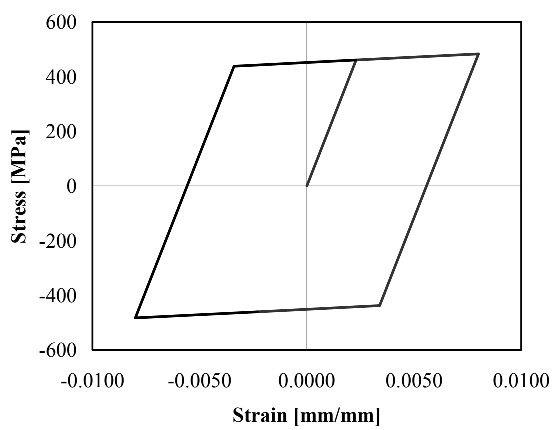

Fig. 3.8 Constitutive models for bonded reinforcing steel.

The ECC was modeled with a total strain-based rotating crack model developed by Han et al. (2002). The model is based on the observed responses from a series of reversed cyclic tests on uniaxially loaded ECC specimens (Kesner and Billington 2001). The envelope curves for the stress-strain behavior are defined as follows. In compression, the ECC is assumed to behave linearly to the peak compressive strain, ε_{cp}, after which it will undergo linear softening to the ultimate compressive strain, ε_{cu}. In tension, the ECC is assumed to behave linearly until the first cracking strain, ε_{t0}, after which it hardens linearly to the peak tensile strain, ε_{tp}. The ECC then softens linearly to the ultimate tensile strain, ε_{tu}. The envelope curves are shown in Figure 3.9.

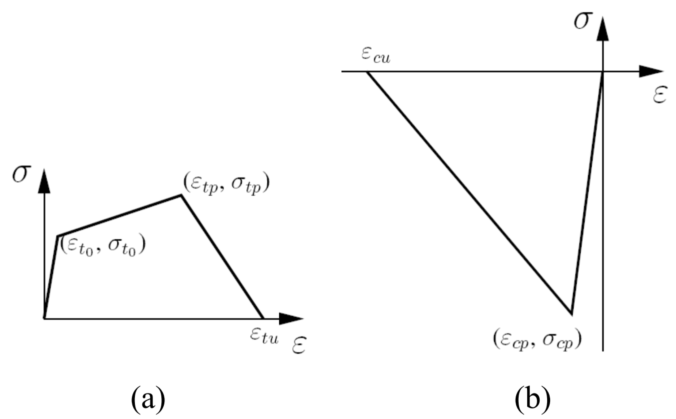

Fig. 3.9 Envelope curves for ECC constitutive model in (a) tension and (b) compression (from Han et al. 2003).

The unloading and reloading paths of the constitutive model were developed to capture the unique cyclic behavior of ECCs. In tension, the model unloads and reloads elastically prior to the cracking strain. After exceeding the cracking strain, i.e., during strain hardening, the model unloads along a polynomial curve defined by two model parameters. The first parameter, α_1, defines the exponent for the polynomial curve along which the unloading occurs. The second parameter, β_1, defines the permanent tensile strain value, which is defined as follows:

$$\varepsilon_{tul} = \left(\varepsilon_{t,\max} - \varepsilon_{t1}\right) \cdot \beta_1 \tag{3.10}$$

where ε_{tul} is the permanent compressive strain, and $\varepsilon_{t,max}$ is the maximum strain value reached in compression. After exceeding the peak tensile strain, i.e., during tensile softening, unloading is again along a polynomial curve, with the exponent defined with the modeling parameter α_s.

Reloading in both the tensile hardening and softening regions is linear. The unloading and reloading behavior in tension is shown in Figure 3.10. The unloading in the softening region is shown with an α_s value of 1, meaning that the unloading path is linear.

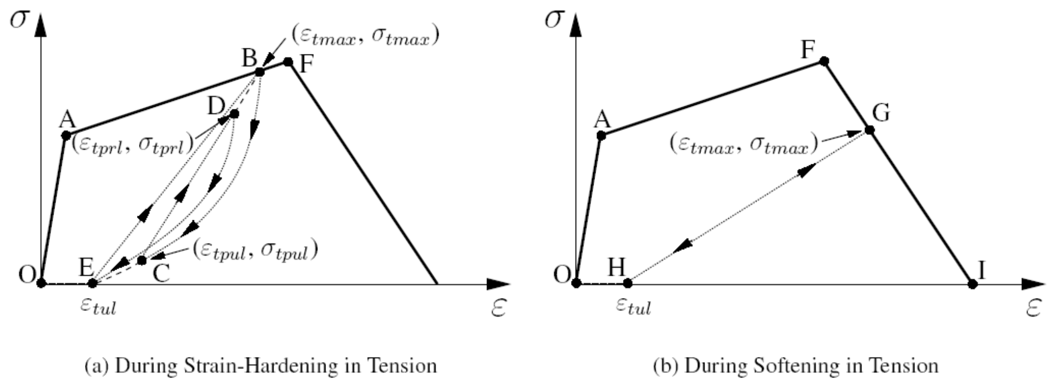

Fig. 3.10 Unloading and reloading behavior for ECC constitutive model in tension during (a) hardening and (b) softening (from Han et al. 2003).

In compression, the model unloads and reloads elastically prior to the peak strain. After exceeding the peak compressive strain, i.e., during compressive softening, the model unloads along a polynomial curve defined by two model parameters. The first parameter, α_2, defines the exponent for the polynomial curve along which the unloading occurs. The second parameter, β_2, defines the permanent compressive strain value, which is defined as follows:

$$\varepsilon_{cul} = \left(\varepsilon_{c,\max} - \varepsilon_{cp}\right) \cdot \beta_2 \tag{3.11}$$

where ε_{cul} is the permanent compressive strain, and $\varepsilon_{c,max}$ is the maximum strain value reached in compression. Reloading in the compressive softening region is linear. The unloading and reloading behavior in compression is shown in Figure 3.11.

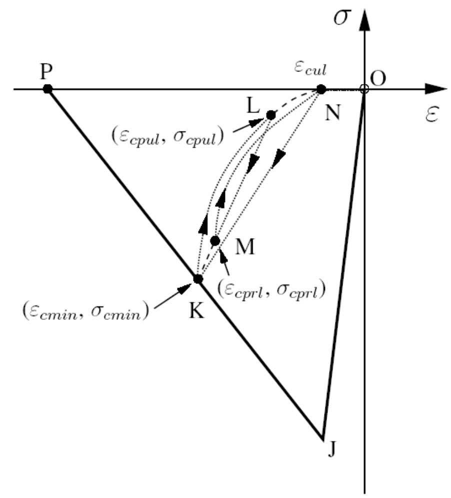

Fig. 3.11 Unloading and reloading behavior for ECC constitutive model in compression (from Han et al. 2003).

The ECC constitutive model was modified to incorporate nonlinearity in the envelope curve in compression. Shown in Figure 3.12 are experimental stress-strain data on a cyclically loaded UHMWPE ECC specimen (Douglas 2006). As shown with the two dashed lines, a linear approximation of the pre-peak portion of the compressive envelope does not represent the true behavior of the ECC. If the peak strain is selected to correspond with the actual value, the model provides a response that is significantly less stiff than the actual behavior. If the peak strain is selected to match the initial stiffness of the model with the actual response, the peak strain of the model is substantially lower than the actual peak strain. Therefore, a nonlinear curve was used in the modified ECC constitutive model. The proposed model follows the Popovics curve, shown in Equation 3.6, with an r value of 5 that was selected to match the observed response.

The tensile stress and strain values for the envelope curve of the model were based on uniaxial tensile tests on the two types of ECC used in the experiments (Rouse 2004), as shown in Figure 3.13a. The peak compressive stress was based on cylinder compression tests (Rouse 2004). As the compressive stress-strain behavior was not measured in the study by Rouse, the assumed peak compressive strain was based on tests performed on ECCs with similar mix proportions as reported by Kesner and Billington (2004). The assumed compressive stress-strain response is shown in Figure 3.13b. The loading and unloading parameters for the constitutive model from Han et al. (2003) were used. The assumed constitutive modeling parameters for the two types of ECC are shown in Table 3.2.

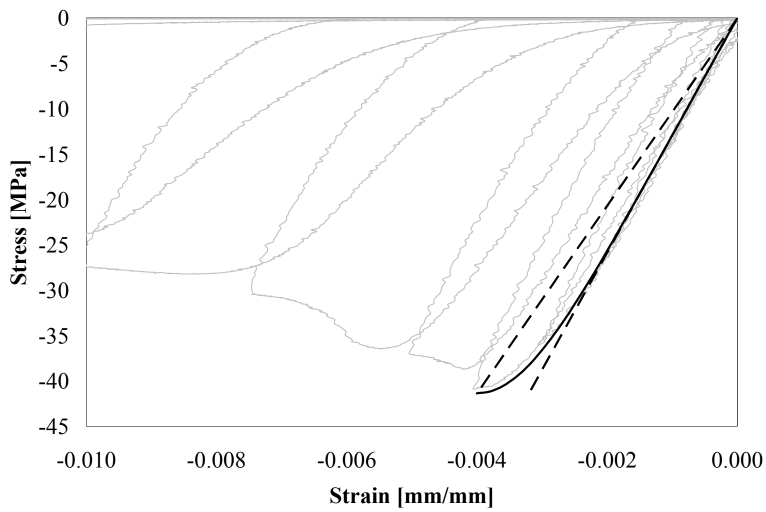

Fig. 3.12 Unloading and reloading behavior for ECC constitutive model in compression (from Han et al. 2003).

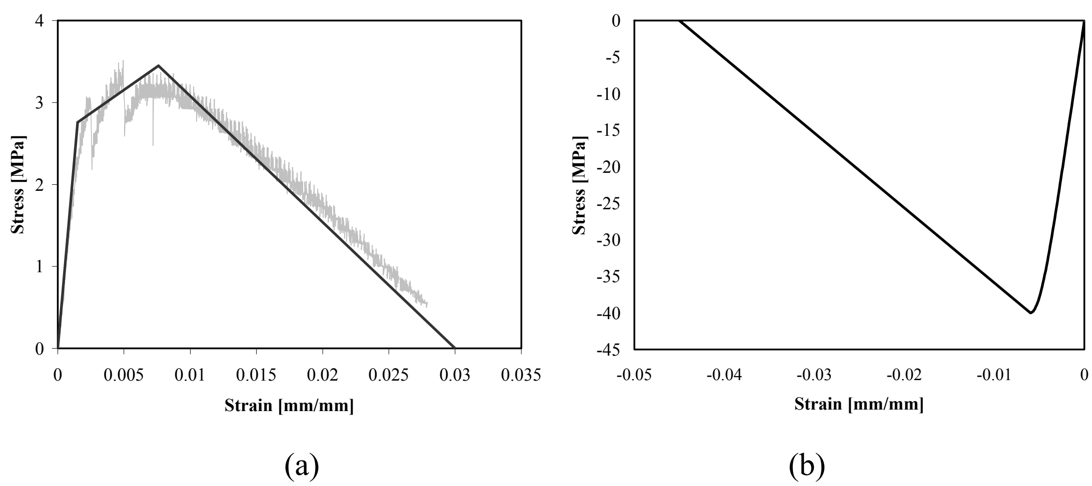

Fig. 3.13 Assumed (a) tensile and (b) compressive envelopes for constitutive models for UHMWPE ECC.

Table 3.2 Assumed parameters for UHMWPE ECC constitutive model.

ECC Type	Tensile Parameters	Compressive Parameters	Unloading/Reloading Parameters
UHMWPE	ε_{t0} = 0.0015 mm/mm σ_{t0} = 2.76 MPa ε_{t1} = 0.0076 mm/mm σ_{t1} = 3.45 MPa ε_{t2} = 0.03 mm/mm	ε_{c0} = -0.006 mm/mm σ_{c0} = -40 MPa ε_{c1} = -0.045 mm/mm	$\alpha_1 = 5$, $\alpha_2 = 2$ $\alpha_s = 1$ $\beta_1 = 0.4$, $\beta_2 = 0.3$

3.2.5 Analysis Procedure

The finite element model was analyzed under monotonic loading as well as cyclic loading. Phased analysis was used to apply the prestress first, then to apply the axial load, and finally the lateral load. The lateral loading was applied under displacement control using control nodes in the cap. Geometric nonlinearity was included in the analysis in addition to material nonlinearity. For the nonlinear analyses, a Newton-Rhapson solution scheme supplemented with a line-search algorithm was used. A force norm was used for the convergence criterion.

3.2.6 Simulation of Specimen 1: Concrete Column with Light Reinforcing

Simulations were first performed on Specimen 1, which had concrete hinge segments with light reinforcing details. The analyses were first performed on Specimen 1 because it was the first of the two columns to fail, rendering Specimen 2 unable to be tested to failure. A monotonic analysis was first performed to determine whether the behavior of the column, in terms of global behavior (stiffness and strength) and local, physical behavior (e.g., locations of damage, failure mode) could be adequately captured. The comparison of the resulting monotonic load versus drift response from simulation with experimental results for Specimen 1 is shown in Figure 3.14. The analysis is performed in the negative drift direction because that was the initial direction of loading in the experiment.

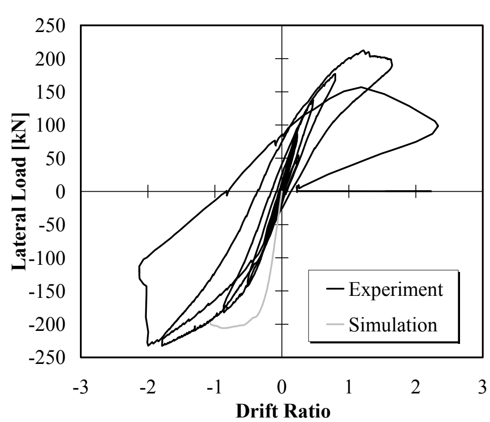

Fig. 3.14 Comparison of simulated and experimental load-drift response of Specimen 1.

In terms of global behavior, the initial stiffness of the finite element model is significantly larger than that of the experiment. The stiffness of the simulation, computed at a drift of 0.15 percent, is more than twice as large as that of the experiment, with values of approximately 9,600 kN/m for the experiment and approximately 19,600 kN/m for the simulation. The stiffness difference is likely due to a number of effects. The primary effect is the flexibility of the reaction frame. Measurements of translations and rotations in the foundation block confirm that significant movements did in fact occur during testing. The foundation block of the specimens was instrumented with three LVDTs, as shown in Figure 3.15 to measure rotation and translation. Horizontal translation readings from LVDT 1s could be directly subtracted from the total deflections measured at the cap. The displacement due to rigid body rotation, δ_{RBR}, was computed using the average of the two foundation displacement recordings, $\delta_{F,ave}$, from LVDTs 2s and 3s by Equation 3.12, and as shown in Figure 3.15. The resulting load-drift response including the direct translation of the foundation block is shown in Figure 3.16a, and the response including the translation due to rigid body rotation is shown in Figure 3.16b.

$$\delta_{RBR} = \frac{H}{W} \delta_{F,ave} \tag{3.12}$$

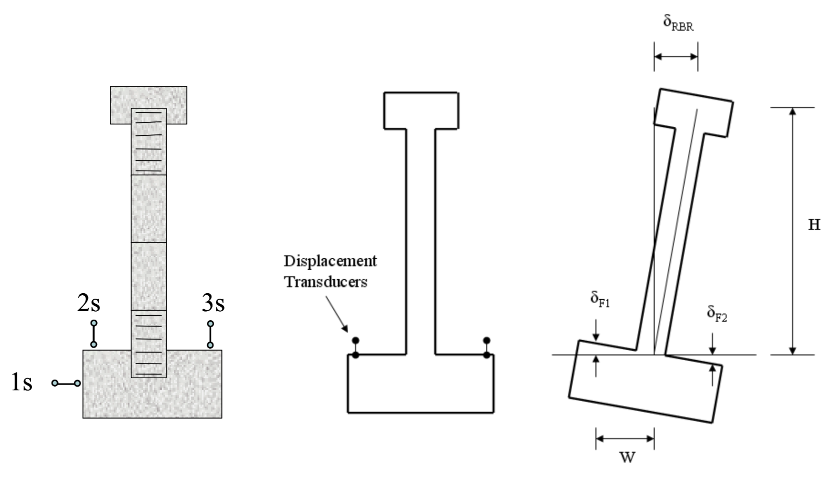

Fig. 3.15 Instrumentation on foundation block, and displacement due to rigid body rotation.

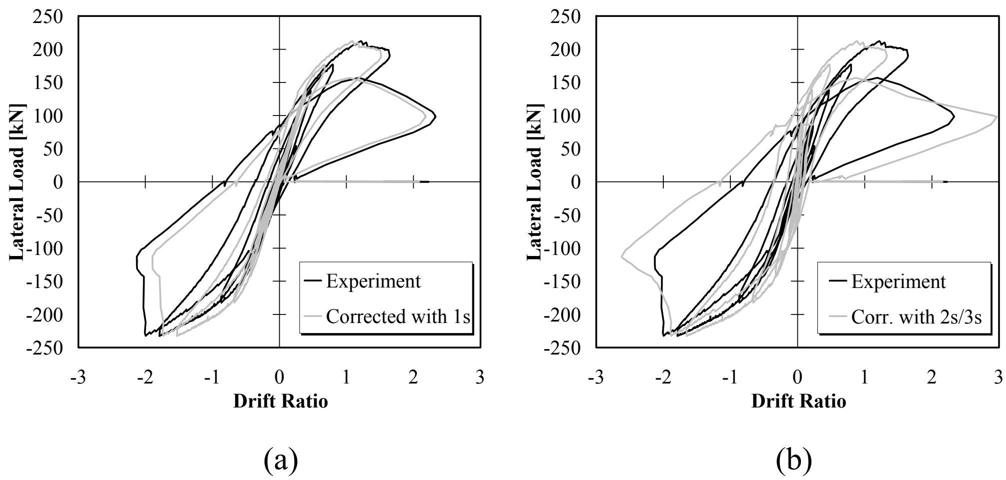

Fig. 3.16 Experimental load-drift response corrected for (a) foundation translation and (b) foundation rotation.

The load-drift response that is corrected with foundation translation shows that there is considerable flexibility in the response that is due to the reaction frame. The load-drift response corrected with foundation rotations shows similar results, but with a more significant contribution to the overall flexibility. However, during the final, large drift cycle, the correction appears to produce spurious results. As the additional displacement due to foundation rotation is being *subtracted* from the overall displacement, the corrected displacement should always be less than or equal to the uncorrected response. It is clear that in the last cycle, the corrected displacements become greater than the uncorrected displacements, meaning that the foundation would have to be rotating in the direction opposite the direction of movement of the column. The point at which this error occurs is the point at which the column fails, and therefore the results following this point should be neglected in any case.

From here on, the load-drift plots will show the response corrected with *both* foundation translation and rotation, with the understanding that the corrected response is representative of the true response until the final large cycle, during which the column fails and in general the experimental response of the column becomes unusable. The response will be shown nonetheless, such that the failure of the column at that time is obvious on the plot. The initial stiffness computed including the recorded movements in the foundation was again calculated, and found to be 19,000 kN/m, resulting in a response that is only approximately 5 percent less stiff than the simulation.

In terms of predicting damage in the column, the simulation captures the general sequence of tensile damage during the initial stages of loading. Cracking first begins to occur in the hinge segments near the cap and foundation blocks, where the moments are the highest. With increasing displacement cycles, the cracking begins to move up the sides of the column. Eventually the moments become large enough that the cracking strength of the concrete at the unreinforced joint is reached (the epoxy joining the segments had a greater tensile strength than the concrete, meaning that cracking would occur in the concrete itself and not the epoxy). With further loading, the crack localizes in the joint region and extremely high tensile strains are shown in the analysis, corresponding to the significant crack opening that was observed in testing. The unarrested crack opening at this region was expected, as no continuous bonded reinforcing was present to prevent it. At this point the stiffness of the column drops significantly as the crack widens. The crack at the unreinforced joint began to bend downward as it moved inward in both the simulation and experiment as expected due to the fact that the flexural tensile stresses began to diminish and cracking became governed by shear.

In terms of peak strength, the simulation predicts a value of 206 kN, which is approximately 12 percent lower than the value of 233 kN observed in the experiment. The low strength is attributed to the failure mode in the analysis, which differs from that which was observed in the test. In the simulation, the analysis diverges when the concrete begins to crush in compression in the hinge segments near the cap and foundation blocks. The compressive stresses are not able to redistribute, as the depth of the compression block is very small. The location of this failure might be expected given the distribution of moment in the column, with the highest moments occurring at the top and bottom. However, such excessive crushing in these areas was not observed in the testing. While the first sign of compressive damage did occur in the hinge segment near the foundation block, the damage consisted of only a small spalled region, as shown in Figure 3.17, and no load drop was observed at the time.

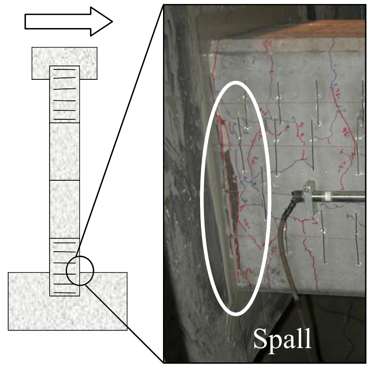

Fig. 3.17 Small spall near foundation of Specimen 1 (at 1.75 percent drift).

Failure finally occurred on the last large cycle at a drift of -2.27 percent (uncorrected) and was due to spalling and crushing of the concrete at a region that was unexpected. The failure was expected to occur either near the cap or foundation blocks, where the moments were the highest, or at the construction joints where the moment capacity of the columns was the lowest due to the lack of continuous bonded reinforcing. However, the actual failure occurred in the third of the hinge segment nearest to the construction joint, and in both of the hinge segments, as shown in Figure 3.18. The failure consisted of crushing and severe spalling in the cap hinge segment, and severe spalling in the foundation hinge segment.

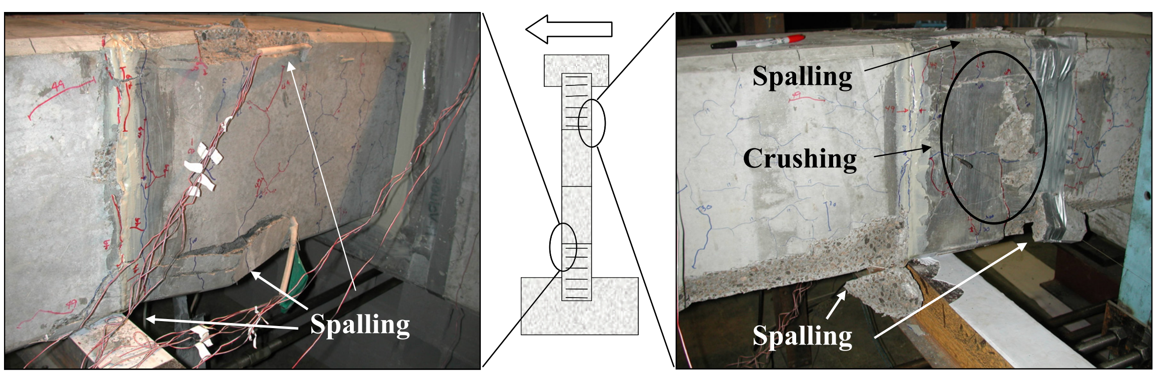

Fig. 3.18 Observed failure of Specimen 1 (at -2.3 percent drift).

The fact that the concrete did not crush extensively in the hinge segments in the area directly adjacent to the foundation and cap was theorized by Rouse (2004) to be due to an increase in compressive strength arising from the confinement provided by the foundation and cap blocks. In addition, this increase in compressive strength near the bases of the columns was expected to play a role in the failure behavior of the column. To investigate this claim, a three-dimensional model of the column was generated to determine whether such an increase was found in the concrete near the cap and foundation.

The constitutive models for concrete in 3D can include the effects of lateral stresses on increasing the compressive strength of concrete. The strength increase with increasing isotropic stress is modeled using the four-parameter Hsieh-Ting-Chen failure surface (Chen 1982). This effect is shown in Figure 3.19. The passive lateral confining stresses from the surrounding concrete of the cap or foundation are incorporated in a three-dimensional model, with the effect on increasing the compressive strength included. The two-dimensional plane stress model used in the previous analyses could not take into account this effect, as stresses in the out of plane direction were assumed to be zero.

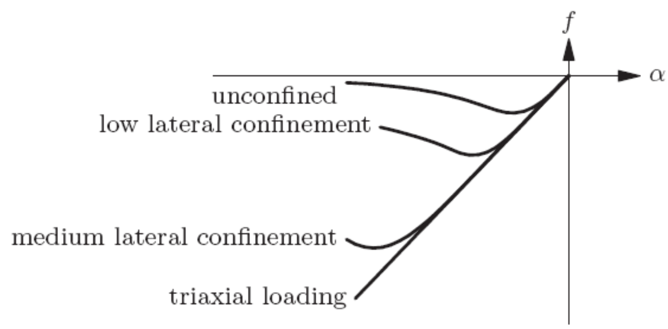

Fig. 3.19 Compressive behavior under lateral confinement (from *DIANA User Manual*).

For the three-dimensional model, eight-noded brick elements with a 2 x 2 x 2 Gauss integration scheme were used to model the cap block, column segments, and foundation block. The mesh is shown in Figure 3.20. Bonded reinforcing was modeled with embedded reinforcing elements, and the post-tensioned tendons were modeled with truss elements. Fixity was provided to the bottom of the model by adding pin support at all nodes on the bottom of the foundation. To provide rotational restraint, rotations were constrained in a fashion similar to that of the two-dimensional model as in Section 3.2.3, but with plate elements rather than beam elements.

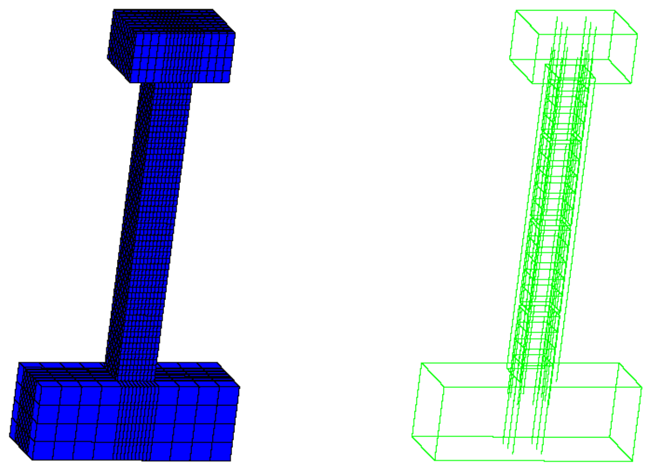

(a) (b)

Fig. 3.20 Finite element mesh for 3D model of UBPT column: (a) shaded view and (b) with reinforcing and PT elements shown.

The elements in the cap and foundation blocks were modeled as elastic, with the same elastic modulus as used in the two-dimensional analysis. The post-tensioning tendons and the bonded reinforcing were modeled with the same constitutive models as the two-dimensional model, namely an elastic model for the post-tensioning tendons and an elastic-perfectly plastic model for the bonded reinforcing steel. The concrete in the column elements was modeled with a smeared, rotating crack model. Loading was applied under displacement control using control nodes in the cap block. Geometric nonlinearity was included in the analysis, and a regular Newton-Raphson scheme with a line search algorithm was used to perform the nonlinear analysis, with a force norm as the convergence criterion.

To determine the increase in compressive strength from the lateral confinement of the cap and foundation, the compressive strength for all concrete in the column was input as 55 MPa (8 ksi), and the stress-strain relationship for a number of elements adjacent to the cap and foundation were recorded as lateral displacement was applied to the model. The increase in strength based on lateral stresses in the elements was then computed automatically in the analysis. The resulting stress-strain curves for the concrete in these elements showed an increase in compressive strength, from a base value of 55 MPa (8 ksi) to approximately 69 MPa (10 ksi), which validated the claims made by Rouse (2004). Based on these three-dimensional analyses, the bottom row of elements in the two-dimensional model were increased to 69 MPa (10 ksi) to capture the confinement effect.

The two-dimensional model was then re-analyzed and compared to the experimental results. While the failure was delayed as compared to the original model, the location of failure was unchanged, and again occurred at the top and bottom of the column. Divergence of the analysis occurred when the elements in the hinge segment near the cap and foundation began to localize in compression. As the location of compressive failure in the model was still not predicted correctly in the simulation, a number of alternative possibilities to explain the observed failure were considered, and are discussed in the following sections.

3.2.6.1 Evaluation of Possible Failure due to Loading of PT Ducts

Rouse (2004) theorized that the observed failure in the column was due to radial expansion of the ducts used for the post-tensioning. Rather than using thin-walled plastic or galvanized steel ducts, as is common practice for post-tensioned construction, the fabricators of the test specimens had used relatively thick-walled, 2.54-cm-outer diameter, 0.28-cm-thick, steel electrical tubing to facilitate placement of the reinforcing cages. Rouse hypothesized that if enough of the compressive stresses in the column were transferred to the ducts, the radial expansion of the pipes due to the Poisson effect could cause lateral cracking in the concrete around the ducts by imposing outward pressure, thus reducing the compressive strength and inducing early failure. This possibility was investigated here with three-dimensional finite element analysis. The mechanism by which axial load was transferred to the pipe is discussed in Rouse (2004), and is thought to be caused by misalignment of the ducts near the construction joints. However, the specific mechanism for the axial load transfer in the experiment is irrelevant in regard to analyzing the effect itself and whether the resulting behavior could have caused the observed failure.

A three-dimensional model of a quarter of the column with a unit thickness was created, as shown in Figure 3.21, to investigate the induced stresses in the concrete surrounding the pipe under compressive loading. Only a quarter of the cross section was modeled to take advantage of symmetry and assuming that half of the cross section is in compression during bending near failure. The concrete was modeled using 20-noded brick elements with a 3 x 3 x 3 Gauss integration scheme. The pipe was modeled using 8-noded curved shell elements with a 2 x 2 Gauss integration scheme. The pipe was modeled as linear elastic with an elastic modulus of 200 GPa (29,000 ksi). The concrete was modeled as elastic in compression and with a rotating crack model in tension with a tensile strength of 3.45 MPa (500 psi). The model was constrained vertically along the bottom face, and in the in-plane directions as shown in Figure 3.21. Vertical displacements were applied to all nodes along the top face of the model, thereby compressing both the concrete elements and the pipe elements. Analysis was performed under displacement control using a Newton-Raphson scheme with a force-based norm as the convergence criteria.

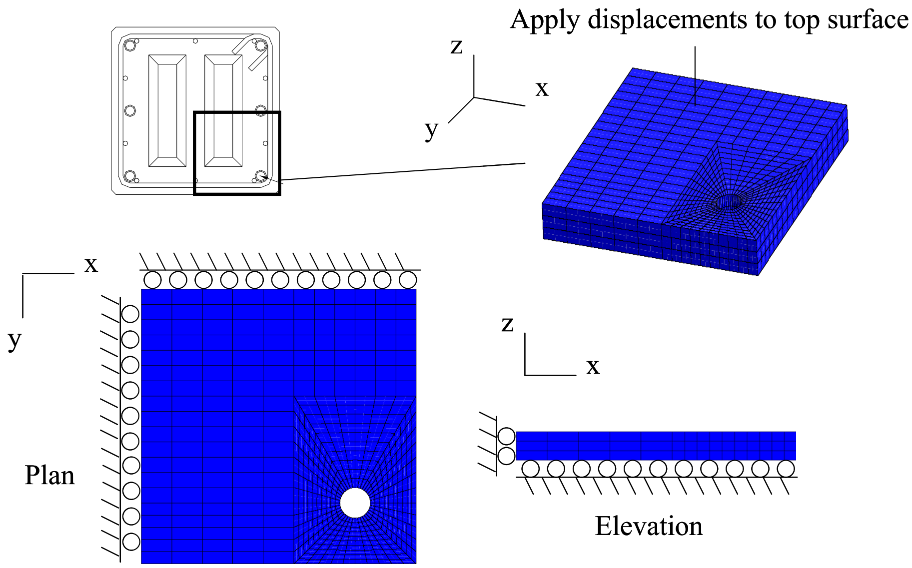

Fig. 3.21 Finite element model of axially loaded pipe in concrete, including boundary conditions.

The results from the analysis show that even if the pipe does become subjected to quite high axial load, the stresses in the concrete caused by the radial expansion of the pipe are below the cracking stress, and the extent to which the induced stresses occur is in only a small region directly surrounding the pipe. A contour plot of principal tensile stresses at an applied vertical displacement corresponding to a vertical strain of 0.001 mm/mm is shown in Figure 3.22. The contour levels are selected such that the maximum tensile stress shown is 3.45 MPa (500 psi).

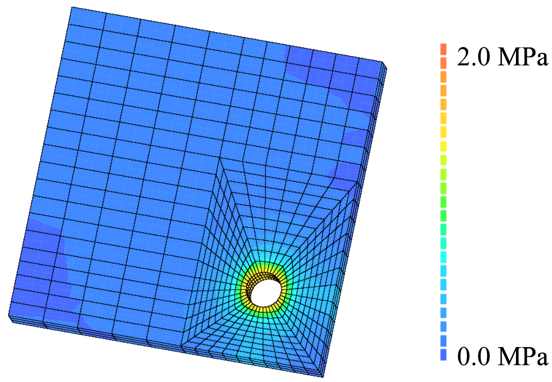

Fig. 3.22 Contour plot of principal tensile stresses in concrete and pipe model.

The figure shows that only a very small region directly surrounding the pipe is stressed to roughly 2 MPa (300 psi), which is only 60 percent of the cracking stress. The analysis shows that even if the pipe were subjected to very high axial compressive stress (200 MPa in the figure, a level which likely could not be attained in the actual column), lateral cracking would not be induced in the concrete surrounding the pipe (the stress in the concrete in the model is 34.5 MPa, or $0.625f'_c$). As the theory of radial expansion of the steel PT ducts as the root of the failure observed in the columns was discounted, alternative possibilities were considered for the observed failure.

3.2.6.2 Effect of Bond in Mild Reinforcing

Insufficient bond in the bonded reinforcing bars is proposed as a possible cause of the column failure location. As the bonded reinforcing bars in the column segments did not have enough development length even in the embedded segments to achieve their full capacity, the moment strength at these sections was subsequently reduced. It was at these sections that the reduced moment strength was exceeded, leading to failure. Before an explanation of this is given, the mechanism of bond between reinforcing and concrete is briefly reviewed.

The ability of a reinforcing bar in concrete to sustain axial forces is dependent on sufficient bond between the two materials, thus preventing slippage between them. The prevention of slippage can be obtained either through anchorage of the reinforcing in the concrete through the use of hooked ends, or by providing sufficient length of the reinforcing bar in the concrete such that adequate bond can be obtained through the mechanical interlocking of the deformations in the bars with the surrounding concrete. Considering a straight reinforcing bar embedded in concrete under tensile load, the bond stresses are essentially zero at the end of the bar, and increase linearly moving away from the end of the bar. After a certain distance, the bond stress becomes high enough that the yield stress of the reinforcement can be reached. This is the development length of the bar.

Now consider the longitudinal bonded reinforcing bars in the column segments of the UBPT specimens, as shown in Figure 3.23. At the top of a given bar near the construction joint, the tensile force that can be sustained by the bar is essentially zero. Moving down the length of the bar, the bond stress increases linearly until the development length is reached, at which point the yield stress of the bar can be achieved. Therefore, until the development length of the reinforcing bars is reached, the full yield stress of the bars cannot be counted on to contribute to the moment capacity of the section. Near the construction joint, the bonded reinforcing bars do not contribute at all to the moment capacity of the column, but moving away from the joint, they begin to contribute to the moment capacity as the stress that can be taken by the bars increases. Hence, the increase in moment capacity of the column due to the bonded reinforcing bars increases linearly moving away from the construction joint. The moment capacity at the base of the column can include the full yield strength of the reinforcing, as the bar continues into the foundation block.

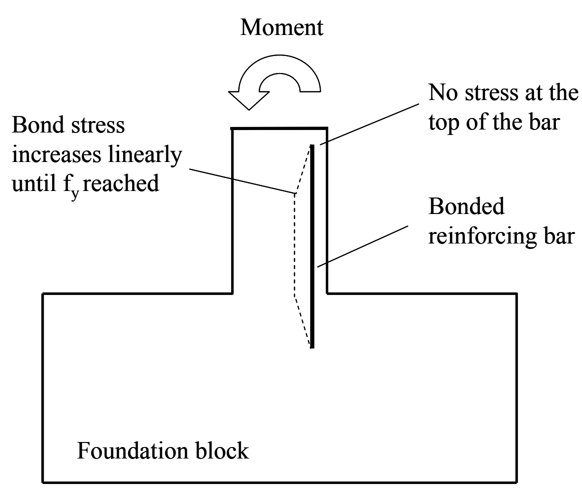

Fig. 3.23 Distribution of bond stresses in reinforcing bar.

Consider the moment diagram in the column under lateral loading, as shown in Figure 3.24. At the construction joint, denoted as section B, the moment capacity of the section is composed of only the compression in the concrete and the tension in the PT tendons. The bonded reinforcing bars do not contribute any moment strength, as they are not continuous at this section. Moving away from the joint and toward the foundation, the moment capacity of the column begins to increase linearly as the bonded reinforcing bars begin to contribute to the moment capacity. However, the applied moment also increases linearly moving away from the joint. Therefore it is possible that while the moment capacity of the column at the joint may be greater than the applied moment, the applied moment may increase faster than the capacity of the column increases, meaning that the column will fail at a location that is not at the joint but somewhere away from it. While the moment at various sections of the column are known from geometry and lateral load, the actual forces in the reinforcing bars can not be computed based on a sectional analysis because the PT tendons are unbonded and strain compatibility does not exist. Other manual methods to determined capacity are cumbersome and as a result, the scenario of reduced reinforcing bar capacity was investigated through simulation.

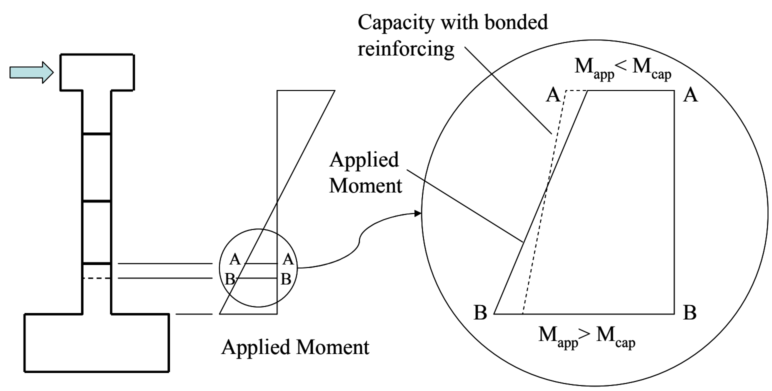

Fig. 3.24 Variation of moments and capacities in UBPT column.

To incorporate the effect of reduced moment capacity of the column near the joints due to insufficient development length of the bonded reinforcing bars, the yield strength of the reinforcing bars was reduced in such a way as to simulate the linear reduction in stress approaching the end of the bar. The development length required for a #4 bar to reach its yield stress was first computed using equations given in Lowes et al. (2004). The required development length was computed to be 35.6 cm (14 in.). The assumed variation in stress capacity was approximated by reducing the yield stress of the reinforcing bar elements as shown in Figure 3.25. The segments with reduced yield strengths were modeled using elastic-perfectly plastic behavior, while the remaining segments were allowed to strain harden as before. The model was then re-analyzed under monotonic loading using the reduced bar strengths.

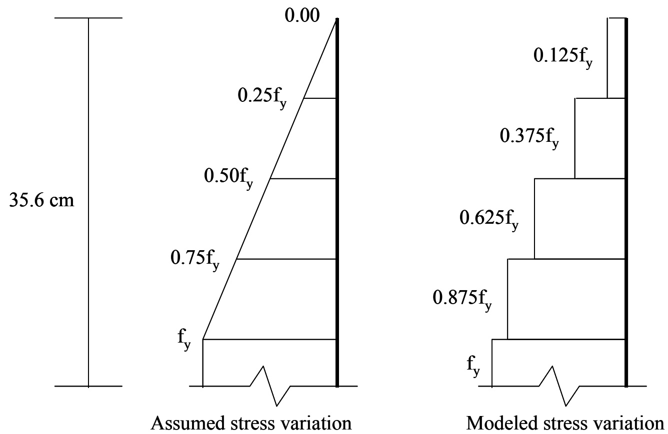

Fig. 3.25 Assume and modeled stress variation in bonded reinforcing bars.

The load-drift response for the monotonic analysis compared to the experimental results is shown in Figure 3.26a. The resulting analysis gives a failure mode that is consistent with that observed in the experiment. The analysis now diverged when some of the concrete elements in the hinges at a region below the construction joint begin to soften in compression. A contour plot of vertical compressive stresses at the step prior to divergence is shown in Figure 3.26b. The contours are mapped such that the maximum level corresponds to a compressive strain of 0.003 mm/mm.

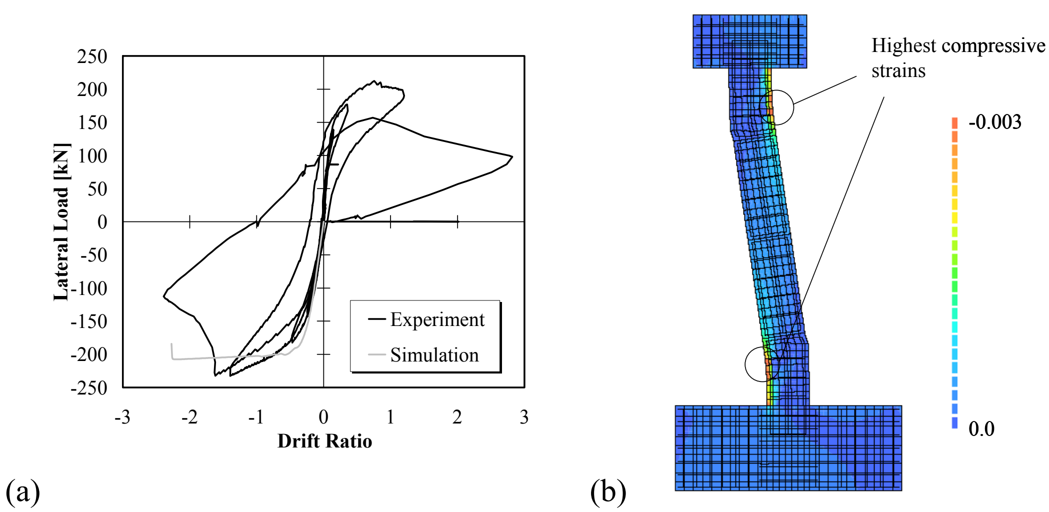

Fig. 3.26 (a) Comparison of simulated monotonic load-drift response of Specimen 1 to experiment with bond effect included. (b) Contour plot of principle compressive strains immediately prior to failure (deformation magnified by a factor of 5).

The compressive crushing can be seen to occur in both hinge segments away from the construction joint in the direction of the cap and foundation, as observed in the experiment (the locations of the joints are easily identified as the location where the mesh is greatly deformed/elongated representing opening of the gap). However, while the failure mode and location are correctly predicted, the drift at failure is overpredicted by the simulation, and the peak strength is underpredicted. As the failure was controlled by compression, the effect of the modeling assumptions on the resulting drift value was examined by performing a sensitivity study on the compressive modeling parameters.

The sensitivity of the failure of the simulation model to the assumed value for the compressive fracture energy of concrete was first investigated. Monotonic analyses were performed again for three additional values of the compressive fracture energy: 7.9, 11.4, and 14.9 N-mm/mm^2 (45, 85, and 105 lb-in./in.^{2}). The resulting load-drift responses are shown in Figure 3.27a. The drift at failure is not highly sensitive to the assumed value for the fracture energy. Increasing the value from the originally assumed value of 11.4 N-mm/mm^2 results in only slight increases of the drift at failure. For example, using the value of 14.9, which is a change of over 60 percent, results in only a 10 percent change in the drift at failure. Reducing the compressive fracture energy to 7.9 N-mm/mm^2 does not change the drift at failure.

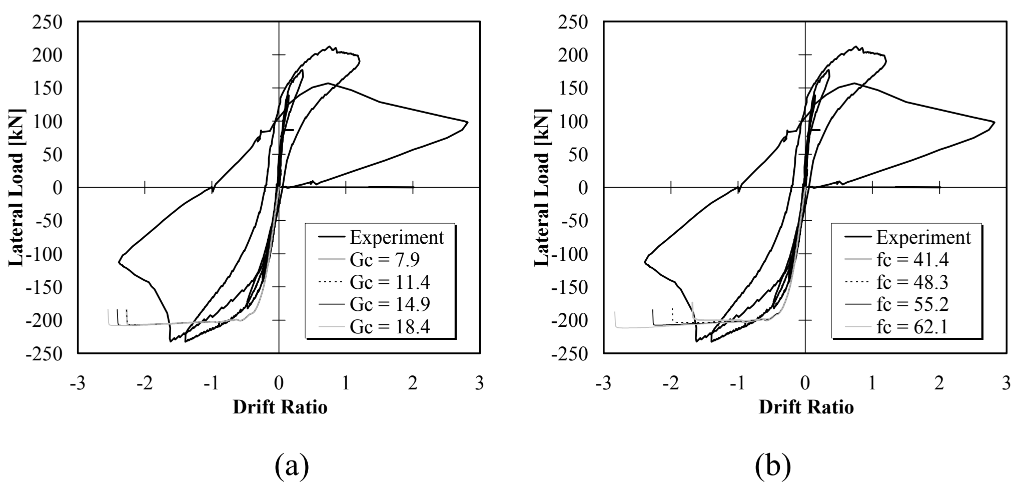

Fig. 3.27 Sensitivity of simulation to (a) compressive fracture energy and (b) compressive strength.

A similar study was performed to determine the sensitivity of the failure to the concrete compressive strength. Three additional values of concrete compressive strength were considered: 41.4, 48.3, and 62.1 MPa (6, 7, and 9 ksi). The resulting responses are shown in

Figure 3.27b. The drift at which failure occurs is much more sensitive to the concrete compressive strength than the compressive fracture energy. The compressive strength value for which the simulation closely matches the experimental results is 41.4 MPa (6 ksi). This is significantly lower than that of the compressive strength obtained from the cylinder testing. The question arises as to whether such a large difference in compressive strengths between the cylinders and that in the column segments is possible.

Variation in compressive strength based on statistical data has been reported by Melchers (ref) as ranging from a standard deviation of 2.8 MPa (400 psi) for "excellent" quality control to a standard deviation of 5.6 MPa (810 psi) for "poor" quality control. The standard deviation for compressive strength for "average" quality control is reported as 4.2 MPa (610 psi). It is therefore not likely that the concrete in the column had a strength that was as low as 41.4 MPa (6 ksi).

That the peak strength is underpredicted and the drift at peak is overpredicted may be due to the difference in secondary stiffness of the column between the simulation and the experiment. Secondary stiffness refers to the stiffness of the second branch of the essentially bilinear behavior that is exhibited under lateral load. The change in stiffness corresponds to the point at which the crack near the joint begins to open. At this point, the stiffness of the column is governed primarily by these joints, and the stiffness of the joints is governed by the stiffness of the concrete in compression and the stiffness of the PT tendons in tension. The difference in stiffness contribution from the PT tendons between the simulation and the experiment is due to the method of modeling used; that is, the modeling of the tendons with truss elements. In the experiment, the tendons must follow the curvature of the column, while in the simulation the truss elements simply move laterally while remaining straight. Therefore with increasing lateral displacement of the column, the PT tendon in the experiment will experience higher strains than the PT elements in the simulation. The fact that in reality the tendons are taking higher loads could lead to the higher stiffness observed. If the curvature in the tendons could be modeled, a better estimation of the peak load and drift at failure might be obtained.

A cyclic analysis was then performed using the lower compressive strength value of 41.4 MPa (6 ksi) to match the failure drift of the experiment. In the analysis a similar displacement history as performed in the experiment was used. Several of the smaller initial cycles were not performed as the column remained essentially in the elastic range except for some cracking of concrete. A comparison of the resulting load-drift response with the experiment is shown in

Figure 3.28. The cyclic behavior of the column is predicted well by the simulation. As expected, the drift at failure is predicted well using the calibrated value of concrete compressive strength.

3.2.6.3 Precast Joint Modeling

As mentioned previously, the joints between the precast segments were not explicitly modeled, and the cracking/gap opening in this region was represented in the finite element model through smeared cracking in the plane stress elements. In many finite element models, regions where cracking is expected to occur are often modeled using interface elements. These interface elements allow cracking to be represented in a more physically realistic manner, but require a priori knowledge of the location of cracking. In the case of the precast segmental system under investigation here, the use of interface elements to model the joints between segments may seem appropriate given that they may appear to be planes of weakness where cracking would be expected. However, the use of interface elements was deemed unnecessary given the material used for joining the segments and the observed behavior of the specimens.

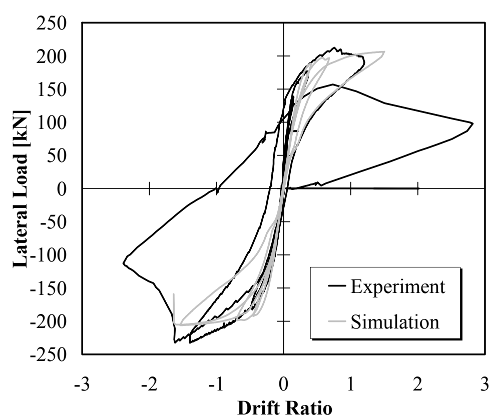

Fig. 3.28 Comparison of cyclic load-deflection behavior of simulation with experiment for Specimen 1.

The material used to join the precast segments was Sikadur 32 Hi-Mod, which is a two-part, high-modulus structural adhesive. According to the product data sheet, the material has a 14-day tensile strength of 40 MPa (5800 psi) and a 14-day flexural strength of 62.8 MPa (9100 psi). The strength of the material joining the segments greatly exceeds the cracking strength of the concrete itself. Therefore the cracking would not be expected to occur in the adhesive material at the joint itself, but rather in the concrete somewhere near the joint. The observed behavior of the specimens during testing confirms this, as shown in Figure 3.29. The cracking can be clearly seen to occur in the concrete below the joint and not in the joint material itself. While the cracking does localize in the region near the joint due to the lack of continuous bonded reinforcing, it does not always occur exactly at the joint, meaning that modeling the joint with interface elements was not necessary.

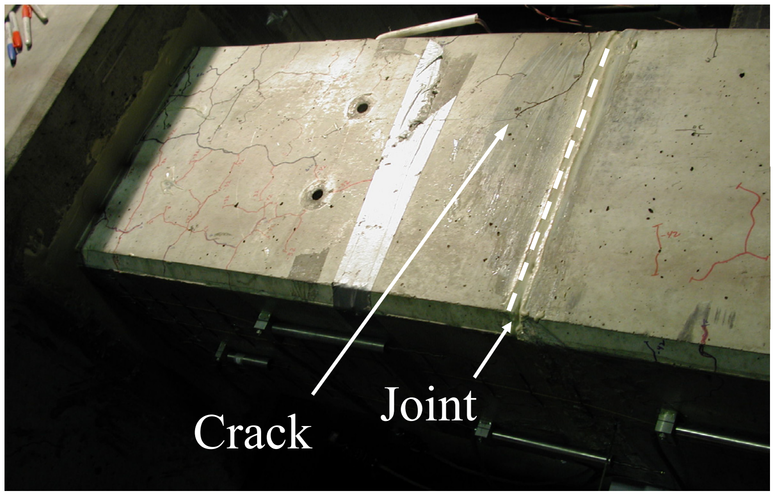

Fig. 3.29 Cracking near precast joint.

3.2.6.4 Shear Behavior

The shear behavior of the UBPT column system was considered as a source of possible concern, as high shear stresses must be transferred in the joint regions where no continuous bonded reinforcing exists. The combination of high shear stresses at the joint with the high compression was considered as possibly being problematic near the construction joints. Based on mechanics principles, however, the combination of compressive stress and shear stress should not present a problem, as the compressive stress would serve to reduce principle tensile stresses when in combination with shear stress. To illustrate, consider an element in the column under two possible stress states: the first being pure shear, and the second having both shear and compression. By transforming the stresses, it can be seen that the principle tensile stress in the second state with compression and shear is lower than that of the state with shear alone, as shown in Figure 3.30. Therefore, it is the shear effect alone that was considered as possibly being problematic at the precast interfaces.

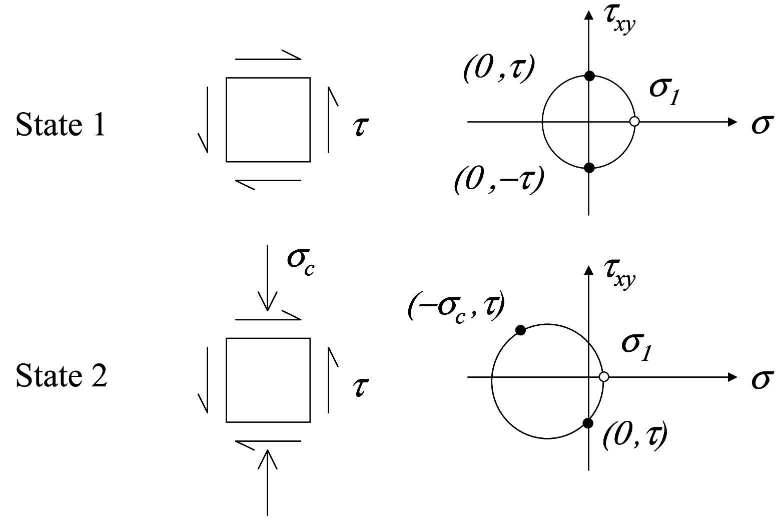

Fig. 3.30 Possible stress states for shear and compression in concrete.

Tsoukantas and Tassios (1989) developed equations for predicting shear resistance of connections between precast concrete elements based on experimental data. The shear resistance between precast elements is provided by two mechanisms: the dowel action of reinforcing bars, and friction at the interface. Empirical equations are presented for computing shear resistance from these two mechanisms individually. In the case of the proposed system, no continuous reinforcing bars cross the joints, meaning that the dowel action is not present, and shear is transferred through friction alone.

The shear resistance due to friction can be computed under monotonic loading conditions depending on whether the interfaces between the two connecting elements are smooth or rough. The frictional resistance is a function of the normal stress in the concrete, where the normal stress is composed essentially of applied axial forces and moments. The ultimate shear stress as a function of normal stress for smooth and rough interfaces is given in the following equations:

$$\tau_{fr,u} = 0.4\sigma_{cc} \qquad \text{(smooth interface)} \qquad (3.13)$$

$$\tau_{fr,u} = 0.5 \cdot \sqrt[3]{f_{ck}^{2}\sigma_{cc}} \qquad \text{(rough interface)} \qquad (3.14)$$

where $\tau_{fr,u}$ is the ultimate frictional shear stress, σ_{cc} is the normal stress in the concrete, and f_{ck} is the compressive strength of the concrete.

The shear resistance under fully reversed displacements can then be computed as a function of the number of cycles and the monotonic shear resistance for smooth and rough surfaces using the following equations:

$$\frac{\tau_{fr,n}}{\tau_{fr,1}} = 1 - \frac{1}{7}\sqrt{n-1} \qquad \text{(smooth interface)} \tag{3.15}$$

$$\frac{\tau_{fr,n}}{\tau_{fr,1}} = 1 - \left[0.002(n-1)\left(\frac{\sigma_{cc}}{f_{ck}}\right)^{-1}\left(\frac{s_n}{s'_u}\right)\right]^{1/3} \qquad \text{(rough interface)} \tag{3.16}$$

where n is the number of cycles, $\tau_{fr,n}$ is the frictional shear stress after n cycles, n is the $\tau_{fr,n}$ is the frictional shear stress after 1 cycle, s_n is the imposed slip displacement after the nth cycle, s'_u is the shear slip of an interface that corresponds to the maximum mobilized friction under monotonic loading.

While no shear slippage or signs of shear failure were observed at the interfaces during testing, the above equations can be used to determine whether such a failure might be impending under the circumstances in the test. First, Equation 3.13 was used to compute the ultimate shear stress for smooth interfaces. A value of 22 MPa (3200 psi) was obtained for the ultimate shear stress given a compressive strength of 55 MPa (8000 psi). To reduce the shear resistance to account for cyclic loading, the number of displacement cycles is conservatively assumed to be 10, giving a reduction factor of 0.57. The reduced shear resistance was then computed as 12.5 MPa (1800 psi). Conservatively assuming that at peak load, only one quarter of the cross section is being utilized for shear resistance, the shear force due to friction would be 12.5 MPa * 0.052 m^2 = 653 kN. This value is significantly larger than the peak shear force sustained by the column, which was less than 250 kN. Therefore, the shear resistance provided by friction is more than adequate to carry the maximum expected shear force in the column.

3.2.7 Simulation of Specimen 2: Concrete Column with Heavy Reinforcing

As mentioned previously, Specimen 2 was not tested to failure, as completion of the test was prevented by the failure of Specimen 1. However, monotonic analysis was performed using the same model as used for Specimen 1. The model was modified to include the heavier reinforcing cage of Specimen 2. In addition, the compressive strength of the concrete in the hinge segments was modified to incorporate the confinement from the transverse hoops according to the Mander model, as described in Section 3.2.4. The compressive strength of the elements in the bottom row was again increased by 13.8 MPa (2 ksi) in order to include the additional confinement from the cap and foundation block. The model was analyzed in order to predict the expected location of failure as well as the drift capacity. The resulting load-deflection response is shown in Figure 3.31a. The experimental data as shown are again corrected with the foundation translation and rotation. A comparison of the corrected response with the uncorrected response is shown in Figure 3.31b. As with Specimen 1, the corrected response shows the expected stiffer response in the low cycles, but begins to look increasingly erratic in the larger drift cycles. Again, the final large cycle should be discounted, as Specimen 1 had failed, resulting in the loss of the intended support conditions.

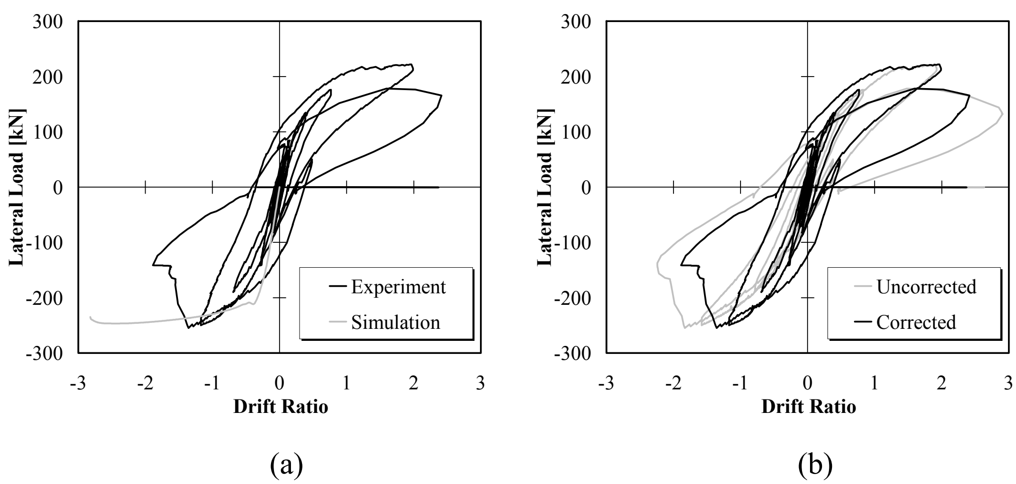

Fig. 3.31 Comparison of (a) monotonic load-deflection response of simulation and experiment and (b) corrected versus uncorrected experimental response of Specimen 2.

The simulation fails to converge at a drift of approximately 2.8 percent. This drift level is higher than that of Specimen 1, but is still quite low in terms of desirable drift capacity. The predicted failure mode is similar to that of Specimen 1, with compressive failure occurring in the hinge segments slightly away from the construction joints. This is shown in the contour plot of vertical compressive stresses shown in Figure 3.32. The fact that the strength and ductility of the concrete is increased due to the heavier confinement leads to a delay in crushing and hence a delay of the failure of the column, but not to a substantial degree. Design modifications for improving the behavior of the UBPT concrete columns will be discussed in Section 3.2.10.

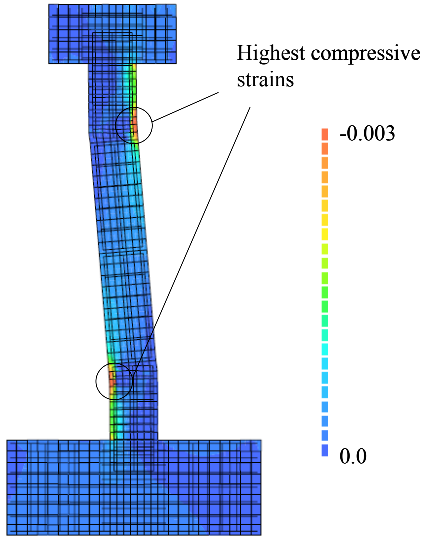

Fig. 3.32 Contour plot of vertical compressive strains of Specimen 2 near failure.

3.2.8 Simulation of Specimen 4: UHMWPE-ECC Column

A monotonic analysis was first performed for Specimen 4 of the tests by Rouse (2004), which contained UHMWPE-ECC in the hinge segments. Analysis was first performed for this specimen, as it was the first of the two specimens to fail. The model was modified such that the hinge segment elements used the ECC constitutive model and parameters described in Section 3.2.4. The finite element model is shown in Figure 3.33a. The resulting monotonic load-drift response compared to the experimental response is shown in Figure 3.33b. The experimental load-drift response was corrected for foundation translation and rotation as described in Section 3.2.6.

In the experiment, the column reached its peak strength during the cycle to approximately 2 percent drift. After the column had reached its capacity, the initial boundary conditions that deformed the specimens in double curvature were no longer being applied as intended. Therefore the final one and a half large cycles (to approximately 3 percent and 4 percent drift) can not be directly compared with the simulated response, which maintains the initial boundary conditions.

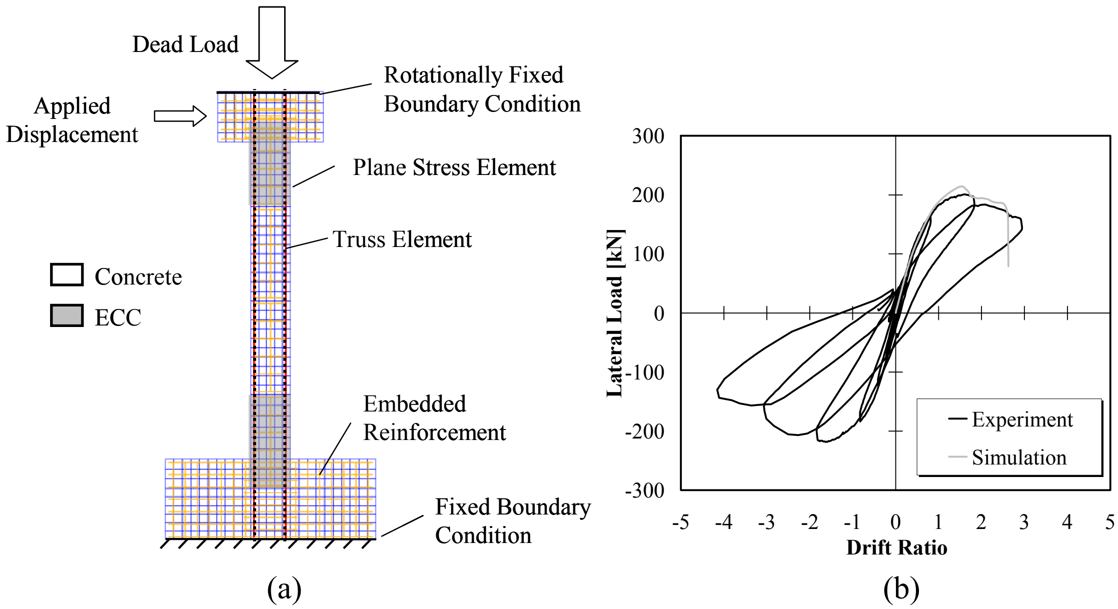

Fig. 3.33 (a) Finite element model for ECC column and (b) comparison of simulated and experimental load-drift response for Specimen 4 with UHMWPE-ECC hinges.

The simulation captures the envelope curve of the response quite well. The peak load predicted in the simulations was 214 kN at a drift of 1.54 percent, while the peak load in the experiment was 201 kN at a drift of 1.62 percent. The initial stiffness of the simulation, computed at a drift of 0.15 percent, was 7770 kN/m, while the initial stiffness of the experiment was 7735 kN/m, a difference of less than 1 percent. The stiffness of this column has roughly 40 percent of the stiffness of the concrete column, and is due to the lower stiffness of the ECC in comparison to the concrete (typically, ECC has a stiffness of roughly 40 percent of the stiffness of a concrete of the same compressive strength).

The lateral load-drift behavior of the UHMWPE-ECC column differs from that of the concrete column with the same reinforcing (Specimen 1). Specimen 1 reaches a point at which the lateral stiffness drops significantly due to localized crack growth at the unreinforced joint, then continues to load until the compressive strength of the concrete is reached, at which point the column fails. In this way, the column exhibits a more clearly bilinear behavior. In contrast, Specimen 4 reaches its peak load near the point at which the crack localizes and begins to widen. The lateral load then begins to drop soon after due to softening of the ECC in compression. This behavior is illustrated with a series of contour plots of tensile and compressive strains in the column as shown in Figure 3.34. The tensile strains are plotted as principal tensile strains and the contour levels are mapped such that the maximum values correspond to the localization strain of the ECC. The compressive strains are plotted as principal compressive strains, with the contour levels mapped such that the maximum values correspond to the peak compressive strain of the ECC.

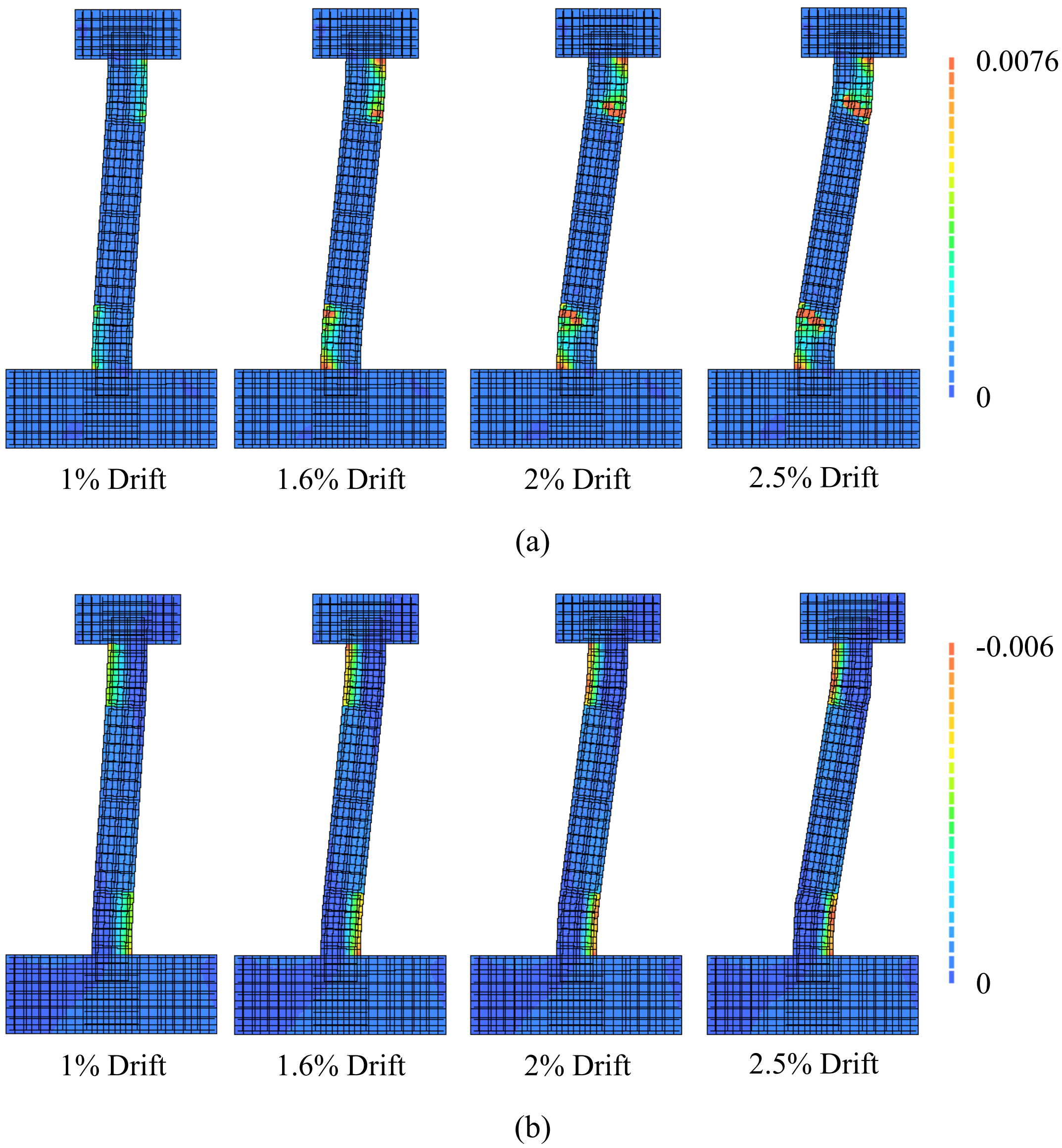

Fig. 3.34 Contour plots of (a) principle tensile strains and (b) vertical compressive strains for Specimen 4 with UHMWPE-ECC hinges (deformation magnified by a factor of 5).

At a drift of 1 percent, the column shows no sign of crack opening at the unreinforced joint and the compressive strains in the hinges are below the peak strain of the ECC. At a drift of 1.6 percent, the peak load of the column is reached and the localization of strain in the ECC at the joints can be seen in the contour plot. At this point, the column begins to lose strength as the ECC begins to soften in tension. Shortly after, the ECC in compression reaches its peak strain capacity and begins to soften. As shown in Figure 3.34 at 2 percent drift, the localized crack at the interface of the two segments has progressed into the column and begun to bend downward due to shear, while the ECC in compression has reached its peak compressive strain. Near failure, at 2.5 percent drift, the failed compressive zone can be seen. The simulation fails to converge at a drift of approximately 2.6 percent, while the actual specimen continued to deform while gradually softening.

Since the pre-peak load-drift response of the simulation followed the experimental response well, the sensitivity of the assumed ECC constitutive modeling parameters affecting post-peak response was investigated. The value corresponding to ε_{cu} in the ECC model was changed to several different values to calibrate it against the experimental response. The original value of 0.045 mm/mm was changed to 0.06, 0.075, and 0.09. The resulting load-drift responses using these values are shown in Figure 3.35.

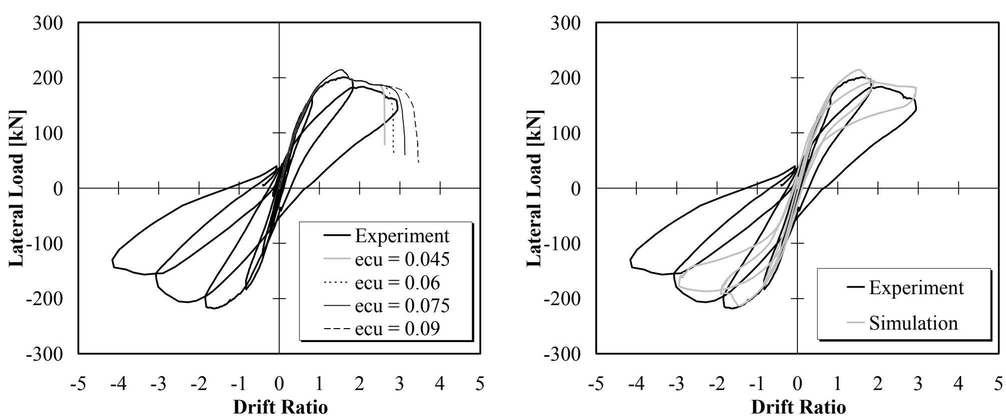

Fig. 3.35 Sensitivity to ECC constitutive model parameter ε_{cu} for Specimen 4 with UHMWPE-ECC hinges.

The response is not highly sensitivity to the assumed value for ε_{cu}, as an increase of a factor of 2 from 0.045 to 0.09 increases the drift at which the simulation fails by only approximately 20 percent. Using the value of 0.09 for ε_{cu}, a cyclic analysis was performed on the simulation model. The value of 0.09 was chosen to allow the model to complete all of the drift cycles without failing to converge. The resulting response is shown compared to the experimental response in Figure 3.43.

The envelope of the cyclic response of the simulations follows the experiment fairly closely. The simulated response appears to poorly match the experimental response at the largest drift cycle (to 3 percent drift) in terms of the unloading behavior, as the simulated response displays the expected origin-oriented response, while the experimental response follows a much less stiff unloading path. It should be noted again that a comparison between the simulated and experimental response for this drift cycle can not be made because the boundary conditions between the two are no longer the same. However, the conclusion can be made that following the drift cycle to 3 percent, the simulation has already exceeded its peak strength, and the ECC is already beginning to soften in compression. The column has essentially failed at this point, and in a more ductile fashion than the similar specimen with concrete hinges.

3.2.9 ECC Parameter Studies

A parameter sensitivity study was performed to determine the effect of the ECC tensile parameters on the load-drift behavior of the columns. Such a study can provide insight into the importance of the ECC material behavior on the structural response, as well as show possible benefits of using ECC with altered mechanical response on overall behavior. As ECC in an engineered material, its tensile response can be tailored to meet the requirements of the engineer. If significant improvements to the structural behavior of the column can be achieved through improvements to the ECC tensile behavior, such modifications to the ECC can be considered a worthwhile pursuit.

To determine the effect of the ECC tensile parameters on the global response, the model was re-analyzed for three different cases. The first case (Model 1) assumed an increase in first cracking strength of the ECC, with no increase in ductility (i.e., the same strain at peak stress). The slope of the hardening branch was kept the same. The second case (Model 2) assumed an increase in ductility by maintaining the same hardening slope but allowing the hardening to occur to 1.37 percent. This was twice the amount of strain hardening as the original model, but still was not as large as values often reported for ECC (i.e., 3 percent). The third case (Model 3) assumed strain-hardening behavior to a higher peak strain of 3 percent, with a stress at peak of

3.45 MPa (500 psi). The assumed tensile stress-strain responses for the three cases considered is shown in Figure 3.36.

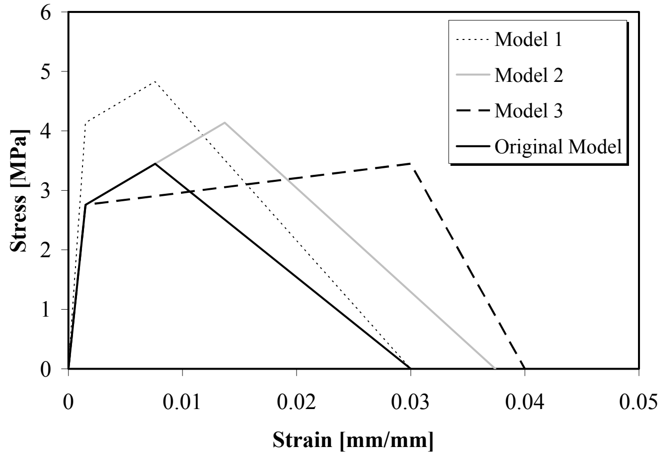

Fig. 3.36 Assumed variations in tensile behavior of ECC.

The resulting load-drift response for Model 1, with increased cracking strength, is shown against the experimental response and the simulated response using the original ECC response in Figure 3.37. The response with increased ECC strength is similar to the original model, but with an increase in the peak load and the drift at peak load. The localization of cracking in this case occurs in the concrete near the hinges rather than in the hinge segments themselves due to the fact that the cracking strength of the ECC now exceeds the concrete strength. The localization in the concrete segments is shown in Figure 3.38. The figure shows a contour plot of principal tensile strains at a drift of 2 percent (corresponding to the peak load), with a maximum plotted value corresponding to the localization strain of the ECC. It is clear in the contour plots that the ECC in the hinge has not approached its localization strain and is therefore still able to contribute its tensile stresses to the moment capacity of the column.

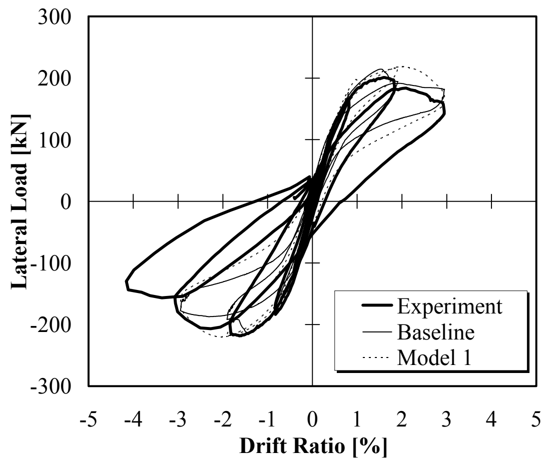

Fig. 3.37 Simulated response using ECC Model 1.

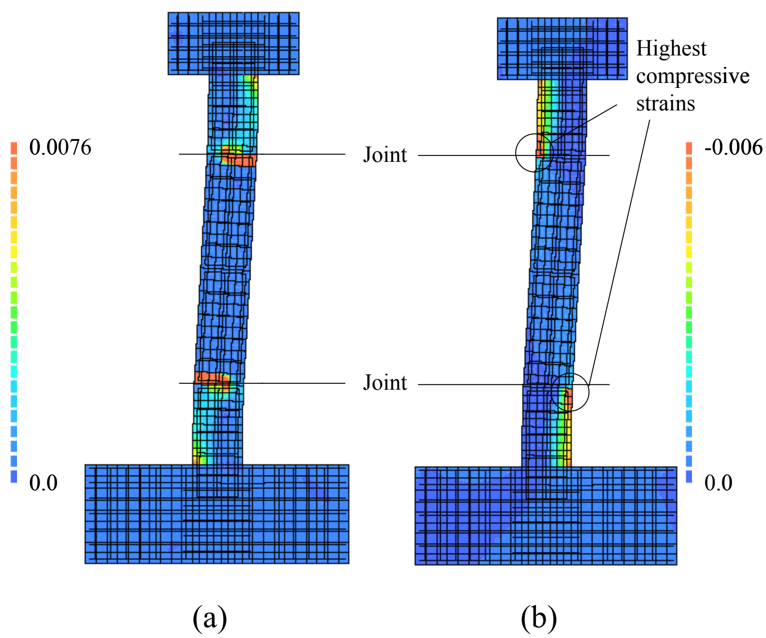

Fig. 3.38 Contour plots of (a) principal tensile strains and (b) vertical compressive strain at 2 percent drift using ECC Model 1 (deformations magnified by a factor of 2).

The column fails when the compressive strength of the ECC is reached at the joint, and begins to soften shortly after. The failure in this case occurs directly at the joint rather than slightly away from it as in the original case. This is because the localization of the cracking occurs in the concrete rather than the ECC. Directly below the localized crack, i.e., at the joint between the concrete and the ECC, the ECC is not able to sustain tensile stresses due to the presence of the crack. Further down the column, i.e., away from the joint, the ECC begins to take tensile stresses and contributes to the moment capacity of the column. In the original model at the section where failure occurred, the ECC was unable to contribute to the moment capacity due the localized crack in the ECC above it, causing the failure. In this case, the ECC was contributing to the moment capacity at this section, and therefore the weakest section was now at the joint itself where there was no contribution from either the bonded reinforcing or the ECC.

The increased strength of the ECC as described by Model 1 did not provide significant improvements to the overall behavior of the column. The peak drift and strength were increased slightly over the original case, but compressive failure still occurred relatively early and near the joint region. The localization of cracking was changed from the hinge segment to the concrete segment, but this did not significantly alter the behavior.

The resulting load-drift response for Model 2, with moderate ductility increase, is shown against the experimental response and the simulated response using the original ECC response in Figure 3.39. Again, the response with increased ECC strength is similar to the original model, but with an increase in the peak load. The localization of cracking again occurs in the concrete segments, but is delayed with respect to the original model. This is because while the ECC in this case cracks at a lower stress than the strength of the concrete, it then hardens to a peak stress higher than the strength of the concrete. The localization of cracking in the concrete segment can be seen in the contour plot of principal tensile strains shown in Figure 3.40. The contours are plotted such that the maximum value is the localization strain of the ECC in tension (1.37 percent). It is clear from the contour plots that again the ECC is far from localization and is therefore able to contribute its tensile stresses to the moment capacity of the column.

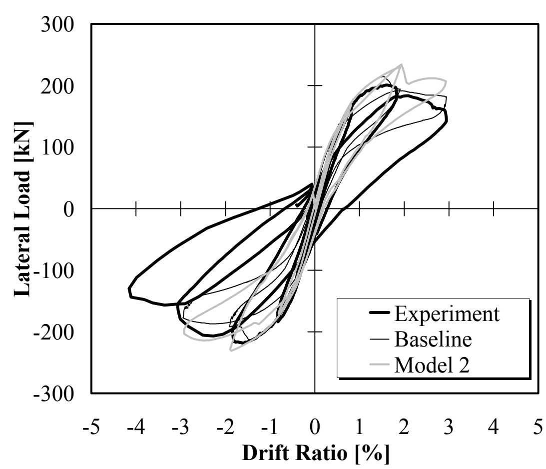

Fig. 3.39 Simulated response using ECC Model 2.

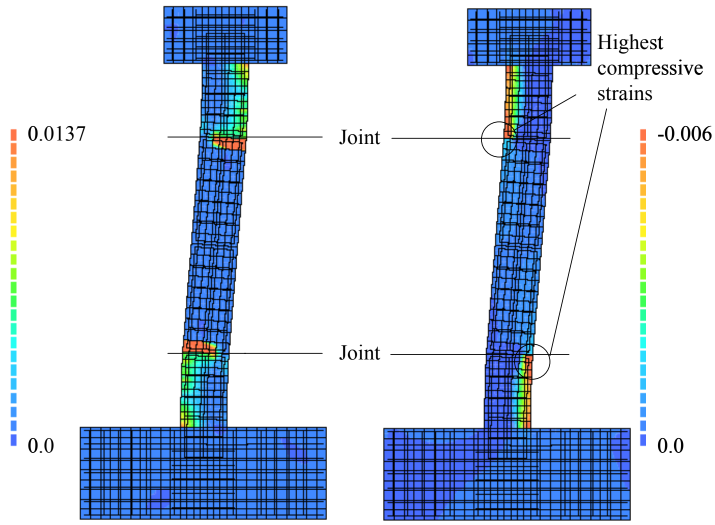

Fig. 3.40 Contour plots of (a) principal tensile strains and (b) vertical compressive strain at 3 percent drift using ECC Model 2 (deformations magnified by a factor of 2).

Similarly to the case of Model 1, the ECC reaches its capacity in compression at the joint itself due to the localization of cracking in the concrete segment. The moderate increase in ductility as described by Model 2 again provides only minimal improvements to the overall behavior of the column. The final model, Model 3, provides an even greater increase in the strain-hardening capacity of the ECC in tension, but perhaps more importantly, limits the peak strength from exceeding the tensile strength of the concrete. The resulting load-drift response for Model 3 is shown against the experimental response and the simulated response using the original ECC response in Figure 3.41.

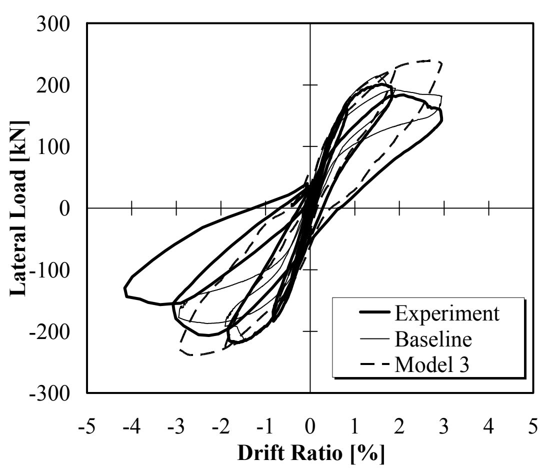

Fig. 3.41 Simulated response using ECC Model 3.

The response of the column with ECC Model 3 shows a distinct difference from the original model and Models 1 and 2. The column does not reach peak strength and begin to soften as with the other cases. In this case, the maximum tensile strains occur at the ends of the columns, and localization of cracking does not occur near the joints. The difference in behavior is illustrated in the contour plot of principal tensile strains shown in Figure 3.42. The strains are plotted such that the maximum strain values is 1 percent, which is a point that is well past cracking but still well before localization. Cracking and strain hardening of the ECC can be seen to be occurring throughout most of the hinge segment, with the most tensile straining occurring at the ends. Localization of cracking does not occur in the concrete because the tensile strains continue to accumulate in the ECC while not reaching a strength exceeding that of the concrete. In terms of the location of the highest compressive strains in the ECC, it has also been moved from near the joint region to the ends of the hinges. This is shown in the contour plot of the vertical compressive strains shown in Figure 3.42. In this figure, the strains are plotted such that the maximum value is equal to the peak compressive strain of the ECC.

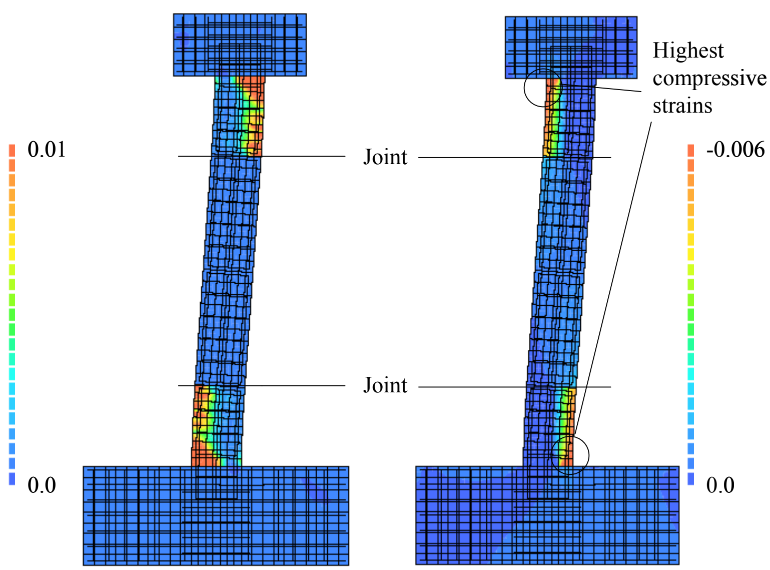

Fig. 3.42 Contour plots of (a) principal tensile strains and (b) vertical compressive strain at 3 percent drift using ECC Model 3 (deformations magnified by a factor of 2).

The sensitivity analyses of the ECC tensile behavior revealed that the best method of improving the performance of the columns is to increase the ductility of the ECC without increasing the ultimate strength. Increasing the ultimate tensile strength of the ECC to a value greater than that of the tensile strength of the concrete led to the movement of localization of cracking outside the hinge zones. This led to compressive failure near the joint between the hinge and adjacent segments. When increasing the tensile ductility while keeping the peak tensile stress below the tensile strength of the concrete, the tensile benefits of the ECC are better utilized. Cracking occurs throughout the hinge segment and localizes at the base of the column. In addition, the location of highest compressive strains moves from the joint region to the base of the column. These lead to the prevention of early compressive failure in the columns.

3.2.10 Design Improvements for UBPT Concrete Column

Overall, the UBPT concrete column performed well in some regards, but did not perform as well in others. In terms of residual displacements, the observed values after all cycles were low, and were below values that might be expected of a similar conventional RC column. The behavior of the segmental system did indeed provide the desired self-centering behavior, which was the primary goal of the system. However, the column underwent brittle compressive failure at a low drift value (less than 2 percent). In seismic regions, such a brittle failure mechanism is undesirable, and the low ductility and drift capacity also make the system unattractive for implementation. Therefore, as the simulation was found to capture the behavior of the experiment well after calibration of modeling parameters, additional analyses were performed to examine possible improvements to the system that would provide additional drift capacity and ductility.

The addition of more bonded longitudinal reinforcing in the segments may not be the most effective way to reduce the compressive stresses in the concrete, as the lack of adequate bond and the resulting inability to utilize the full capacity of the reinforcing will not significantly improve the behavior. Providing continuous reinforcing between the precast segments could prevent the compressive failure, and the model was re-analyzed for such a situation. The resulting cyclic response is shown compared with the experimental data in Figure 3.43. As expected, the presence of the continuous bonded reinforcing prevented early compressive failure, but also caused the cyclic behavior to revert back to that of traditional RC systems, i.e., with large residual displacement due to significant yielding of the reinforcing steel. The amounts of bonded reinforcing and PT reinforcing could be readjusted to retain the self-centering hysteretic behavior as shown in Kwan and Billington (2003a, 2003b). However, to continue to make use of the segmental system without continuous reinforcing, an alternative method for improving the behavior was considered.

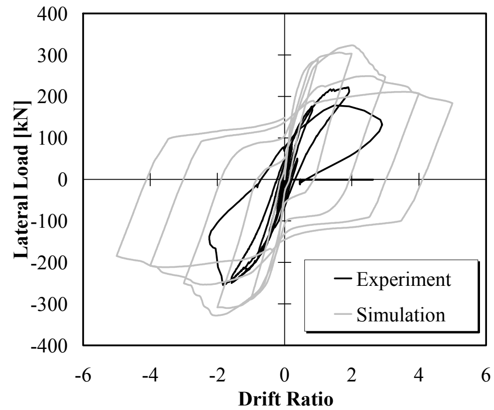

Fig. 3.43 Simulation of cyclic behavior of UBPT column with continuous bonded reinforcing.

To prevent early compressive failure while still maintaining the self-centering ability by using a system without continuous bonded reinforcing, the compressive strength and strain capacity of the concrete must be significantly increased. This strength and ductility increase can be brought about by the use of additional heavy confinement. The transverse reinforcement in Specimen 2 consisted of #4 bars at a spacing of 76 mm (3 in.), resulting in a volumetric reinforcing ratio of 1.6 percent. The computed peak strength and strain for the concrete from Mander's model for this level of reinforcing were computed as 77 MPa (11200 psi) and 0.006 mm/mm, respectively.

A new transverse reinforcing layout of #6 bars at a spacing of 51 mm (2 in.), corresponding to a volumetric reinforcing ratio of 5.4 percent, is proposed to provide an even greater increase in strength and ductility to the concrete. The computed peak strength and strain of the concrete for this level of transverse reinforcing is computed from the Mander model as 114 MPa (16500 psi) and 0.013 mm/mm, respectively. The model was re-analyzed using these parameters for the concrete constitutive model in the hinge segments. The resulting load-drift response is shown compared to the experiment in Figure 3.44.

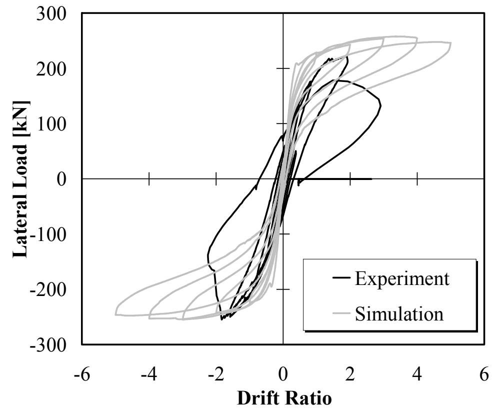

Fig. 3.44 Simulation of cyclic response of UBPT column with increased confinement.

The column with increased confinement to the concrete in the hinge segments has significant improvement in the cyclic behavior. The column is able to sustain drift cycles in excess of twice the amount previously obtained without suffering a compression failure in the hinges. The column exhibits classic flag-shaped hysteretic behavior, with self-centering accompanied by some energy dissipation. While the behavior exhibited by this column could now be considered ideal, the question remains as to whether such high confinement can be practically applied to the hinge concrete. Such high amounts of confinement have been suggested in other research by Kurama et al. (2002) for precast segmental UBPT walls, where the hinge segments are designed with transverse volumetric reinforcing ratios of up to 7.3 percent. For the columns in this study, transverse reinforcing consisting of #6 ties at a spacing of 51 mm (2 in.) may seem impractical but could be done. If providing this level of reinforcing using standard reinforcing bars is considered infeasible, alternate methods of providing confinement could also be utilized, such as the use of steel or FRP jacketing. These methods can provide even greater confinement than closely spaced spiral reinforcing.

3.3 SUMMARY

The enhanced performance UBPT system investigated here was found to be satisfactorily simulated through the use of continuum finite element analysis. Through the analysis, the cause of failure of the concrete UBPT system was able to be determined. The failure of the columns at low drifts was due to a combination of two factors that significantly reduced the moment capacity of the critical sections, i.e., low compressive ductility of concrete due to inadequate confining and reduced capacity of bonded reinforcing in tension due to inadequate bond. Cyclic analyses performed assuming that the concrete is well confined showed stable, self-centering behavior up to high drift levels, indicating that the best means of improving the performance of the columns is to provide additional confinement to the hinge segments.

The UBPT columns with ECC hinges showed improved behavior with respect to the columns with concrete hinges, in that when compressive failure occurred, it progressed in a much less brittle fashion. However, the columns also failed at relatively low drift levels due to compressive failure near the joints. The ECC was expected to provide improvements to the structural performance of the columns due to both its compressive and tensile characteristics. In terms of the compressive behavior, the damage-tolerant, self-confining behavior of the ECC did indeed provide improvements to the failure behavior and observed damage in the column. In terms of the tensile behavior, the added tensile capacity of the ECC did not provide as much improvement as expected. Sensitivity studies showed that increasing the tensile strain capacity of the ECC without increasing the peak strength was the best means of altering the ECC behavior to improve the behavior of the columns.

Two other important conclusions were drawn from the analyses performed. The first conclusion involved the particular system investigated here. While the system holds promise for improving the post-earthquake functionality of bridge structures, it makes use of a number of novel systems (namely UBPT, precast construction without continuous reinforcing between segments, strain-hardening cementitious composites) whose behavior is fundamentally different than that of commonly used conventional systems. The use of new and untested materials and systems is generally not accepted quickly by practicing engineers, who tend to be very conservative. This is particularly true in seismic regions, as earthquake loading is more unpredictable and more severe than loads in nonseismic regions.

Discussion with bridge engineers at the California Department of Transportation has revealed that they are indeed uncomfortable with all of the aforementioned technologies in their bridges. In addition, even the square cross section used in this system is not typical of bridge columns in California, whose bridge piers are almost entirely of circular cross sections. For this reason, an alternative system that still allows for self-centering, but which differs less drastically from currently used systems, is studied in the remainder of the research. This system consists of a monolithic column with circular cross section and only a single, concentric post-tensioning tendon, and will be discussed and analyzed in Chapter 4. The similarity of this system to current systems may allow for more rapid adoption of the use of UBPT in columns in seismic regions, which could pave the way for the use of the additional technologies considered here.

The second conclusion drawn from the analysis here is that the use of detailed, continuum finite element analysis may not be suitable for the types of analyses required for a full performance-based assessment using the PEER methodology. The PEER PBEE assessment requires dynamic, nonlinear analyses of analytical models under one or more suites of ground motion acceleration histories scaled to multiple intensity levels. Given that a simple cyclic nonlinear analysis of one of the continuum models presented here requires several hours of computing time on a relatively new personal computer, it quickly becomes clear that performing perhaps hundreds of dynamic analyses on even larger, full structure models becomes unreasonable. Therefore the continuum analysis used here will make way for less-detailed but far more computationally efficient fiber element modeling.

4 Prediction of Residual Displacements

4.1 INTRODUCTION

In Chapter 3, a precast segmental UBPT system was proposed to provide self-centering and reduced residual displacements to bridge columns in seismic regions. While the system showed promise, it made use of a number of new and untried technologies that may make structural engineers hesitant to adopt the system in new designs. An alternative system that makes use of UBPT for self-centering was proposed for RC bridge columns by Sakai and Mahin (2003, 2004a, 2004b), with the goal of keeping the system as similar as possible to currently designed bridge columns, thereby making it more attractive for adoption by bridge engineers. The system starts with a typical Caltrans column configuration, i.e., a circular column with spiral reinforcing, and to reduce residual displacements simply adds a single concentric unbonded post-tensioning tendon to the column while simultaneously reducing the bonded longitudinal reinforcing. The optimal proportioning of PT reinforcing to bonded reinforcing was determined through extensive analytical studies by Sakai and Mahin (2003, 2004a, 2004b).

To study the benefits of such a system, a comparison between a conventional RC column system and the aforementioned UBPT self-centering system of Sakai and Mahin is made and is presented in Chapter 5. The comparison uses a benchmark bridge structure and the PBEE assessment methodology developed by the Pacific Earthquake Engineering Research Center (PEER). The assessment methodology requires extensive analysis and as such, the ability of simulation models to predict the behavior of both the conventional and UBPT systems must be validated. As the continuum finite element modeling methods used in Chapter 3 were found to be too expensive computationally for the PBEE assessment, a more efficient fiber element method was chosen for the analyses. In this chapter, fiber element models were validated against experimental data from shaking table tests of the UBPT system performed by Sakai et al. (2005). In particular, the ability of the dynamic behavior of both the RC and UBPT systems are considered, with the primary goals being accurate prediction of both peak and residual displacements.

While predicting the dynamic response of RC structures using fiber element models has been extensively studied, it is the ability of the models to capture the dynamic response of the UBPT columns that is one of the primary goals of the investigation. More importantly, the ability of the fiber element models to predict residual displacements in conventional RC structures under dynamic loading, a subject that has not received as much attention, is investigated. The properties of the fiber element model and their effects on the residual displacement response prediction are studied. Methods of improving the prediction of residual displacements with the fiber element models, including an enhanced constitutive model for concrete, is presented and discussed.

4.2 SIMULATION OF RC AND UBPT COLUMNS UNDER DYNAMIC LOADING

4.2.1 Background on Experiments

The experimental program to be simulated consisted of the dynamic testing of a set of roughly 1/6-scale RC and UBPT bridge columns tested at the University of California, Berkeley, by Sakai et al. (2005). The two specimens modeled are the RC and UBPT single-column specimens. The only difference between the specimens was the presence of the UBPT, and the purpose was to evaluate the response of the self-centering column in comparison to that of the conventional RC column.

A schematic diagram of the test specimens with reinforcing details can be seen in Figure 4.1. The RC column was a single 406-mm-diameter circular column with a longitudinal reinforcing ratio of 1.20 percent and a transverse volumetric reinforcing ratio of 0.76 percent. Axial load in the columns, representing dead load, was applied through the use of large rectangular concrete blocks attached to the top of the column. In this way, the P-Delta effect of the dead load would be represented in the experiment. The axial load ratio of the column from the dead load was 7 percent. The UBPT column specimen was a 406-mm-diameter single circular column with a longitudinal reinforcing ratio of 0.66 percent and a transverse volumetric reinforcing ratio of 0.76 percent. The UBPT column had a single 32-mm-diameter unbonded post-tensioned rod in the center of the cross section that was stressed to an initial prestressing force of 330 kN, which corresponds to a stress of approximately $0.4f_{su}$. The total axial load ratio (including both the dead load and the axial load from prestress) of the column was 15 percent. The measured fundamental periods of the columns were 0.77 sec and 0.75 sec for the RC and UBPT columns, respectively. The concrete in both columns had a nominal 28-day compressive strength of 32 MPa.

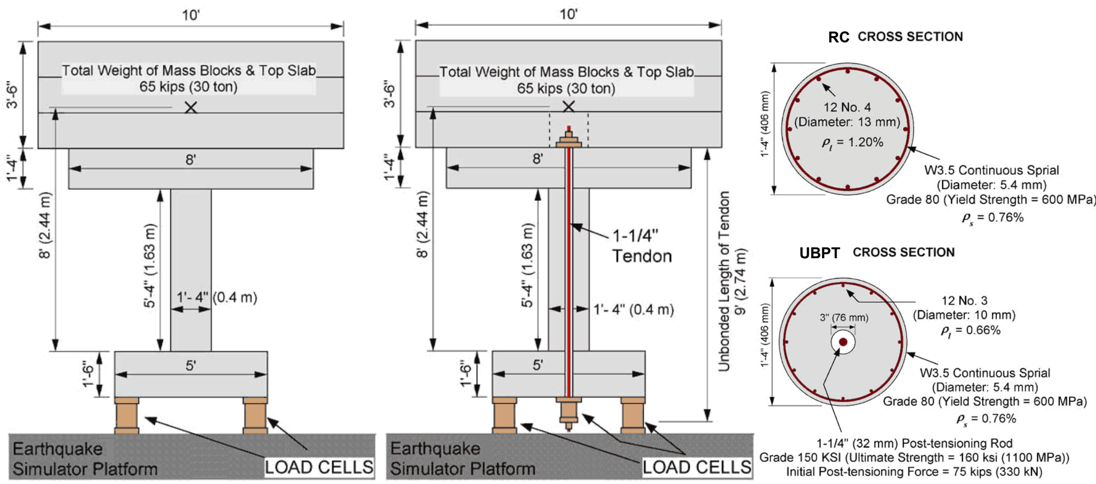

Fig. 4.1 Details of RC and UBPT single-column specimens (from Sakai REF).

The column was tested on a bi-directional shaking table and was subjected to increasing levels of excitation using two orthogonal components (fault normal and fault parallel) of the Los Gatos record from the 1989 Loma Prieta earthquake in California. The PGA of the fault-normal component was 0.74 g, while the PGA of the fault-parallel component was 0.45 g. The record was a near-fault record from a magnitude 7 event and at a distance of 3.5 km. The elastic response spectra with 2 percent damping of the two components of motion are shown in Figure 4.2. The time values for the record were reduced by a factor of 2.12, due to specimen scaling effects, as discussed in Sakai et al. (2005). The columns were first subjected to two low-intensity inputs, corresponding to the record scaled to 7 and 10 percent. The columns were then subjected to a "design level" motion, with the motion scaled to 70 percent. The design level motion was intended to impose a displacement ductility demand in the specimen of roughly 4. Finally, the columns were subjected to a "maximum level" motion, with the motion scaled to 100 percent. The maximum level motion was intended to impose a displacement ductility demand in the specimen of roughly 8.

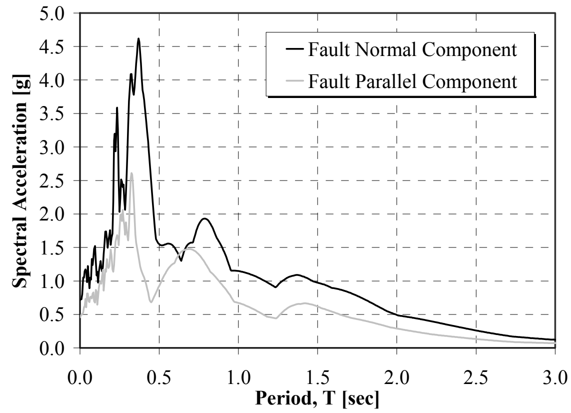

Fig. 4.2 Elastic response spectra with 2 percent damping, Los Gatos record.

4.2.2 Finite Element Model

All fiber element modeling performed herein was done using the OpenSees platform, which is an open-source software framework for earthquake analysis of structures developed by PEER (http://opensees.berkeley.edu). Many options exist for modeling beam and column elements, for example the use of displacement versus force-based elements, or distributed- versus concentrated-plasticity elements. Because nonlinear plastic hinging behavior is expected in the members investigated, the model must be able to capture this deformation behavior accurately. The requirement of numerous displacement-based elements to model accurately a single beam or column undergoing plastic hinging behavior precludes their use as an efficient element for modeling. Force-based elements are therefore considered a better choice in this case, as force equilibrium rather than displacement compatibility is satisfied, allowing for the use of a single element to model a single beam or column.

The column is modeled with a single force-based concentrated-plasticity (or lumped-plasticity) fiber element. The element is not a lumped-plasticity element in the conventional sense, wherein the nonlinear behavior is lumped into moment-rotation springs at the ends of an element. Rather, the element is still a fiber-based element but with nonlinear constitutive behavior limited to specified plastic hinge regions at the ends of the element. The remainder of the element behaves linear elastically. A schematic representation of the element is shown in Figure 4.3. The element used was the *BeamWithHinges3* element in OpenSees, and full details of the element formulation can be found in Scott and Fenves (2006). This recently developed element makes use of a modified Gauss-Radau quadrature rule for integrating element stiffness to eliminate objectivity in nonlinear response while maintaining the exact response under linear conditions.

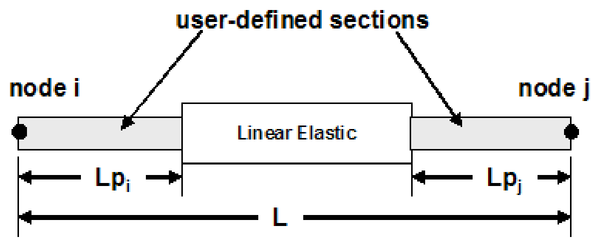

Fig. 4.3 Representation of *BeamWithHinges* element (source: opensees.berkeley.edu).

The plastic hinge length for the column was calculated using an equation given in the Caltrans Seismic Design Criteria for reinforced concrete columns, as follows:

$$L_p = 0.08L + 0.022 f_{ye} d_{bl} \geq 0.044 f_{ye} d_{bl} \text{ (mm, MPa)} \tag{4.1}$$

where L_p is the plastic hinge length, L is the column length, f_{ye} is the expected yield strength of the reinforcing steel, and d_{bl} is the diameter of the longitudinal reinforcing bars. The equation is an adaptation of an equation by Priestley et al. (1987). The elastic portion of the element is defined with three parameters: the elastic modulus and the moments of inertia in the two orthogonal bending directions. The elastic modulus used was that of the concrete, 560 MPa (3865 ksi) computed using the ACI equation presented in Chapter 3 for normal weight concrete. The moment of inertia was computed using figures presented in the Caltrans Seismic Design Criteria, which give the elastic stiffness ratio I_e/I_g (effective moment of inertia over gross moment of inertia) for circular or rectangular reinforced concrete members as a function of axial load ratio and longitudinal reinforcing ratio. The figure for circular reinforced concrete members is shown in Figure 4.4.

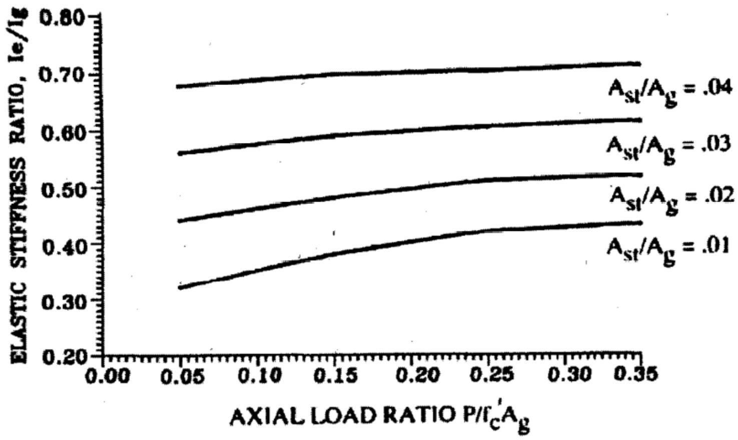

Fig. 4.4 Elastic stiffness ratios for circular reinforced concrete members (source: Caltrans SDC).

A three-dimensional model was created so that both components of the ground motion could be applied as in the experiment. The column is assumed fixed at the base. The *Concrete01* model in OpenSees was used to describe the stress-strain behavior of both the unconfined and confined concrete. The stress-strain relationship described by *Concrete01* follows the Kent-Scott-Park model (Scott et al. 1982) in compression and has no tensile strength. The use of a concrete constitutive model with no tensile strength was assumed to be appropriate for modeling of this column because a number of lower-intensity inputs were applied to the columns before the design and maximum level earthquakes were applied. These low-level inputs were assumed to cause the concrete to crack but to not cause any other significant nonlinear behavior in the column. Unloading and reloading in the *Concrete01* model is assumed to be linear with a degraded stiffness according to work by Karsan and Jirsa (1969).

The fiber section used for the beam elements was discretized into core fibers (assumed to be confined by the spiral reinforcing) and cover fibers (unconfined). The unconfined compressive strength of the concrete was measured as 31.7 MPa, and this value was used to define the behavior of the cover concrete fibers. For the core concrete fibers, the peak compressive stress and strain were increased due to the confinement effect based on the Mander et al. (1983) model. According to the Mander model, the peak confined compressive strength for concrete confined by spirals or circular hoops can be computed using the following equation:

$$f'_{cc} = f'_{co}\left(-1.254 + 2.254\sqrt{1+\frac{7.94 f'_l}{f'_{co}}} - 2\frac{f'_l}{f'_{co}}\right) \tag{4.2}$$

where f'_{cc} is the confined compressive strength, f'_{co} is the unconfined compressive strength, and f'_l is the effective lateral confining stress on the concrete from the spiral reinforcing. The effective lateral confining stress, f'_l, can be computed using the following equation:

$$f'_l = \frac{1}{2} k_e \rho_s f_{yh} \tag{4.3}$$

where k_e is the confinement effectiveness coefficient, ρ_s is the ratio of the volume of transverse confining steel to the volume of confined concrete core, and f_{yh} is the yield strength of the transverse reinforcing. The value ρ_s can be computed as follows:

$$\rho_s = \frac{4A_{sp}}{d_s s} \tag{4.4}$$

where A_{sp} is the cross-sectional area of the transverse reinforcing, d_s is the diameter of the transverse reinforcing, and s is the center-to-center spacing of the transverse reinforcing. The confinement effectiveness coefficient, k_e, can be computed using the following equation:

$$k_e = \frac{\left(1 - \frac{s'}{2d_s}\right)^2}{1 - \rho_{cc}} \tag{4.5}$$

where s' is the clear vertical spacing between the transverse reinforcing and ρ_{cc} is the ratio of the longitudinal reinforcement to the area of the core section. Finally, the confined peak compressive strain can be computed using the following equation:

$$\varepsilon_{cc} = \varepsilon_{co}\left[1 + 5\left(\frac{f'_{cc}}{f'_{co}} - 1\right)\right] \tag{4.6}$$

where ε_{cc} is the peak confined compressive strain, and ε_{co} is the peak unconfined compressive strain (assumed to be 0.002 mm/mm).

The *Steel02* model in OpenSees was used for the bonded longitudinal reinforcing. The stress-strain relationship described by the *Steel02* model follows the Giuffre-Menegotto-Pinto model (Taucer et al. 1991), which incorporates the Bauschinger effect for cyclic loading. Bond-slip in the reinforcing was not included in the model. Based on tension tests of the reinforcing bars, the yield strengths for the #4 and #3 bars were set as 455 and 424 MPa, respectively. A hardening ratio of 2 percent of the initial elastic modulus was assumed. The spiral reinforcing was a Grade 80 steel with a tensile strength of 600 MPa as measured by Sakai and Mahin (2005). This value was used for the confining reinforcement in the computation of confined concrete strength. The stress-strain behavior for the steel and confined concrete are shown in Figure 4.5.

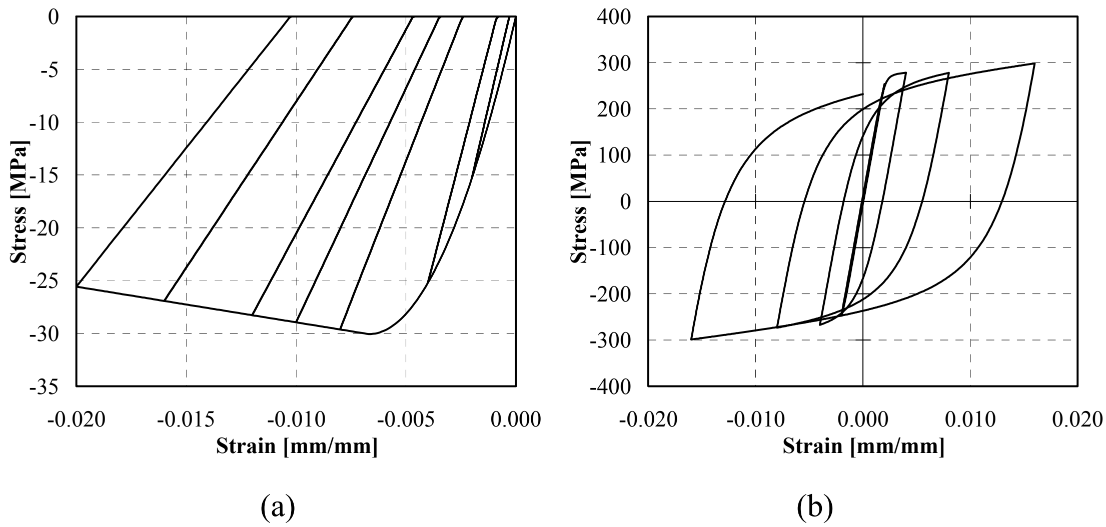

Fig. 4.5 Stress-strain response for (a) *Concrete01* and (b) *Steel02* models.

A point mass was used to model the large rectangular concrete slabs above the column. Translational mass as well as rotational mass moments of inertia for a rectangular prism were defined for the point mass. For the UBPT column, a truss element (the *co-rotational truss* element in OpenSees) was used to model the post-tensioning bar and was connected at nodes above and below the column at the anchorage locations. Curvature in the PT bar was therefore not modeled. The post-tensioning steel was designed to remain elastic under all loading levels; therefore an elastic model was used with a prescribed initial strain to provide the prestress. The *ElasticPP* (elastic-perfectly plastic) uniaxial model in OpenSees allows for the input of an initial strain value, which provides the desired prestress. The initial strain was set to achieve a prestressing force of 403 kN, which after elastic shortening of the column would result in a prestress force of 374 kN (the value that was measured in the experiment). The assumed elastic modulus for the prestressing steel model was 190 GPa, and the yield strain was set to a sufficiently large dummy value such that bar would remain elastic.

Rigid links were used to model the foundation block and to connect the column to the PT bar anchorage location and also to the point mass. A schematic representation of the model used for the self-centering column is shown in Figure 4.6. An eigenvalue analysis of the model yielded first-mode periods of 0.68 sec and 0.69 sec for the RC and UBPT columns, respectively (as compared to 0.77 and 0.75 sec found experimentally).

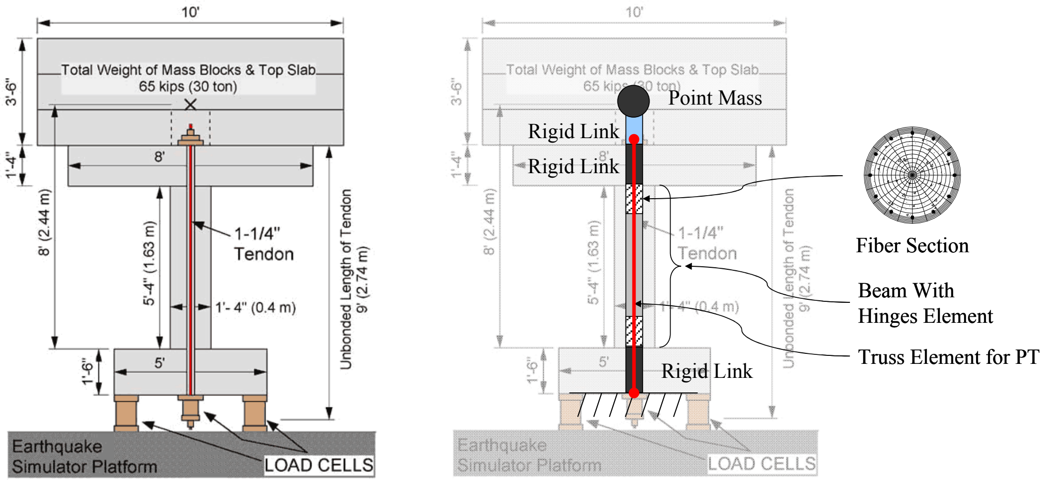

Fig. 4.6 Schematic of model for self-centering column.

4.2.3 Analysis Procedure

The dynamic analyses were performed using the Newmark method with average acceleration. Damping was applied using Rayleigh damping with a damping ratio of 2 percent. The solution algorithm was a Newton-Raphson scheme with an energy norm as the convergence criterion. An additional 10 sec of free vibration (analysis with input acceleration of zero) was performed following each analysis to allow the column to come to rest such that residual displacements could be recorded.

4.2.4 Simulation Results

4.2.4.1 RC Column

The two column models were subjected initially to the Los Gatos motion at the design level (i.e., scaled to 70 percent), followed by the same record at the maximum level (i.e., scaled to 100 percent). The simulated displacement response histories in the fault-normal direction of motion of the RC column for both levels of motion, recorded at the center of mass of the top blocks, are shown compared to the experimental response, also measured at the center of mass of the top blocks, in Figures 4.7 and 4.8.

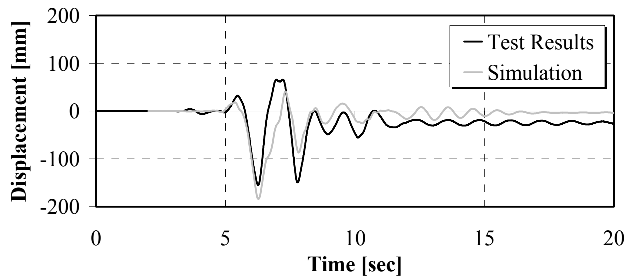

Fig. 4.7 Comparison of experimental and simulated displacement response histories in the fault-normal direction for RC column subjected to 70 percent of Los Gatos record.

For the design level motion, the peak displacement was predicted well. The simulation predicted a peak displacement of 165 mm, while the experimental peak value was 155 mm (corresponding to a drift ratio of roughly 6.4 percent), a difference of approximately 6 percent. The residual displacement of the column, however, was not as well predicted. In the experiment, the column sustained a residual displacement of approximately 25 mm, corresponding to a drift of slightly more than 1 percent. The simulation predicted a residual displacement of essentially zero. The fact that the simulation was unable to capture this residual displacement revealed a severe limitation in the predictive ability of the model, which will be addressed in Section 4.3.

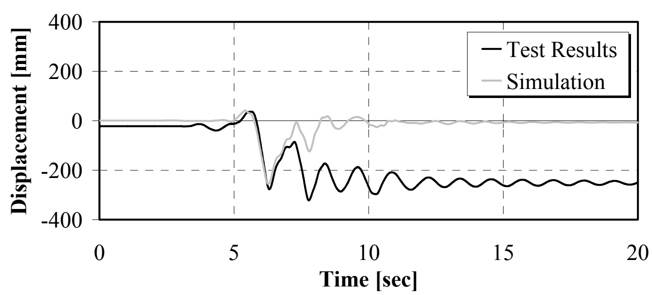

Fig. 4.8 Comparison of experimental and simulated displacement response histories in the fault-normal direction for RC column subjected to 100% of Los Gatos record.

For the maximum level motion, the peak displacement was again predicted well. The peak displacement of the simulation was 312 mm, while that of the experiment was 323 mm, a difference of less than 4 percent. The residual displacement of the column in the experiment was extremely high following the maximum level motion, with a value of 252 mm, which corresponds to a drift ratio of over 10 percent. Again, the residual displacement predicted by the simulation was essentially zero, even with an extremely large peak displacement demand (a peak drift ratio of greater than 13 percent).

Although the simulation was again unable to capture any residual displacement in the case of the maximum level motion, its predictive ability for this extremely high level of motion was considered to be of less importance than for the design level motion. To explain, recall that the intended ductility demands for the design and maximum level earthquakes were 4 and 8, respectively. The resulting ductility demand that actually occurred during the design level earthquake was found by Sakai et al. (2005) to be closer to that of the intended level of the maximum level event. Correspondingly, the actual ductility demand experienced during the maximum level run was even greater than that expected of an actual maximum level event.

In the case of an even-larger-than-maximum level earthquake, post-earthquake performance becomes unimportant as collapse prevention becomes the overriding concern. This was indeed the case for the RC column under the 100 percent motion, where a drift ratio of over 13 percent was observed. Such a value should be considered alarmingly large even for a seismically detailed member. The fact that the column had a residual drift of greater than 10 percent showed that in this case the residual displacement was not merely a serviceability issue, but was a sign of impending collapse. The simulations are not intended or expected to capture collapse behavior, which is beyond the scope of this research. Therefore the behavior under the 70 percent level motion was considered to be representative of a maximum level motion, and considered to be representative of the type of behavior of interest in this research.

4.2.4.2 UBPT Column

The simulated displacement response histories in the fault-normal direction of motion of the UBPT column for both levels of motion (recorded at the center of mass of the top blocks) are shown compared to the experimental response (also measured at the center of mass of the top blocks) in Figures 4.9 and 4.10.

For the design level motion, the two parameters of interest, i.e., the peak and residual drift, were found to be predicted well by the simulation. For the design level motion, the simulation predicted a peak displacement of 160 mm, while the experimental peak value was 147 mm (corresponding to a drift ratio of roughly 6 percent), a difference of approximately 8 percent.

The residual displacement of the column in the experiment was essentially zero, and was predicted to be essentially zero in the simulation as well.

For the maximum level motion, the peak displacement was again predicted well. The peak displacement of the simulation was 284 mm, while that of the experiment was 256 mm, a difference of less than 10 percent. The residual displacement in the experiment was approximately 55 mm, corresponding to a residual drift ratio of 2.25 percent. However, upon inspection following the test, it was found by Sakai et al. (2005) that one of the longitudinal reinforcing bars had fractured during the motion. This fracture presumably occurred during the main pulse. As the model for reinforcing steel does not include the effect of fracture, the simulation would not be expected to predict the experimental response well. The simulation did, however, predict a residual displacement close to that of the experiment, but this was likely due to coincidence, as the results of the simulation at such high displacement demands is likely to be erroneous.

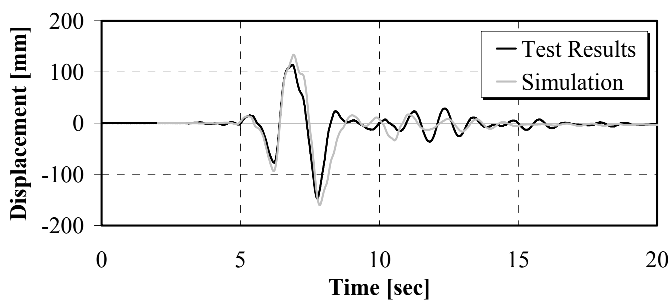

Fig. 4.9 Comparison of experimental and simulated displacement response histories in the fault-normal direction for UBPT column subjected to 70% of Los Gatos record.

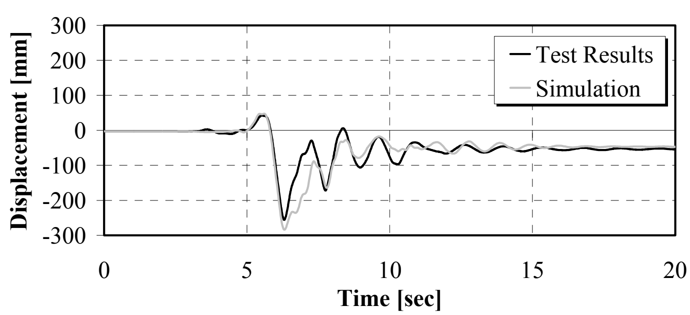

Fig. 4.10 Comparison of experimental and simulated displacement response histories in the fault-normal direction for UBPT column subjected to 100% of Los Gatos record.

As with the RC column, the 100 percent Los Gatos motion applied during the testing was larger than expected even for a maximum level motion. The design level motion was again found by Sakai et al. (2005) to provide a closer match to the intended ductility demand for a maximum level motion. For this reason, the results from the 70 percent motion were considered to be representative of a maximum level motion, and the simulation of the results of the 100 percent motion were not considered as part of the research.

One of the main conclusions from the modeling of the columns by Sakai et al. (2005) was that the simulations were able to capture the peak displacements for both columns well. The ability to predict residual displacements in the UBPT column is uncertain, and is discussed in Section 4.4. In the RC column, the residual displacements were not well predicted, and in fact no residual displacements were predicted at all. Therefore an investigation was performed to determine the cause of the inability to predict residual displacements in the model and to correct it.

4.3 PREDICTION OF RESIDUAL DISPLACEMENTS IN RC COLUMNS

4.3.1 Review of Previous Studies

A limited number of studies have been performed by a few researchers specifically with regard to predicting residual displacements. These studies include work by Mahin and Bertero (1981), MacRae and Kawashima (1997), Kawashima et al. (1998), Borzi et al. (2002), Christopoulos et al. (2003), Pampanin et al. (2003), Ruiz-Garcia and Miranda (2005), and Yazgan and Dazio (2006). With the exception of Yazgan and Dazio (2006), all of these studies involved the use of simplified hysteretic models for analyzing SDOF or MDOF structures under earthquake excitations. While these studies provided a wealth of information regarding the effect of a number of parameters for various hysteretic models (e.g., strength, post-yielding stiffness) on residual displacement responses, none of them addressed the issue faced here, which is the inability of the fiber element model to predict non-negligible residual displacements. The study by Yazgan and Dazio (2006) showed only the effect that is observed here, but made no mention of its causes.

The inability of fiber element models specifically to predict any sort of significant residual displacement has been found in other studies, such as Sakai and Mahin (2004a), Sakai et al. (2005), and Ufuk and Dazio (2006). For example, in the study by Sakai and Mahin (2004a), a fiber element model of an RC column subjected to a suite of near-fault ground motions sustained peak drifts of on average 5 percent, and ending with residual drifts of on average only 0.2 percent. As shown in experiments (e.g., Sakai et al. 2005; Hachem et al. 2003) as well as actual RC columns following earthquakes (e.g., following the Kobe earthquake), greater residual displacements should be expected than are predicted by the fiber element models.

4.3.2 Analysis with Fiber Element Model

To determine whether the inability to predict residual displacements in the previous analyses was due to the model or was a function of the ground motion selected, the model was subjected to a suite of 20 additional unscaled near-fault ground motions (shown in Table 4.1). The ground motions were not selected based on any specific criteria, and were expected to provide a random sampling of near-fault motions. The fault-normal component of motion was used for all of the ground motions. The motions were originally selected for a different study, and their details will be given in Chapter 5. Again, near-fault motions were selected, as they were expected to provide a more severe response than far-field motions.

The resulting peak and residual displacements are plotted in Figure 4.11 for the 20 earthquake ground motions. While several of the ground motions caused only low responses in the column (e.g., motions 13 through 17), a number of them caused significant peak displacements, with the largest peak displacement of approximately 360 mm resulting from ground motion 7. While some of these values are extremely large and would likely lead to collapse in a physical column, the important observation is that in no case does the model retain any significant residual displacement. This would not be expected in an actual RC column. Although residual displacements will not always occur following an earthquake, it is highly unlikely that in all of these cases, no residual displacement would be observed. The results therefore strengthen the argument that it is the fiber element model itself that is unable to capture the residual displacements that would be expected in a physical system.

While the prediction of residual displacements under dynamic loading using analytical models is generally accepted to be imprecise, the failure of the model used here to predict any residual displacements at all is unacceptable, given that a goal of the analysis is to provide a comparison of residual displacement between two systems. The prediction of residual displacement in structures subjected to dynamic loading has not been extensively studied, receiving almost negligible attention compared to the study of prediction of other demand parameters, most of which are *peak* values. However, the prediction of residual displacements in conventional RC systems has become more important in response to the adoption of performance-based criteria and interest in improvement of overall structure functionality following an earthquake. Therefore, improvements to modeling methods that can predict residual displacements are essential.

Table 4.1 Near-fault ground motions use in analysis.

Number	Earthquake	Moment Magnitude	Station	Distance (km)
1	Erzincan, Turkey	6.7	Erzincan	1.8
2	Kobe, Japan	6.9	Kobe JMA	0.5
3	Loma Prieta	7	Corralitos	3.4
4	Loma Prieta	7	Gavilan	9.5
5	Loma Prieta	7	Gilroy Historic	12.7
6	Loma Prieta	7	Lexington Dam Abutment	6.3
7	Loma Prieta	7	Los Gatos Presentation Center	3.5
8	Loma Prieta	7	Saratoga Aloha Ave.	8.3
9	Tottori, Japan	6.6	Kofu	10.0
10	Tottori, Japan	6.6	Hino	1.0
11	Coyote Lake	5.7	Coyote Lake Dam Abutment	4.0
12	Coyote Lake	5.7	Gilroy #6	1.2
13	Parkfield	6.0	Temblor	4.4
14	Parkfield	6.0	Array #5	3.7
15	Parkfield	6.0	Array #8	8.0
16	Livermore	5.5	Fagundes Ranch	4.1
17	Livermore	5.5	Morgan Territory Park	8.1
18	Morgan Hill	6.2	Coyote Lake Dam Abutment	0.1
19	Morgan Hill	6.2	Anderson Dam Downstream	4.5
20	Morgan Hill	6.2	Halls Valley	2.5

To discover the reason that fiber element models are unable to predict residual displacements whereas other modeling methods do not share this problem, the hysteretic shape of the fiber element model was first studied. As a cyclic column test was not performed by Sakai and Mahin, the cyclic response of the fiber element model was compared to cyclic experimental data on a column of the same diameter and reinforcing ratio (i.e., 406.4 mm and 1.2 percent) tested by Hamilton et al. (2002). The column tested by Hamilton et al. (2002) had no axial load, and therefore for the sake of this comparison, the fiber element model was analyzed with zero axial load (no P-Delta effects). The cyclic response of the fiber element model of Sakai and Mahin's RC column with no P-Delta is shown in Figure 4.12a. The response is typical of a well-detailed RC member, showing roughly bilinear behavior with the hysteretic behavior controlled primarily by the behavior of the reinforcing steel. The experimental data from Hamilton et al. (2002) are shown in Figure 4.12b.

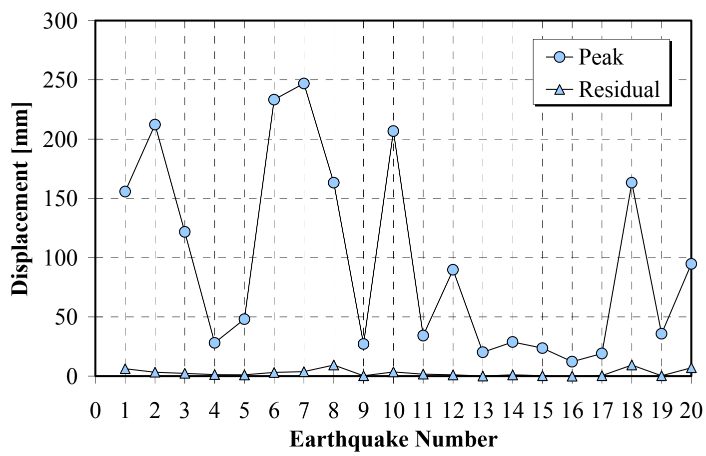

Fig. 4.11 Comparison of peak and residual displacements for fiber element model subjected to near-fault ground motions.

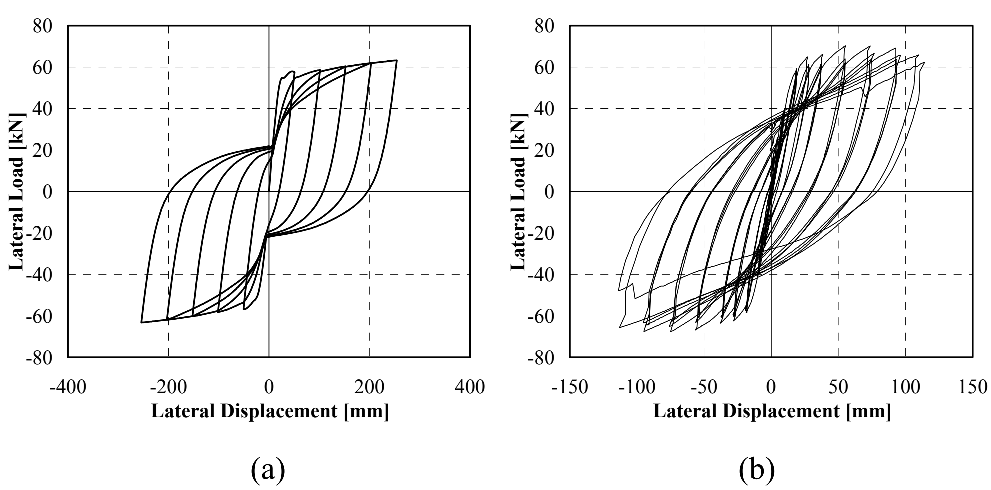

Fig. 4.12 Hysteretic response of (a) fiber element model and (b) experimental data (right, from Hamilton et al. 2002) for similar RC cantilever columns.

The simulated and experimental load-displacement plots appear to have similar behavior. Comparing the static residual displacements after reaching a drift of 100 mm, the simulation predicts a value that is roughly 20 percent less than the value found in the experiment. The difference in the two can be found in the region from unloading in one direction to loading in the other direction. Consider first the final large cycle of the experimental response. The load-displacement plot traces out a smooth curve in moving from the positive to the negative loading direction. In contrast, this same portion of the curve in the fiber element model response is quite different, displaying abrupt changes in stiffness and a flat region of near zero stiffness near the origin. This behavior can be seen as a sort of "pinching" in the hysteretic response and arises from the assumptions made in the constitutive models used in the fiber element model.

When the column is loaded in the fiber element model to a large displacement, the concrete and the steel in compression are both loaded, and the steel in tension has yielded. The concrete in tension has high tensile strains, and takes no tensile load, which represents cracking. When the loading direction is reversed, the concrete that was in compression unloads quickly and soon takes no compressive stress. The concrete that was in tension begins to move in the positive direction, but still takes no compression. Therefore as the column is unloading, the stiffness results from the reinforcing steel only, with no contribution from the concrete. At some point the steel begins to yield in both tension and compression, which corresponds to the flat portion of the curve.

At a displacement of 0 mm, a large increase in stiffness is seen. This large jump in stiffness is due to the concrete that was previously cracked in tension beginning to load in compression. As this concrete begins to reload in compression, the stiffness of the column increases rapidly. This effect leads to the pinched behavior that is observed in the cyclic behavior of the fiber element model. However, this pinched behavior in the fiber element model, which led to the difference between it and the experimental response could not without further investigation be assumed to be the cause of the inability to predict residual displacements.

4.3.3 Analysis with SDOF Models

To determine whether the inability of the fiber element model to capture residual displacements was due to its pinched hysteretic shape, a study was performed wherein SDOF models with varying hysteretic behaviors were subjected to earthquake motions and their residual displacement responses were monitored. First, an SDOF model was created with a hysteretic shape meant to emulate that of the fiber element model. To capture the essential characteristics of the hysteretic shape of the fiber element model, it was necessary to have the region of near-zero stiffness followed by the abrupt increase in stiffness near zero displacement during the change in loading direction.

OpenSees was used to perform the analysis due to the availability of a large variety of hysteretic models and the ability to combine them in series or parallel to create new models. The *PinchingDamage* uniaxial material model (Ibarra and Krawinkler 2005) was used as the base model for the SDOF hysteretic behavior. The *PinchingDamage* model is a peak-oriented model that, as the name implies, can incorporate pinching behavior and damage accumulation. The envelope curve has an elastic portion, followed by a linear hardening portion and a linear softening portion. The model can also include strength and stiffness degradation, but these effects are not incorporated here. The general behavior of the model, with several of the key model parameters highlighted, is shown in Figure 4.13.

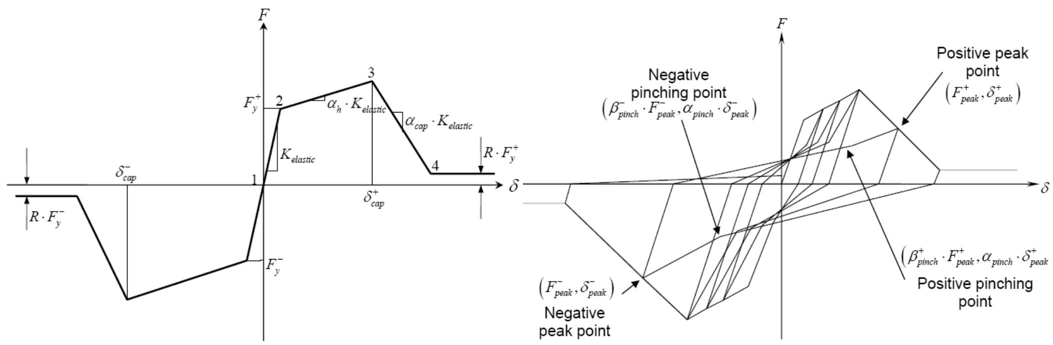

Fig. 4.13 *PinchingDamage* uniaxial material model (from Ibarra 2003). Backbone curve (left) and cyclic behavior (right).

During unloading and reloading, the *PinchingDamage* model dictates that the path will aim for the peak point after reaching zero force. Such behavior is not observed in the fiber element model hysteresis, as the force continues past the zero point and into the opposite direction before flattening out and aiming for the peak point. To incorporate this behavior, the *PinchingDamage* uniaxial model was combined in parallel with the *ElasticPP* uniaxial material model. To achieve the abrupt increase in stiffness near zero displacement, the model was again combined in parallel with a bilinear elastic model (coded as a user-supplied uniaxial material model in OpenSees). The three individual uniaxial models and the resultant model when the three are combined in parallel are shown in Figure 4.14. The parameters used to define the three models are given in the figure. The combined model displays the pinched effect as observed in the fiber element model, and will herein be referred to as the *FiberPinched* model. The *FiberPinched* model was created to have an initial stiffness equal to that of the fiber element model.

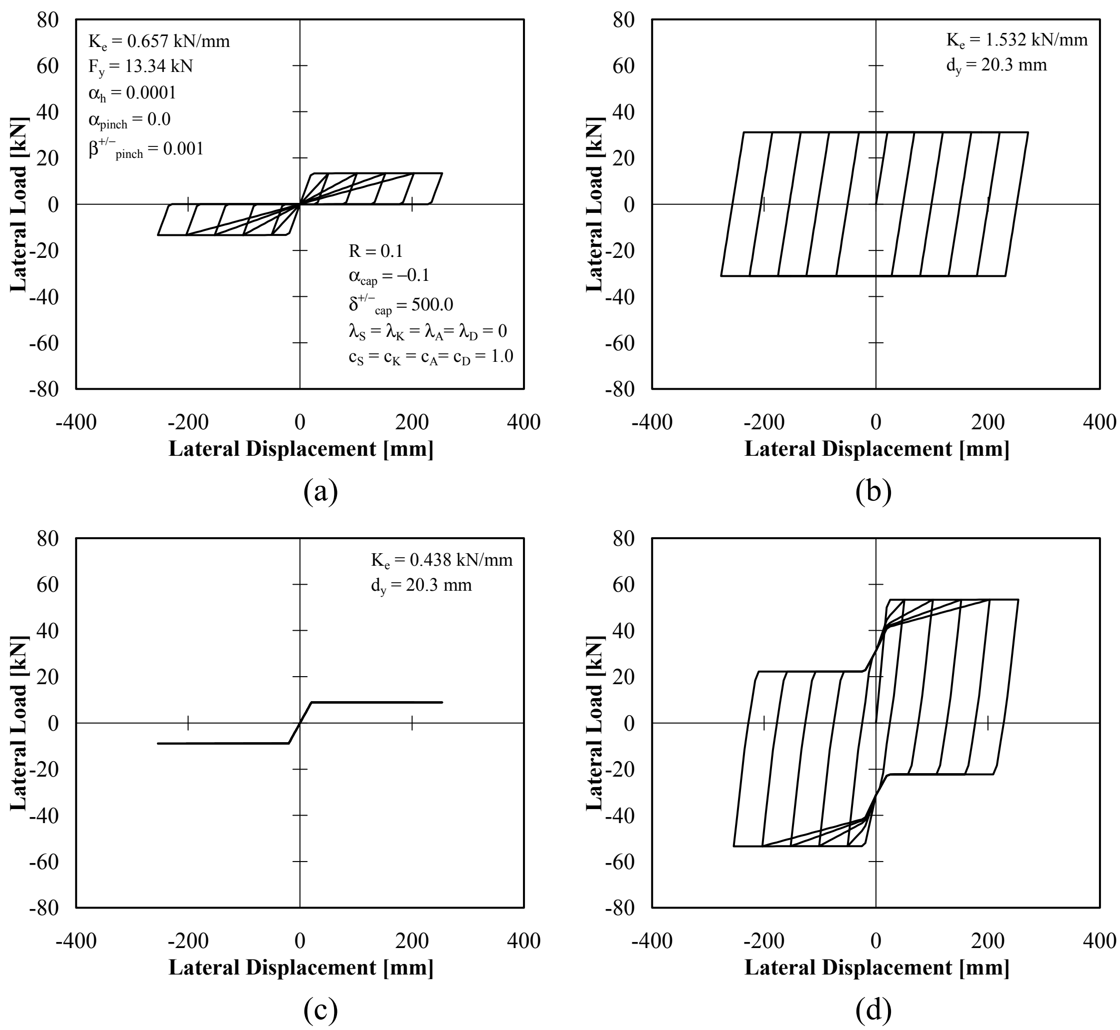

Fig. 4.14 Uniaxial models used to generate hysteretic model for SDOF analysis: (a) *PinchingDamage* model, (b) *ElasticPP* model, (c) bilinear elastic model, and (d) combined model.

To determine whether the inability to capture residual displacement is due to the pinching in the hysteretic shape, the *FiberPinched* model was modified to eliminate the pinching. The new model, which will herein be referred to as the *FiberNoPinching* model, was created by combining the *PinchingDamage* and *ElasticPP* models, as before. The *FiberNoPinching* and its individual components (along with associated parameters) are shown in Figure 4.15. For comparison, the fiber element model hysteresis is also shown. Again, the initial stiffness of the *FiberNoPinching* model was the same as that of the fiber element model.

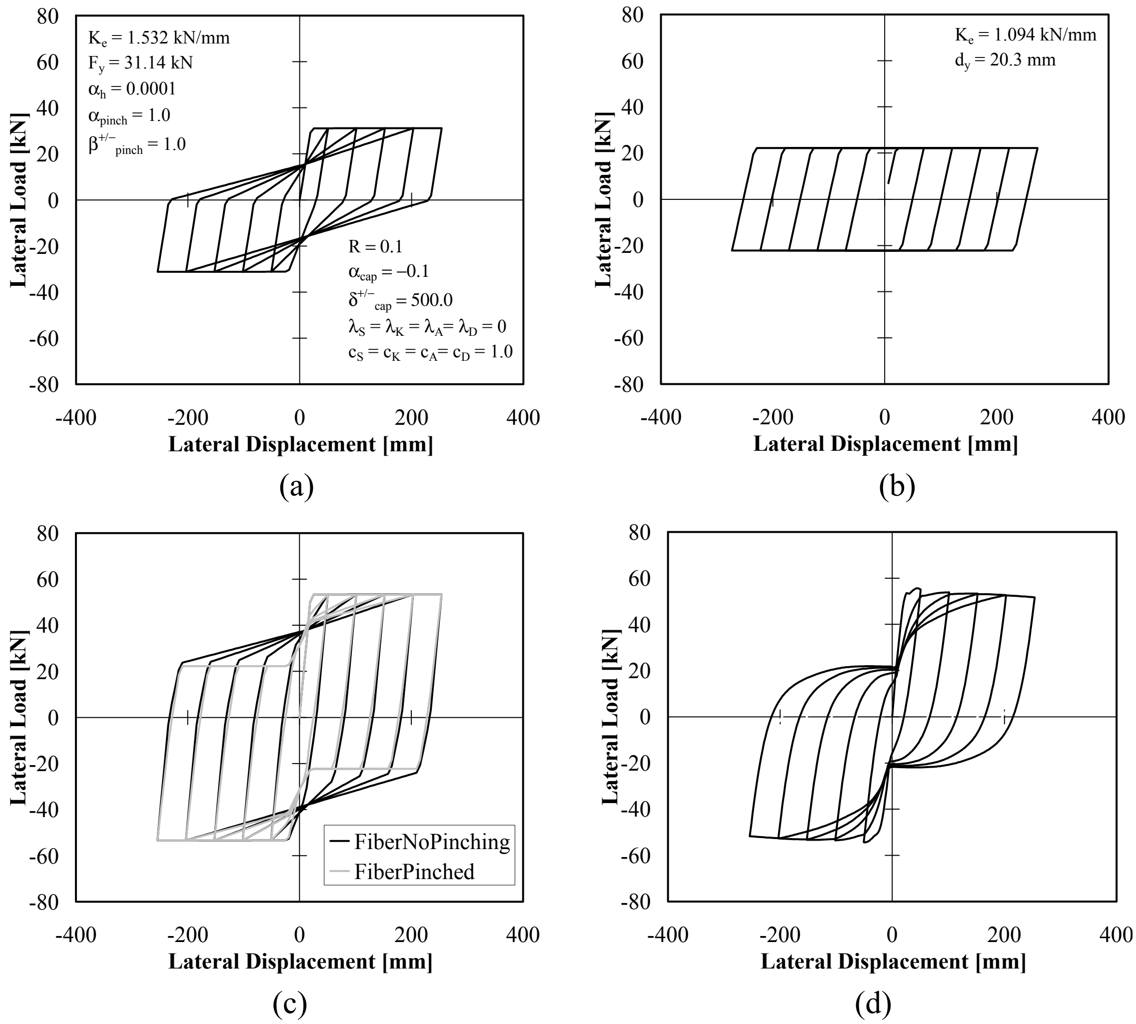

Fig. 4.15 Uniaxial models used to generate hysteretic model for SDOF analysis: (a) *PinchingDamage* model, (b) *ElasticPP* model, (c) combined models, and (d) fiber model.

Two SDOF models, using the *FiberPinched* and *FiberNoPinching* hysteretic models, were then analyzed using the same suite of 20 earthquake records. The analyses were performed with viscous damping using a dashpot element and with a damping ratio of 2 percent. The mass for the SDOF model was computed using the initial stiffness and period of the model, which were selected to match that of the fiber element model. The peak and residual displacement responses for the SDOF models using the *FiberPinched* and *FiberNoPinching* hysteretic models are shown in Figure 4.16 and Figure 4.17, respectively. For reference, the results from the fiber element model analyses are shown in gray.

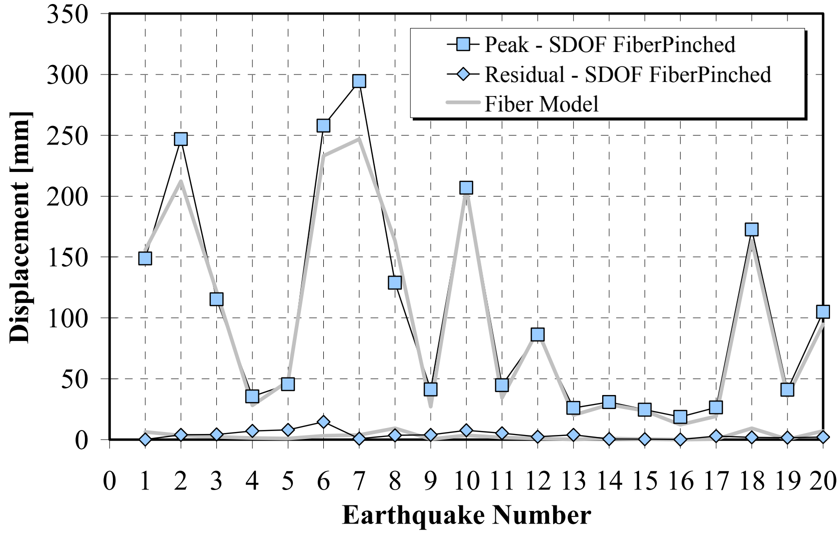

Fig. 4.16 Peak and residual displacement response for SDOF system with *FiberPinched* hysteretic model subjected to near-fault ground motions.

The results from the SDOF model with the *FiberPinched* hysteretic model show similar results to that of the fiber element model. Such behavior was expected, as the *FiberPinched* model was created to mimic the behavior of the fiber element model. As expected, the residual displacements were again essentially zero for all ground motions. The results from the SDOF model with the *FiberNoPinching* hysteretic model show similar peak displacements to the fiber element model, but, in contrast to the *FiberPinched* model, show significant residual displacements for several of the ground motions (6 out of 20). The results of the analyses show that the flattened pinching behavior of the fiber element model does prohibit the ability to capture residual displacements. When the hysteretic behavior is modified to remove this behavior, residual displacements can then be captured. While the accuracy of these values can not be verified, the key observation is that the values are non zero. The accuracy in the predictions will be discussed in Section 4.3.5

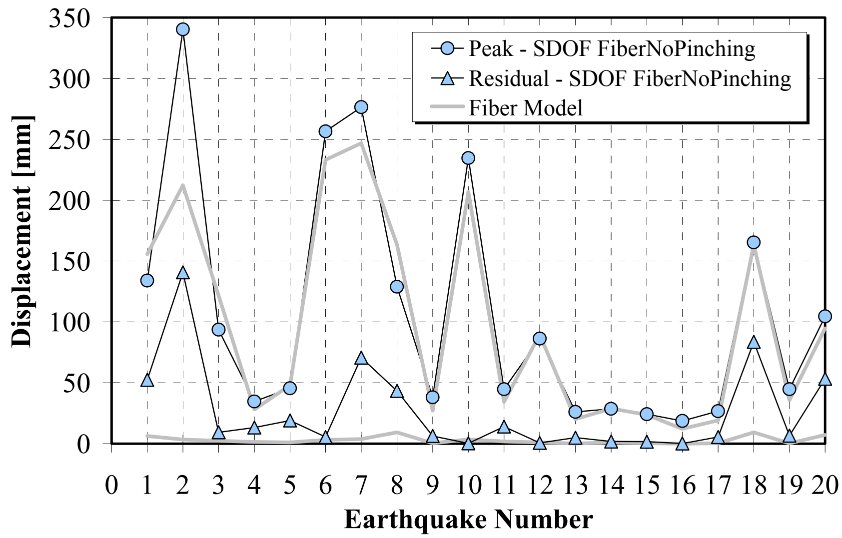

Fig. 4.17 Peak and residual displacement response for SDOF system with *FiberNoPinching* hysteretic model subjected to near-fault ground motions.

To understand why the hysteretic shape of the fiber element model leads to very low residual displacements following dynamic loading, it is useful to examine more closely the results obtained from the SDOF analysis. Consider the response from earthquake motion 20, which illustrates the effect well. For this ground motion, the peak displacement response of the two SDOF models are approximately equal, and also approximately equal to the value from the fiber element model. However, the residual displacement value for the *FiberNoPinching* model is much larger than that of the *FiberPinched* model, which is almost zero. The displacement time history and force-displacement response are shown for the two models in Figure 4.18.

The residual displacement can be seen to occur following the large pulse in the ground motion. Such behavior might be expected intuitively. The reason that the *FiberNoPinching* model retains a large residual displacement whereas the *FiberPinched* model does not is evident in the force-displacement response (Fig. 4.18b). During the main pulse, the system is pushed to its maximum displacement of roughly 103 mm (shown with arrow A in Fig. 4.18). The ground motion then gives the system a strong push in the opposite direction (shown with arrow B in Fig. 4.18). In the case of the *FiberPinched* model, the stiffness during this push in the opposite direction has an almost zero stiffness, which allows the system to be pushed to near-zero displacement again. The system then reaches a jump in stiffness again near zero displacement, which tends to keep the system near zero displacement. In the case of the *FiberNoPinching* model, on the other hand, the system has stiffness during the push in the toward zero displacement, so it does not get pushed all the way back to near-zero displacement again (point C in Fig. 4.18b). For this reason, the *FiberNoPinching* model retains residual displacement, while the *FiberPinched* model does not.

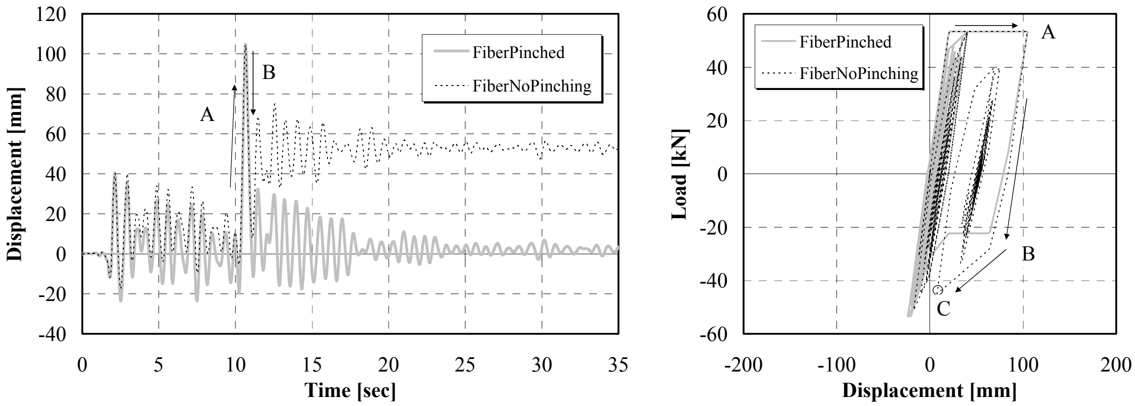

(a) (b)

Fig. 4.18 Comparison of (a) displacement time history and (b) force-displacement response for SDOF models under earthquake motion 20.

In the case of ground motion 2, the peak displacement was also much larger for the *FiberNoPinching* model than the *FiberPinched* model. The cause of this larger peak displacement can be seen by inspecting the displacement response history and force-displacement response, which are shown in Figure 4.19. The larger peak displacement is due to the same effect as described above, which is the low stiffness in the direction of movement toward zero displacement. At time 10 sec in the displacement response history, the *FiberPinched* model can be seen to be pushed back to near zero displacement, whereas the *FiberNoPinching* model is not pushed back that far. In the subsequent movement away from zero displacement, the *FiberNoPinched* model is pushed to a larger peak displacement because it is starting at a larger displacement than the *FiberPinched* model. Again, the *FiberPinched* model eventually gets pushed back to zero displacement, while the *FiberNoPinching* model does not due to its stiffness.

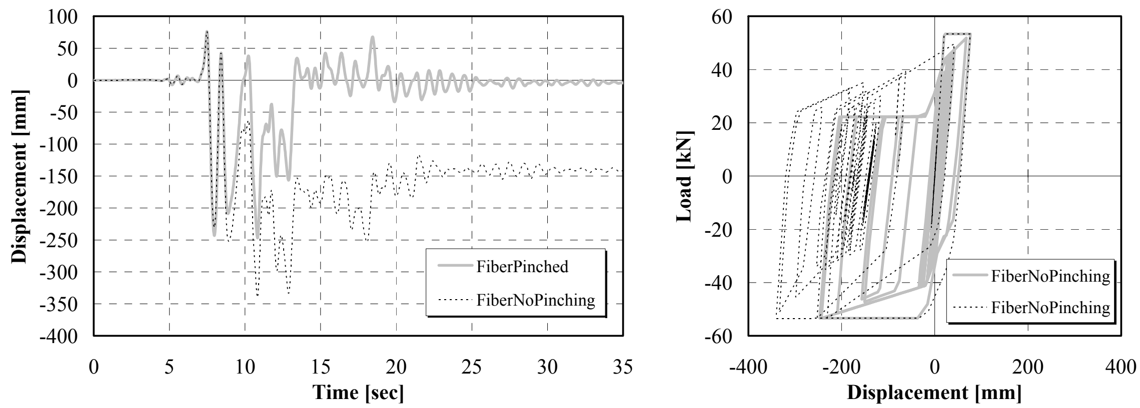

(a) (b)

Fig. 4.19 Comparison of (a) displacement time history and (b) force-displacement response for SDOF models under earthquake motion 18.

4.3.4 Modified Concrete Constitutive Model

As the pinching behavior was identified as the cause of the inability of the fiber element model to capture residual displacements, it was then necessary to determine the source of the pinching in the fiber element model. If the root of the behavior could be identified and corrected, it would allow for better prediction of residual displacement using fiber element models. In fact, the cause of the pinching behavior in the fiber element model was easily identifiable. The pinching was found to result from the constitutive behavior of the concrete.

Consider a concrete fiber on the left face of a column, whose behavior will be followed through part of the loading cycle of the column, as shown in Figure 4.20. As the column is pushed to its maximum negative displacement (region 1 in Fig. 4.20a), the concrete is somewhere on the envelope curve in compression (region 1 in Fig. 4.20b). As the column unloads (changes direction and begins to move in the positive direction, region 2 in Fig. 4.20a), the concrete fiber unloads and quickly reaches zero stress (region 2 in Fig. 4.20b). As the column continues to move in the positive direction (region 3 in Fig. 4.20a), the concrete fiber begins to go into tension, and still contributes no stiffness (at zero stress) to the column (region 3 in Fig. 4.20b).

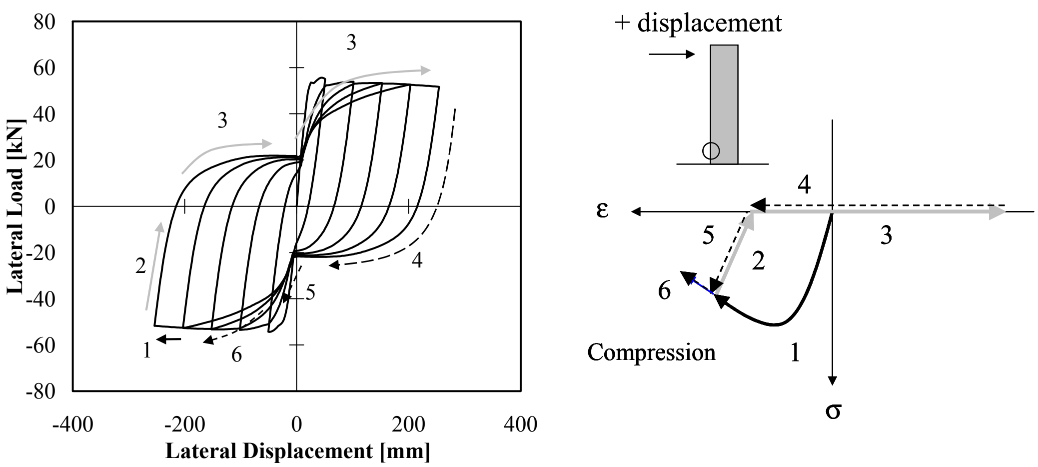

(a) (b)

Fig. 4.20 Effect on (a) fiber element model hysteresis from (b) constitutive behavior of concrete.

When the column reaches its maximum positive displacement, the column again changes direction and begins to unload (region 4 in Fig. 4.20a). During this portion, the concrete fiber reaches its maximum tensile strain then begins to move back in the positive direction (region 4 in Fig. 4.20b) along the zero stress axis, meaning that it provides no stiffness to the column. At some point, the concrete fiber reaches the point of unloading, and begins to reload to the peak compressive strain (region 5 in Fig. 4.20b). It is at this stage where the concrete in compression again begins to contribute to the stiffness of the column. This point is easily identifiable in the load-displacement plot of the column where the stiffness abruptly increases (region 5 in Fig. 4.20a). As the column continues to load (region 6 in Fig. 4.20a), the concrete again moves along the envelope curve (region 6 in Fig. 4.20b).

The pinching effect was therefore identified as arising from the reloading behavior of the concrete constitutive model from tension to compression. To smooth the unloading and reloading behavior of the fiber element model's load-displacement behavior, it was necessary to modify the behavior of the concrete constitutive model when moving from tension back to compression. It was necessary for the model to be modified such that reloading could occur at a strain value (point B in Fig. 4.21b) prior to that of the original unloading strain value (point A in Fig. 4.21a and b).

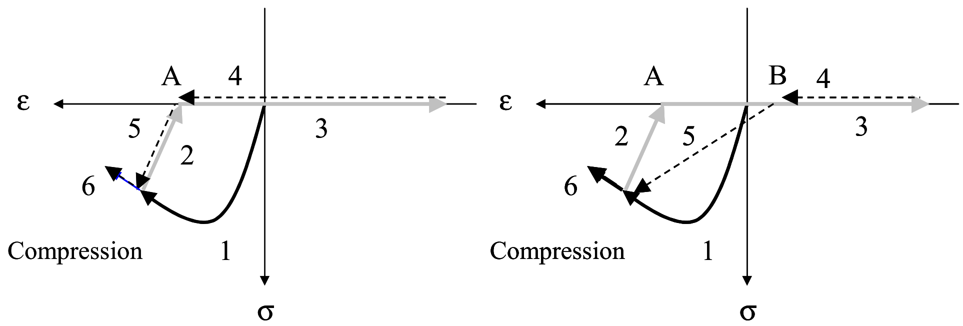

Fig. 4.21 Constitutive behavior of concrete in (a) *Concrete01* and (b) modified model during unloading and reloading.

The behavior represented by the modified model shown in Figure 4.21b has been observed in previous experimental research by Ma et al. (1976). It was observed that cracks in reinforced concrete members under cyclic loading can become partially filled with broken particles of hardened cement paste or aggregate, allowing load to be transferred across the crack before it has closed fully. Additionally, it is probable that when large cracks open and then close again, they will not align exactly as they did in the unfractured material, providing another mechanism for the transfer of stresses before the crack fully closes. Stanton and McNiven (1979) developed a constitutive model for concrete that incorporated this behavior. The model, shown in Figure 4.22, allowed for reloading into compression to occur at a strain value (ε_4) prior to the strain value of unloading (ε_2). The unloading and reloading behavior during the reloading path shown from ε_4 to ε_1 is defined using a series of rules described in Stanton and McNiven (1979).

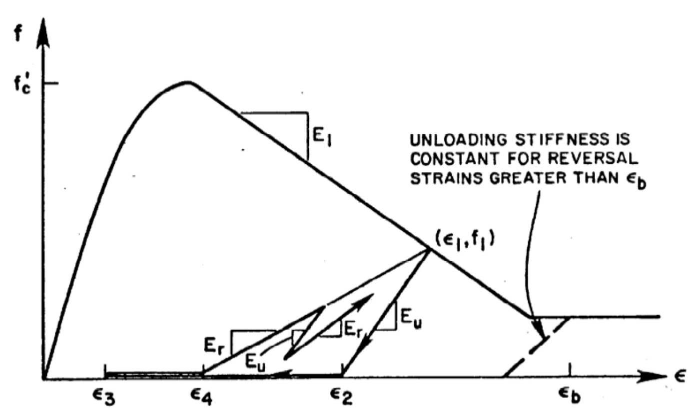

Fig. 4.22 Concrete constitutive model of Stanton and McNiven (1979), as taken from Stanton and McNiven (1979).

A constitutive model for concrete incorporating the effect of aggregate trapped in cracks based on the Stanton and McNiven model was developed for this research for the purpose of reducing the pinching observed in the fiber element models, thereby allowing for improved prediction of residual displacement. The model was based on the *Concrete01* model in OpenSees, in that the concrete is assumed to have zero tensile strength and the backbone compressive envelope was based on the Kent-Park-Scott model. Unloading was assumed to occur linearly according to the Karsan and Jirsa (1969) model.

It is the reloading behavior after undergoing large tensile strains that is novel to the modified model developed here. The reloading behavior was kept as simple as possible, as the only purpose of its introduction was to provide necessary modifications to the hysteretic shape of the fiber element model. In the modified model, the concrete reloads at a strain prior to the previous unloading strain. The model was set to be peak oriented as with the *Concrete01* model, i.e., the stress path during reloading will aim toward the peak point (maximum compressive strain reached) on the envelope curve.

Unlike the model proposed by Stanton and McNiven (1979), where the reloading strain value is a function of the initial unloading strain value and the peak strain reached during unloading (ε_2 and ε_3, respectively, in Fig. 4.22), the model developed here assumes the strain value to be a constant. This strain value at which reloading is assumed to occur, defined now as the reloading strain (ε_r), is assumed to be a positive (tensile) value and is an additional parameter that must be specified for the model. Because the reloading strain is set at a constant positive value, the model will function in exactly the same manner as the *Concrete01* model if this value is not exceeded, i.e., if the concrete does not go that far into tension. Only if the strain exceeds this value will the alternate reloading be "activated" and the model will become different from the *Concrete01* model. The physical reason for this is that cracks are assumed to have to reach a certain size before particles can become trapped in them.

In the Stanton and McNiven model, the unloading and reloading behavior once the primary reloading has occurred (along segment 5 shown in Fig. 4.21b), has a set of rules to define its behavior. In the model developed here, the unloading is assumed to occur along the same path for simplicity. In reality, the unloading would be expected to occur more quickly, i.e., along a steeper path, as shown in Fig. 4.22). However, the simplification modeled here is not expected to affect significantly the overall behavior of the column.

The modified concrete material model will be referred to herein as the *Concrete01WithSITC* model. The model is named after the *SITC* effect, a term coined by Stanton (2005), which essentially refers to the presence of broken aggregate in the cracks. SITC can in essence be paraphrased as *Substances* (aggregates, cement paste) *In The Cracks*. The method for implementation of the model is described as follows.

The evaluation of the stress occurs as a function of the strain value as well as an index value, which serves as a status parameter. The index value identifies the status of the material model (e.g., loading, unloading, etc.). The index values are defined as follows:

Index = 1	Concrete is on the compressive envelope.
Index = 2	Concrete is unloading/reloading on the branch of unloading from the compressive envelope.
Index = 3	Concrete is moving in the tensile direction at zero stress.
Index = 4	Concrete is in the tensile region but moving in the compression direction, and at zero stress.
Index = 5	Concrete is unloading/reloading on the branch of reloading from zero stress (due to the SITC effect).

In addition, there is one history variable, ε_{cmin}, to record the minimum (i.e., maximum compressive) strain reached during the entire loading history. The index values and their associated meanings are shown graphically, along with some of the key points defining the model's behavior, in Figure 4.23.

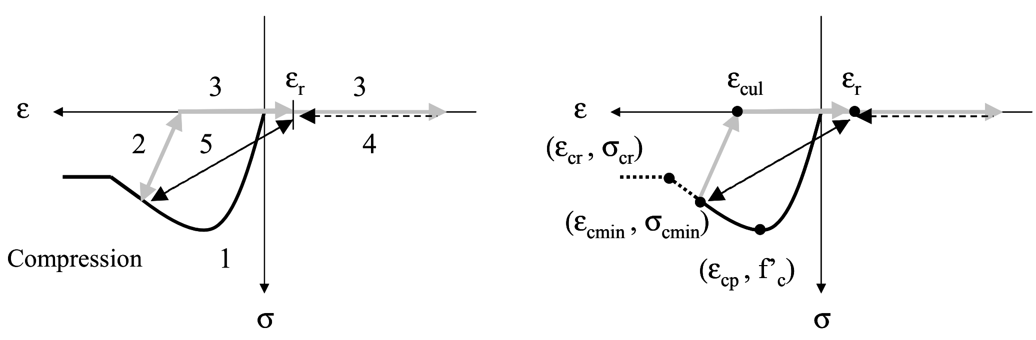

Fig. 4.23 Behavior of *Concrete01WithSITC* material model.

The stress, σ_c, when index = 1 (i.e., on the compressive envelope) as a function of the strain, ε_c, is evaluated as follows:

$$\sigma_c = f'_c\left(2\frac{\varepsilon_c}{\varepsilon_{cp}} - \left(\frac{\varepsilon_c}{\varepsilon_{cp}}\right)^2\right) \qquad \text{for } \varepsilon_c > \varepsilon_{cp} \tag{4.7}$$

$$\sigma_c = f'_c + \frac{f'_c - \sigma_{cr}}{\varepsilon_{cp} - \varepsilon_{cr}} \cdot \left(\varepsilon_c - \varepsilon_{cp}\right) \quad \text{for} \qquad \varepsilon_{cp} > \varepsilon_c > \varepsilon_{cr} \tag{4.8}$$

$$\sigma_c = \sigma_{cr} \qquad \text{for} \qquad \varepsilon_{cr} > \varepsilon_c \tag{4.9}$$

Again, the portion of the envelope curve up to peak follows (Eq. 4.7) the Kent-Scott-Park model. After peak, the model softens linearly to a certain point, after which it maintains a constant stress level. The stress when index = 2 (i.e., on the unloading/reloading path of the compressive envelope) is evaluated as follows:

$$\sigma_c = (\varepsilon_c - \varepsilon_{cul}) \cdot \frac{\sigma_{c\min}}{\varepsilon_{c\min} - \varepsilon_{cul}} \tag{4.10}$$

where σ_{cmin} is computed from the envelope curve based on ε_{cmin} (Eqs. 4.7–4.8). The stress when index = 3 and index = 4 is zero. The stress when index = 5 (i.e., on the unloading/reloading path of reloading from zero stress due to the SITC effect) can be computed as follows:

$$\sigma_c = (\varepsilon_c - \varepsilon_r) \cdot \frac{\sigma_{c\min}}{\varepsilon_{c\min} - \varepsilon_r} \tag{4.11}$$

The value of ε_{cul} is computed according to Karsan and Jirsa (1969) as follows:

$$\varepsilon_{cul} = \gamma(\varepsilon_c) \cdot \varepsilon_{cp} \tag{4.12}$$

where $\gamma(\varepsilon)$ is computed as:

$$\gamma(\varepsilon_c) = 0.707\left(\frac{\varepsilon_c}{\varepsilon_{cp}} - 2\right) + 0.834 \qquad \text{for } \varepsilon_c > 2\varepsilon_{cp} \tag{4.13}$$

$$\gamma(\varepsilon_c) = 0.145\left(\frac{\varepsilon_c}{\varepsilon_{cp}}\right)^2 + 0.13\left(\frac{\varepsilon_c}{\varepsilon_{cp}}\right) \qquad \text{for } \varepsilon_c < 2\varepsilon_{cp} \tag{4.14}$$

With the evaluation of the stress as a function of the strain and index value fully described, the rules defining the determination of the index value were then defined. As the model was developed for use in analysis using an incremental-iterative procedure, the stress at each trial step is computed with knowledge of the stress, strain, index value, and history parameter from the last converged step. In addition, the strain increment from the last converged state to the current trial step is also known. Given this information, the index for the trial step is computed based on a certain set of rules. The code is entered with a trial value of strain, $\varepsilon_{c,trial}$, for the trial step.

Once the index value is known, it is used in conjunction with the trial strain value to determine the stress value. In addition, the value of the tangent stiffness is also computed depending on the strain value and the index value. The *Concrete01WithSITC* model as described above was implemented in OpenSees as a uniaxial material model. The source code for the material model (written in C++) as developed for implementation in OpenSees is given in Appendix A.

4.3.5 Analysis of Fiber Element Model with Modified Concrete Constitutive Model

The original fiber element model for the RC column tested by Sakai et al. (2005) (Section 4.2.4.1) was reanalyzed using the *Concrete01WithSITC* model with various values of the reloading strain value, ε_r. The *Concrete01WithSITC* model was used for the core fibers only in the fiber section, while the cover fibers were modeled with the same unconfined *Concrete01* model as before. The results from a cyclic analysis are shown below in Figure 4.24, along with the behavior of the original model using the *Concrete01* model.

It can be seen that depending on the value of ε_r that is used, the level of pinching that occurs in the fiber element model can be reduced to varying degrees. For a value of $\varepsilon_r = 0.02$, the abrupt stiffness change at around zero displacement for the fiber element model is smoothed out to some degree. Although this change is subtle, its effect on the residual displacement response of the fiber element is in fact quite substantial. The fiber element model using the *Concrete01WithSITC* model was again analyzed under the suite of 20 ground motions as done previously (Section 4.3.2) and the peak and residual displacement responses were monitored. The results of these analyses are shown in Figure 4.25.

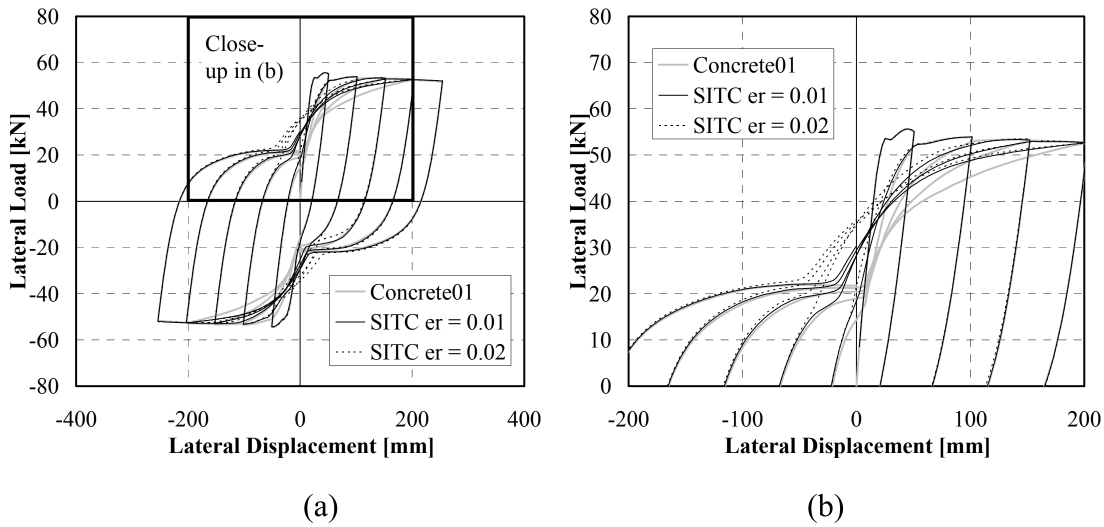

Fig. 4.24 (a) Load-displacement behavior of fiber element model and (b) close-up view of SITC effect on hysteresis behavior.

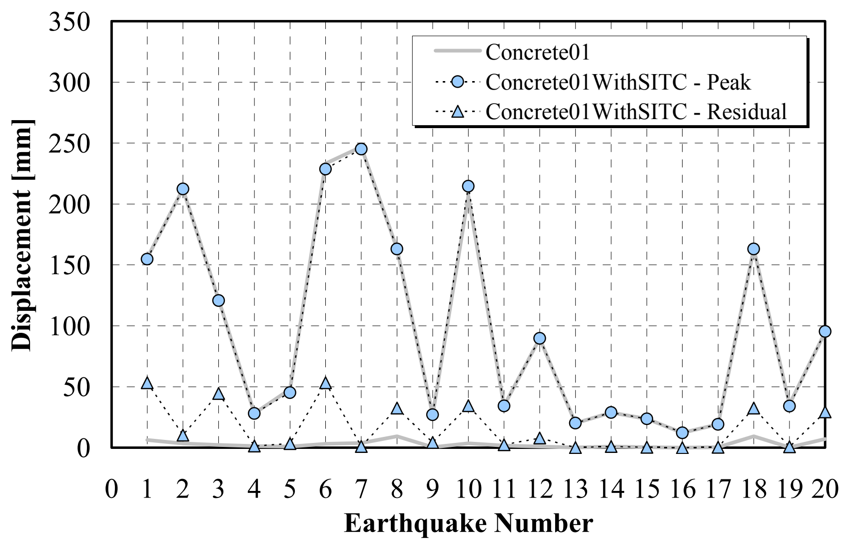

Fig. 4.25 Comparison of peak and residual displacement response for fiber element model with *Concrete01* and *Concrete01WithSITC* models subjected to near-fault ground motions.

The peak displacements predicted by the model with *Concrete01WithSITC* are all essentially the same as those predicted by the model with *Concrete01*. In this regard, the model performed well, as the values should not have changed. The results show that the use of the *Concrete01WithSITC* constitutive model can allow for some prediction of residual displacements. It can be seen that for several of the ground motion records, there are residual displacements where none were predicted using the *Concrete01* model. Furthermore, many of these residual displacement values are not negligible and arise even after what might not be considered as excessive peak displacements. For example, ground motion 20 causes a peak displacement of 95 mm (a drift ratio of approximately 3.9 percent), and results in a residual displacement of 29 mm (a drift of roughly 1.2 percent). This residual displacement value would likely be considered as leaving the structure at or near an unusable state.

It is important to note that the magnitude of the residual displacement does not necessarily correlate to the peak displacement reached. For example, ground motion 1 has a peak displacement 1.4 times greater than ground motion 2, but a residual displacement 5.2 times smaller. Some researchers have tried to develop predictions of residual displacement based in part on functions of peak displacements (e.g., Kawashima et al. 1998). While large peak displacements may often be accompanied by large residual displacement, it would appear that in general the magnitude of residual displacements may not necessarily be as well predicted by the magnitude of the peak displacements.

While the new constitutive model allows the fiber element model to predict residual displacements, the value of ε_r used to define the *Concrete01WithSITC* model is not based on any theory and so should be calibrated to experimental data. However, two problems arise regarding the calibration of this parameter. The first is the fact that the value is a parameter defining the constitutive behavior of the concrete, but is likely more dependent on a number of other factors relating to the member (such as geometry, reinforcing ratio, etc.) than the concrete itself. The second is the question of whether the value should be calibrated by adjusting the value to match the simulation to the hysteretic curves of quasi-static, cyclic testing data, or whether the value should be calibrated by adjusting the value so that the simulation matches the residual displacements of dynamic testing data. The results of Section 4.3.2 suggest that matching residual displacements of cyclic data may not be adequate for predicting residual displacements under dynamic loading. If calibration to dynamic testing data is performed, the additional problem of lack of large numbers of tests also arises.

The goal of introducing the *Concrete01WithSITC* model was to provide a simple means of predicting residual displacements. The parameter ε_r was selected based on a calibration with residual displacement results from dynamic testing of RC columns. The sensitivity of the ε_r parameter was evaluated in future analyses (see Chapter 5).

The fiber element model with the *Concrete01WithSITC* model was first compared against the experimental response of the RC column tested by Sakai et al. (2005). A value of $\varepsilon_r = 0.02$ was found to provide a close prediction of the residual displacement observed in the experiment. The response of the model with *Concrete01WithSITC* is shown against both the experimental response and the response with the *Concrete01* in Figure 4.26. The response of the model with *Concrete01WithSITC* predicts the same peak displacement as the model with *Concrete01*, but clearly provides an improved prediction of residual displacement, where none was predicted before.

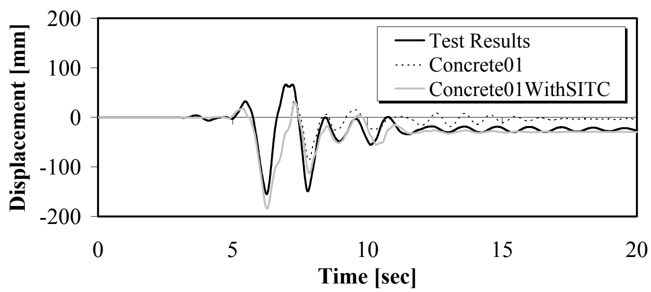

Fig. 4.26 Experimental and simulated displacement response histories using *Concrete01WithSITC* model in the fault-normal direction for RC column subjected to 70 percent of Los Gatos record.

The model with the same value of $\varepsilon_r = 0.02$ was then compared against another shaking table test of a circular RC column performed by Hachem et al (2003). In this test, an RC column specimen identical to that of the RC column tested by Sakai and Mahin was tested on a shaking table and subjected to the Olive View record from the 1994 Northridge earthquake. Since the column specimen was identical to the column tested by Sakai et al. (2005), the same fiber element model was used, only with a different input acceleration history. The record was recorded at a distance of 6.4 km from the fault rupture, and the Northridge earthquake had a magnitude of 6.7. The record was modified by scaling the accelerations by a factor of 1.09 and reducing the time by a factor of 2.12. The reasons for these modifications are discussed in Hachem et al (2003).

A comparison of the displacement response history for the experimental results and fiber element models using the *Concrete01* and *Concrete01WithSITC* models is shown in Figure 4.27. Again, the model with *Concrete01WithSITC* predicts the same peak displacement as the model with *Concrete01*, but provides a better prediction of the residual displacement. The residual displacement is predicted well using the value of ε_r = 0.02. Due to the lack of other available experimental data on dynamic tests of conventional RC columns, the value of ε_r = 0.02 was taken to be the value that will be used in further modeling.

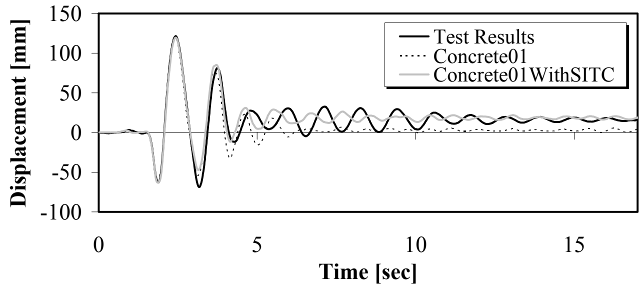

Fig. 4.27 Experimental and simulated displacement response histories using *Concrete01WithSITC* constitutive model in the fault-normal direction for RC column subjected to Olive View record.

4.4 PREDICTION OF RESIDUAL DISPLACEMENTS IN UBPT COLUMNS

In terms of predicting the residual displacement response of the UBPT column, the simulation showed essentially no residual displacement following the design level motion. The natural question that follows is whether the zero residual displacement that is predicted is caused by some flaw in the analytical model, as was the case with the RC column, or whether the model is accurately simulating the behavior of the true column and the residual displacements would in reality be zero anyway. The answer is likely the latter. The claim is supported by the experimental response, as essentially zero residual displacements were found in the UBPT column. As the model of the UBPT system predicted zero residual displacements with the unmodified concrete constitutive model, the next question that arises is whether the *Concrete01WithSITC* model is required for modeling the UBPT column. This can be answered by examining the hysteretic behavior of the model.

First, the general cyclic behavior of UBPT concrete systems is considered. The experimental cyclic response of a UBPT cantilever concrete column (Zatar and Mutsuyoshi 2000) and a UBPT concrete beam-column connection (El-Sheikh et al. 2000) are shown in Figure 4.28a and Figure 4.28b, respectively. It is clear from the figures that the cyclic response of UBPT specimens is origin-oriented, as intended by their design. The behavior observed in the

RC experimental response is not observed here; in that there is indeed a pinched hysteretic response observed in the experimental response of the UBPT members.

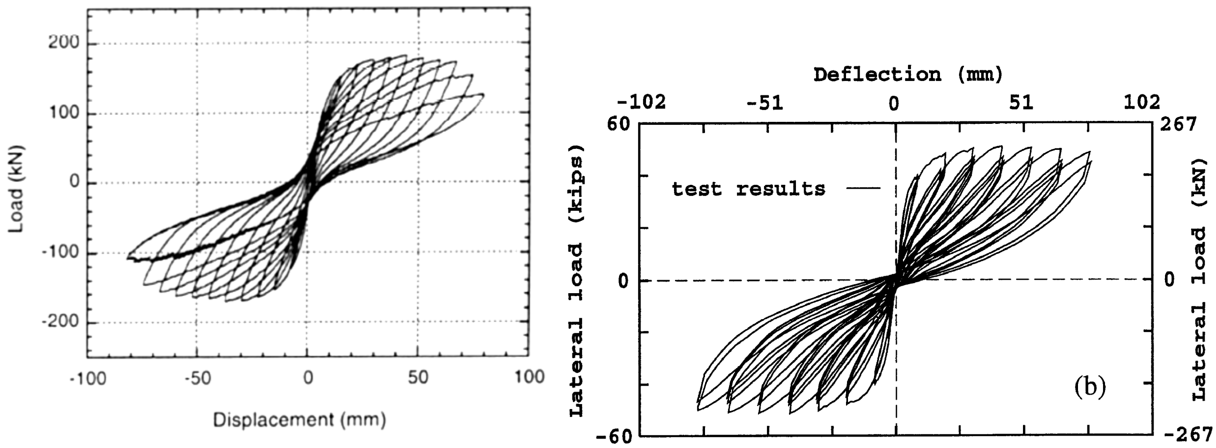

(a) (b)

Fig. 4.28 Cyclic experimental response of a UBPT concrete (a) cantilever column (Zatar and Mutsuyoshi 2000) and (b) beam-column connection (El-Sheikh et al. 2000).

As cyclic tests were not performed by Sakai et al. (2005) on their UBPT column specimen, the experimental cyclic response is unknown. However, it is fair to assume that the general behavior is similar to that shown in Figure 4.28. The cyclic response of the fiber element model of the UBPT column of Sakai et al. (2005) with the unmodified concrete constitutive model is shown below in Figure 4.29a. For comparison, the same column but with the *Concrete01WithSITC* model is shown in Figure 4.29b.

Clearly, the response shown in Figure 4.29a is the behavior that would be expected from the UBPT column. The origin-oriented response looks typical of experimental cyclic responses of UBPT concrete elements. There is no artificial pinching in the simulated response that is not present in the experimental response, meaning that the use of a modified constitutive model meant to introduce the pinching (i.e., the *Concrete01WithSITC* model) would be unnecessary in this case. When the *Concrete01WithSITC* model is used, as shown in Figure 4.29b, the simulated response changes drastically and loses the expected origin-oriented response. The reduction in pinching introduced by the *Concrete01WithSITC* in this case is not desired, and therefore the model should not be used with the UBPT column.

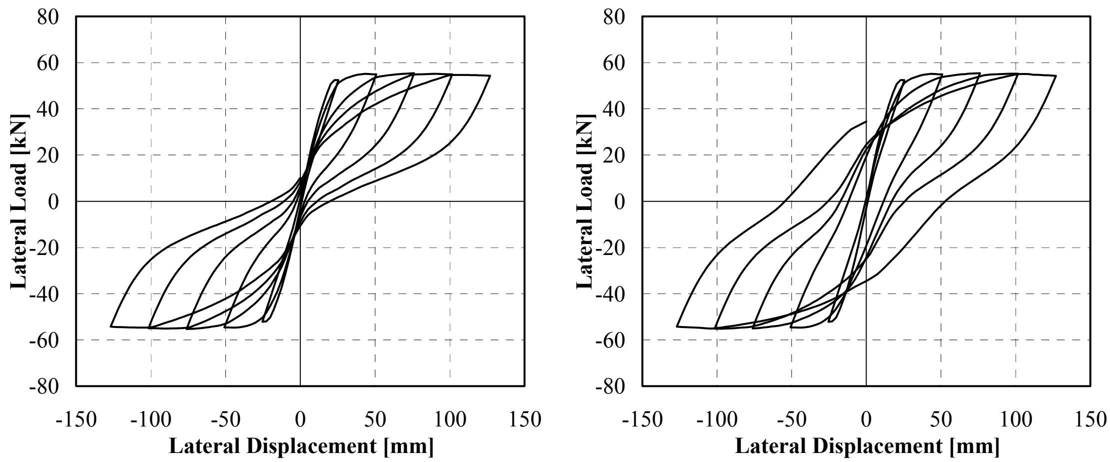

(a) (b)

Fig. 4.29 Comparison of UBPT column fiber element model cyclic response using (a) *Concrete01* and (b) *Concrete01WithSITC* constitutive models.

The final question that arises is the following. Although the use of a modified constitutive model may not be *necessary* in the case of the UBPT column, surely its use should not cause incorrect responses to be simulated if the constitutive model is incorporating behavior that is actually occurring in the experiment. The cause of this is not as well understood. One possible explanation is that the added axial load due to the post-tensioning causes the aggregate trapped in the cracks to be crushed rather than allowing them to bear and transfer load, as the post-tensioning more than doubles the axial load on the column due to the dead load alone. If this were true, then the use of the *Concrete01WithSITC* would not be applicable to post-tensioned members with high axial loads.

4.5 SUMMARY

The ability of fiber element models to simulate the dynamic behavior of RC and UBPT columns was assessed by comparison to experimental data. The fiber element models were able to predict the peak displacements of the RC column well, as expected, but were also able to predict the peak displacements of the UBPT column well. The residual displacements for the RC column however, were not well predicted by the fiber element model. This was identified as a significant weakness in the fiber element model. The residual displacements for the UBPT column were predicted well, and no modifications to the model for the UBPT system were deemed necessary.

To determine the cause of the inability of the fiber element model to predict residual displacements, a small study was performed using SDOF models, and the cause was found to be the pinched shape of the hysteretic response of the fiber element model. The pinching in the fiber element model hysteresis was found to be caused by the constitutive model for concrete. A new constitutive model was proposed for concrete and was implemented in OpenSees. Analysis using the new concrete constitutive model led to improvements in residual displacement prediction. Comparisons with experimental data led to an estimate of a parameter required to define the constitutive model. The value was assumed to provide a starting point for analysis, with the understanding that a high variability should be expected and incorporated into any future analysis using the model.

5 PBEE Assessment of Bridge with UBPT Columns

5.1 INTRODUCTION

In Chapter 4, simulation models were identified that were able to predict the structural response parameters necessary to make a quantitative, performance-based comparison between a conventional RC concrete bridge and a bridge using UBPT columns for self-centering. In this chapter, the quantitative comparison between the two systems is performed using PEER's PBEE assessment methodology. The comparison is performed using a realistic bridge structure designed by Caltrans engineers. Presented in this chapter are a description of the bridge structure studied, details of the procedure for performing the PBEE assessment, and the results from the analyses. A baseline analysis is first performed using a given set of assumptions in all four steps of the PEER assessment, and the sensitivity to these assumptions is evaluated with further analyses. Finally a summary of the results from the analyses are presented.

5.2 BASELINE BRIDGE FOR COMPARATIVE ANALYSIS

The design of the bridge used in this study was performed by engineers at the California Department of Transportation (Caltrans) according to the Caltrans Bridge Design Specification and Seismic Design Criteria (SDC) (Caltrans 2001). The bridge was one of a set of bridges designed to represent the majority of highway overpass bridges in California, and full details of the design and assumptions are given in Ketchum et al. (2004). The design corresponded to the "Ordinary Bridge" standard as defined in the Caltrans SDC (Caltrans 2001). The geometry and configuration of the bridge are shown in Figure 5.1. To minimize unnecessary complications, factors such as skew, variable columns heights, and difficult foundation considerations were not considered. While a specific site was not considered during the actual design, the bridge was assumed to be located within 10 km of the Hayward fault, and was designed assuming a stiff soil site (Caltrans SDC Soil Class D). The superstructure, shown in Figure 5.2, was designed as a cast-in-place, post-tensioned concrete box girder with a width of 11.9 m to carry two lanes of traffic.

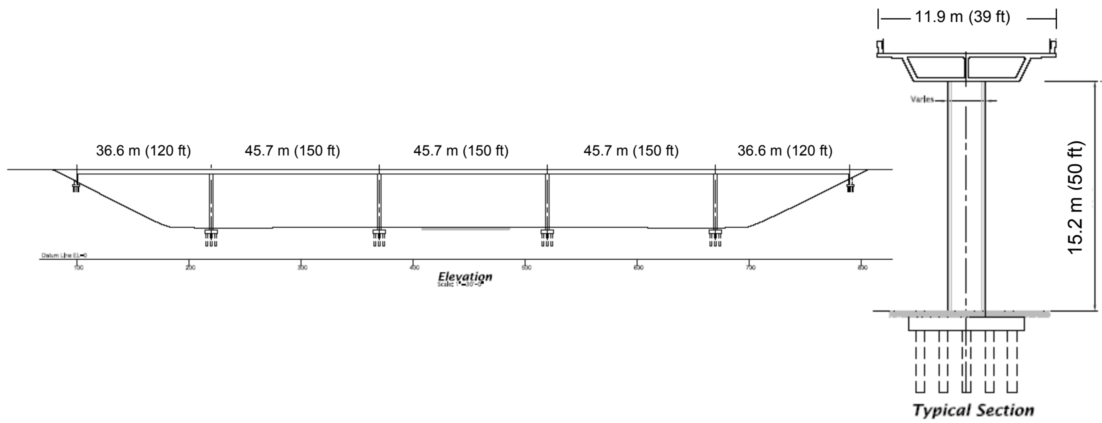

Fig. 5.1 Bridge configuration and geometry (adapted from Ketchum et al. 2004).

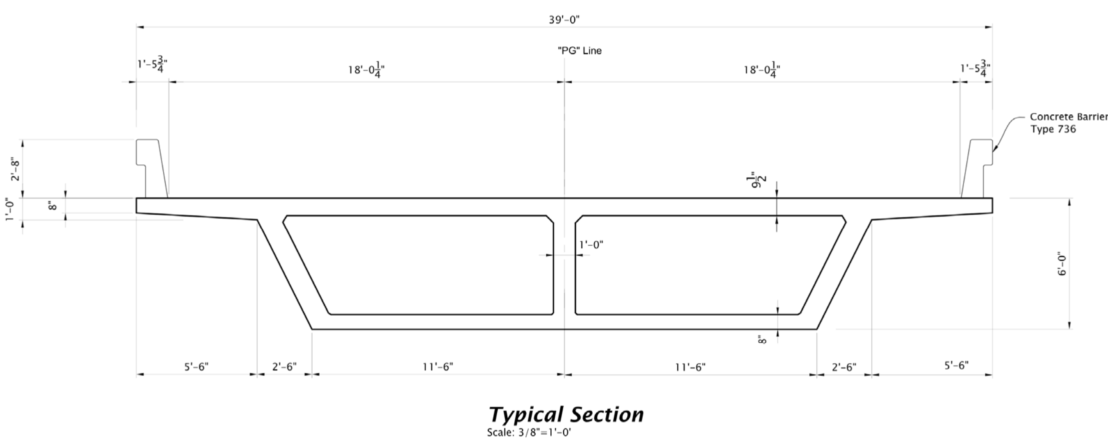

Fig. 5.2 Bridge superstructure – concrete box girder (from Ketchum et al. 2004).

The bridge was designed with five spans, the inner three spans having a length of 45.7 m (150 ft) and the outer two spans having a length of 36.6 m (120 ft). The bridge had four single-column bents, where each column had a height of 15.2 m (50 ft) and a diameter of 1.8 m (72 in.). The column concrete was assumed to have an unconfined compressive strength of 27.6 MPa (4 ksi). The longitudinal reinforcing consisted of 52 #11 bars in bundles of two bars, which corresponded to a reinforcing ratio of 1.9 percent. The transverse reinforcing consisted of #7 spirals with a center-to-center spacing of 8.26 cm (3.25 in.), which corresponded to a volumetric reinforcing ratio of 1.1 percent. A number of different foundation types were considered in the design; however, the actual foundation type is not important here because soil-structure-foundation interaction is disregarded in this study. In this way, the effect of the columns themselves can be isolated and therefore more easily studied.

5.3 HAZARD ANALYSIS

The first portion of PEER's PBEE methodology involves determining the appropriate seismic hazard of the site in question. The hazard is specific to the site of the structure; therefore a specific site was chosen for the baseline bridge. The chosen site was in Oakland, California, and was also the site of another test-bed structure study performed by PEER on the I-880 viaduct. The site is located within 10 km of the Hayward fault. The site has a latitude and longitude of 37.80 N x 122.30 W.

5.3.1 Probabilistic Seismic Hazard Analysis

To compute the hazard at a given site, a probabilistic seismic hazard analysis (PSHA) was performed. The PSHA yields the mean annual frequency of exceedance for various values of a given earthquake intensity measure, most commonly the spectral acceleration at the first-mode period, $S_a(T_1)$ (or simply S_a). The procedure for performing a PSHA can be found in, for example, Kramer (1995).

Hazard data are often obtained from the U.S. Geological Survey (USGS). The USGS (http://earthquake.usgs.gov) provides hazard data for S_a given the latitude and longitude of a site; however their hazard analysis is performed by incorporating a number of different attenuation functions and assumptions and uses a weighted average for producing a design curve. Several software packages also exist for performing the PSHA that allow the user to select a number of parameters and models, including the attenuation relationship. In this research, the PSHA and resulting hazard curves were obtained from Tothong (2006). The Abrahamson and Silva (1997) attenuation model was used in the baseline analysis, and sensitivity studies in the PSHA considered variation only in the attenuation model (as described in Section 5.7.2).

The most common intensity measure (IM) used in a hazard analysis is S_a, and was therefore assumed for the baseline analysis. To determine the sensitivity in the choice of IM, a newly developed scalar intensity measure by Tothong and Cornell (2006) was also used in addition to S_a. To compare against the baseline analysis, the attenuation model was kept the same (i.e., using the Abrahamson and Silva (1997) model), and only the alternate IM was used. This new IM was the inelastic spectral displacement, S_{di}, which as the name implies incorporates the use of a nonlinear single-degree-of-freedom (SDOF) oscillator for computing response spectral values. Full details of this intensity measure and its attenuation relationship can be found in Tothong and Cornell (2006a), but a brief description will be presented here.

The most commonly used IM, S_a, is obtained from a ground motion using an elastic SDOF oscillator essentially as a filter. Because the SDOF oscillator is elastic, much information (e.g., frequency content) contained in the ground motion is lost in S_a. The use of a nonlinear SDOF was proposed by Tothong and Cornell (2006) to capture more information from ground motions, primarily with respect to near-fault, pulse-like ground motions. The nonlinear SDOF in the case of S_{di} is simply a bilinear system (with a 5 percent hardening stiffness ratio) with a specified yield displacement and period. The use of S_{di} was proposed to provide improvements to conventional scalar IMs (e.g., by reducing dispersion in structural responses when scaling motions, by making detailed record selection unnecessary) by allowing for nonlinear behavior in the SDOF response.

Since the two intensity measures, S_a and S_{di}, are both structure dependent, they required values specific to the structure in question. Based on an eigenvalue analysis of a model of the structure, a fundamental period of 1 sec was assumed for S_a (the modeling is presented in Section 5.4). Based on a monotonic pushover analysis, the yield displacement was taken as 14 cm (5.5 in.). The hazard curves for S_a (using the two different attenuation models) and S_{di} for the site are shown in Figure 5-3. For convenience, S_a is plotted as elastic spectral displacement, S_{de}, where the two are related by the following equation: $S_a \approx (2\pi / T)^2 \cdot S_{de}$. Note the large difference in the S_{de} (S_a) hazard curves that is possible from simply changing the attenuation relationship.

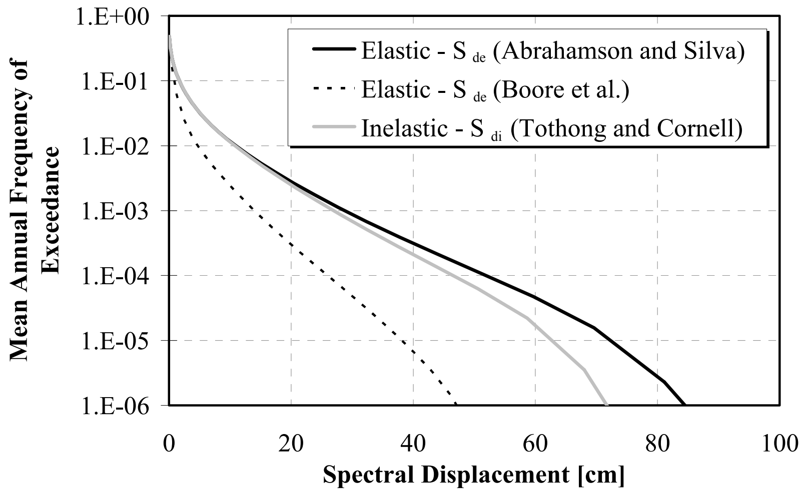

Fig. 5.3 Hazard curves for elastic and inelastic spectral displacement for Oakland site using Abrahamson and Silva (1997) and Boore et al. (1997) attenuation models.

5.3.2 Ground Motions

To perform dynamic analysis on a model of a structure, a set of ground motions is required. For this research, a set of ground motions (Table 5.1) was assembled from a record set prepared by Somerville and Collins (2002) with additional records added to increase the set size from Tothong (2006). The set consisted entirely of near-fault ground motions because the bridge site in question and the vast majority of bridges in California in general are within 10 km of a major fault. While the fact that a structure is located near a fault does not mean that it will be subjected only to pulse-like ground motions, the use of a bin of only near-fault motions also does not mean that the structure will suffer the effect of the pulse for each motion, as the pulse period will vary with the motion.

The set of motions from Somerville and Collins (2002) was developed for a similar study on California highway bridges. The set consisted of 20 near-fault ground motions with three components each, which were fault normal, fault parallel, and vertical. These 20 ground motions were the motions used in the SDOF analysis of Chapter 4. The set consisted of 10 motions which were to be scaled to the 50% in 50 year hazard level, and 10 motions which were to be scaled to the 10% and 2% in 50 year hazard levels. For the incremental dynamic analysis (IDA) performed in this study, scaling of the ground motions was to relatively high levels of intensity. Therefore, only the 10 motions of the 10%/2% in 50 year bin were used for the IDA in this study.

Table 5.1 Ground motion set for PBEE analysis.

Earthquake	Number	Mw	Station	Distance (km)
From Somerville and Collins (2002) - 2%/10% in 50 yrs				
Erzincan, Turkey	1	6.7	Erzincan	1.8
Kobe, Japan	2	6.9	Kobe JMA	0.5
Loma Prieta	3	7	Corralitos	3.4
Loma Prieta	4	7	Gavilan	9.5
Loma Prieta	5	7	Gilroy Historic	12.7
Loma Prieta	6	7	Lexington Dam Abutment	6.3
Loma Prieta	7	7	Los Gatos Presentation Center	3.5
Loma Prieta	8	7	Saratoga Aloha Ave.	8.3
Tottori, Japan	9	6.6	Kofu	10.0
Tottori, Japan	10	6.6	Hino	1.0
Additional Motions				
Superstition Hills	11	6.5	El Centro Imp. Co. Cent	18.2
Superstition Hills	12	6.5	Parachute Test Site	0.9
Loma Prieta	13	7	Gilroy Array #2	11
Loma Prieta	14	7	Gilroy Array #4	14.3
Northridge	15	6.7	Canoga Park-Topanga Can	14.7
Northridge	16	6.7	Newhall-W. Pico Canyon Rd.	5.5
Northridge	17	6.7	Sylmar-Olive View Med	5.3

In addition to the 10 ground motions from Somerville and Collins (2002), another seven ground motions were added to the set, to bring the total number of ground motions to 17. These seven motions were selected based on their pulse periods (~1.5–2.0 sec), which were larger than that of the fundamental period of the structure (roughly 1 sec). The records were selected with data obtained from Tothong (2006). These records were selected to provide more balance to the ground motion set, as the original 10 motions from Somerville and Collins had pulse periods lower than that of the fundamental period of the baseline structure. These additional seven ground motions, also shown in Table 5.1, were included to incorporate more damaging records.

5.4 STRUCTURAL ANALYSIS

The second portion of PEER's PBEE methodology involves determining the engineering response of a structure given a ground motion input. This requires building an analytical model of the structure, and then analyzing the structure using, for example, IDA to determine the structural response. In this section, the simulation model and analysis procedure are presented, along with the results of the analyses.

5.4.1 Model of Baseline Bridge with RC Columns

The baseline bridge was modeled using the OpenSees platform. A schematic representation of the bridge model is shown below in Figure 5.4. The model was three-dimensional, allowing two components of the ground motion to be used in the analysis. Although the third component (the vertical direction) was available, it was not used in the analysis. The bridge was modeled using fiber elements, as their ability to capture the important dynamic behavior of both RC and UBPT systems was validated in Chapter 4. The skeleton of the bridge model (superstructure elements and abutments) was created for related studies on performance-based assessment of various bridge systems by researchers at the University of California, Berkeley (Mackie 2005a), and the remainder of the model was created by the author.

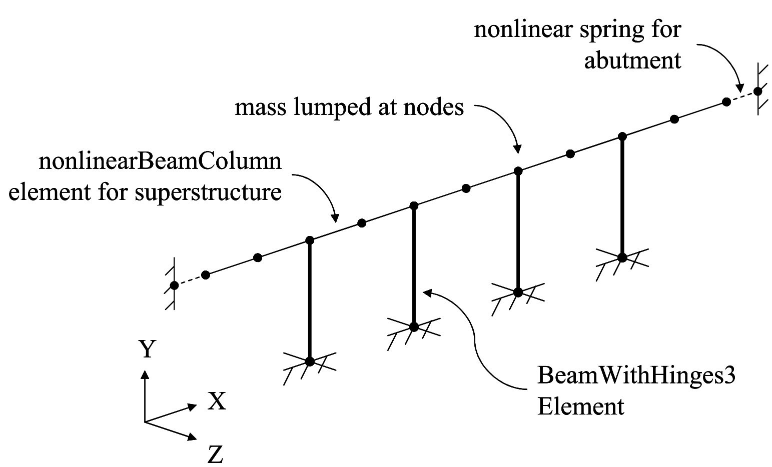

Fig. 5.4 Schematic representation of bridge model.

The superstructure was modeled with flexibility-based fiber beam-column elements with five integration points (*nonlinearBeamColumn* element). A fiber section was defined for the superstructure elements based on the geometry and reinforcing layout of the deck (shown in Figure 5.2). Each span was modeled with two elements. The concrete was assumed to have an unconfined compressive strength of 34.5 MPa (5 ksi). No significant nonlinear behavior was expected to occur in the superstructure, as intended by the design guidelines of the Caltrans SDC (where the members are detailed so that nonlinear behavior will concentrate in the columns, along the same lines, although reversed, as the strong column–weak beam guideline typical for building design). In the longitudinal direction, the superstructure was expected to act as a rigid diaphragm between the columns. Finally, mass due to the weight of the superstructure and the column was lumped at the element end nodes.

The abutments were modeled using a number of spring elements combined in parallel and series with nonlinear behavior that incorporated the behavior of the bearing pads, backfill, and backwall. Note that the overall range of movement in the longitudinal direction was restricted by the backwall, and because of the stiffness provided by the abutments, the motion in the longitudinal direction was not expected to be as significant as the motion in the transverse direction.

As in the validation study of Chapter 4, each column was modeled with a single, concentrated plasticity fiber beam-column element (*BeamWithHinges3* element), as shown in Figure 5.5. The plastic hinge length and cracked stiffness values for the elastic region of the beam were computed using Caltrans SDC (2003) guidelines, as described in Chapter 4. The columns are assumed fixed at the base.

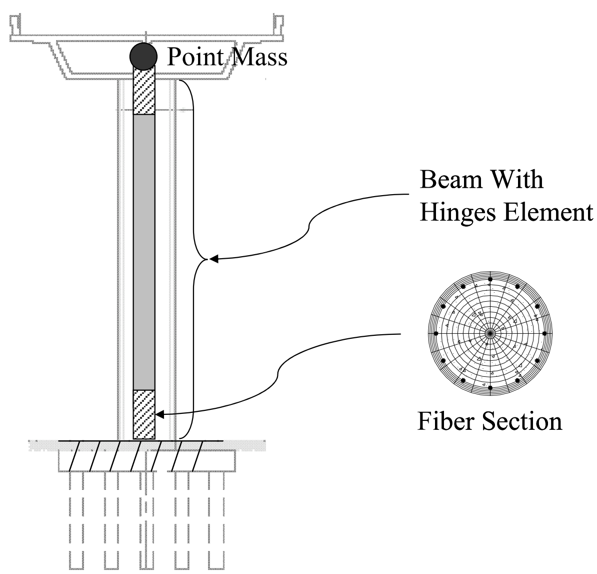

Fig. 5.5 Schematic representation of column model.

The column concrete was assumed to have an unconfined compressive strength of 27.6 MPa (4 ksi). For the core concrete, the peak compressive stress and strain were increased due to the confinement effect based on Mander et al. (1983), as described in Chapter 4. The

Concrete01 model in OpenSees was used for the cover concrete, and the *Concrete01WithSITC* model developed in Chapter 4 was used for the core concrete for improved residual displacement prediction. As in Chapter 4, the fiber section was discretized into core and cover fibers, where the unconfined values were used for the cover fibers and the confined values were used for the core fibers.

The bonded mild steel reinforcing was assumed to have a yield strength of 469 MPa (68 ksi). This value is given in the Caltrans SDC (2003) as the *Expected Yield Strength* of Grade 60 reinforcing steel, and is intended to provide a more realistic value of the actual strength of the steel rather than the minimum required value. The stress-strain relationship for the bonded mild steel reinforcing was assumed to follow the Giuffre-Menegotto-Pinto model (Taucer et al. 1991), which incorporates the Bauschinger effect for cyclic loading. The *Steel02* model in OpenSees was used for the reinforcing steel. Strain hardening at 2 percent of the initial elastic modulus was assumed for the model.

As discussed in Chapter 4, the intended purpose of the bridge model is to capture the behavior of the bridge undergoing moderate levels of nonlinearity and its residual displacement response, but not such excessively high responses at which collapse may occur. An eigenvalue analysis of the bridge model yielded a first-mode period of approximately 1.1 sec, and the mode shape of this period corresponded to motion in the transverse direction of the bridge, as expected.

5.4.2 Model of Baseline Bridge with UBPT Columns

To compare the UBPT system to the conventional RC system, the same bridge model was to be used, except that the RC columns would be replaced with self-centering UBPT columns. A goal of the UBPT design is that the column size, stiffness, and strength remain similar to standard RC columns, such that the reductions in residual displacements and subsequent improvement to post-earthquake functionality could be directly compared between the two systems. Sakai and Mahin (2003, 2004b) demonstrated that by adding a concentric post-tensioning tendon to a circular concrete column while also reducing the bonded longitudinal reinforcing, a column with similar yield strength and initial stiffness as the original column could be obtained that displayed self-centering behavior. Sakai and Mahin (2003, 2004b) found in their studies that if roughly half of the area of bonded longitudinal reinforcing was removed and an equivalent area of post-tensioned reinforcement was added, the self-centering behavior could be achieved while keeping the stiffness and strength similar to that of the original column.

Using Sakai and Mahin's recommendation as a starting point, a series of cyclic analyses were performed by altering the amounts of bonded and unbonded reinforcing to determine the values that would allow for self-centering while keeping the strength and stiffness similar to that of the original column. The resulting design used a PT tendon with an area of 200 cm^2 (31 $in.^2$) and a prestress of 689 MPa (100 ksi). The UBPT column was modeled in the same fashion as described in Chapter 4, using a co-rotational truss element to model the PT tendon and an elastic material model (*ElasticPP*) with an initial strain value to apply the prestress. The initial prestress of 690 MPa (100 ksi) was intentionally selected to be low to prevent any yielding of the PT tendon under seismic loading.

In addition to reducing bonded reinforcing when added the post-tensioning, Sakai and Mahin (2003, 2004b) also recommended increasing the spiral reinforcing to increase the strength and ductility of the concrete to account for the increasing axial load due to the post-tensioning. To accommodate the additional axial load from the post-tensioning, the strength of the concrete was increased from 27.6 MPa (4 ksi) to 56.2 MPa (8 ksi), and the amount of confinement was increased to provide additional ductility. In the final design, the longitudinal reinforcing ratio was reduced from 1.9 percent (52 bundled #11 bars) in the traditional RC column to 0.9 percent (24 equally spaced #11 bars) in the UBPT column and the transverse volumetric reinforcing ratio was increased from 1.1% (#7 spirals at a spacing of 8.26 cm) in the RC column to 1.4% (#8 spirals at a spacing of 8.26 cm) in the self-centering column. The results from a cyclic analysis using these values for each column is shown in Figure 5.6.

When constructing the entire bridge model, the building of the individual components of the model and application of the prestress in the columns had to performed in a specific order so as to prevent unrealistic stresses from occurring in the model. If the entire model were built (columns, superstructure, etc.) first, and then the prestress were applied, the columns would immediately shorten elastically. This elastic shortening would impose vertical deformations on the superstructure, leading to initial flexural stresses that were not desired. To prevent this from occurring, the following procedure was followed. The UBPT columns and associated nodes were first created, and an analysis step with a load pattern consisting of a load with zero magnitude was performed to generate the prestress force and allow the columns to shorten elastically. Following this "zero-force" step, the remainder of the nodes and elements of the bridge model were created. In this way, no initial stresses were formed in the superstructure elements.

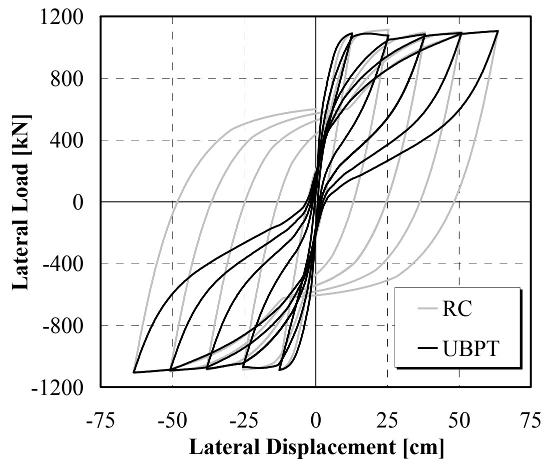

Fig. 5.6 Cyclic analysis of RC and UBPT columns for baseline bridge.

5.4.3 Analysis Procedure

Geometric nonlinearity was included in all analyses. The dynamic analyses were performed using the Newmark Method with average acceleration. Damping was applied using Rayleigh damping. The damping ratio used in the analysis was considered to be a random variable, and is discussed in the Section 5.4.4. The solution algorithm was a Newton-Raphson scheme with an energy norm as the convergence criterion. However, because the analysis was often unable to converge to a solution with the original Newton-Raphson scheme, a solution procedure script was developed within the analysis file that tried a number of different solution algorithms, time steps, and convergence criterion until a solution could be achieved if the Newton-Raphson method failed. An additional 10 sec of free vibration (analysis with input acceleration of zero) was performed following the end of each ground motion to allow the bridge to come to rest such that residual displacements could be recorded.

The dynamic analyses were performed using two components of motion for each ground motion record. Again, these two components were the fault-normal and fault-parallel components. In the analyses, the fault-normal component (the more severe of the two components) was applied in the transverse direction of the bridge, as motion in the longitudinal direction was expected to be more limited due to the stiffness of the abutments.

To perform the IDA for the two cases of S_a and S_{di} (as discussed in Section 5.4.7), the ground motions had to be scaled to various intensity levels. Determining the scale factors in the case of S_a is a straightforward procedure, as the scale factors can be found easily, since the SDOF oscillator is linear. In the case of S_{di}, the scaling is not as straightforward. To scale to a certain level of displacement with a nonlinear oscillator requires an iterative procedure to find the scale factor that will achieve the desired displacement level. A number of different scale factors must be tried before the desired value can be identified. However, this procedure can be automated in Matlab, for example. In this study, the motions were scaled based on the fault-normal component of motion, and the same scale factor was applied to the fault-parallel component of motion. This procedure was recommended in Somerville and Collins (2002).

The IDA for S_a was performed at seven different intensity levels. Three of the intensity levels corresponded to the hazard levels of 50%, 10%, and 2% in 50 years, based on the baseline hazard curve (i.e., using the Abrahamson and Silva (1997) model) presented in Section 5.3.1. Three other intensity levels were chosen in between these values to provide additional information at these intermediate intensity levels. A final intensity level greater than the 2% in 50 year level was also chosen.

The intensity levels chosen for the IDA are shown in Table 5.2. For convenience, the S_{de} values corresponding to the S_a values are also shown. The intensity levels for S_{di} were chosen to correspond to the same mean annual frequency of exceedance values as the intensity levels chosen for S_a. The intensity levels for S_{di} are also shown in Table 5.2.

Table 5.2 Intensity levels chosen for scaling of ground motions in IDA.

Level	Mean Annual Frequency of Exceedance	$S_a(T_1)$ [g]	S_{de} [cm]	S_{di} [cm]
1	0.0139 □ (50% in 50)	0.36	8.9	9.0
2	0.0038	0.70	17.4	17.2
3	0.0021□ (10% in 50)	0.91	22.6	21.4
4	0.0012	1.10	27.3	25.7
5	0.0007	1.30	32.3	30.1
6	0.0004□ (2% in 50)	1.52	37.8	35.1
7	0.00025	1.70	42.3	38.8

5.4.4 Uncertainty in Structural Modeling

In addition to the uncertainty that is present in the ground motions (record-to-record variability), there is also uncertainty in the structural modeling itself. This uncertainty comes from many areas, including the uncertainty in the parameters used to define the material models due to variability in material properties, and the uncertainty due to the assumptions made in the modeling (e.g., damping, element type). To include this modeling uncertainty, a number of modeling parameters are assumed to be random variables (RVs) in the analysis, and their uncertainty is incorporated using the first-order second-moment (FOSM) method (Baker and Cornell 2003a, 2003b). The FOSM method allows additional known information about the first two moments of a distribution of a random variable (e.g., mean and standard deviation of yield strength of reinforcing steel) to be easily added to the record-to-record variability to provide the overall variance of an engineering demand parameter (EDP).

In the FOSM method, an EDP is assumed to be a function of a number of parameters that are assumed to be random (e.g., steel yield strength, concrete compressive strength). The EDP is computed from the random parameters, typically through the use of nonlinear dynamic analysis. There is therefore a distribution of the EDP, with mean, μ_{EDP}, and standard deviation, σ_{EDP}, that is being estimated. The mean value of the EDP can be estimated by setting all of the n random variables, x_i , i = 1,2,…,n, to their mean values, as follows:

$$\mu_{EDP} \cong g(\widetilde{X}_M); \qquad \widetilde{X} \cong \{x_1, x_2, \ldots, x_n\}^T \tag{5.1}$$

where $\widetilde{X}_M$ is the mean vector of random variables (and in general $\widetilde{X}$ is the vector of random variables), and g represents some function or method of computing the EDP based on the random parameters (in this case, it is nonlinear dynamic analysis).

The FOSM method then uses a mean-centered first-order (linear) approximation of the distribution of the EDP (the g function) to approximate the variance of the EDP. This is accomplished through a mean-centered Taylor series expansion, as follows:

$$Var[EDP] \cong \sum_{i=1}^{n}\sum_{j=1}^{n}\left[\frac{\partial g(\widetilde{X})}{\partial x_i}\frac{\partial g(\widetilde{X})}{\partial x_j}\right]_{\widetilde{X}=\widetilde{X}_M} \rho_{ij}\sigma_i\sigma_j \tag{5.2}$$

where *Var[EDP]* is the variance of the EDP, $\partial g(\widetilde{X})/\partial x_i$ is the gradient of the g function with respect to random variable x_i, ρ_{ij} is the correlation between random variables i and j, and σ_i the standard deviation of random variable i. The correlations and standard deviations are values that are obtained either from statistical data or from engineering judgment. The gradient can not be computed analytically, but it can be approximated using finite differences. The gradient can be approximated as follows:

$$\left[\frac{\partial g(\widetilde{X})}{\partial x_i}\right]_{\widetilde{X}=\widetilde{X}_M} \cong \frac{g\left(\widetilde{X}_{M\pm\sigma_{x_i}}\right)-g\left(\widetilde{X}_M\right)}{\sigma_{x_i}} \tag{5.3}$$

$$g\left(\widetilde{X}_{M\pm\sigma_{x_i}}\right)\cong\left\{\mu_{x_1},\mu_{x_2},\ldots,\mu_{x_i},\cdots,\mu_{x_n}\right\}^T \pm\{0,0,\ldots,\sigma_i,\cdots,0\}^T$$

where $g\left(\widetilde{X}_{M\pm\sigma_{x_i}}\right)$ is the vector of random variables with all values equal to their means except for random variable x_i, to which σ_i is either added or subtracted. Either of these two values (i.e., computed using plus or minus σ_{xi}) can be used to approximate the gradient, or alternatively an average of the two can be used. In this study, an average of the two values is taken. Using this finite difference method to approximate the gradient means that to compute each gradient value for each variable, the analyses are re-run by adding or subtracting one standard deviation to the mean value of the random variable. When the gradients are all computed, they are combined together with the correlations and standard deviations of the individual random variables using Equation 5.1 to provide the variance due to structural modeling. This variance value can then simply be added to the variance that arises from record-to-record variability to provide a measure of overall variance in the EDP.

The random variables chosen for the FOSM analysis for both the RC and UBPT bridges are steel reinforcing yield strength, concrete compressive strength, plastic hinge length, effective moment of inertia for the elastic segment of the beam elements, and damping. There is one additional random variable that is applicable to the individual bridges. For the RC bridge, it is the reloading strain value for the *Concrete01WithSITC* material model. For the UBPT bridge, it is the initial prestress in the PT tendons. The random variables were chosen to include a number of the important assumptions made in the model. The mean and standard deviation values for the random variables for both the RC and UBPT bridges are shown in Table 5.3 and Table 5.4, respectively.

Table 5.3 Random variables for FOSM analysis of RC bridge.

Random Variable	No.	Mean, μ_i	Standard Deviation, σ_i	Sources
Steel Yield Strength, f_y	1	469 MPa (68 ksi)	27.6 MPa (4 ksi)	Caltrans SDC (2003), Melchers (1999)
Concrete Compressive Strength, f'_c	2	27.6 MPa (4 ksi)	4.2 MPa (610 psi)	Melchers (1999)
Plastic Hinge Length, *PHL*	3	152 cm (60 in)	21.3 cm (8.4 in)	Caltrans SDC (2003), Priestley and Park (1987)
Cracked Moment of Inertia Ratio, I_{cr}/I_g	4	0.45	0.16	Caltrans SDC (2003), Elwood and Eberhard (2006)
Damping Ratio, ξ	5	2%	0.5%	Assumed
Concrete Reloading Strain, ε_r	6	0.02 mm/mm	0.01 mm/mm	Assumed

Table 5.4 Random variables for FOSM analysis of UBPT bridge.

Random Variable	No.	Mean, μ_i	Standard Deviation, σ_i	Sources
Steel Yield Strength, f_y	1	469 MPa (68 ksi)	27.6 MPa (4 ksi)	Caltrans SDC (2003), Melchers (1999)
Concrete Compressive Strength, f'_c	2	55.2 MPa (8 ksi)	2.8 MPa (410 psi)	Melchers (1999)
Plastic Hinge Length, *PHL*	3	152 cm (60 in)	21.3 cm (8.4 in)	Caltrans SDC (2003), Priestley and Park (1987)
Cracked Moment of Inertia Ratio, I_{cr}/I_g	4	0.36	0.13	Caltrans SDC (2003), Elwood and Eberhard (2006)
Damping Ratio, ξ	5	2%	0.5%	Assumed
Initial Prestress, f_{ps}	6	690 MPa (100 ksi)	104 MPa (15 ksi)	Tadros et al. (2003)

For the steel yield strength, a standard deviation was obtained from existing statistical data on Grade 60 reinforcing bars (Melchers 1999). For the concrete compressive strength, Melchers (1999) provides standard deviation values for ranges of compressive strengths and levels of quality control, which were *Poor*, *Average*, and *Excellent*. For the RC column, the standard deviation value for concrete compressive strength was taken for *Average* quality control, which was assumed for normal strength concrete. For the UBPT column, the standard deviation value for compressive strength was taken for *Excellent* quality control, as better quality control is expected for higher-strength concretes.

For the plastic hinge length, the mean value was computed using the equation found in the Caltrans SDC (2003), which comes directly from the Priestley and Park (1987) equation. A coefficient of variation of 0.14 was found by Priestley and Park (1987) in terms of their prediction for plastic hinge length as compared with experimental data, so this value was used to compute the standard deviation. For the effective stiffness, a recommended coefficient of variation of 0.35 is given by Elwood and Eberhard (2006) for reinforced concrete columns. For the damping ratio, a mean value of 2 percent is assumed. Priestley et al. (1996) gives a range of damping values for concrete structures of between 2 and 7 percent. In building structures, a value of 5 percent is commonly used. Because typical highway bridges do not contain a large quantity of nonstructural components, the damping from these items is not present. Therefore a commonly used damping value for bridges is 2 percent, and that value is used here (Hart and Vasudevan 1975). For the standard deviation, a value of 0.5 percent was assumed.

As discussed in Chapter 4, a large standard deviation (corresponding to a coefficient of variation of 0.5) was assumed for the reloading strain value for the *Concrete01WithSITC* model due to the large variability expected in this value. For the value of prestressing force in the PT tendon, the actual prestress force can be expected to vary significantly due to the fact that prestress losses arise from a number of different sources. Prestress losses come about from elastic shortening of the concrete, shrinkage of concrete, creep of concrete, and relaxation in the PT tendons, and can result in losses of 276 to 380 MPa (40 to 55 ksi) (Lin and Burns 1981). In addition to the variation in predicting losses from the various sources described above, the process is also time dependent, and so the prestress loss will vary depending on the time after construction that an earthquake occurs. Based on a study performed by Tadros et al. (2003) on comparing theoretical and experimental prestress losses in concrete girders, a coefficient of variation of 0.15 was assumed for the prestress in the post-tensioned tendons.

In addition to the mean and standard deviation values, the correlation between the random variables was also required for the FOSM analysis. Because statistical information on these correlations is not readily available, the correlations were again assumed based on engineering judgment. For most of the random variables, the correlations were assumed to be zero. The correlation values for the random variables used in the FOSM analysis are shown in Table 5.5 and Table 5.6 for the RC and UBPT bridges, respectively.

Table 5.5 Correlation between random variables for FOSM analysis of RC bridge.

Random Variable	Number	1	2	3	4	5	6
Steel Yield Strength, f_y	1	1.0	0.0	1.0	0.0	0.0	0.0
Concrete Compressive Strength, f'_c	2	0.0	1.0	0.0	0.0	0.0	0.0
Plastic Hinge Length, PHL	3	1.0	0.0	1.0	0.0	0.0	0.0
Cracked Moment of Inertia Ratio, I_{cr}/I_g	4	0.0	0.0	0.0	1.0	0.0	0.0
Damping Ratio, ξ	5	0.0	0.0	0.0	0.0	1.0	0.0
Concrete Reloading Strain, ε_r	6	0.0	0.0	0.0	0.0	0.0	1.0

Table 5.6 Correlation between random variables for FOSM analysis of UBPT bridge.

Random Variable	Number	1	2	3	4	5	6
Steel Yield Strength, f_y	1	1.0	0.0	1.0	0.0	0.0	0.0
Concrete Compressive Strength, f'_c	2	0.0	1.0	0.0	0.0	0.0	0.0
Plastic Hinge Length, PHL	3	1.0	0.0	1.0	0.0	0.0	0.0
Cracked Moment of Inertia Ratio, I_{cr}/I_g	4	0.0	0.0	0.0	1.0	0.0	0.0
Damping Ratio, ξ	5	0.0	0.0	0.0	0.0	1.0	0.0
Initial Prestress, f_{ps}	6	0.0	0.0	0.0	0.0	0.0	1.0

5.4.5 Results from Mean Value Analysis

5.4.5.1 Analysis with S_a as an IM

An IDA was first performed on the baseline bridge using the mean values of all random variables, and using S_a as the IM for scaling of the ground motions. The two EDPs of interest in the structural analysis were the peak drift ratio and the residual drift ratio at the tops of the columns. As the analysis was performed with two components of ground motion, two directions of movement exist for the columns. The total drift was calculated at each time step using both the transverse and longitudinal directions of motion by taking the square root of the sum of the squares (SRSS) of the two components. The peak drift was taken to be the peak value of this total drift and not the peak value in either the transverse or longitudinal direction alone. The peak was also taken as the maximum of all four columns. The displacement responses of the four columns were very similar due to the stiffness of the superstructure and the fact that the same acceleration history was applied uniformly to the bases of all of the columns.

The results from the IDA using S_a as an IM are shown below in Figure 5.7 and Figure 5.8. The resulting EDP values for each ground motion are shown at each intensity level. The computed median values (assuming that the EDP values are log-normally distributed) are shown with a solid line and the plus and minus one standard deviation values are shown with dashed lines. The values are plotted using S_a on a secondary ordinate and the associated value of S_{de} on the primary ordinate. S_{de} was used for plotting to facilitate comparison with the results from the analysis using S_{di}, presented in Section 5.4.5.2.

In Figure 5.7, a comparison is made between the peak drift ratios of the RC and the UBPT bridges. In general, the peak drifts for the two systems are close for a given intensity level. The results contradict the notion that systems with lower hysteretic energy dissipation will have greater displacement demands as similar systems with more hysteretic energy dissipation. Although the IDA appears to be almost linear, the bridge itself of course does not remain in the elastic range.

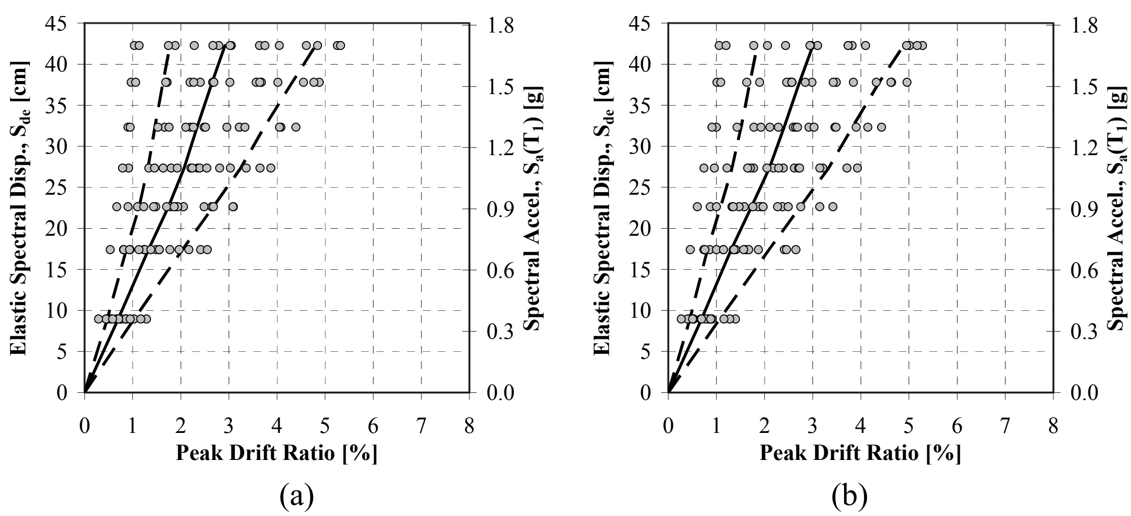

Fig. 5.7 Comparison of peak drifts for bridge with (a) RC columns and (b) UBPT columns using S_a as an IM.

The performance of the UBPT columns with respect to peak drift response was as desired, i.e., in the design of the UBPT columns, the goal was to proportion the columns such that the peak drift response would be similar to that of the RC columns. The purpose of this goal was to ensure that the peak drift response of the UBPT columns would be no worse than that of the currently used, conventional RC system. In this way, any expected damage in bridge components related to peak drifts would be comparable in the two systems and the UBPT bridge would not produce additional damage that would make it disadvantageous as compared to the RC system.

In terms of the actual magnitudes of the peak drifts of the bridges, the results reflect the conservatism in design practiced by Caltrans engineers. At the 50% in 50 years IM level, the median peak drift ratio of the two bridges was approximately 0.7 percent, which corresponds to a drift ratio that is within the elastic range. At the 2% in 50 years IM level (S_a of 1.52 g), the median peak drift ratio of the two bridges was roughly 2.6 percent, which corresponds to a ductility demand of less than 3. At this level of drift, yielding of the columns occurs, but the ductility demand is low enough that the safety of the structure would not be comprised. In the context of design based on current codes, the bridge meets expectations, as collapse prevention has been successfully met. Another important note is that since this drift level is well below any level where collapse might be expected, it is within the realm of behavior that can be adequately captured in the simulation models.

A comparison between the residual drift ratios of the RC and the UBPT bridges is shown in Figure 5.8. Unlike with the peak drift response, there is a clear difference in the response of the two bridge systems. With increasing intensity, the bridge with RC columns begins to sustain significant residual displacements, with large variation in the magnitudes of the residual displacements for the different ground motions. On the other hand, the bridge with UBPT columns retains substantially lower residual displacements with increasing intensity, with much less variation in the results.

At the 50% in 50 years IM level (S_a of 0.36 g), the median residual drift ratio of the RC columns is approximately 0.1 percent, while the median residual drift ratio of the UBPT columns in approximately 0.04 percent. This magnitude of residual displacements for both column systems is low enough that both bridges would likely be considered usable following an earthquake. At the 2% in 50 years IM level, a weakness in the RC column system is exposed. For the RC column system, four of the records led to residual displacements of greater than 1 percent in the columns , and a median residual drift of 0.6 percent with plus/minus one standard deviation values of 0.29 and 1.24 percent, respectively. In the cases where the residual drift ratio exceeded 1 percent, the functionality of the bridge in this state is questionable. For the UBPT column system, the median residual drift ratio at the 2% in 50 years hazard level was 0.25 percent with plus/minus one standard deviation values of 0.15 and 0.42 percent, respectively. In no case do any of the records lead to a residual drift ratio of greater than 1 percent, and the maximum value was 0.67 percent. These lower residual drift ratios sustained by the UBPT column would likely leave the bridge in an operational state following an earthquake.

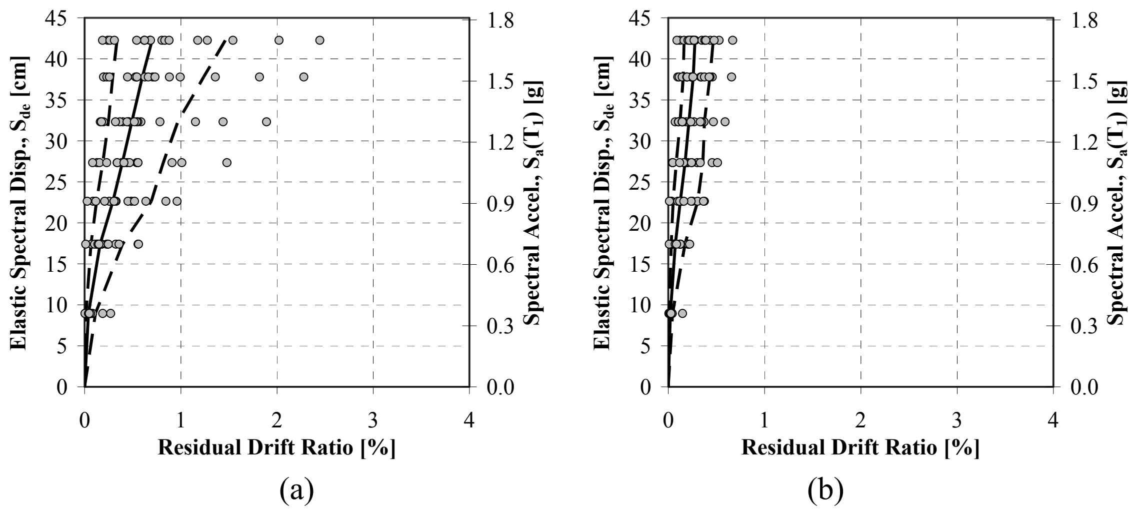

Fig. 5.8 Comparison of residual drifts for bridge with (a) RC columns and (b) UBPT columns using S_a as an IM.

5.4.5.2 Analysis with S_{di} as an IM

An IDA was performed again on the baseline bridge with all random variables set to their mean values, but instead using S_{di} as the IM for scaling the ground motions. Comparisons of peak drifts and residual drifts between the two bridge systems are shown in Figure 5.9 and Figure 5.10, respectively. The results show the same general behavior as shown from the IDA using S_a as an IM, as expected. The purpose of using S_{di} as an IM was partially to assess whether it could provide an improved response prediction to using S_a (in terms of reducing dispersion, among other things) but more importantly to determine the effect of the choice of the IM on the results of the overall PBEE assessment. The sensitivity of the final results on the choice of IM will be discussed in Section 5.7.2, when all of the portions of the PBEE assessment are combined. Here, a comparison of the IMs in terms of response prediction is presented.

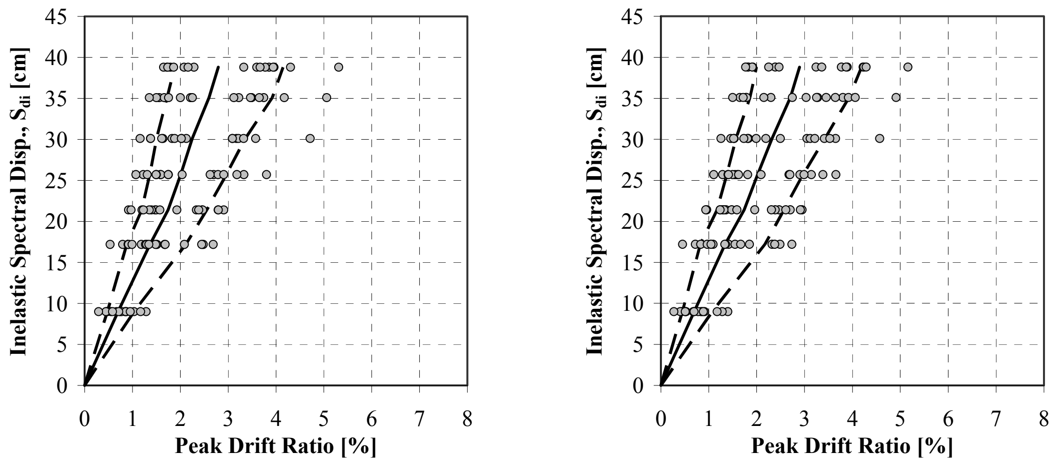

(a) (b)

Fig. 5.9 Comparison of peak drifts for bridge with (a) RC columns and (b) UBPT columns using S_{di} as an IM.

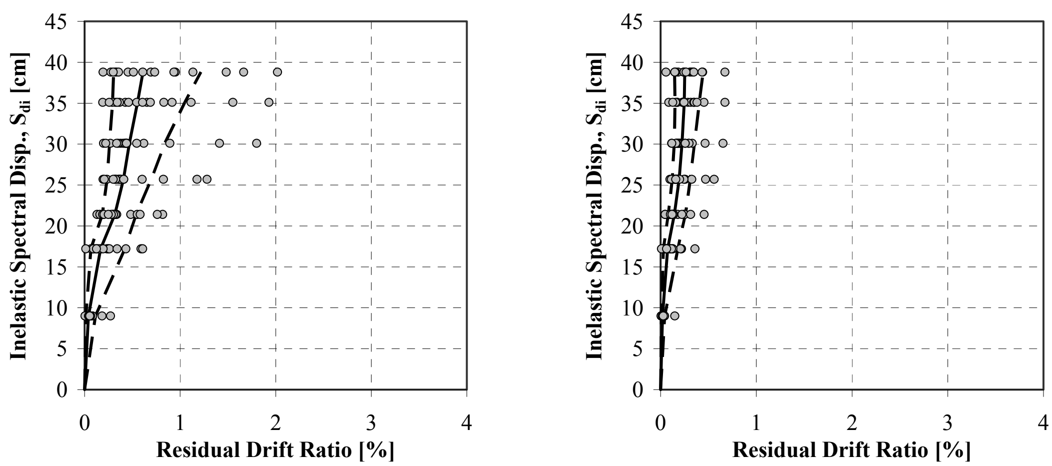

(a) (b)

Fig. 5.10 Comparison of residual drifts for bridge with (a) RC columns and (b) UBPT columns using S_{di} as an IM.

To compare the two IMs, the variance in the responses for a given median EDP level is compared. The variance at several values of peak drift is computed using interpolation from the IDA results. The resulting values for the RC bridge are plotted as standard deviations against the EDP, and are shown in Figure 5.11. At lower drift values, the standard deviation values are similar. This is expected, because at low drift levels, when the system is essentially elastic, the two should be the same. With increasing EDP, the standard deviations in the responses become increasingly larger. For a peak drift of 2.75 percent, the standard deviation in the responses using S_{di} as an IM is roughly 80 percent of the standard deviation in the responses using S_a as an IM. A similar trend can be seen in the values for the UBPT bridge shown in Figure 5.12.

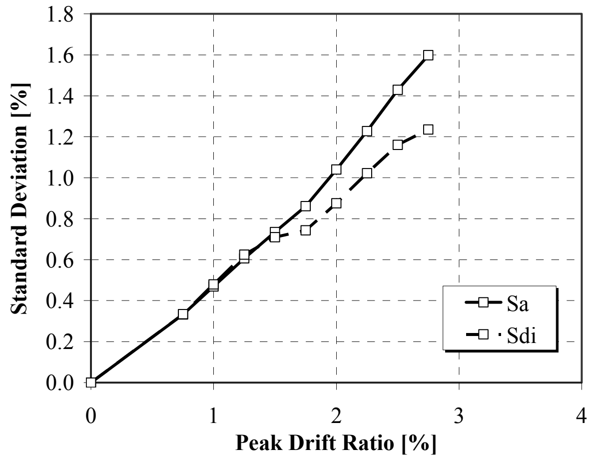

Fig. 5.11 Comparison of standard deviations in peak drift ratio responses for RC bridge using S_a and S_{di} as IMs.

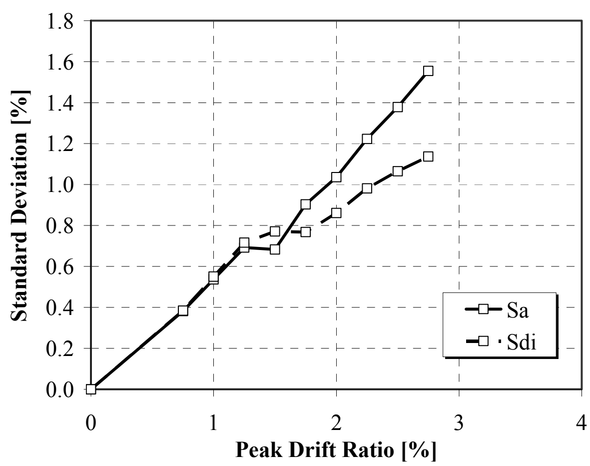

Fig. 5.12 Comparison of standard deviations in peak drift ratio responses for UBPT bridge using S_a and S_{di} as IMs.

As the drift values from the IDA were not very large (due to the large size of the columns), it is not possible to compute the variance in the EDP results at higher EDP values. However, based on the trend shown in Figure 5.11 and Figure 5.12, the difference in the variances using the two IMs will continue to increase with increasing peak drift ratio. For analysis at higher levels of structural demand, for example in a collapse study, the benefits of using S_{di} as opposed to S_a for reducing dispersion in the EDP might be more apparent. The reduction in dispersion is also evident here, but the reduction is less pronounced due to the fact that the structural response of the bridge is not especially severe.

5.4.6 Results from FOSM Analysis Using S_a as an IM

The bridge models were analyzed again using the IDA procedure while varying the random variables using the FOSM method to incorporate the modeling uncertainty. The analysis was first performed using the scale factors computed using S_a as an IM. The FOSM analysis allows the sensitivity of the EDPs to the individual random variables to be seen easily by plotting the results in a figure called a *tornado diagram* (Howard 1988, Porter 2001). The tornado diagram shows the variation in the EDP with respect to the individual random variables, and the results are plotted with the most sensitive random variable at the top and the least sensitive at the bottom, such that the plot resembles a tornado.

5.4.6.1 Results for RC Bridge

The tornado diagram for the EDP of peak drift is shown in Figure 5.13 for the RC bridge. The plot is shown for the highest intensity level to which the records were scaled (1.7 g) such that the variation in response could be most easily seen (similar plots could be shown for all of the scaling levels). The median peak drift ratio when all variables are set to their mean values is 2.9 percent and is shown with the heavy black line. The gray lines show the variability in the median peak drift when each individual random variable is changed from mean-minus-one standard deviation to mean-plus-one standard deviation.

Overall, the median peak drift ratio is not very sensitive to all of the random variables. For the random variable that has the largest sensitivity, plastic hinge length (PHL), the median peak drift ratio ranges from 2.87 to 2.97, which is not a significant variation. The other two somewhat sensitive random variables are the effective moment of inertia, I_{eff}, and the damping, ξ. The peak drift ratio is not sensitive to the reloading strain value of the *Concrete01WithSITC* model, ε_r. This result is desired, as the modification to incorporate the reloading effect was intended to improve residual displacement response prediction without altering the peak displacement response prediction.

The tornado diagram for the EDP of residual drift ratio for the RC bridge is shown in Figure 5.14. Again, the diagram is shown for the scaling level of 1.7 g. The residual drift ratio is most sensitive to the reloading strain value, as expected. The damping also causes relatively high sensitivity of the residual drift ratio values as compared to the other random variables. In general, however, the overall magnitude of the variation in response is not especially high for any of the random variables, similarly to the peak drift ratio values.

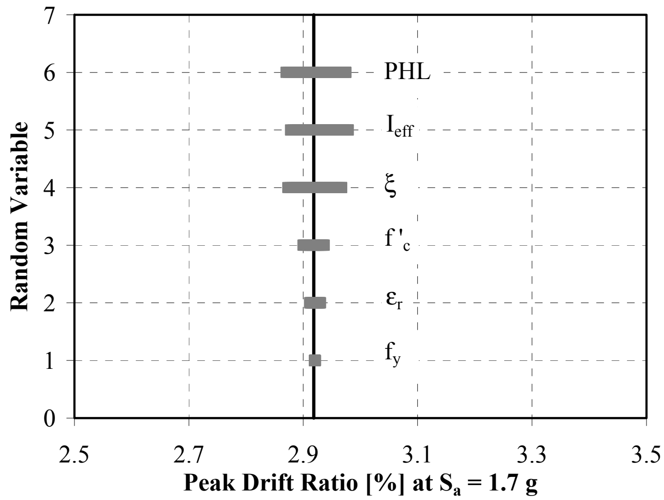

Fig. 5.13 Sensitivity of peak drift ratio to RVs for RC bridge at S_a = 1.7 g.

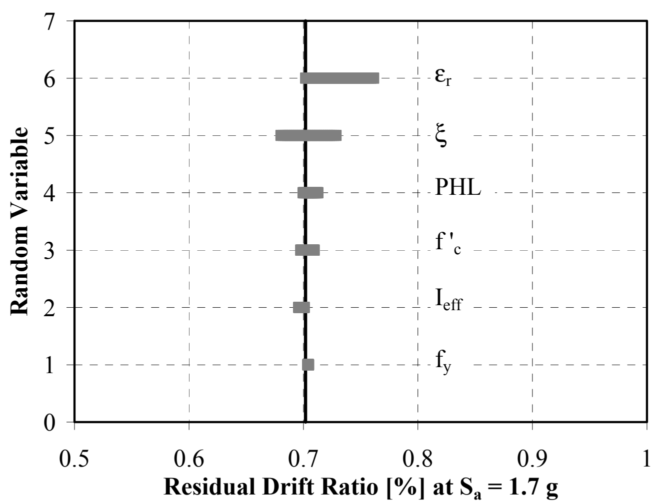

Fig. 5.14 Sensitivity of residual drift ratio to RVs for RC bridge at S_a = 1.7g.

The additional variance in the EDPs was computed at all scaling levels as described in Section 5.4.4, and was added to the overall variance. The IDA plots incorporating this modeling uncertainty for both peak and residual drift ratio are shown in Figure 5.15. The new plus/minus-one-standard-deviation lines incorporating the modeling uncertainty are shown with black lines. For comparison, the original plus/minus-one-standard-deviation lines are shown with gray lines. The plots show that the incorporation of modeling uncertainty in this case does not significantly add to the overall variance in the EDP response prediction. This is a valuable finding, as it shows that the results are not overly sensitive to assumptions made in the modeling.

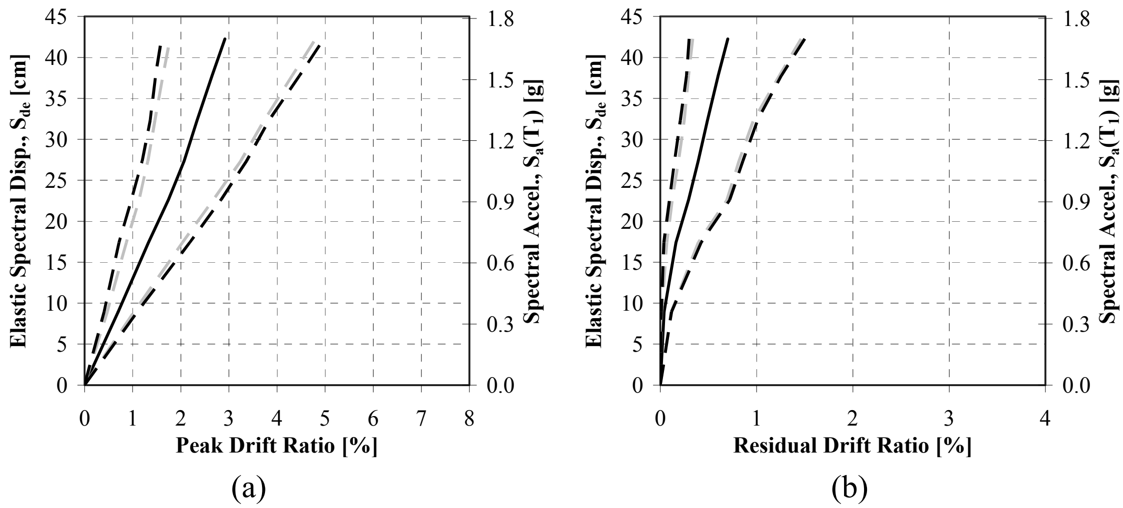

Fig. 5.15 IDA plots for (a) peak drift ratio and (b) residual drift ratio incorporating modeling uncertainty using FOSM method for RC bridge using S_a as an IM.

5.4.6.2 Results for UBPT Bridge

The tornado diagram for the EDP of peak drift is shown in Figure 5.16 for the UBPT bridge. The plot is shown for the highest intensity level to which the records were scaled to, which was 1.7 g. The median peak drift ratio when all variables are set to their mean values, shown with the heavy black line, was 3.01 percent. Similar to the RC bridge, the median peak drift ratio is not especially sensitive to any of the random variables. The random variable that has the largest sensitivity is the effective moment of inertia, I_{eff}, and the median peak drift ratio ranges from 2.95 to 3.07. The next most sensitive random variable is the damping, ξ. The peak drift ratio is not overly sensitive to the prestress value.

The tornado diagram for the EDP of residual drift ratio for the UBPT bridge is shown in Figure 5.17. The median value of the peak drift, shown with the heavy black line, was 0.28 percent. The residual drift ratio is most sensitive to the prestress value, as expected. However, the overall magnitude of the variation with respect to the prestress in not exceptionally large.

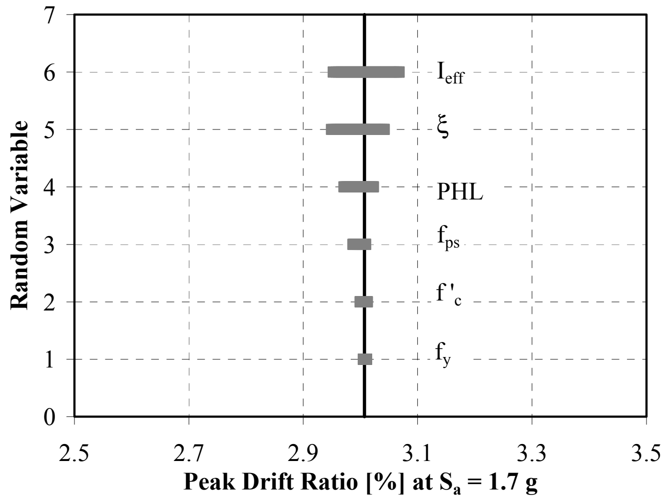

Fig. 5.16 Sensitivity of peak drift ratio to RVs for UBPT bridge at S_a = 1.7 g.

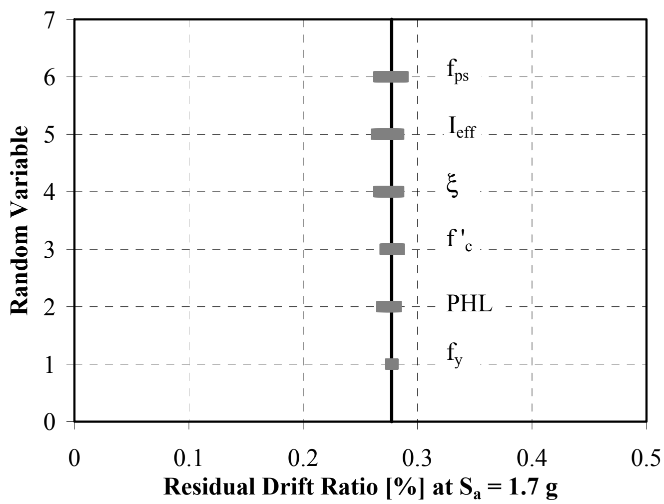

Fig. 5.17 Sensitivity of residual drift ratio to RVs for UBPT bridge at S_a = 1.7 g.

The additional variance in the EDPs was computed at all scaling levels for the UBPT analyses as and was added to the overall variance. The IDA plots incorporating this modeling uncertainty for both peak and residual drift ratio are shown in Figure 5-18. The plots show that, like the RC bridge, the incorporation of modeling uncertainty in this case does not significantly add to the overall variance in the EDP response prediction. Again, it can be concluded that excessive attention to obtaining precise values of the material and modeling parameters is unnecessary.

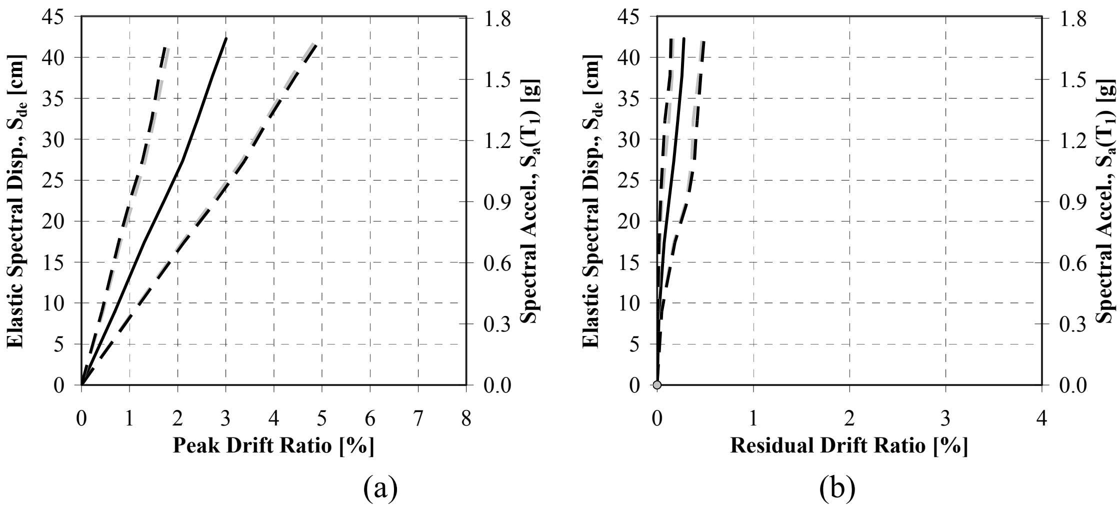

Fig. 5.18 IDA plots for (a) peak drift ratio and (b) residual drift ratio incorporating modeling uncertainty using FOSM method for UBPT bridge using S_a as an IM.

5.4.7 Results from FOSM Analysis Using S_{di} as an IM

A similar set of analyses to evaluate the impact of modeling uncertainty as performed in Section 5.4.6 was again performed, using S_{di} for the scaling in the IDA rather than S_a. If the FOSM analyses was performed using both IMs, then the results from the two could be more readily compared. The results are presented in the following sections.

5.4.7.1 Results for RC Bridge

The tornado diagrams for the RC and UBPT bridges at the highest level to which the motions were scaled (Sdi of 38.3 cm) are shown in Figure 5.19 and Figure 5.20. Similar to the case when S_a is used as an IM, the results are not highly sensitive to the random variables used in the analysis. Again, the sensitivity to these variables might be more pronounced had the overall peak responses of the structure been greater. With larger levels of nonlinearity in the structure, the responses would be expected to vary more. The sensitivity to the random variables is however lower than in the case of the of S_a as an IM.

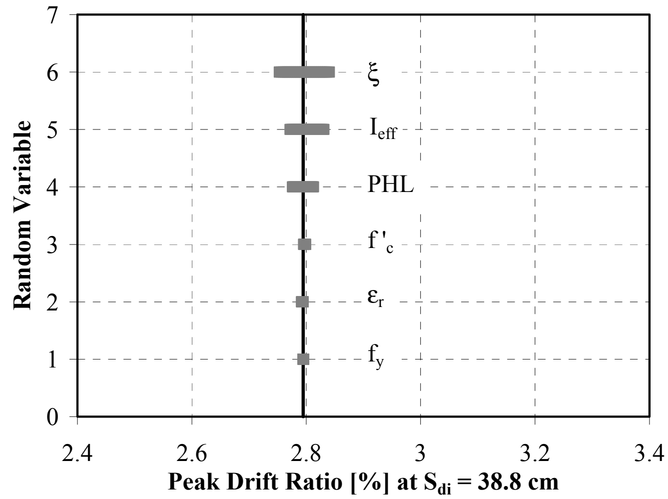

Fig. 5.19 Sensitivity of peak drifts to random variables for RC bridge at S_{di} = 38.8 cm.

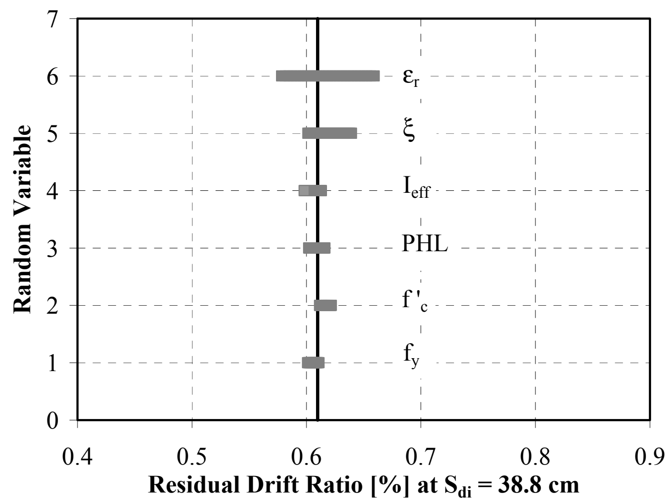

Fig. 5.20 Sensitivity of residual drifts to random variables for RC bridge at S_{di} = 38.8. cm

Again, the additional variance in the EDPs was computed at all scaling levels and was added to the overall variance. The IDA plots incorporating this modeling uncertainty for both peak and residual drift ratio are shown in Figure 5.21. The plots show that, as with the case of S_a as an IM, the incorporation of modeling uncertainty in this case does not significantly add to the overall variance in the EDP response prediction. The large size of the columns may mean that material and modeling variations play a minor role in the response in comparison to the geometry itself.

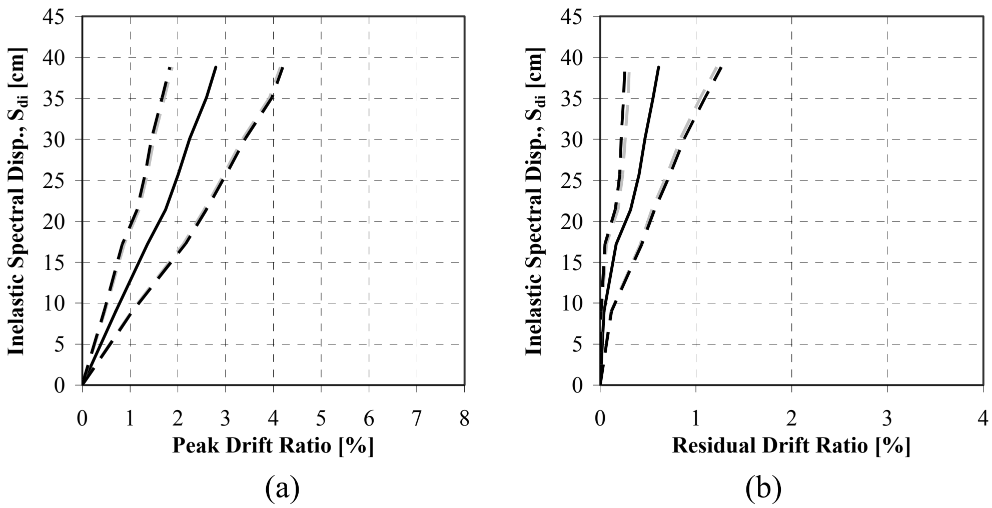

Fig. 5.21 IDA plots for (a) peak drift ratio and (b) residual drift ratio incorporating modeling uncertainty using FOSM method for RC bridge using S_{di} as an IM.

5.4.7.2 Results for UBPT Bridge

The tornado diagrams for the peak drift ratio and residual drift ratio are shown in Figure 5.22 and Figure 5.23, respectively for the UBPT bridge. Similar results are seen for the UBPT bridge when S_a is used as an IM. The IDA plots incorporating the modeling uncertainty for both peak and residual drift ratio are shown in Figure 5.24. In terms of peak drifts, the results were most sensitive to the effective moment of inertia. The overall sensitivity was low, however, with the median EDP changing by only a few tenths of a percent. In terms of the residual drift, the results were most sensitive to the prestress. The impact was large relative to the other RVs. In terms of most accurately predicting residual displacements, the prestress should be most closely controlled. The plots show that, as with the case of S_a as an IM, the incorporation of modeling uncertainty in this case does not significantly add to the overall variance in the EDP response prediction.

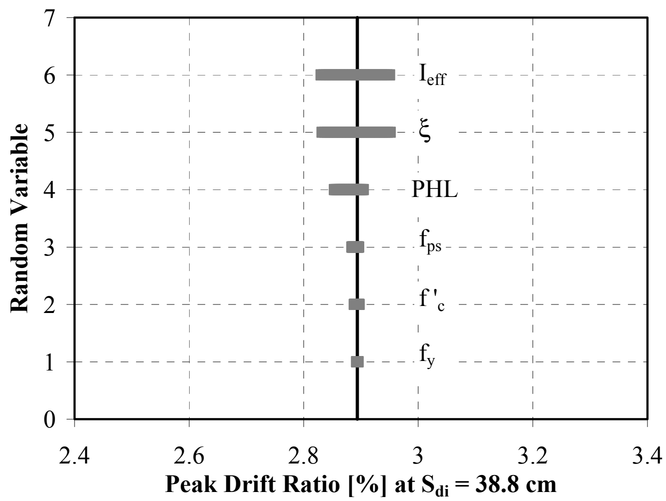

Fig. 5.22 Sensitivity of peak drifts to random variables for UBPT bridge at S_{di} = 38.8 cm.

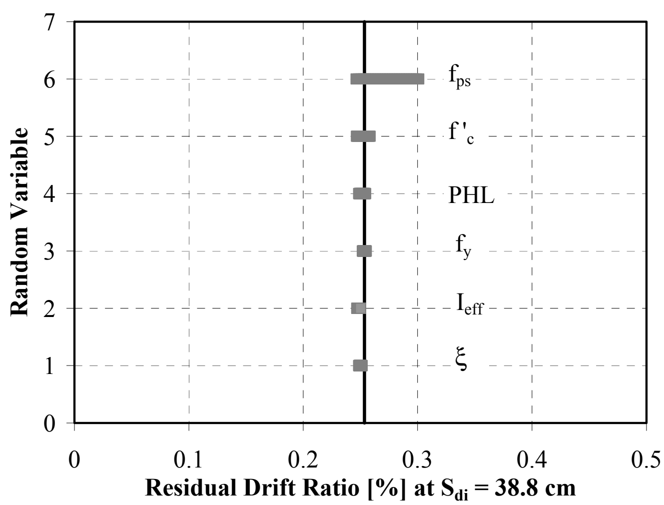

Fig. 5.23 Sensitivity of residual drifts to random variables for UBPT bridge at S_{di} = 38.8 cm.

5.4.8 Summary of FOSM Analysis

The results from the FOSM analysis of both the RC and UBPT bridge systems showed that the two EDPs (peak drift and residual drift) were not overly sensitive to the several of the modeling parameters used in the analysis. In comparison to the record-to-record variability, the variation in EDP due to the randomness in the RVs was almost negligible. The same conclusion was found when using either S_a or S_{di} as the IM. The results from the analyses showed that predicting precisely the modeling parameters is not necessary, as the resulting EDP values are not expected to vary substantially with variation in the assumed values.

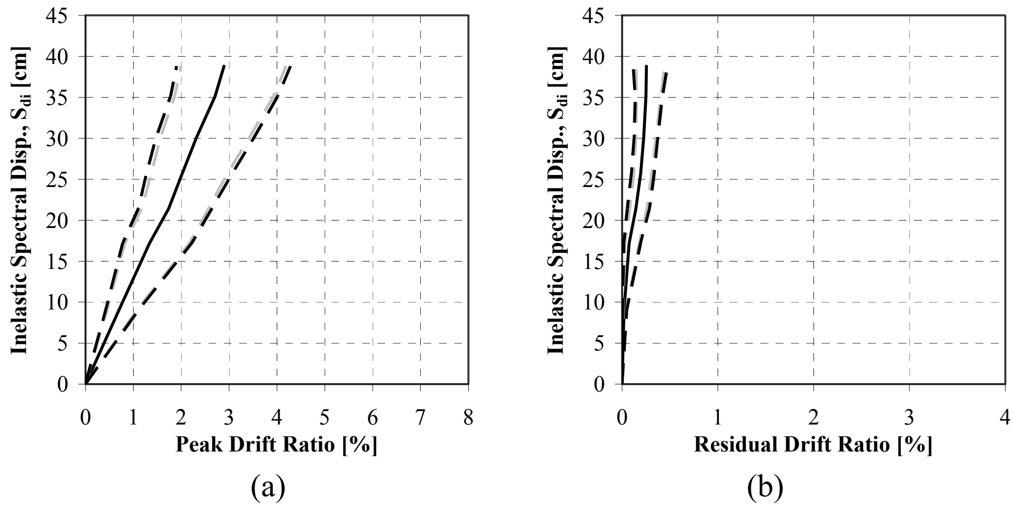

Fig. 5.24 IDA results for (a) peak drift ratio and (b) residual drift ratio incorporating modeling uncertainty using FOSM method for UBPT bridge using S_{di} as an IM.

5.5 DAMAGE ANALYSIS

The third portion of PEER's PBEE assessment is to use the results from the structural analyses to predict the levels of expected damage in the structure. In order to do this, it is necessary to first select damage states appropriate for the structure, and then to obtain fragility curves, which relate structural response to expected damage. Presented in this section are the selected damage states for the bridge and their corresponding fragility curves.

5.5.1 Damage States

The damage states considered for the bridge were assumed to be related the columns only, as the columns are the elements in which most of the damage is expected to occur. Damage in the columns was assumed to be manifested in three forms, which were spalling of the cover concrete, presence of residual displacements, and buckling of longitudinal reinforcing bars. These three forms of damage were expected to represent the dominant forms of damage in tall, flexure-dominated columns such as the ones in this study. Spalling of cover concrete corresponds to minor damage, where the column is in usable condition but requires some cosmetic repair. Residual displacements represent a state in which the column has undergone nonlinear (e.g., yielding of mild steel) behavior and will still be operational depending on the level of residual displacement. Buckling of longitudinal reinforcement corresponds to an extreme level of damage, where major repair would be required. The same three forms of damage were assumed to be appropriate for both the conventional RC columns and the self-centering, UBPT columns.

Typically, damage states selected in the PEER framework are discrete, meaning that they are assumed either to happen or not to happen. For example, one damage state for reinforced concrete slab-column connections studied by Aslani and Miranda (2005) was punching shear failure. In this case, it is clear that the punching shear failure damage state either occurs or does not. In the case of the spalling of cover concrete and buckling of longitudinal reinforcing, there are of course varying levels of spalling that can occur, and different numbers of bars that can buckle. However, for this study, these two states are assumed to be discrete (e.g., spalling either occurs or does not).

In the case of the residual displacements, it would seem natural to consider residual displacement as a continuous value rather than a discrete state, as any value of residual displacement is possible. However, a low residual displacement may not be considered to affect significantly the functionality of a bridge. Therefore, to keep the presence of residual displacements consistent with the notion of discrete damage states, the damage state associated with the residual displacements is defined here as having two states. In the first state, the residual displacement is below some threshold value, meaning that the bridge is still assumed to be functional and not in the residual displacement damage state. In the second state, the residual displacement has exceeded this threshold value, meaning that the bridge would be considered unusable and is in the residual displacement damage state. If the bridge were in this damage state, it would have to be demolished and replaced; thus the damage state will be henceforth referred to as *replacement-level residual displacement*. Of course, this damage state is not easily broken down into a 'yes' or 'no' state, and the decision to deem a bridge unusable due to residual displacements would have to be made by an engineer at the site. Further discussion will be given in Section 5.5.2. To summarize, the three damage states considered in the assessment of the bridges were:

(1) spalling of cover concrete,

(2) buckling of longitudinal reinforcing, and

(3) replacement-level residual displacement.

5.5.2 Fragility Functions

To relate structural response to damage, fragility functions are used. The fragility functions give the probability of a structure or component being in a discrete damage state given the structural response (EDP), as discussed in Chapter 2. Fragility functions are typically based on experimental data, and in the case of RC columns, a large amount of data exists for use in this type of damage analysis. Berry and Eberhard (2003) for example developed empirical fragility curves for RC columns. In their study, a large database of cyclic tests on RC columns was compiled, and statistical analyses were performed on the data to develop predictive equations for two damage modes in RC columns, which were cover concrete spalling and longitudinal bar buckling. Equations for estimating the mean drift at which spalling or bar buckling would occur, along with values of the variance of the predictions, were developed. Their proposed equation is:

$$\frac{\Delta_{spall}}{L}(\%) \cong 1.6\left(1-\frac{P}{A_g f'_c}\right)\left(1+\frac{L}{10D}\right) \tag{5.4}$$

where Δ_{spall} is the drift at spalling, L is the length of the column, P is the axial load, A_g is the gross cross-sectional area, f'_c is the concrete compressive strength, and D is the diameter. Associated with this equation is a coefficient of variation of 0.35 for spiral-reinforced columns. The proposed equation for bar buckling is:

$$\frac{\Delta_{bb}}{L}(\%) \cong 3.25\left(1+150\rho_{eff}\frac{d_b}{D}\right)\left(1-\frac{P}{A_g f'_c}\right)\left(1+\frac{L}{10D}\right) \tag{5.5}$$

where Δ_{bb} is the drift at bar buckling and ρ_{eff} is the effective confinement ratio, computed by:

$$\rho_{eff} = \frac{\rho_s f_{ys}}{f'_c} \tag{5.6}$$

where ρ_s is the volumetric reinforcing ratio and f_y is the yield stress of the transverse reinforcing. Associated with this equation is a coefficient of variation of 0.26 for spiral reinforced columns.

The coefficient of variation values can then be used to compute standard deviations or variances once the mean value is computed. These equations are used to represent the damage behavior of the columns in this research.

Using the mean and standard deviation values and assuming a distribution (e.g., log-normal), a fragility curve can be created using the cumulative distribution function (CDF) of the distribution. In the case of these two damage states of spalling and bar buckling, the EDP in the fragility curve is the drift ratio. These equations were used to create the fragility curves for the conventional RC columns, and they were also assumed to be applicable to the UBPT columns. The UBPT columns are essentially the same as the RC columns, and the differences in the longitudinal reinforcing ratio, transverse reinforcing ratio, and axial load (due to the prestress) were all factors incorporated in the predictive equations. The mean drift ratio values for spalling and bar buckling for the RC column computed using Equations 5.4 and 5.5 were 2.8 percent and 8.4 percent, respectively. Similarly, the mean drift ratio values for spalling and bar buckling for the UBPT column were computed as 2.6 percent and 7.1 percent, respectively. Assuming a log-normal distribution, the fragility curves for the two damages states of spalling and bar buckling for the both columns are shown in Figure 5.25.

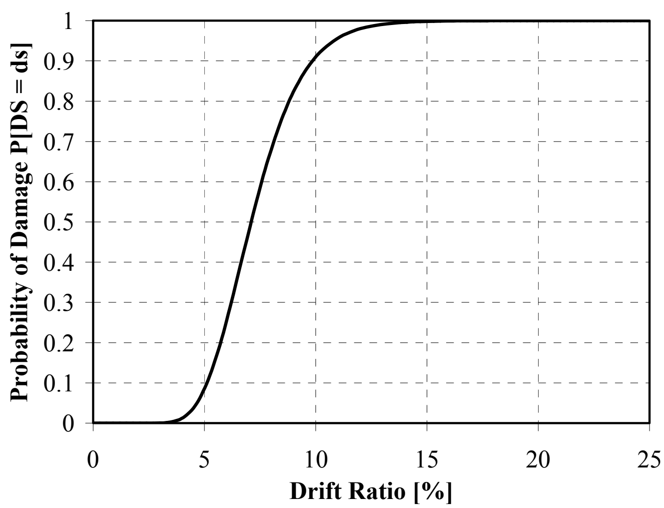

Fig. 5.25 Fragility curve for UBPT-ECC column for bar buckling damage state.

The mean drift ratio at spalling for the two columns is similar, as expected, since in the equation the only difference between the two columns is the axial load ratio. Although the axial load of the UBPT column is higher than that of the RC column, the compressive strength is also higher, so that the overall axial load ratio is similar. In the case of the mean drift ratio at bar buckling, the value for the UBPT column is lower than that of the RC column. This is also expected, since the drift at bar buckling should be reduced for the UBPT column due to the increased axial load that is present from the post-tensioning.

For the damage state of replacement-level residual displacements, the fragility curve can not be created in the same way as for the spalling and bar buckling damage states, for two reasons. First, the decision that a bridge is no longer usable due to excessive residual displacements is subjective. Two different engineers may give opposing recommendations for the same damaged column. In addition, although the residual displacement will be a primary factor, the decision will likely be based on additional observable damage, such as the actual level of spalling and cracking in the column and other components. The second reason is that much less data exist for this type of damage state. The type of data that could be used are the actual decisions made on replacing columns following actual earthquakes. The data on the decisions for the hundreds of bridge columns following the Kobe earthquake in Japan would be a good starting point; however, these data are not readily available.

The lack of available data and subjectivity in the damage state are common obstacles that will be faced when trying to develop fragility curves for the PEER framework if any type of new system or material is considered. However, an estimate of the fragility curve can be made based on engineering judgment and some recently adopted Japanese bridge design guidelines. Although this may not be the "true" fragility curve, it serves the purpose of providing a method of comparing two different systems, and a sensitivity study can be performed on the assumptions used to provide bounds on the analysis results.

To create the fragility curve for the damage state of excessive residual displacements, a different approach was used from the cases of spalling and bar buckling. In general, an EDP that is closely related to the damage is first identified, and then an empirical relationship between the magnitude of the EDP and the presence of the damage state is computed. Therefore, the first step is to identify an appropriate EDP. An EDP of the residual displacement itself was chosen. This is an EDP that is obtained directly from the analysis, and is a direct measure of whether a bridge could be deemed unusable. The peak drift was considered but did not seem appropriate, as the magnitude of the residual displacement is not always closely correlated to this value (as shown in Chapter 4).

The fragility curve was modeled with a linear function. A limit of residual displacement was assumed after which a bridge would be deemed unusable no matter the conditions of the other components of the bridge. To select this limiting value, the newly adopted Japanese code for highway bridge design (Japan Road Association 2006) was used. In this code, a limit of 1.5 percent residual drift following an earthquake is placed on the design of new highway bridges. For residual drifts below this limiting value, the bridge may still be considered unusable due to the combination of some residual displacement and other observed damage in the bridge. The assumption is made that residual drifts greater than 1 percent may possibly still be considered large enough to warrant replacement depending on other damage in the bridge. Therefore a linear function, ranging from 1 percent to 1.5 percent drift, was assumed for the fragility curve, as shown in Figure 5.26. The residual displacement fragility curve is assumed to be applicable to both the RC and UBPT columns. The value of 1.5 percent residual drift ratio was assumed for the baseline analysis. For the sensitivity analyses, values of 1.25 and 1.75 percent were used as the limiting values.

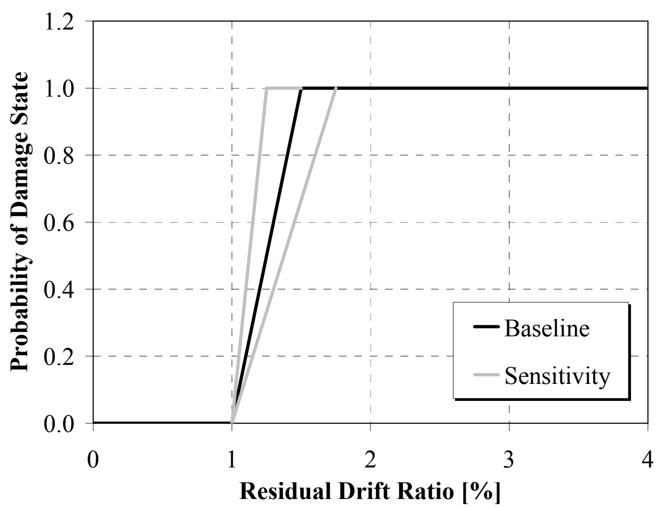

Fig. 5.26 Fragility curve for RC and UBPT columns for damage state of replacement-level residual displacement.

5.6 LOSS ANALYSIS

The fourth and final portion of PEER's PBEE assessment is to compute decision variables (DVs) for the structure given the expected levels of damage obtained from the previous steps. These DVs allow engineers, owners, and, in general, any decision makers to easily compare and assess structures in terms that are comprehensible to all parties. Examples of DVs are "dollars, downtime and deaths" (e.g., Porter 2003). The DVs considered to be most applicable to highway bridges are "dollars," i.e., repair or replacement costs for damaged components, and "downtime," i.e., the time that is required to bring the structure back to an operational state either through repair or replacement of the entire structure. Expected repair and replacement costs are an obvious choice for comparison of alternative structures in the case of any type of structure. In the case of highway bridges in particular, downtime is a good choice because the loss of functionality of important links in the transportation network could be devastating following an earthquake.

Compared to the three previous portions of the PEER PBEE assessment (i.e., hazard analysis, structural analysis, and damage analysis), the loss analysis portion of the assessment has received substantially less research attention to date. Loss modeling advancements have recently been made in the areas of structural and nonstructural components in buildings (e.g., Miranda and Aslani 2005; Haselton et al. 2005). Loss modeling in highway bridges has been minimal in comparison, although some limited data are currently available and provide a starting point, described in Sections 5.6.1 and 5.6.2.

5.6.1 Spalling and Bar Buckling

Damage in typical highway bridges during an earthquake can occur in numerous components. Mackie et al. (2006) compiled and processed damage and cost data from Caltrans statistics and post-earthquake case histories (Billington 2006; Caltrans 2004, 2005) to estimate the expected costs for damage of various bridge components. They found that damage for the bridge type in this study primarily consists of damage to the columns, expansion joints, bearings, back walls, shear keys, approach slabs, and deck. Except for the columns, the damage in these components should be similar for the two bridges, since they will essentially be based on the displacement response of the bridges, which were found to be similar in Section 5.4.5. Therefore in this study, whose goal is the comparison of the two systems and not an assessment of the individual systems, only costs due to columns are considered.

The damage states described in Section 5.5.1 were spalling, excessive residual displacements, and bar buckling. For the damage state of spalling, Mackie et al. (2006) reported the cost of repair to be a function of the square footage of spalled concrete. Specifically, a cost of $100 per square foot is given. The damage models do not give expected areas of spalled concrete, but rather give whether a column has experienced spalling or not. Here an estimate must be made of the area of spalling that occurs in the columns if spalling occurs. For the sake of comparison, an approximation is made and used consistently between the two systems. The approximation assumed is that if spalling occurs, it is assumed to occur along the entire plastic hinge length. For the mean plastic hinge length value of 152 cm (60 in.), this corresponds to an area of 8.76 m^2 (94.25 ft^2). For four columns, the total cost of repairing spalling if it occurs is therefore $37,700. A standard deviation of $10 per square foot is assumed for the repair cost, giving a standard deviation in total repair cost for spalling of $3,770. The mean and standard deviation values are assumed to be applicable to both the RC and UBPT bridge columns.

For the damage state of buckling of longitudinal reinforcement, the repair actions required are assumed based on Mackie et al. (2006) to be replacement of longitudinal and spiral reinforcing, and addition of steel column casing. The cost of steel reinforcing is given to be $2 per kilogram, and the cost of steel column casing is given to be $2,000 per linear foot. Standard deviations of these costs are assumed by the author to be $0.20 and $200 for steel reinforcing and column casing, respectively. To determine the total cost of repair when in the damage state of buckling, assumptions must be made on the amount of steel reinforcing to be replaced and the amount of steel casing required. Mackie et al. (2006) assume values of 1562 kg of steel reinforcing to be replaced and 50 linear feet of steel casing required per column using the same baseline bridge in their work as used in this research. For four columns, the total cost of repairing the columns in the buckling damage state is $412,500, with a standard deviation of $40,020.

The damage state of spalling is assumed to be repairable without loss of functionality of the bridge, i.e., the bridge can remain operational while repairs are made. For the damage state of bar buckling, some loss of functionality may be expected during repair depending on the severity of the bar buckling. However, downtime due to the possibility of excessive bar buckling is not considered. Under this assumption, the two damage states of spalling and bar buckling correspond only to repair costs and do not have any associated downtimes. The damage states and their associated EDP (i.e., peak drift ratio) are therefore not coupled with downtime losses.

In another study (Lee and Billington 2006), damage costs were predicted using the HAZUS99 SR2 Technical Manual (FEMA 1999), which presents replacement costs as a function of the initial cost when a bridge is in a given state of damage (ranging from slight to extensive). The HAZUS99 Manual was not used here because the damage states are very general, and also incorporate damage from all of the components of the bridge rather than the columns only.

Therefore in order to consider the columns alone and to incorporate Caltrans data for repair costs, the HAZUS Manual was not used.

5.6.2 Residual Displacements

For the damage state of excessive residual displacements, repair is unlikely (as there is currently no method for "straightening" deformed bridges), leaving demolition and replacement of the entire bridge as the only option. In the case where the bridge is no longer usable and must be demolished, there is of course an associated cost for replacement, but this cost is of secondary importance as compared to the actual downtime of a bridge. The loss of use of a bridge can have significant consequences on the transportation network, and is the primary problem that the use of UBPT is attempting to avoid. For this reason, as well as to simplify the analysis by decoupling this damage state from the previous two, only downtime losses are considered when dealing with the excessive residual drift damage state and monetary losses are not considered.

The HAZUS99 SR2 Technical Manual (FEMA 1999) is used to obtain rough estimates of downtime for the damage state of excessive residual displacements. The HAZUS Manual was developed for loss estimation following natural hazards such as earthquakes. The HAZUS Manual presents mean values for restoration times for highway bridges. These values are based partially on past data from earthquakes, but primarily on estimations based on expert opinion (due to the paucity of past data). The damage state of replacement-level residual displacement is assumed to correspond to the *extensive damage* state in HAZUS99. The state of extensive damage for bridges in HAZUS is "defined by any column degrading without collapse — shear failure — (column structurally unsafe), significant residual movement at connections, or major settlement approach, vertical offset at abutment, differential settlement at connections, shear key failure at abutments" (FEMA 1999).

The mean restoration time, or downtime, for a highway bridge in the *extensive* damage state is reported as 75 days with a standard deviation of 42 days. This value is for a standard bridge and likely would not apply to the UBPT bridge, due to the additional time required for construction of the post-tensioned columns. Therefore, a 20 percent higher value was assumed for the mean restoration time, i.e., 90 days, with the same value of 42 days assumed for the standard deviation. As this new assumed mean restoration time was not based on existing data, the sensitivity in this value was considered in Section 5.7.2.4.

5.7 INTEGRATION OF RESULTS: PBEE ASSESSMENT

The results from the four steps of the PEER analysis can be combined using the framing integral (Eq. 2.1 in Chapter 2) to produce loss hazard curves. More in-depth discussion and examples of performing these calculations can be found in, for example Baker and Cornell (2003b) and Mackie and Stojadinovic (2005).

5.7.1 Baseline Analysis

The results from the four steps of the PEER analysis using the baseline assumptions were combined using the framing integral to generate repair cost and downtime hazard curves. To summarize, the important baseline assumptions (for which sensitivity was then assessed) in each of the four steps are as follows: (1) hazard analysis — Abrahamson and Silva (1997) attenuation model in PSHA, (2) structural analysis — S_a as the IM for scaling in IDA, (3) damage analysis — assumed limiting value of 1.5 percent for residual drift damage state, and (4) loss analysis— the UBPT bridge downtime is 20 percent greater than that of the RC bridge. The repair cost and downtime hazard curves for both bridges from the baseline analysis are shown in Figures 5.27 and 5.28.

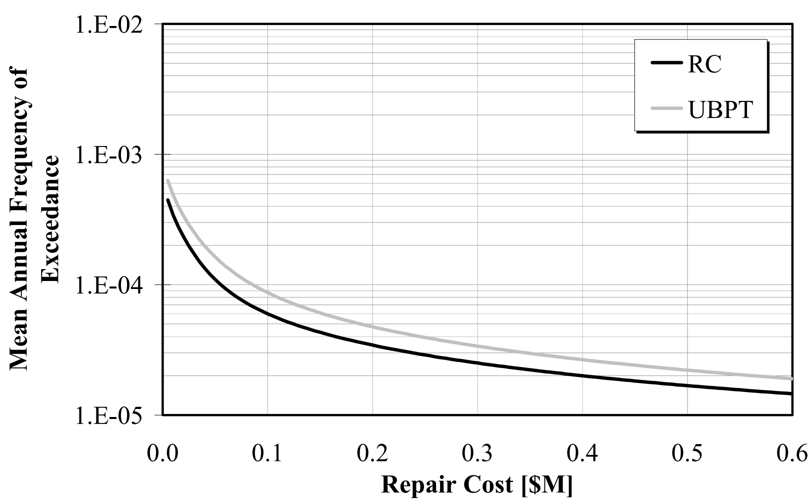

Fig. 5.27 Repair cost hazard curves from baseline analysis.

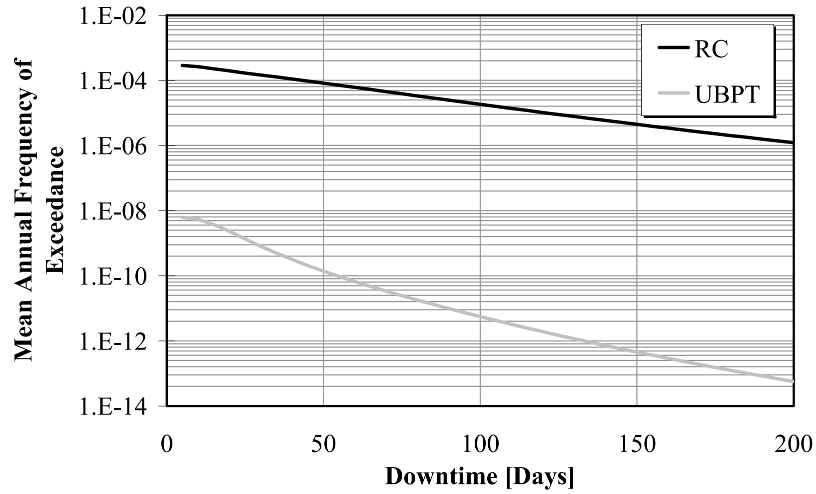

Fig. 5.28 Downtime hazard curves from baseline analysis.

The repair cost hazard curves for the two bridge systems are very similar. For a given mean annual frequency of exceedance, the repair cost for the UBPT system is slightly higher than that of the RC system. Such a trend was expected, as the repair costs are based on peak drift values, which in the IDA results were found to be higher for the UBPT system. In this sense, the UBPT system performed very well, as the expected repair costs due to column damage not from residual drifts are similar to that of the RC system.

When comparing the downtime hazard curves for the two bridges, the benefits of the UBPT system become evident. For a given value of downtime, the mean annual frequency of exceedance of the UBPT system is significantly lower than that of the RC system. For example, for a downtime of 30 days, the RC system has a mean annual frequency of exceedance of approximately 1.5E-4, which corresponds to a probability of 0.75 percent in 50 years. In comparison, for a downtime of 30 days, the UBPT system has a mean annual frequency of exceedance of approximately 8.0E-10, which corresponds to a probability of only 0.000004 percent in 50 years. With increasing values of downtime, the difference between the two systems increases.

Considering the RC system alone can allow for a benchmarking of a typical California overpass bridge designed according to current code. In terms of peak drifts at the 2 percent in 50 year IM level, the RC bridge experiences a median value of roughly 2.6 percent, which corresponds to a ductility demand of less than 3. In terms of residual drifts at the same intensity level, the bridge sustains a median value of 0.6 percent. Structurally speaking, these values may seem to correspond to acceptable performance for a 2 percent in 50 year S_a value. In terms of repair costs that can be expected with a probability of 2 percent in 50 years, the RC bridge was found to have a value of approximately \$6800. The downtime expected with a probability of 2 percent in 50 years was less than 1 day. Code-conforming RC bridges therefore seem to perform quite well then, with low expected repair costs and almost no expected downtime. This level of performance may be adequate for an ordinary bridge, but a bridge with a higher importance may require even greater expected performance.

The results from the baseline analysis provide an assessment of the performance of the UBPT system relative to the RC system. This quantitative performance assessment can be used to decide whether the use of the UBPT system is warranted. If a given highway bridge does not have a high traffic volume or is in an area that is not highly populated or traveled, it may not considered of great importance in the transportation network. In this case, the use of the UBPT would not be necessary, as the expected repair costs between the two systems would be similar, and the downtime of the bridge following an earthquake would not be critical. The additional up-front costs of the UBPT system would therefore not be warranted. However, in the case of a highly traveled bridge in a key location, a significant downtime for replacement could be a crucial blow to the transportation network in that area, and the social effects could be devastating. In this situation, the use of UBPT columns would be desired.

The power of the PEER PBEE assessment methodology is demonstrated in this study, in that a quantitative comparison is made between two competing structural systems. This quantitative comparison allows for more informed decision-making that incorporates post-earthquake functionality and operability. The benefits of the UBPT system are also demonstrated here, not only in terms of engineering response (i.e., reduced residual displacements), but in terms of response that is related to impact on structure owners and to society in general (i.e., reduced structure downtime and reduced disruption to the transportation network). The results presented to this point are therefore useful in themselves; however, to provide further insight into the PEER methodology and its use, additional analyses were performed to determine the sensitivity of the final results to some of the many assumptions made in the PEER analysis.

5.7.2 Sensitivity Analysis

To determine the sensitivity of the final results to the assumptions made in the various portions of the analysis, the analysis was performed again using alternate assumptions.

5.7.2.1 Sensitivity in Hazard Analysis

The integration of the four steps was repeated using the Boore et al. (1997) attenuation relationship in the PSHA rather than the Abrahamson and Silva (1997) model. Recall from Section 5.3.1 that the S_a hazard curve produced using the Boore et al. attenuation relationship was considerably lower at a given value of IM than that of the Abrahamson and Silva model. The repair cost and downtime hazard curves for the two bridge systems are shown in Figure 5.29 and Figure 5.30, respectively, where RC and UBPT refer to the baseline analysis and RC-Sens and UBPT-Sens refer to the analysis using the Boore et al. attenuation relationship.

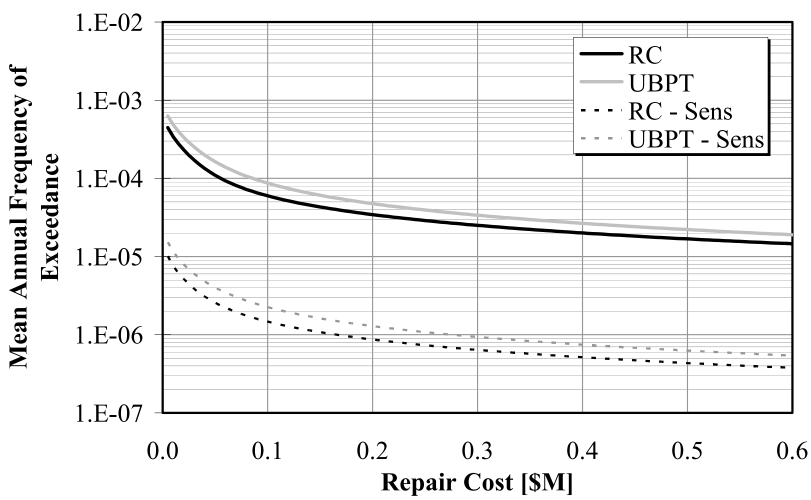

Fig. 5.29 Repair cost hazard curves showing sensitivity in hazard analysis.

The figures show that the actual magnitudes of the values of the loss hazard curves are highly sensitive to the attenuation function that is chosen in the PSHA. The lower intensities of the IM hazard curve in the Boore et al. (1997) attenuation relationship translate into significantly lower loss hazard values. If the goal of the analysis is to generate absolute predictions of downtime or repair cost values for the two systems, then the sensitivity to the chosen attenuation relationship in the PSHA should be noted as being quite large. However, if the goal of the analysis is simply to provide a comparison between the two systems, then the relative difference in the two systems between the two different attenuation relationships remains similar.

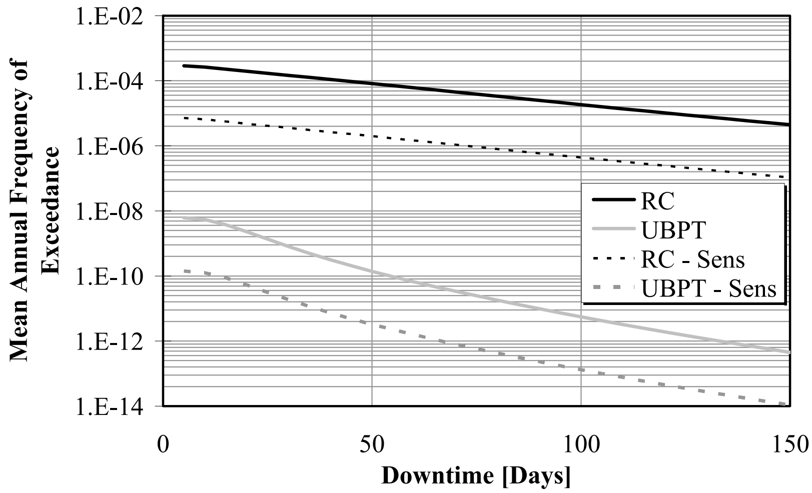

Fig. 5.30 Downtime hazard curves showing sensitivity in hazard analysis.

5.7.2.2 Sensitivity in Structural Analysis

The integration of the four steps was performed using the alternate IM, S_{di}, in the analysis while holding all of the other baseline parameters constant. Recall that the baseline analysis used S_a as the IM for scaling of ground motions in the IDA. Recall also that the dispersion in EDP was lower using S_{di} rather than S_a. Therefore it was expected that the resulting repair costs and downtimes using S_{di} would be less conservative than those using S_a as the IM. The repair cost and downtime hazard curves for the RC and UBPT bridges using S_{di} as the IM in the analysis are shown in Figure 5.31 and Figure 5.32, respectively, where in the legend *RC* and *UBPT* refer to the baseline analysis and *RC-Sens* and *UBPT-Sens* refer to the analysis using S_{di} as the IM.

The cost hazard curves for the two systems are not highly sensitive to the choice of IM, but the downtime hazard curves are fairly sensitive to it. The downtime hazard curves using S_{di} are slightly lower (i.e., lower mean annual frequency of exceedance for a given value of downtime) than those using S_a. Using S_a as an IM provides an overly conservative estimate of the downtimes or losses because the dispersion in the EDP results is larger. If S_{di} is used, the dispersion in the EDP is reduced and the unnecessary conservatism found in the results using S_a can be reduced.

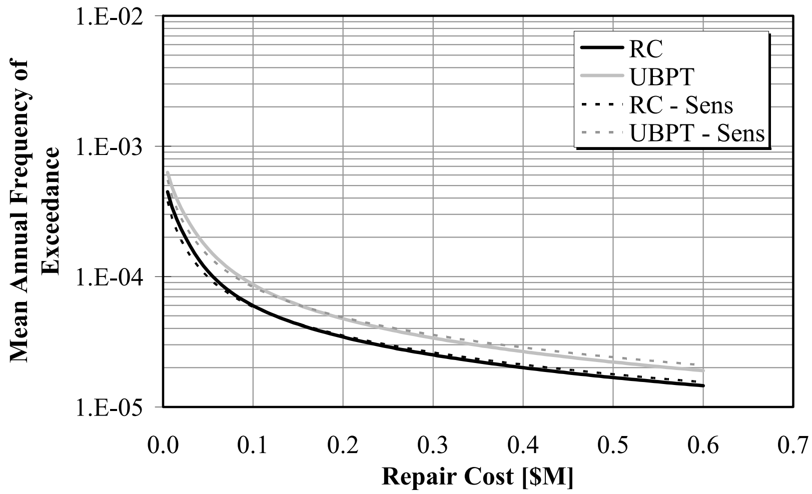

Fig. 5.31 Repair cost hazard curves showing sensitivity in IM used for IDA.

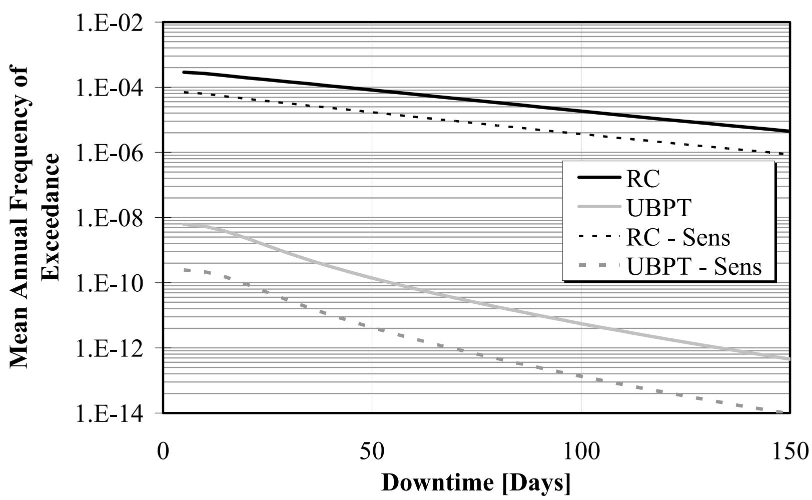

Fig. 5.32 Downtime hazard curves showing sensitivity in IM used for IDA.

5.7.2.3 Sensitivity in Damage Analysis

The integration of the four steps was performed again using different values to define the fragility curve for the damage state of replacement-level residual displacement. In the baseline analysis, the limiting residual drift ratio value was assumed to be 1.5 percent. In the sensitivity analyses, the limiting drift ratio value was changed to 1.25 percent and to 1.75 percent. Because the cost hazard curves were based on empirically developed fragility curves (i.e., for spalling and bar buckling), the sensitivity of the cost hazard curves was not investigated. The downtime hazard curves considering the different values of limiting drift in the fragility curve are shown in

Figure 5.33. The results from the baseline analyses are shown with solid lines, and the results from the sensitivity analyses are shown with dashed lines and described in the legend.

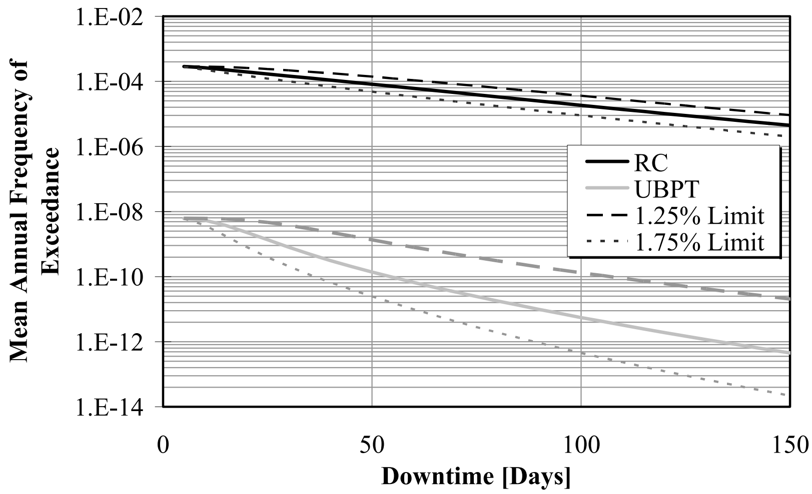

Fig. 5.33 Downtime hazard curves showing sensitivity in residual drift fragility curve.

The sensitivity of the downtime hazard curve to the assumed limiting residual drift value appears greater for the UBPT bridge than the RC bridge. The relative difference between the baseline curve with the curve considering the alternate drift limits is larger for the UBPT bridge. However, the absolute difference between the baseline curve and the curve considering the alternate drift limits is lower the RC bridge. The mean annual frequency of exceedance values for the UBPT bridge are lower than 10^{-8}, so any change in value is still several orders of magnitude below those of the RC bridge. For the RC bridge, considering a downtime of 30 days, the change in the drift limit for the fragility curve from the baseline value of 1.5 percent to 1.25 percent results in a change of mean annual frequency of exceedance from 1.5×10^{-4} to 2.2×10^{-4}. This is equivalent to a change from 0.7 percent to 1.1 percent in 50 years, which is not overly large. Comparatively speaking, even considering the possible differences in the actual values given the sensitivity in the assumed fragility curve, the RC bridge still performs much more poorly than the UBPT bridge, seeing much higher mean annual frequency of exceedance values for a given downtime value.

5.7.2.4 Sensitivity in Loss Analysis

The integration of the four steps was performed again using different values for the mean downtime loss values for the damage state of replacement-level residual displacement. Recall that in the baseline analysis, the mean value of the downtime for the RC bridge in this damage state was assumed to be 75 days based on Hazus, and the mean value of the downtime for the UBPT bridge was assumed to be 20 percent higher, i.e., 90 days. In the sensitivity analyses, the mean values for both the RC and UBPT bridges were changed by 20 percent, i.e., to 60 and 90 days for the RC bridge and 72 and 108 days for the UBPT bridge. The downtime hazard curves considering the different values of mean downtime are shown in Figure 5.34. The results from the baseline analysis are shown with solid lines, and the results from the sensitivity analyses are shown with dashed lines.

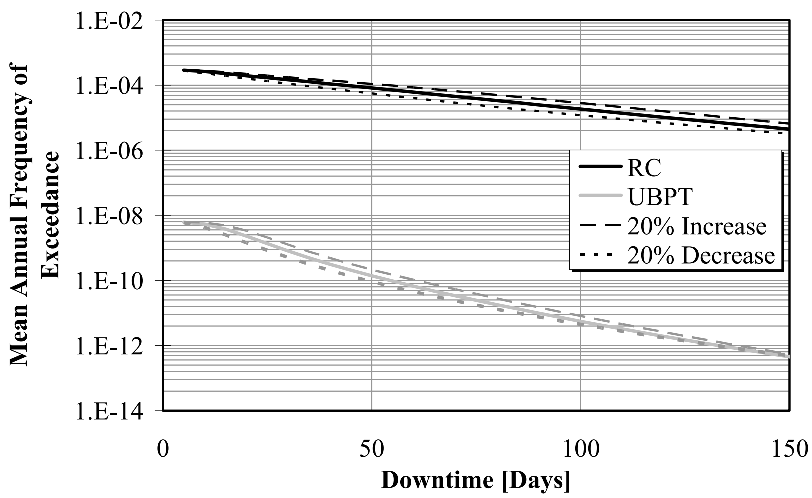

Fig. 5.34 Downtime hazard curves showing sensitivity in residual drift fragility curve.

The downtime hazard curves are not sensitive to changes in the assumed mean downtime for the damage state. The relative difference between the two systems remains similar. The results also show that high levels of accuracy may not be necessary in modeling of losses as compared to the other portions of the analysis, such as the damage/fragility analysis, particularly when a relative comparison between two systems is sought.

5.7.2.5 Summary of Sensitivity Study

To assess the overall sensitivity of the final results to the various assumptions in the four major portions of the PEER PBEE assessment, the results from the preceding sections were compared together. To determine the sensitivity in each of the four parts, the mean annual frequency of exceedance values were compared at a given value of downtime, namely 30 days. The value of 30 days was chosen arbitrarily, as a reasonable time period (roughly one month) that would be considered extremely detrimental to the transportation network. The values are shown in the form of a tornado diagram, similarly to the results of the FOSM analysis of Sections 5.4.6 and 5.4.7. That is, the value of the baseline analysis is shown with a vertical line, and the values from the sensitivity analyses are shown for each of the different portions. The tornado diagrams are shown for the RC and UBPT bridges in Figure 5.35 and Figure 5.36, respectively. In these plots, the scales in the figures for the RC and UBPT bridges differ. The purpose of these two plots is to show the relative magnitudes of the sensitivity to the assumptions *within* a system, while the comparison *between* systems will be considered following this.

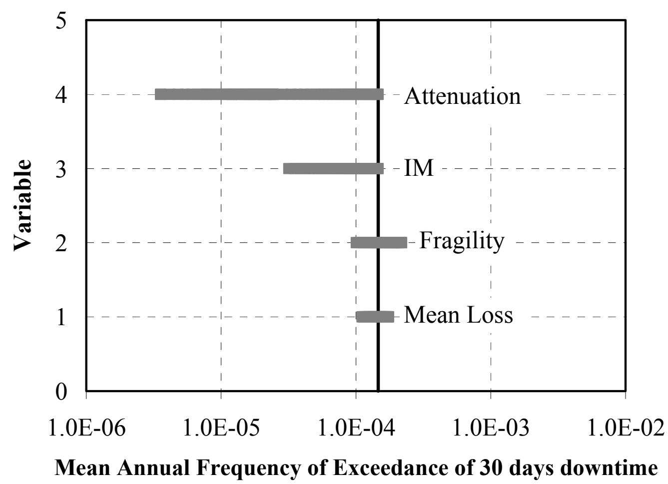

Fig. 5.35 Sensitivity of mean annual frequency of exceedance of 30 days downtime to assumptions in PBEE analysis for RC bridge (log scale).

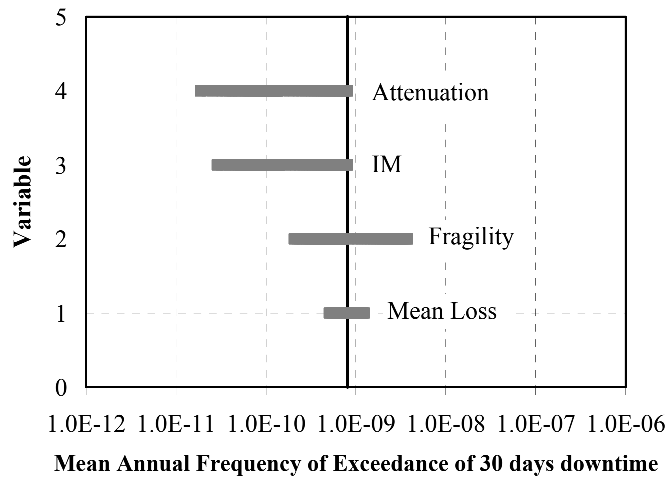

Fig. 5.36 Sensitivity of mean annual frequency of exceedance of 30 days downtime to assumptions in PBEE analysis for UBPT bridge (log scale).

It is difficult to directly compare the sensitivities of the various portions of the analysis, as the changes in analysis that were performed to determine the sensitivity study in each of the portions is not directly related. For example, changing the IM from S_a to S_{di} does not have a directly comparable analog in the loss sensitivity, where the mean loss value was changed (in this case by 20 percent) to evaluate sensitivity. However, for the sake of examining general trends, the sensitivity study considers plausible differences in the choices that can be made in performing the analysis. For example, it is possible that the Boore et al. (1997) model may be chosen for the PSHA as opposed to the Abrahamson and Silva (1997) model, and that the mean losses may differ from the true value by around 20 percent. It is less likely, however, that the losses will differ from the true value by 80 or 90 percent. Therefore, the comparisons made between the different portions of the analysis are assumed to be general trends and the absolute differences in values are not considered.

In both bridge systems, the mean annual frequency of exceedance for the downtime loss is most sensitive to the attenuation relationship chosen for the PSHA. In both systems, the sensitivity in the attenuation relationship is followed by the choice of IM, the sensitivity in the fragility function, and the sensitivity in the assumed mean downtime losses. For the choice of IM, the use of S_{di} for the RC bridge leads to a reduction in mean annual frequency of exceedance because of the reduction in dispersion in the EDP. The effect of reducing dispersion in the EDP is larger than that of the assumed differences in the fragility curve as well as the assumed differences in downtime loss.

In Figures 5.37 and 5.38, the same results from the sensitivity analyses shown in Figures 5.35 and 5.36 are shown, but at the same scale level. In this way, the results can be compared between the two bridges. Considering the absolute values of the results, the mean annual frequency of exceedance values from the sensitivity analyses vary more from the baseline analysis in the RC system than the UBPT systems. This larger variation in the RC system is because the UBPT bridge has such a low probability of exceeding 30 days of downtime that any reasonable changes in the assumptions still lead to very low values. Had the UBPT system had similar baseline values to the RC system, a comparison of the difference in sensitivity of the two systems to the different portions of the PEER analysis could have been made. However, because the values for the UBPT system are so much lower, it is difficult to make a comparison to the values from the RC system.

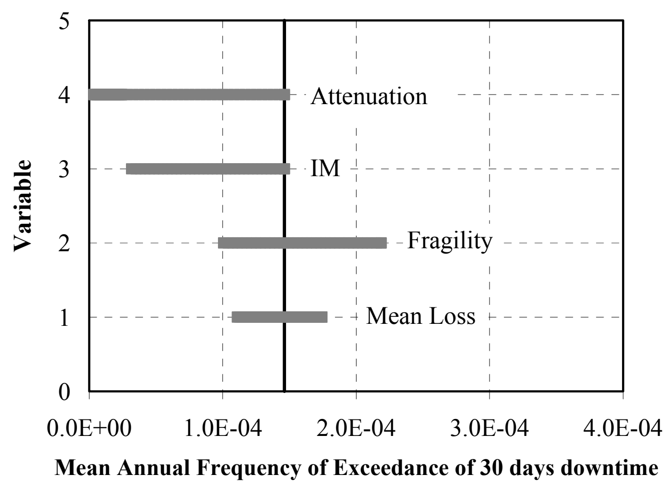

Fig. 5.37 Sensitivity of mean annual frequency of exceedance of 30 days downtime to assumptions in PBEE analysis for RC bridge (non–log scale).

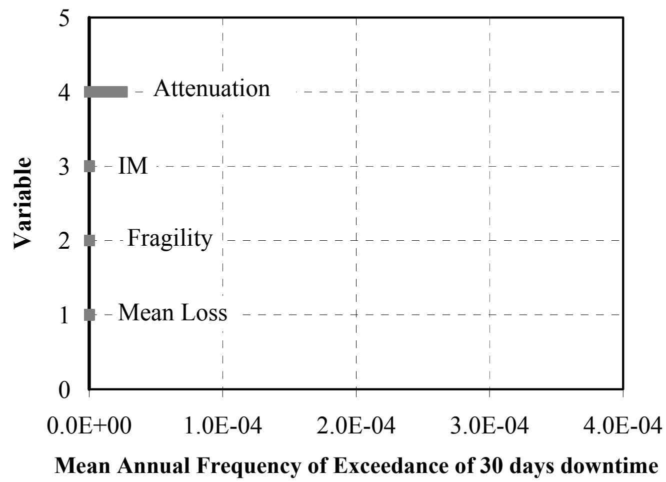

Fig. 5.38 Sensitivity of mean annual frequency of exceedance of 30 days downtime to assumptions in PBEE analysis for UBPT bridge (non–log scale).

In general, the results give valuable insight into the relative magnitudes of the uncertainties in the four portions of the analysis to the overall results. For example, although ground motion uncertainty is generally considered to be the largest contributor to overall uncertainty in such types of analyses, it is helpful to see a verification of this using realistic structures. Areas that are most sensitive to the assumptions may warrant more study to reduce uncertainty. The relatively large sensitivity to the IM shows that research in improved IMs can be more beneficial to reducing uncertainty in the results and is therefore a worthwhile direction of study.

5.8 SUMMARY OF PBEE ASSESSMENT

Reinforced concrete highway bridges designed by current seismic design codes are expected to undergo large inelastic deformations in their columns during earthquakes, leading to possibly large residual deformations and therefore reduced post-earthquake functionality. A system for providing self-centering to the columns through the use of vertical, unbonded post-tensioning is proposed for use in highly seismic regions to improve post-earthquake functionality. Two benchmark highway bridge structures, using either conventional or self-centering technology, were modeled and evaluated quantitatively using a probabilistic, performance-based earthquake engineering assessment methodology.

From the structural analyses, the bridge with self-centering columns was found to perform well, sustaining similar peak drift demands as compared to the bridge with conventional columns but with significantly reduced residual deformations. A study was performed using the FOSM method (Baker and Cornell 2003a, 2003b) to evaluate the additional uncertainty due to assumptions made in the structural modeling. The results from the analyses showed that the structural response was not highly sensitive to assumptions made in the modeling, and was found to be true regardless of the IM used.

After integrating all four steps of the PEER analysis, the UBPT bridge was found to have similar but slightly higher expected repair costs than the RC bridge, due to the fact that the bridges had similar peak drift responses. The reduced residual displacements in the UBPT bridge, however, were found to translate into significantly reduced expected downtime losses that would normally arise due to the required demolition and replacement of permanently deformed columns. The conventional RC bridge was found to perform well, and had a relatively low probability of exceeding a moderate amount of downtime. For example, for a downtime of 30 days, the mean annual frequency of exceedance for the RC bridge corresponded to a 0.7 percent probability in 50 years. The value for the UBPT bridge was essentially zero. This might be considered adequate for an ordinary bridge, but may be considered too high for an important, highly traveled bridge.

The sensitivity in a number of assumptions made throughout the PBEE assessment was studied, by systematically varying a number of parameters within the four portion of the analysis. The assumed attenuation relationship in the PSHA was found to have the largest effect on the final results for both bridge systems. The final results were next most sensitive to the choice of IM used in the analysis. Finally, the results were found to be least sensitive to the assumptions in the mean downtime losses.

In the next chapter, additional technologies are considered for further improving the post-earthquake performance of the bridge columns. Namely, the use of highly ductile, damage-tolerant fiber-reinforced cementitious composite materials are proposed for use in the columns to reduce damage due to cracking and spalling and for providing additional confinement against buckling of longitudinal reinforcing bars. The system will be assessed using the PEER PBEE assessment methodology as in this chapter, and will then be compared against both the conventional RC and UBPT bridges.

6 PBEE Assessment of Enhanced-Performance UBPT Bridges

6.1 INTRODUCTION

In Chapter 5, the post-earthquake performance of a benchmark reinforced concrete highway bridge with self-centering, UBPT columns was compared to that of the same bridge with conventional RC columns. The comparison was performed using the PEER PBEE assessment methodology. With increasing earthquake intensity, the bridge with UBPT columns was found to sustain significantly lower residual deformations than the bridge with RC columns, leading to substantial reductions in expected downtime. The peak drift responses of the two column systems were found to be similar, which led to similar levels of expected repair costs due to drift related damage. To reduce expected damage further and thereby further reduce future repair costs, the use of enhanced-performance technologies are proposed in addition to the UBPT. The proposed systems are (1) using damage-tolerant cementitious materials rather than ordinary concrete and (2) providing a steel jacket to the column with ordinary concrete.

6.1.1 Hinge Regions Made with Engineered Cementitious Composites

To minimize damage in the columns due to spalling and cracking, and to delay buckling of longitudinal reinforcing, the use of a highly ductile, damage-tolerant fiber-reinforced cementitious composite material is proposed. Specifically, the material proposed for use is engineered cementitious composites (ECC, discussed in Chapters 2 and 3), a composite that contains Portland cement, fly ash, fine sand, high aspect ratio, and high-modulus polymeric fibers at a 2 percent volume fraction. The ECC has a high tensile strain capacity relative to traditional cement-based materials and is resistant to spalling. Although this material currently will have a higher initial cost than concrete, its use may be warranted by its improved response when subjected to cyclic loading, which has been well documented (e.g., Billington and Yoon 2003, Rouse and Billington 2003).

ECC does not undergo localized cracking immediately upon reaching its cracking strength, but rather forms multiple, fine cracks under continued tensile loading. The fact that large cracks do not localize prevents large strains from localizing in the steel reinforcing in these locations, thus delaying steel fracture. These fine cracks also slow the ingress of moisture that can lead to corrosion. Aesthetically, small cracks are also an improvement over large, unsightly cracks.

In addition to the improved tensile behavior of the ECC relative to concrete, the compressive behavior is expected to significantly reduce the damage in the columns. Recall from Chapter 2 that ECC is a self-confining material and does not spall in compression. The fact that the ECC does not spall entirely eliminates one of the damage states requiring repair in the columns made of concrete only. In addition, because the ECC does not spall and hence continues to provide confinement to the longitudinal reinforcing bars, the buckling of bars in compression (the second damage state) can be delayed.

Due to the higher initial cost of the ECC with respect to concrete, it is proposed for use only in the areas where the impact of its use would be most beneficial, namely in the potential plastic hinging zones. In the columns of the benchmark bridge in this study, which deform in single curvature, the plastic hinging zones are expected at the bases of the columns. In this chapter, the same benchmark bridge is analyzed, with the exception that the columns will now incorporate ECC in the hinges in addition to UBPT for further reduction to damage during earthquake loading.

6.1.2 Hinge Regions with Steel Jackets

The second system, proposed by Sakai et al. 2005, incorporates the use of a steel jacket to provide confinement and hence added ductility to the columns. Steel jackets are thin circular plates that are typically welded together at the bases of existing columns for retrofit. The use of a steel jacket can eliminate the damage state of cover spalling by providing confinement to the entire section. In addition, buckling of longitudinal reinforcing should also be prevented by the use of the steel jacket. The jacketing is designed to provide passive confinement only, and not to add any flexural strength to the column (Priestley et al. 1996). This type of behavior is achieved by using a jacket with a radius slightly larger than that of the column, and then filling the resulting gap with grout, as shown in Figure 6.1. Because the flexural strength is not increased, the lateral response of the jacketed column should be similar to that of an unjacketed column, but with reduced damage. The combination of jacketing with UBPT has been shown to be successful in experimental shaking table tests (Sakai et al. 2005). In their study, the jacket thickness was proportioned to provide a similar level of confinement to that of the spiral reinforcing. The same proportioning is used for the jacketed columns in this study.

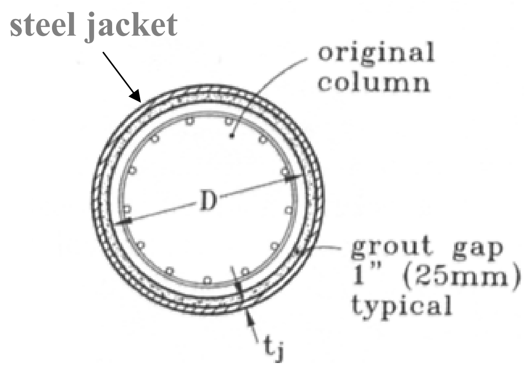

Fig. 6.1 Steel jacket for circular reinforced concrete column (adapted from Priestley et al. 1996).

6.2 PBEE ASSESSMENT

The two enhanced performance bridge column systems are analyzed using the PEER PBEE assessment and their performance is compared to that of the benchmark bridge with RC columns and UBPT concrete columns. Only the portions of the analysis that differ from the analyses of Chapter 5 will be discussed in detail. In this chapter are a description of the modeling and analyses performed for the PBEE assessment and the conclusions drawn from them. Sensitivity studies are not performed, and the two bridge systems are compared against the baseline analyses of Chapter 5.

6.2.1 Hazard Analysis

The site for the bridge was located in Oakland, California, with a latitude and longitude of 37.80 N x 122.30 W. The PSHA and resulting hazard curve was obtained from Tothong (2006). The

IM used in the analysis was spectral acceleration at the first-mode period (S_a). The S_a hazard curve for the site at a period of 1 sec is shown in Figure 6.2. A total of 17 ground motions were used for the dynamic analyses. The ground motions set was compiled by Somerville and Collins (2002), with additional ground motions from Tothong (2006) added. The ground motions are given in Table 5.1 of Chapter 5.

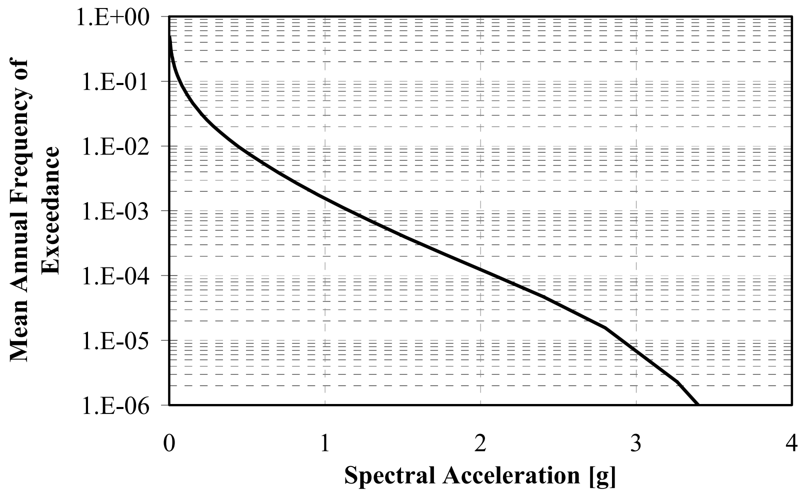

Fig. 6.2 Hazard curve for spectral acceleration for Oakland site.

6.2.2 Structural Analysis

6.2.2.1 Model of Baseline Bridge with UBPT-ECC Columns

Aside from the columns, the bridge model was the same as the models described in Section 5.4. A schematic representation of the column model is shown in Figure 6.3. Each column is modeled with a single, concentrated plasticity fiber beam-column element (*BeamWithHinges3* element). The length of the ECC hinge used was the plastic hinge length computed according to Caltrans SDC (2003). The cracked stiffness values for the elastic region of the beam were computed using Caltrans SDC (2003) guidelines, as described in Section 4.2.2. The concrete in the remainder of the column was assumed to have an unconfined compressive strength of 55.2 MPa (8 ksi). As only elastic properties are required for the segment of the beam that is outside of the hinges, only an elastic modulus for the concrete was required. The elastic modulus was computed using the ACI equation for normal weight concrete (given in Section 3.2.4) as 24.8 GPa (3600 ksi). The columns are assumed fixed at the bases.

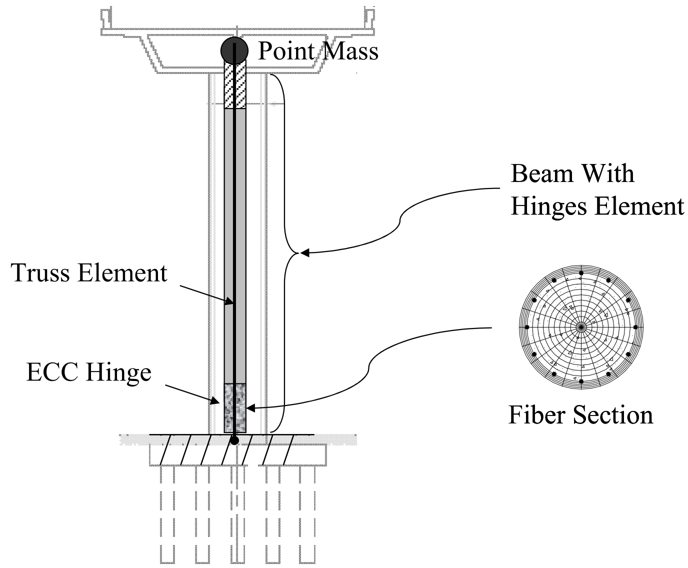

Fig. 6.3 Schematic representation of column model.

The bonded mild steel reinforcing was assumed to have a yield strength of 469 MPa (68 ksi). This value is given in the Caltrans SDC (2003) as the *Expected Yield Strength* of Grade 60 reinforcing steel. The stress-strain relationship for the bonded mild steel reinforcing was assumed to follow the Giuffre-Menegotto-Pinto model (Taucer et al. 1991), which incorporates the Bauschinger effect for cyclic loading. The *Steel02* model in OpenSees was used for the reinforcing steel. Strain hardening at 2 percent of the initial elastic modulus was assumed for the model. A co-rotational truss element was used to model the PT tendon and an elastic model (*ElasticPP* material model with a very large yield strain) was used with an initial strain value to apply the prestress. An initial prestress of 690 MPa (100 ksi) was assumed, which was intentionally selected to be low to prevent any yielding of the PT tendon.

The ECC is modeled using the Han et al. (2003) model modified with the compressive envelope modified using the Popovic's curve (1973), as discussed in Section 3.2.4. The general stress-strain behavior for the ECC is shown in Figure 6.4. The tensile behavior is trilinear, with linear behavior to first cracking, followed by a linear hardening phase and concluding with a linear softening phase. The model includes polynomial unloading and linear reloading in both tension and compression as seen in material testing of ECC materials. To use this model in the analyses, the constitutive behavior was coded as a Uniaxial Material Model for use in OpenSees. The source code is given in Appendix A, and a full description of the implementation of the model can be found in Han et al. (2003).

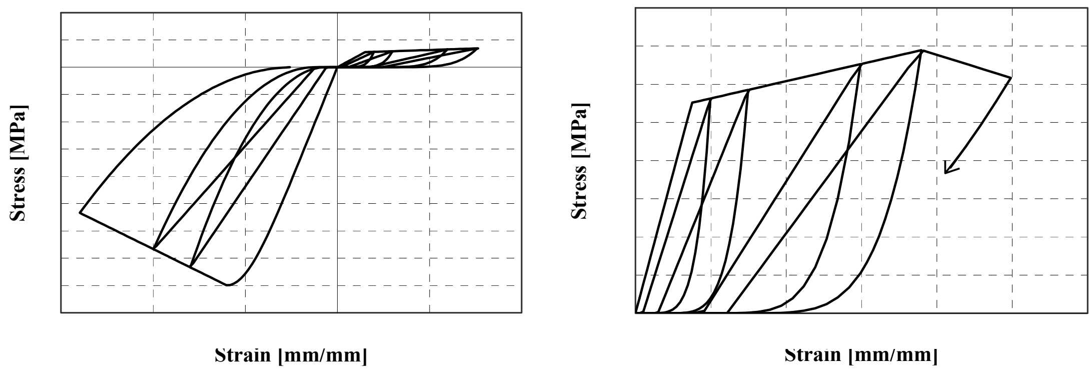

(a) (b)

Fig. 6.4 Constitutive behavior of ECC: (a) full behavior and (b) tensile behavior.

The selected tensile material parameters for the ECC are based on Douglas and Billington (2006), who performed cyclic experimental testing on cylindrical specimens of ECC with PVA fibers. The tensile parameters are as follows: first cracking stress of 1.4 MPa (200 psi), peak tensile strength of 2.1 MPa (300 psi), peak tensile strain of 0.005 mm/mm, and ultimate tensile strain of 0.02 mm/mm. The unconfined peak compressive strength and strain were assumed to be 48 MPa (7 ksi) and 0.004 mm/mm respectively. These values are lower than the values that are often reported for ECC based on thin, plate-like specimens. The values from Douglas and Billington (2006) are used because they are based on cylindrical specimens rather than thin specimens, and are therefore expected to be more representative of the ECC in structural applications. The peak compressive stress and strain are increased for confining effects from the spiral reinforcing, and are computed using the Mander (1987) model assuming that it is applicable to ECC. Recall also that the compressive modulus of ECC is roughly 40 percent of a concrete of a similar compressive strength.

The ECC is assumed as a direct replacement for concrete in the hinge of the column. Because of the self-confining effect and inherent ductility that is expected in the ECC under compression, the spiral reinforcing is reduced from the amount used in the concrete UBPT column (i.e., #8 spirals at a spacing of 8.26 cm) to the amount used in the RC column (i.e., #7 spirals at a spacing of 8.26 cm). Even further reductions in spiral reinforcing are likely possible with the ECC due to its self-confining nature, but are not considered at this time.

A cyclic analysis was performed on the UBPT column with ECC in the hinge (herein referred to as the UBPT-ECC column). The response is compared with that of the RC and UBPT columns in Figure 6.5. The behavior of the UBPT-ECC column is quite similar to that of the

UBPT column. The initial stiffness of the UBPT-ECC column is roughly 25 percent lower than that of the concrete UBPT column. This reduction in stiffness is expected because of the lower elastic modulus of the ECC as compared to the concrete. Following yielding, the capacity of the column is roughly 80 kN higher than that of the RC and UBPT columns; this is due to the additional contribution of the tensile strength of the ECC to the capacity of the column. This increase in peak flexural strength of the column provided by the ECC is not significant, and is therefore not expected to be problematic for other bridge elements that are capacity-protected.

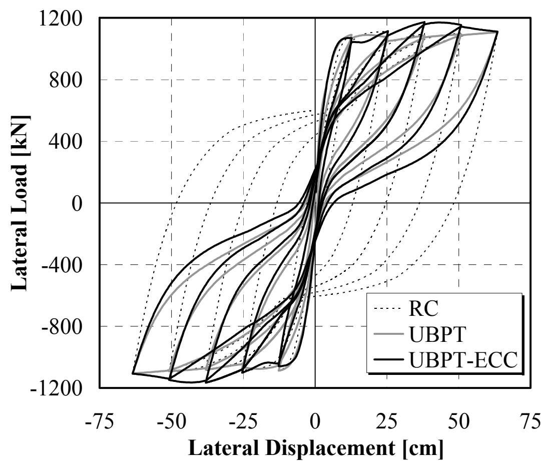

Fig. 6.5 Cyclic behavior of UBPT-ECC column compared to RC and UBPT columns.

6.2.2.2 Model of Baseline Bridge with UBPT-Steel Jacket Columns

The model of the UBPT-Steel Jacket columns was almost identical to that of the UBPT column. Recall that the steel jacket provides only passive confinement to the column and is not intended to contribute significantly to the flexural strength. In addition, the jacket thickness is chosen in this study to provide equivalent confinement to that of the spiral reinforcing. Steel jacketing is assumed to be equivalent to continuous hoop reinforcing (Priestley et al. 1996). Therefore when modeling the UBPT column with steel jacketing, the same model is used as that of the UBPT columns in Chapter 5, except that the cover fibers that had previously been modeled with an unconfined concrete model are now modeled with the confined concrete model. The remainder of the model is unchanged. Therefore, the lateral behavior of this bridge with UBPT columns with steel jacketing is expected to be similar to that of the bridge with UBPT columns without the jacketing.

The cyclic behavior of the UBPT concrete column with steel jacketing (herein referred to as the UBPT-steel jacket system) is shown in Figure 6.6 compared with the RC and UBPT columns. Because the cover concrete is no longer unconfined in the UBPT-Steel Jacket but is now confined changes the behavior of the column somewhat. The stiffness of the column after yielding is increased as compared to the UBPT column. This leads to higher forces in the UBPT-Steel Jacket column at higher drifter levels. At a drift of 50 cm, the force in the UBPT-Steel Jacket column is roughly 15 percent higher than that of the UBPT column. This slight increase in post-yield stiffness is not expected to significantly change the dynamic response of the bridge. In addition, the increase in flexural strength is again not expected to affect other capacity-protected elements in the bridge.

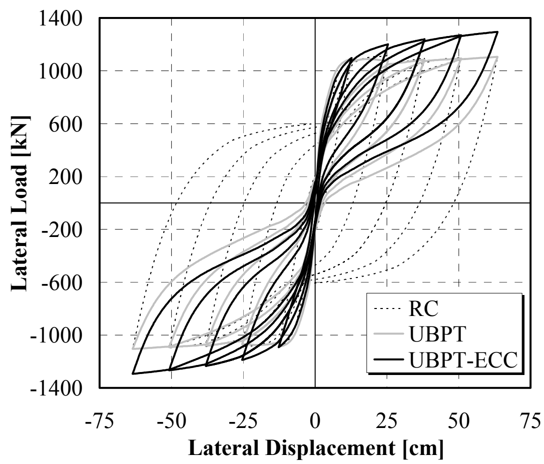

Fig. 6.6 Cyclic behavior of UBPT-Steel Jacket column compared to RC and UBPT columns.

6.2.3 Analysis Procedure

The dynamic analyses were performed using the Newmark method with average acceleration. Damping was applied using Rayleigh damping with a damping ratio of 2 percent. An additional 10 sec of free vibration (analysis with input acceleration of zero) was performed following the end of each record to allow the bridge to come to rest such that residual displacements could be recorded. Geometric nonlinearity was included in the analyses.

The dynamic analysis was performed using the fault-normal and fault-parallel components of motion for each ground motion record. In the analyses, the fault-normal component (the more severe of the two components) was applied in the transverse direction of the bridge, as motion in the longitudinal direction was expected to be more limited due to the abutments. The motions were scaled based on the fault-normal component of motion, and the same scale factor was applied to the fault-parallel component of motion, as recommended in Somerville and Collins (2002).

The incremental dynamic analyses (IDA) were performed at seven different S_a intensity levels. Three of the intensity levels corresponded to the hazard levels of 50%, 10%, and 2% in 50 years, based on the baseline hazard curve (i.e., using the Abrahamson and Silva (1997) model) presented in Section 6.2.1. Three other intensity levels were chosen in between these values to provide additional information at these intermediate intensity levels. A final intensity level greater than the 2% in 50 year level was also chosen. The intensity levels chosen for the IDA are shown in Table 5.2 of Chapter 5.

The two EDPs of interest in the structural analysis were again the peak drift ratio and the residual drift ratio at the tops of the columns. As the analysis was performed with two components of ground motion, two directions of movement exist for the columns. The total drift was calculated at each time step using both the transverse and longitudinal directions of motion by taking the square root of the sum of the squares of the two components. The peak drift was taken to be the peak value of this total drift and not the peak value in either the transverse or longitudinal direction alone. The peak was also taken as the maximum of all four columns, although the displacement responses of the four columns were very similar due to stiffness of the superstructure and the fact that the same acceleration history was applied uniformly to the bases of all of the columns.

6.2.4 Results from Incremental Dynamic Analysis

The peak and residual drifts ratios from the IDA are shown for the UBPT-ECC and UBPT-Steel Jacket bridges in Figures 6.7 and 6.8. The resulting EDP values for each ground motion are shown at each intensity level. The computed median values (assuming that the EDP values are log normally distributed) are shown with a solid line and the plus and minus one standard deviation values are shown with dashed lines. The results appear similar to those of the UBPT bridge (compare with Figures 5.6 and 5.7). The peak drifts are on the same order as those of the UBPT bridge, and the residual drifts are again minimal even at high S_a intensity levels.

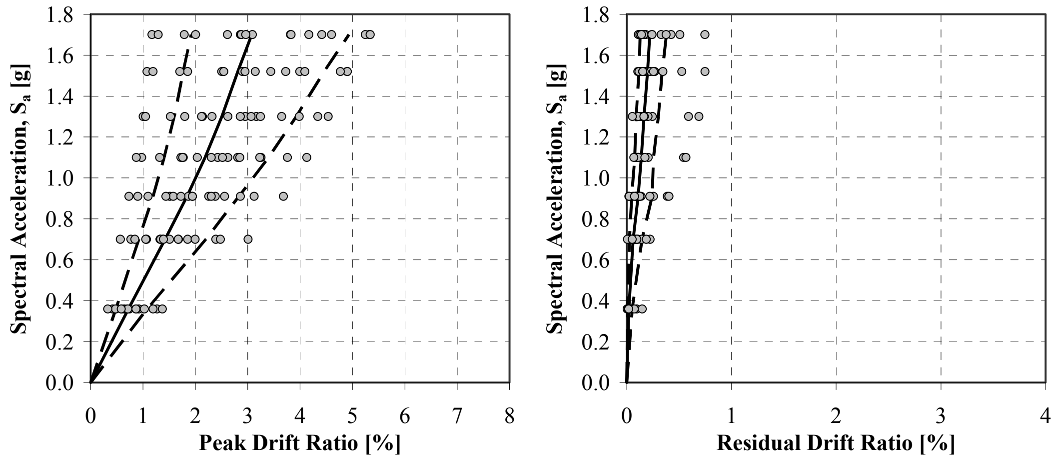

(a) (b)

Fig. 6.7 IDA results for (a) peak and (b) residual drift ratio for UBPT-ECC bridge.

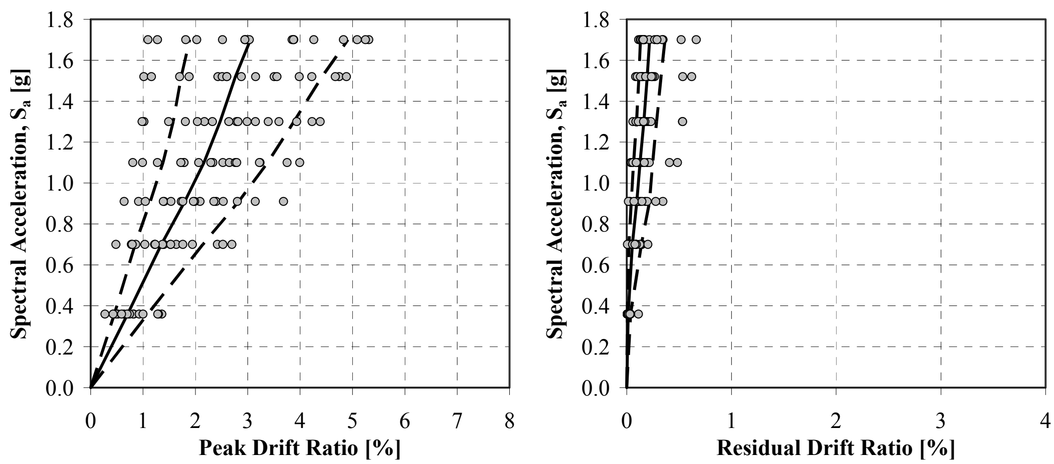

(a) (b)

Fig. 6.8 IDA results for (a) peak and (b) residual drift ratio for UBPT-steel jacket bridge.

In Figure 6.9, a comparison is made between the peak drift ratios of the RC, UBPT-ECC, and UBPT-Steel Jacket bridges. As with the ordinary UBPT bridge, the peak drifts for the two new systems are close to that of the RC bridge for a given intensity level. At an intensity level of 1.52 g (corresponding to 2 percent in 50 years intensity), the median peak drift ratios for the UBPT-ECC and UBPT-Steel Jacket columns are 2.81 and 2.76 percent, respectively. Both of these are slightly greater than the ordinary UBPT columns. The fact that the UBPT-ECC columns had larger peak drifts was expected due to the lower stiffness arising from the ECC in the hinges. The UBPT-Steel Jacket was expected to have slightly lower peak drifts than the ordinary UBPT column because it is slightly stiffer; however, the difference in median peak drift is minimal.

In terms of residual displacements, the two UBPT columns again show significantly reduced residual displacements as compared to the RC column. At the 2 percent in 50 years level IM of 1.52 g, the median residual drift ratios for the UBPT-ECC and UBPT-Steel Jacket columns are both 0.22 percent, which is roughly 30 percent of the median value for the RC column. The standard deviations on the values are much lower than that of the RC bridge however, and the UBPT-Steel Jacket has a slightly smaller standard deviation than that of the UBPT-ECC bridge.

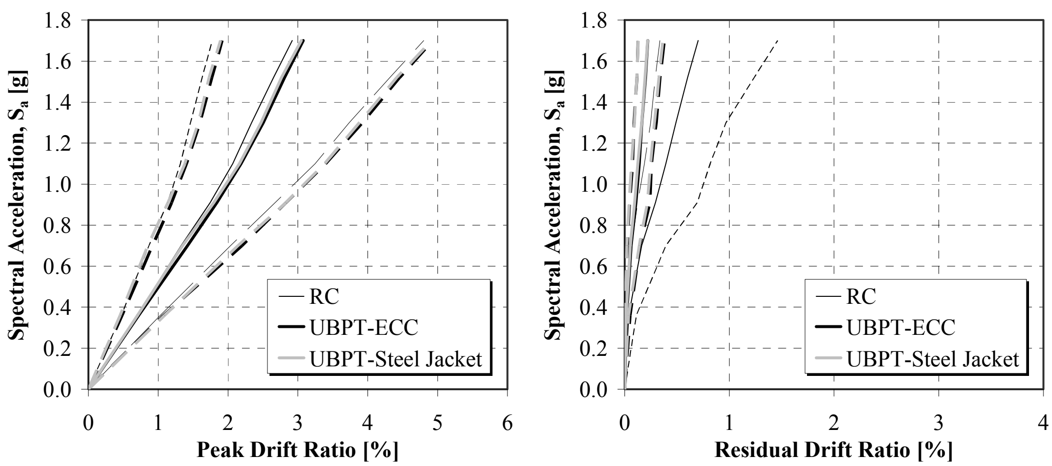

(a) (b)

Fig. 6.9 Comparison of (a) peak drifts and (b) residual drifts of UBPT-ECC and UBPT-Steel Jacket bridges with RC bridge.

6.3 DAMAGE ANALYSIS

For the UBPT column with steel jacketing, the damage states of spalling and bar buckling should be eliminated, leaving only the residual drift damage state. For the case of ECC, which does not spall in compression, the damage state of spalling no longer applies. This essentially eliminates the consideration of repair costs due to this damage state. For the damage state of buckling of longitudinal reinforcing, the fact that the ECC does not spall would presumably delay the drift at which buckling would occur. However, as the drift at which buckling would finally occur in an ECC column is unknown, it is conservatively assumed that the buckling would not significantly be delayed. Therefore the median bar buckling drift is kept the same as that of the UBPT column with plain concrete, i.e., 6.8 percent. Assuming a log-normal distribution, the fragility curve for the bar buckling for the UBPT-ECC column is shown in Figure 6.10.

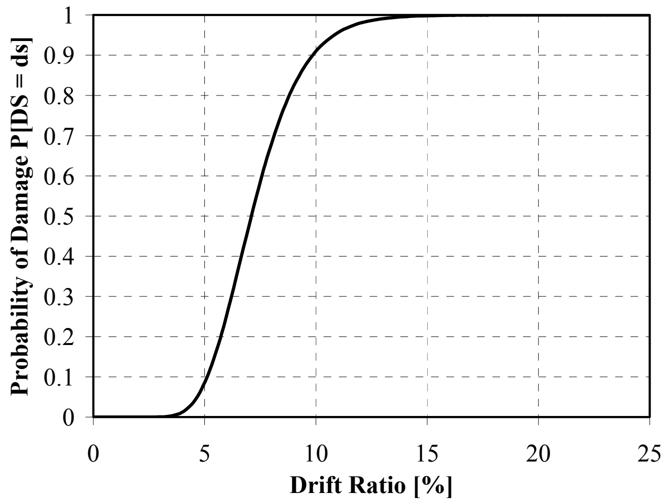

Fig. 6.10 Fragility curve for UBPT-ECC column for bar buckling damage state.

For the damage state of the replacement-level residual displacements, the fragility curve was again modeled with a linear function as in Section 5.5.2, using a limiting value of 1.5 percent based on the Japanese code for highway bridge design (Japan Road Association 2006). For residual drifts below this limiting value, the bridge may still be considered unusable due to the combination of some residual displacement and other observed damage in the bridge. The assumption is made that residual drifts greater than 1 percent may possibly still be considered large enough to warrant replacement depending on other damage in the bridge. Therefore a linear function was assumed for the fragility curve, and is shown in Figure 6.11.

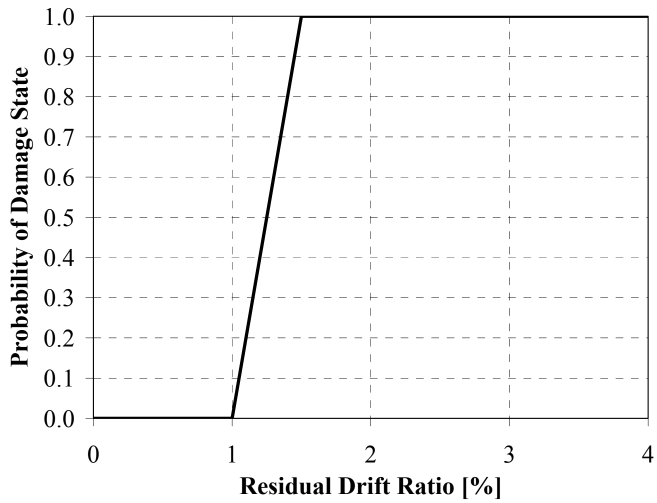

Fig. 6.11 Fragility curve for UBPT-ECC columns for damage state of replacement-level residual displacement.

6.4 LOSS ANALYSIS

For the two UBPT columns with ECC and steel jacketing, the damage state of spalling no longer exists, and therefore has no associated repair costs. For the damage state of buckling of longitudinal reinforcing (applicable only to the UBPC-ECC column), the repair actions required are assumed to be replacement of longitudinal and spiral reinforcing, and additional steel column casing based on Mackie et al. (2006), as discussed in Section 5.6. The cost of steel reinforcing is given to be $2 per kilogram, and the cost of steel column casing is given to be $2,000 per linear foot. Standard deviations of $0.20 and $200 for steel reinforcing and column casing, respectively, are assumed. To determine the total cost of repair of being in the damage state of buckling, assumptions must be made on the amount of steel reinforcing to be replaced and the amount of steel casing required. Mackie et al. (2006) propose values of 1562 kg of steel reinforcing to be replaced and 50 linear feet of steel casing required per column, which is adopted here. For four columns, the total cost of repairing the columns in the buckling damage state is assumed to be $412,500, with a standard deviation of $40,020.

For the damage state of excessive residual displacements, the mean downtime for a highway bridge in the *extensive* damage state is reported as 75 days with a standard deviation of 42 days. This value is for a standard bridge and likely would not apply to the UBPT columns, due to the additional time required for construction of the post-tensioned columns. Therefore, a higher value was assumed for the mean restoration time, with the same value of 42 days assumed for the standard deviation. The new value was assumed to be 20 percent higher than that of the RC bridge, i.e., 90 days, similarly to the UBPT column analyzed and presented in Chapter 5. The value was not assumed to be higher than that of the UBPT column because ECC can be mixed and placed in the same manner as ordinary concrete. Finally, the addition of the steel jackets to the columns is also not expected to add significantly to the overall construction time, and the value of 90 days was also used for the UBPT-Steel Jacket bridge.

6.5 INTEGRATION OF RESULTS: PBEE ASSESSMENT

The results from the four steps of the PEER analysis using the baseline assumptions were combined using the framing integral to generate repair cost and downtime hazard curves. The repair cost and downtime hazard curves for both bridges from the baseline analysis are shown in Figures 6.12 and 6.13.

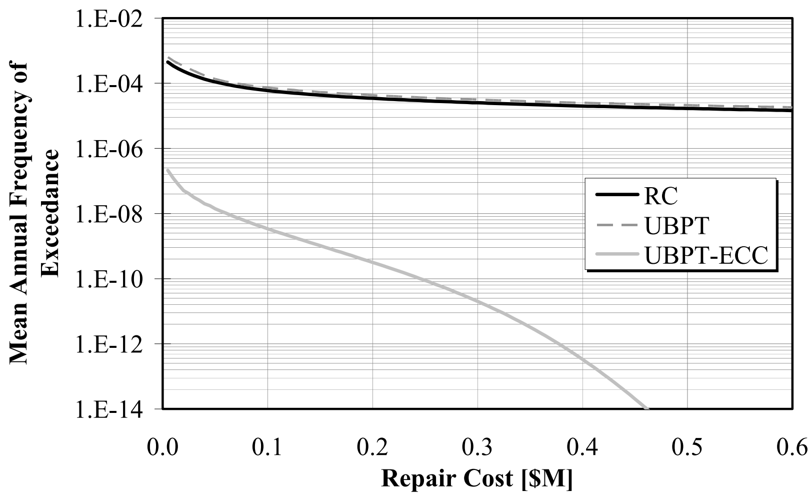

Fig. 6.12 Repair cost hazard curves from baseline analysis.

Recall from Chapter 5 that the UBPT bridge had similar expected repair costs (from spalling and bar buckling) to the RC bridge column. The reason for the similarity in repair costs is that those damage states are drift based, and the two column systems displayed similar peak drifts. Unlike the UBPT bridge, the UBPT-ECC has significantly lower mean annual frequency of exceedance values for a given repair cost than the RC because the damage due to spalling is no longer present for the UBPT-ECC column. Without the spalling damage, which has a relatively high likelihood of occurrence as compared to buckling, the expected repair costs are significantly reduced. For example, for a repair cost of \$100,000, the RC bridge had a mean annual frequency of exceedance value of $6x10^{-5}$ (roughly 0.3 percent in 50 years), while the UBPT-ECC bridge had a value of $3.4x10^{-9}$ (essentially zero). There is no repair cost hazard curve for the UBPT-Steel Jacket bridge, because the damage states of spalling and bar buckling on which the repair costs are based are assumed not to occur with the use of the steel jacket.

The downtime hazard curves for the four bridges are shown in Figure 6-13. Much like the UBPT bridge, the UBPT-ECC and UBPT-Steel Jacket bridges have significantly lower expected downtimes for any given value of mean annual frequency of exceedance. Both have mean annual frequency values several orders of magnitude lower than that of the RC bridge, and are essentially equal to zero for all levels of downtime. While the values are lower than those of the UBPT bridge, they are all essentially zero. Therefore, from these analyses it can be expected that effectively no downtime will occur due to excessive residual displacements in any of the UBPT systems.

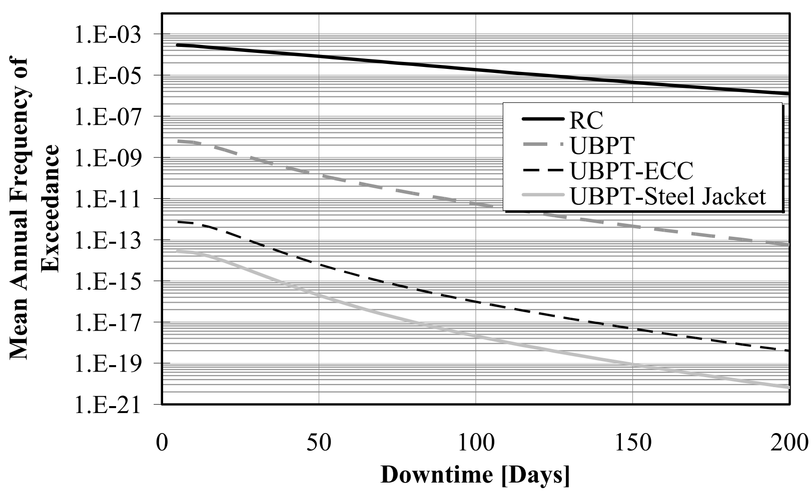

Fig. 6.13 Downtime hazard curves from baseline analysis.

Overall, the use of the ECC and steel jacketing will reduce damage due to spalling and buckling. In terms of expected downtimes, the expected response is basically the same as that of the UBPT column, in that essentially no downtime is expected due to excessive residual displacement. However, it is less clear from the analyses whether the use of such technologies are warranted, given their likely higher initial costs as compared to the ordinary UBPT system or conventional RC system. For example, the expected repair costs may be low enough that an engineer may consider them acceptable and that additional preventative measures are unnecessary.

To try to assess the merits (or lack thereof) of using the enhanced performance technologies, the expected losses will be compared with estimates of initial costs. From Chapter 5, the cost of providing steel casing to all four bridge columns can be computed as $400,000. The cost of ECC is currently around three times that of ordinary concrete (Li 2006). Assuming a standard value of $100 per cubic yard for concrete, the ECC would cost an extra $200 per cubic yard. The additional cost of using ECC as opposed to concrete in the hinges for four columns is computed to be only approximately $4200. Based on these cost alone, the use of ECC appears to be the better option for the columns, with a cost roughly 1/10th that of the steel jacketing. However, it may be useful to examine the results from the PBEE analysis to compare mean annual frequency of exceedance values for these values of repair costs in order to determine whether the use of the candidate systems is practical. Some of these values are shown in Table 6.1.

Table 6.1 Results from PBEE analysis of RC and UBPT bridge systems.

Column System	Mean Annual Frequency of Exceeding $4200 in Repair Costs	Probability of Exceeding $4200 in Repair Costs [% in 50 years]	Mean Annual Frequency of Exceeding $400,000 in Repair Costs	Probability of Exceeding $400,000 in Repair Costs [% in 50 years]	Probability of Exceeding 30 days downtime [% in 50 yr]
RC	4.7E-04	2.35%	2.1E-05	0.11%	0.70%
UBPT	6.6E-04	3.30%	2.5E-05	0.13%	0.00%
UBPT-ECC	2.3E-07	0.00%	0	0.00%	0.00%
UBPT-Steel Jacket	0	0.00%	0	0.00%	0.00%

The mean annual frequency of exceedance values for a repair cost of $4200 (a cost equal to the initial cost of using ECC) for the four bridge systems are shown in the first column, followed by the associated value in terms of a probability in 50 years. The RC column and UBPT bridges are only likely to exceed the $4200, the initial cost of using the ECC in the hinges, with about a probability of about 3 percent in 50 years. This probability is rather low, and may not justify the use of ECC in the columns. In terms of exceeding $400,000 in costs, i.e., the initial cost of jacketing all of the columns of the bridge, the results again show a very low probability. Like the ECC, the use of steel jacketing is not justified based on the expected repair costs due to earthquake damage alone. However, it should be noted that other long-term maintenance advantages may warrant the use of ECC, such as improved resistance to corrosion.

In addition to repair costs, the expected downtime between the four column systems is compared. A downtime of 30 days (one month) is chosen for examination, as it is a time period that could be considered unacceptable for a highly traveled, important bridge. The final column of Table 6-1 gives the probability of exceeding 30 days of downtime in 50 years. The RC column has roughly a 0.7 percent probability in 50 years of exceeding 30 days of downtime. All three UBPT bridge systems have essentially a zero probability of exceeding 30 days downtime in 50 years. While a 0.7 percent in 50 years probability might be considered adequately low for an ordinary highway bridge, this may be considered too high for an important highway bridge. In this case, any of the UBPT systems would provide the desired behavior of zero expected downtime.

Considering both expected repair costs and expected downtime for the four candidate bridge systems, the ordinary UBPT system seems to be the optimal choice. For ordinary bridges, the performance of the RC system might be considered adequate. For important bridges, the possible expected downtime under more rare earthquakes may be considered unacceptable, meaning that one of the three UBPT systems should be used. While the two enhanced performance UBPT systems can reduce damage and hence repair costs to the columns, the improvement to reducing repair costs may not justify their higher initial costs for these particular designs. Therefore the most favorable candidate for use in this example would be the ordinary UBPT column system.

There is, however, another benefit of the use of ECC and steel jacketing that is not considered in this analysis: both are expected to significantly improve the collapse behavior of the columns. Although the results of Chapters 5 and 6 showed that the bridge would not reach levels close to collapse even under rare earthquakes, if ever there were to occur a sufficiently large earthquake as to cause collapse in the RC or ordinary UBPT columns, the enhanced-performance columns would be less likely to collapse because of the added ductility and prevention of longitudinal bar buckling. In the experiments by Sakai et al. (2005), the UBPT column under extremely high loading eventually collapsed, while the UBPT column with steel jacketing under the same loading was in a usable state. As a study on collapse analysis was not the goal of this research, a quantitative assessment of the benefits of collapse behavior is not available, but can be an area of future research.

Finally, the results presented here are for only one specific bridge design at a specific site. While the enhanced-performance technologies may not have shown a great impact in this specific case, their use should not in general be discounted. For a different bridge geometry or configuration, the enhanced-performance technologies may have had a much larger impact. In addition, if the use of the enhanced-performance technologies could be accompanied by changes (e.g., in column size, pushover backbone) to the bridge, the performance could optimized with minimized cost.

6.6 SUMMARY

The use of enhanced performance technologies, namely ECC and steel jacketing, are proposed for use in addition to UBPT in bridge columns for reducing damage during earthquakes while maintaining self-centering behavior. The use of these two technologies is intended to delay or inhibit both spalling and buckling of longitudinal reinforcing bars. The prevention of these forms of damage would then reduce expected repair costs following an earthquake. To determine whether the use of these technologies, which would result in a higher initial cost, would be warranted, the two candidate systems were assessed using PEER's PBEE assessment methodology. The systems were compared to the conventional RC and concrete UBPT systems of Chapter 5.

The results from an IDA of the two candidate systems revealed similar peak drifts to both the RC and UBPT systems. As expected, the residual displacements of the two candidate systems were again quite low as compared to the conventional RC system. Because the residual displacements were again very low, expected downtimes as compared to the RC system were essentially zero. In terms of expected repair costs, the two candidate systems are of equal value in terms of lowering repair costs. However, it is expected that they would be more expensive to implement.

The effect on repair costs of the two candidate systems was not significant not only because of the inefficacy of the technologies themselves, but primarily because the RC and UBPT systems are not expected to sustain large amounts of expected damage and thus repair costs. Because the columns of the bridge are so large, in part because of the conservatism in the Caltrans design, they are not subjected to large displacement demands even under high-intensity earthquakes. As the damage in the columns is displacement dependent, the absence of large displacements means that excessive damage will not be sustained. The more frequent, lower-intensity earthquakes therefore cause essentially no damage to the columns, leading to very low expected repair costs. The result is that the overall expected repair costs for the RC and UBPT systems are already minimal.

The use of ECC and steel jacketing can be considered unnecessary for the bridge considered in this study. The ordinary UBPT system provides reduced downtime from excessive residual displacements, and the expected repair costs are low enough that the use the enhanced performance technologies are not required. Alternatively, the same technologies could be used, but with smaller column sizes such that the expected repair costs would be similar. Savings here would be made in initial costs. Alternative and less conservative designs can be shown to provide the same level of safety while still remaining economical. In other situations, for example at a different site or for a less conservative design, the use of these technologies should demonstrate a greater impact on reducing expected repair costs.

PEER's PBEE assessment methodology was again shown to be an effective, systematic tool for assessing new technologies and systems. Because spalling and buckling are known to be inhibited or delayed by the use of ECC or steel jacketing, and that the IDA results showed similar engineering responses between the UBPT systems, the new technologies may have been considered to be a worthwhile system for the bridge under consideration. However, when combining with the seismic hazard and loss models, the expected repair costs were found to be low enough in the UBPT system that the enhanced-performance technologies would be considered unnecessary in this bridge. Such an assessment of the candidate systems would be difficult to make without the use of a formalized framework.

7 Summary and Conclusions

7.1 SUMMARY

With recent developments in performance-based design, the post-earthquake condition of structures has been a topic of increasing interest in the earthquake engineering community. One key measure of post-earthquake performance in a structure is the amount of residual displacement that occurs after a structure has undergone inelastic deformations. Such residual displacements have been the impetus to closing or demolishing major bridges, for example in Japan following the Kobe earthquake. To minimize or prevent these residual displacements, a number of systems have been proposed to provide self-centering to structures. The focus of this research is on the use of unbonded, post-tensioned steel reinforcing to provide self-centering to concrete highway bridge columns. In this research, methods of simulating the cyclic and dynamic response of both reinforced concrete (RC) and unbonded post-tensioned (UBPT) systems for bridges, specifically with respect to residual displacements are evaluated and validated. One system for circular UBPT concrete bridge columns is considered in greater detail, and is quantitatively compared to a conventional RC system using a performance-based earthquake engineering (PBEE) assessment methodology developed by the Pacific Earthquake Engineering Research Center (PEER). In addition, alternate methods for providing improved damage tolerance to the UBPT column, namely the use of high-performance fiber-reinforced cement-based materials known as engineered cementitious composites (ECC) and steel jacketing, are evaluated through a PBEE assessment.

7.2 FINDINGS AND CONCLUSIONS

7.2.1 Simulation of Precast Segmental UBPT Columns

In Chapter 3, a UBPT system for rectangular bridge piers is investigated. The system uses precast, segmental construction, and incorporates multiple, eccentric UBPT tendons to provide self-centering. The system has the option of using damage-tolerant ECC materials in the hinge segment for improved performance. The goal of the investigation is to validate simulation methods and constitutive models against large-scale experimental testing results from such a system. The simulations are first used to investigate the observed failure behavior in the specimens, as the failures were somewhat unexpected. The simulations are then used to assess the behavior of the specimens that could not be tested to failure due to the configuration of the test setup. The simulations are finally used to assess possible improvements to the system and to assess the affect of variations in ECC tensile properties, as ECC is a material whose properties can be tailored. The main conclusions are as follows:

- The failure mode of the concrete column with light reinforcing cages in the hinge segments, which consisted of compressive failure near the edges of the hinge segments away from the specimen ends, is found to be related to the fact that the bonded reinforcing bars are not fully developed throughout the entire segment (in addition to the fact that the concrete was inadequately confined in compression). The bonded reinforcing was unable to contribute its full yield strength to the moment capacity of the section in some regions and appears to have led to the failure of the column at those locations.
- Failure of the columns due to inadvertent axial loading of the steel PT ducts used in the specimens and subsequent radial expansion, which was theorized as a possible cause of the failure (Rouse 2004), is ruled out after simulation results revealed low induced tensile stresses in the concrete even under high axial loading in the ducts.
- Simulation of the concrete column with heavy reinforcing cages, which could not be tested to failure due to the testing setup, failed in the same fashion as the column with light reinforcing cage, and at a relatively low drift. The results indicate that the additional transverse reinforcement (as compared to the specimen with light reinforcing) was not sufficient enough to provide adequate confinement to the concrete, leading to the low drifts at failure.
- When significant amounts of confinement are provided to the hinge segments in the simulations, the columns are able to sustain greater lateral drifts, and maintain the desired

origin-oriented behavior. When a large enough level of confinement is provided (an amount that is greater than typically used in columns), the effect of the undeveloped, bonded reinforcing is negated.

- The simulation of the column with ultra-high molecular weight polyethylene ECC showed that the observed failure mode of the column, which was similar to that of the concrete columns, was again related to the undeveloped bonded reinforcing bars.
- Sensitivity studies on the tensile parameters of the ECC showed that the best way to improve the performance of the columns is to increase the ultimate tensile strain of the ECC without increasing the cracking stress or peak tensile stress. The added ductility of the ECC delays localization near the construction joint and allows for greater drift capacity in the column. Increasing the ECC tensile strength to a value greater than the tensile strength of the concrete led to localization of cracking and finally failure outside of the hinge segments, which is undesirable. To keep cracking confined to the hinge segments, the tensile strength of the ECC should remain lower than that of the concrete.
- The detailed continuum modeling used to assess the precast segmental system, while necessary for the investigation in this chapter, was found to be too expensive computationally for a full PBEE assessment, which requires extensive nonlinear dynamic time-history analyses.

7.2.2 Prediction of Residual Displacements

In Chapter 4, an alternate system is considered for providing self-centering to circular concrete bridge columns that are typical of bridges designed in highly seismic regions such as California. The system incorporates a single, concentric UBPT tendon. The method of analysis is fiber element analysis due to its computational efficiency. The ability of fiber elements to predict the dynamic structural response of both UBPT and conventional RC columns, in terms of peak displacements but more importantly of residual displacements, is assessed through comparison with experimental testing data. The main conclusions are:

- The fiber element models are able to capture the peak displacements of both the RC and UBPT columns well, but the residual displacements of the RC column are not predicted well.
- Dynamic analyses with a suite of 17 ground motions indicated that the poor residual displacement prediction in the RC column is due to constitutive modeling rather than ground motion effects.

- The constitutive model for concrete used in fiber element models causes pinching in the hysteretic response of the RC column that is not observed in experimental responses. The cause of the pinching in the model stems from the reloading behavior of the concrete constitutive model, namely when moving from high tensile strains back to compression.
- Dynamic analysis of SDOF models representing the RC column revealed that the pinching in the hysteretic behavior leads to poor residual displacement prediction. Removal of the pinching allows for improved residual displacement prediction in the SDOF models.
- A modified concrete constitutive model is proposed and implemented for the RC column that incorporates changes to reloading behavior when moving from high tensile strain back to compression. Analysis of the fiber element model of the RC column using the modified concrete constitutive model led to improvements in residual displacement prediction.
- Calibration of fiber element model residual displacements with dynamic experimental data led to an estimate of the reloading strain parameter required to define the constitutive model.
- The use of the modified constitutive model for the UBPT column is deemed unnecessary based on evaluation of the hysteretic response, and furthermore if used leads to an incorrect response because pinching that should exist in the model is undesirably removed.

7.2.3 PBEE Assessment of Bridges with RC and UBPT Columns

In Chapter 5, the UBPT system is evaluated in a benchmark bridge structure that has a geometry and configuration representative of a majority of bridges in California and that is designed according to current code by Caltrans engineers. The performance of the benchmark bridge using both conventional RC columns and UBPT columns is assessed using PEER's PBEE assessment methodology. In addition, the sensitivity to the results of the PEER PBEE assessment to various assumptions made throughout the analyses is investigated. The main conclusions are as follows:

- For a bridge having UBPT columns detailed to have a similar pushover curve to that of a comparable, conventional RC column, incremental dynamic analysis (IDA) results showed that similar peak drifts would be obtained between the two systems, with the UBPT system showing slightly higher values. At a spectral acceleration corresponding to a probability of 2 percent in 50 years, the bridge with conventional RC columns has a median peak drift ratio of 2.65 percent, while the bridge with UBPT columns had a median peak drift ratio of 2.73 percent.

- With increasing earthquake intensity, the bridge with RC columns begins to sustain significant residual displacements, while the bridge with UBPT columns retains minimal residual displacements. At a spectral acceleration corresponding to a probability of 2 percent in 50 years, the bridge with RC columns has a median residual drift of 0.6 percent with a log standard deviation value of 0.47, while the bridge with UBPT columns had a median residual drift of 0.26 percent with a log standard deviation value of 0.16.
- The additional uncertainty in the structural response due to modeling uncertainty was evaluated using the first-order second-moment method (Baker and Cornell 2003a, 2003b). The response was found to be not highly sensitive to the modeling parameters considered.
- Repair cost hazard curves generated for both bridge systems showed similar costs for a given mean annual frequency of exceedance value, with the UBPT systems showing slightly higher values. The higher costs for the UBPT system are because repair costs are based on damage states that are dependent on peak drifts in the columns, and the UBPT system experienced higher peak drifts.
- Downtime hazard curves generated for the two bridge systems showed significantly lower downtimes for the UBPT system for a given mean annual frequency of exceedance value due to the low residual displacements sustained.
- For a downtime of 30 days, the RC system has a 0.7 percent in 50 years probability of exceedance, while the UBPT system has essentially a 0 percent in 50 years probability of exceedance. Given this information, the conventional RC system may be considered sufficient if the bridge is an ordinary bridge. However, this downtime may be considered too high if the bridge is classified as being very important to the transportation network.
- Analysis using inelastic spectral displacement (Tothong and Cornell 2006) rather than spectral acceleration as an earthquake intensity measure in the PEER PBEE assessment showed reductions in dispersion in the IDA, but these reductions in dispersion did not significantly affect the final comparison of repair costs and downtime. The benefits of using inelastic spectral displacement are expected to be more noticeable in systems where significant nonlinear behavior occurs. The columns in the bridge analyzed here are quite large and well reinforced, meaning that excessive nonlinear behavior is not observed even at high earthquake intensities.
- Overall, the final repair cost and downtime values from the PEER PBEE assessment were found to be most sensitive to the hazard analysis portion of the analysis, with the difference in attenuation models (between the Abrahamson and Silva 1997 and Boore et al. 1997

models) resulting in larger variation than the choice of earthquake intensity measure (between spectral acceleration and inelastic spectral displacement), the assumed variation in the fragility curve, and the assumed variation in the mean loss values of the damage states.

Overall, the PEER PBEE assessment methodology was demonstrated as a powerful tool for quantitatively comparing new systems to conventional systems. Such analyses can help to speed the adoption of new technologies that can provide improvements over existing systems. Even when sufficient data do not exist for some portions of the analyses, an obstacle that is likely to be encountered when dealing with new systems or materials, assumptions can be made in the analyses to produce relative comparisons between systems, which can be used for decision making.

7.2.4 Assessment of Bridge with Enhanced UBPT Columns

Enhancements to the UBPT column system were evaluated in Chapter 6. As the use of UBPT led to the desired reductions in expected downtime due to residual displacements, methods of reducing expected repair costs are investigated. Namely, the use of ECC and the use of steel jacketing, which are expected to minimize or prevent the primary forms of damage in the columns (i.e., spalling and bar buckling), are investigated using PEER's PBEE methodology. Their performance is compared to that of the UBPT and conventional RC systems presented in Chapter 5. The main conclusions are as follows:

- From the IDA results, both of the enhanced-performance UBPT systems are shown to have peak drifts similar to those of the ordinary UBPT and RC systems.
- Again, both of the enhanced-performance UBPT systems show significantly lower residual displacements at higher earthquake intensity levels as compared to the conventional RC system.
- The fact that ECC can prevent spalling significantly reduces the expected repair costs of the UBPT systems with ECC as compared to the ordinary UBPT system.
- When considering the downtime of the two enhanced-performance UBPT systems, each shows essentially no downtime expected when compared to the RC system at a given mean annual frequency of exceedance value.
- Based on an examination of the expected increases in initial cost to use the enhanced-performance technologies as compared to the likelihood of seeing these costs in terms of

repair, the enhanced-performance systems were not considered warranted for the bridge under consideration. The chance of seeing repair costs exceeding the initial costs for the two candidate systems was found to be quite low. The conclusion then is that the ordinary UBPT system is the optimal system in terms of minimizing repair costs due to drift-based damage and minimizing downtime under severe earthquakes.

7.3 FUTURE WORK

In terms of the modified concrete constitutive model proposed in Chapter 4, several improvements could be made. First, the loading and unloading behavior when on the alternate loading branch should be modified. In the current model, the unloading and reloading on this branch follows the same path. This should be changed so that unloading occurs on a stiffer path, which in turn will change the reloading. Also, the reloading strain value, ε_r, could be modified so that it is a function of other history parameters as proposed by Stanton and McNiven (1979) rather than being a constant value. Further calibration of the model parameter should be performed as additional dynamic testing data become available.

Many areas of future research should be explored to examine more fully the improvements possible to the performance of bridge columns using self-centering, UBPT systems. In this study, only a single bridge with a given geometry and configuration was considered. A wider range of bridge structures should be analyzed in the same fashion as in this research to determine the effect of the use of UBPT on bridge structures as a whole, or the effect on classes of bridge structures. A number of different geometry parameters could be considered, including column height, span length, and skew. Additionally, bridges that incorporate variable column heights or multiple column bents should be considered. Improvements to the bridge model itself, such as modeling of the soil, foundation, and soil-structure interaction should be included in the model. Finally, different acceleration time-histories applied to different columns, as well as for the abutments, on multi-span bridges should be evaluated.

For the UBPT columns using ECC, validation of simulations against experimental dynamic testing data should be performed when results become available. Very little dynamic experimental work has been published to date on ECC structural components. In addition, while the tensile properties of the ECC did not seem to greatly affect the response of the columns in this study, its use in columns of a different size or in a different configuration may show greater benefits, for example in shear-dominated columns. Again, different bridge geometries and configurations where the ECC could be more valuable should be assessed.

An improved PBEE analysis should be performed on the same bridge when more data and research become available on the damage and loss portions of the analysis. Several assumptions were made in both of these sections due to lack of sufficient data, and more accurate values (e.g., for standard deviations of repair costs) should be used to provide more precise repair cost and downtime predictions.

REFERENCES

AASHTO. 1983. Guide Specifications for Seismic Design of Highway Bridges, American Association of State and Highway Transportation Officials.

AASHTO. 1996. Standard Specifications for Highway Bridges, American Association of State and Highway Transportation Officials.

ACI. 2005. Building Code Requirements for Structural Concrete (ACI 318-05) and Commentary (ACI 318R-05), American Concrete Institute, Farmington Hills, Michigan, 2005.

ATC. 1996a. Improved Seismic Design Criteria for California Bridges: Provisional Recommendations, Report No. ATC-32, Applied Technology Council, California Seismic Safety Commission, Sacramento, California.

ATC. 1996b. Methodology for Evaluation and Upgrade of Reinforced Concrete Buildings, Report No. ATC-40, Applied Technology Council, California Seismic Safety Commission, Sacramento, California.

Abrahamson, N.A. and Silva, W.J. 1997. Empirical Response Spectral Attenuation Relations for Shallow Crustal Earthquakes, Seismological Research Letters, 68(1): 94-127.

Aslani, H. and Miranda, E. 2005. Fragility Assessment of Slab-Column Connections in Existing Non-Ductile Reinforced Concrete Buildings, Journal of Earthquake Engineering, 9(6): 777-804.

Baker, J.W. and Cornell, C.A. 2003a. Uncertainty Specification and Propagation for Loss Estimation Using FOSM Methods, Proceedings of the Ninth International Conference on Applications of Statistics and Probability in Civil Engineering, San Francisco, California.

Baker, J.W. and Cornell, C.A. 2003b. Uncertainty Specification and Propagation for Loss Estimation Using FOSM Methods, PEER Report 2003/07, Pacific Earthquake Engineering Research Center, University of California, Berkeley, California.

Baker, J.W. and Cornell, C.A. 2005. A Vector-Value Ground Motion Intensity Measure Consisting of Spectral Acceleration and Epsilon, Earthquake Engineering and Structural Dynamics, 34(10): 1193-1217.

Bazzurro, P., Cornell, C., Menun, C. and Motahari, M. 2004. Guidelines for Seismic Assessment of Damaged Buildings, Proceedings of the 13th World Conference on Earthquake Engineering, Vancouver, Canada, August, 2004. Paper No. 1550.

Berry, M. and Eberhard, M. 2003. Performance Models for Flexural Damage in Reinforced Concrete Columns, PEER Report 2003/18, Pacific Earthquake Engineering Research Center, University of California, Berkeley, California.

Billington, S. and Yoon, J. 2003. Simulation of Cyclically Loaded Columns Made with Ductile Cement-Based Composites, Proceedings of the EURO-C 2003 Conference on Computational Modeling of Concrete Structures, Balkema, Rotterdam, The Netherlands, 2003.

Billington, S. and Yoon, J. 2004. Cyclic Response of Unbonded Posttensioned Precast Columns with Ductile Fiber-Reinforced Concrete, Journal of Bridge Engineering, 9(4): 353-363.

Billington, S. 2006. Personal communication.

Boore, D.M., Joyner, W.B., and Fumal, T.E. (1997). Equations for Estimating Horizontal Response Spectra and Peak Acceleration from Western North American Earthquakes: A Summary of Recent Work, Seismological Research Letters, 68(1): 128-153.

Borzi, B., Calvi, G.M., Elnashai, A.S., Faccioli, E. and Bommer, J.J. 2001. Inelastic Spectra for Displacement-Based Seismic Design, Soil Dynamics and Earthquake Engineering, 21(1): 47-61.

Caltrans. 2001. *Seismic Design Criteria V. 1.2.*, California Department of Transportation, California, USA.

Caltrans. 2004. Construction Statistics Based on Bid Openings, California Department of Transportation, Division of Engineering Services.
www.dot.ca.gov/hg/esc/estimates/Construction_Stats_2004.xls

Caltrans. 2005. Bridge Design Aids – Section 11: Estimating, California Department of Transportation, Division of Engineering Services.
www.dot.ca.gov/hq/esc/techpubs/manual/bridgemanuals/bridge-design-aids/bda/html

Canbolat, B., Parra-Montesinos, G., and Wight, J. 2005. Experimental Study on Seismic Behavior of High-Performance Fiber-Reinforced Cement Composite Coupling Beams, ACI Structural Journal, 102(1): 159-166.

CEB-FIP. 1990. Model code 1990. Bulletin d'information, CEB, Lausanne, Switzerland.

Chen, W.F. 1982. Plasticity in Reinforced Concrete, McGraw-Hill, New York.

Cheokh, G., Stone, W. and Kunnath, S. 1998. Seismic Response of Precast Concrete Frames with Hybrid Connections, ACI Structural Journal, 95(5): 527-539.

Christopoulos, C., Pampanin, S., and Priestley, M.N. 2003. Performance-Based Seismic Response of Frame Structures Including Residual Deformations. Part I: Single-Degree of Freedom Systems, Journal of Earthquake Engineering, 7(1): 97-118.

Deierlein, G. and Haselton, C. 2005. Benchmarking the Collapse Safety of Code-Compliant Reinforced Concrete Moment Frame Building Systems, Proceedings of the ATC/JSCA US-Japan Workshop on Improvement of Structural Design and Construction Practices, Kobe, Japan, October, 2005.

Douglas, K.S. 2006. Personal communication.

Douglas, K.S. and Billington, S.L. 2006. Modeling the Impact of Rate Dependence of HPFRCC Materials on the Behavior of Infill Panels, Proceedings of the 8th U.S. National Conference on Earthquake Engineering, San Francisco, California, April, 2006.

El-Sheikh, M., Pessiki, S., Sause, R. and Lu, W. 2000. Moment Rotation Behavior of Unbonded Post-Tensioned Precast Concrete Beam-Column Connections, ACI Structural Journal, 97(1): 122-131.

El-Sheikh, M., Sause, R., Pessiki, S. and Lu, W. 1999. Seismic Behavior and Design of Unbonded Post-Tensioned Precast Concrete Frames, PCI Journal, 44(3): 54-71.

Elwood, K.J. and Eberhard, M.O. 2006. Effective Stiffness of Reinforced Concrete Columns. PEER Research Digest No. 2006-1, Pacific Earthquake Engineering Research Center, University of California, Berkeley, California.

FEMA. 1997. NEHRP Guidelines for Seismic Rehabilitation of Buildings, Report No. FEMA-273, Federal Emergency Management Agency, Washington, D.C.

FEMA. 1999. HAZUS99 Service Release 2 Technical Manual, Federal Emergency Management Agency, Washington, D.C., USA.

FEMA. 2000. Prestandard and Commentary for the Seismic Rehabilitation of Buildings, Report No. FEMA-356, Federal Emergency Management Agency, Washington, D.C.

Feenstra, P.H., Rots, J.G., Arnesen, A., Teigen, J.G., and Hoiseth, K.V. 1998. A 3D Constitutive Model for Concrete Based on a Co-Rotational Concept, Proceedings of the Euro-C Conference on Computational Modeling of Concrete Structures, Austria, 1998.

Fischer, G. and Li, V. 2003a. Deformation Behavior of Fiber-Reinforced Polymer Reinforced Engineered Cementitious Composite Flexural Members under Reversed Cyclic Loading Conditions, ACI Structural Journal, 100(1): 25-35.

Fischer, G. and Li, V. 2003b. Intrinsic Response Control of Moment Resisting Frames Utilizing Advanced Composite Materials and Structural Elements, ACI Structural Journal, 100(2): 166-176.

Hachem, M.M., Mahin, S.A., and Moehle, J.P. 2003. Performance of Circular Reinforced Concrete Bridge Columns Under Bidirectional Earthquake Loading, PEER Report 2003/06, Pacific Earthquake Engineering Research Center, University of California, Berkeley, California.

Hamilton, C.H., Pardoen, G.C., and Kazanjy, R.P. 2002. Experimental Testing of Bridge Columns Subjected to Reversed-Cyclic and Pulse-type Loading Histories, Report No. 2001-03, Civil Engineering Technical Report Series, University of California, Irvine.

Han, T.S., Feenstra, P.H., and Billington, S.L. 2002. Constitutive Model for Highly Ductile Fiber-Reinforced Cementitious Composite, Technical Report 02-04, Cornell University, Ithaca, New York.

Han, T.S., Feenstra, P.H., and Billington, S.L. 2003. Simulation of Highly Ductile Cement-Based Composites, ACI Structural Journal, 100(6): 749-757.

Hart, G.C. and Vasudevan, R. 1975. Earthquake Design of Buildings: Damping, Journal of the Structural Division, Proceedings of the ASCE, 101(ST1): 11-30.

Haselton, C., Mitrani-Reiser, J., Goulet, C., Deierlein, G., Beck, J., Porter, K., Stewart, J., and Taciroglu, E. 2005. An Assessment to Benchmark the Seismic Performance of a Code-Conforming Reinforced-Concrete Moment-Frame Building, PEER Report 2005, Pacific Earthquake Engineering Research Center, University of California, Berkeley, California.

Howard, R.A. 1988. Decision Analysis: Practice and Promise, Management Science, 34(6).

Ibarra, L.F. and Krawinkler, H. 2005. Global Collapse of Frame Structures Under Seismic Excitations, Blume Center Technical Report No. 152, John A. Blume Earthquake Engineering Center, Stanford University, Stanford, California.

Ikeda, S. 1998. Seismic Behavior of Reinforced Concrete Columns and Improvement by Vertical Prestressing, Proceedings of the 13th FIP Congress on Challenges for Concrete in the Next Millennium, Amsterdam, May, 1998.

Ito, T., Yamaguchi, T., and Ikeda, S. 1997. Seismic Performance of Reinforced Concrete Piers Prestressed in the Axial Direction, Proceedings of the Japanese Concrete Institute, 19(2): 1197-1202.

Japan Road Association. 2006. *Specifications for Highway Bridges*. Japan.

Karsan, I.D. and Jirsa, J.O. 1969. Behavior of Concrete Under Compressive Loadings, Journal of the Structural Division, ASCE, 95(12): 2543-2563.

Kanakubo, T., Shimizu, K., Katagiri, M., Kanda, T, Fukuyama, H., and Rokugo, K. 2005. Tensile Characteristics Evaluation of DFRCC – Round Robin Test Results by JCI-TC, Proceedings of the International Workshop on High Performance Fiber Reinforced Cementitious Composites in Structural Applications, Honolulu, Hawaii, May, 2005.

Kawashima, K., MacRae, G., Hoshikuma, J. and Nagaya, K. 1998. Residual Displacement Response Spectrum, Journal of Structural Engineering, 124(5): 523-530.

Kawashima, K. and Unjoh, S. 1997. The Damage of Highway Bridges in the 1995 Hyogo-Ken Nanbu Earthquake and its Impact on Japanese Seismic Design, Journal of Earthquake Engineering, 1(3): 505-541.

Kesner, K. and Billington, S. 2003. Experimental Response of Precast Infill Panel Connections and Panels Made with DFRCC, Journal of Advanced Concrete Technology, 1(3): 1-7.

Kesner, K. and Billington, S. 2004. Tension, Compression and Cyclic Testing of Engineered Cementitious Composite Materials, Technical Report MCEER-04-0002, Multidisciplinary Center for Earthquake Engineering Research, University at Buffalo, State University of New York.

Kesner, K. and Billington, S. 2005. Investigation of Infill Panels Made from Engineered Cementitious Composites for Seismic Strengthening and Retrofit, Journal of Structural Engineering, 113(11): 1712-1720.

Kesner, K., Billington, S., and Douglas, K. 2003. Cyclic Response of Highly Ductile Fiber-Reinforced Cement-Based Composites, ACI Materials Journal, 100(5): 381-390.

Ketchum, M., Chang, V., and Shantz, T. 2004. Influence of Design Ground Motion Level on Highway Bridge Costs. *PEER Technical Report D601*. Berkeley, California, USA: Pacific Earthquake Engineering Research Center.

Kramer, S. 1995.Geotechnical Earthquake Engineering. New Jersey, Prentice Hall.

Kurama, Y. 2001. Simplified Seismic Design Approach for Friction-Damped Unbonded Post-Tensioned Precast Concrete Walls, ACI Structural Journal, 98(5): 705-716.

Kurama, Y., Sause, R., Pessiki, S. and Lu, L. 1999. Lateral Load Behavior and Seismic Design of Unbonded Post-Tensioned Precast Concrete Walls, ACI Structural Journal, 96(4): 622-632.

Kurama, Y., Sause, R., Pessiki, S., and Lu, L. 2002. Seismic Response Evaluation of Unbonded Post-Tensioned Precast Walls, ACI Structural Journal, 99(5): 641-651.

Kwan, W. and Billington, S. 2001. Simulation of Structural Concrete Under Cyclic Load. *Journal of Structural Engineering*, 127(12): 1391–1401.

Kwan, W. and Billington, S. 2003a. Unbonded Posttensioned Concrete Bridge Piers. I: Monotonic and Cyclic Analyses, Journal of Bridge Engineering, 8(2): 92-101.

Kwan, W. and Billington, S. 2003b. Unbonded Posttensioned Concrete Bridge Piers. II: Seismic Analyses, Journal of Bridge Engineering, 8(2): 101-111.

Lee, W.K. and Billington, S.L. 2006. Analytical Assessment of the Post-Earthquake Condition of Self-Centering vs. Traditional Concrete Bridge Pier Systems, Proceedings of the 3rd International Conference on Bridge Maintenance, Safety and Management, Porto, Portugal, July 2006.

Li, V.C. and Leung, C. 1992. Steady-State and Multiple Cracking of Short Random Fiber Composites, Journal of Engineering Mechanics, 118(11): 2246-2264.

Li, V.C., Mishra, D.K., and Wu, H.C. 1995. Matrix Design for Pseudo-Strain Hardening Fibre Reinforced Cementitious Composites, Materials and Structures, 28(184): 586-595.

Li, V.C., Wang, S. and Wu, H.C. 2001. Tensile Strain-Hardening Behavior of Polyvinyl Alcohol Engineered Cementitious Composite (PVA-ECC), ACI Materials Journal, 98(6): 483-492.

Li, V.C. and Wu, H.C. 1992. Conditions for Pseudo-Strain Hardening in Fiber Reinforced Brittle Matrix Composites, Journal of Applied Mechanics Review, 45(8): 390-398.

Li, V.C. 1993. From Micromechanics to Structural Engineering – The Design of Cementitious Composites for Civil Engineering Applications, JSCE Journal of Structural Mechanics and Earthquake Engineering, 10(2): 37-48.

Li, V.C. 1998. Engineered Cementitious Composites – Tailored Composites Through Micromechanical Modeling, Fiber Reinforced Concrete: Present and the Future, edited by N. Banthia, A. Bentur and A. Muft, Canadian Society of Civil Engineering, Montreal, Canada, 64-97.

Li, V.C. 2002. Advances in ECC Research, ACI Special Publication on Concrete: Materials Science to Applications, SP 206-23: 373-400.

Li, V.C. 2006. Bendable Composites: Ductile Concrete for Structures, Structure Magazine, July 2006 Issue, 45-48.

Lin, T.Y. and Burns, N.H. 1981. Design of Prestressed Concrete Structures, New York, John Wiley and Sons.

Lowes, L.N., Mitra, J. and Altoontash, A. 2004. A Beam-Column Joint Model for Simulating the Earthquake Response of Reinforced Concrete Frames, PEER Report 2003/10, Pacific Earthquake Engineering Research Center, University of California, Berkeley, California.

Luco, N., Bazzurro, P. and Cornell, C. 2004. Dynamic Versus Static Computation of the Residual Capacity of a Mainshock-Damaged Building to Withstand an Aftershock, Proceedings of the 13th World Conference on Earthquake Engineering, Vancouver, Canada, August, 2004. Paper No. 2405.

Ma, S., Bertero, V. and Popov, E. 1976. Experimental and Analytical Studies on the Hysteretic Behavior of Reinforced Concrete Rectangular and T-Beams, Report No. EERC 76-2, Earthquake Engineering Research Center, University of California, Berkeley.

Mackie, K. and Stojadinovic, B. 2004. Residual Displacements and Post-Earthquake Capacity of Highway Bridges, Proceedings of the 13th World Conference on Earthquake Engineering, Vancouver, Canada, August, 2004. Paper No. 1550.

Mackie, K. 2005a. Personal correspondence.

Mackie, K. and Stojadinovic, B. 2005b. Fragility Basis for California Highway Overpass Bridge Seismic Decision Making, Report 2005/12, Pacific Earthquake Engineering Research Center, University of California, Berkeley, California.

Mackie, K., Wong, J.-M., and Stojadinovic, B. 2006. Method for Post-Earthquake Highway Bridge Repair Cost Estimation, Proceedings of the 5th National Seismic Conference on Bridges and Highways, September, 2006.

MacRae, G. 1998. Residual Displacements of Reinforced Concrete Bridge Columns Subject to Seismic Loading, Proceedings of the 6th U.S. National Conference on Earthquake Engineering, Seattle, Washington, May-June, 1998.

MacRae, G. and Kawashima, K. 1997. Post-Earthquake Residual Displacements of Bilinear Oscillators, Earthquake Engineering and Structural Dynamics, 26: 701-716.

Mahin, S. and Bertero, V.V. 1981. An Evaluation of Inelastic Seismic Design Spectra, Journal of Structural Engineering, 107, No. ST9: 1777-1795.

Mander, J., M. Priestley, and R. Park, 1983. Seismic Design of Bridge Piers, Research Report 84-02, University of Canterbury, Christchurch, New Zealand.

Mander, J. and Cheng, C. 1997. Seismic Design of Bridge Columns Based on Control and Repairability of Damage, National Center for Earthquake Engineering Research Technical Report NCEER-97-0014.

Marshall, B., Cox, B. and Evans, A. 1985. The Mechanics of Matrix Cracking in Brittle Matrix Fiber Composites, Acta Metall., 33(11): 2013-2021.

Melchers, R.E. 1999. Structural Reliability Analysis and Prediction. Chichester, England, John Wiley and Sons, Inc.

Moehle, J. and Deierlein, G. 2004. A Framework Methodology for Performance-Based Earthquake Engineering. *Proceedings of the 13th World Conference on Earthquake Engineering*, Vancouver, Canada, August, 2004, Paper No. 679.

Olsen, C. and Sulc, D. 2004. CEE-299 Independent Study Project Report, December, Stanford University.

Neville, A. 1996. Properties of Concrete. New York, John Wiley and Sons, Inc.

Parra-Montesinos, G., Peterfreund, S., and Chao, S. 2005. Highly Damage-Tolerant Beam-Column Joints Through Use of High-Performance Fiber-Reinforced Cement Composites, ACI Structural Journal, 102(3): 487-495.

Pampanin, S., Christopoulos, C., and Priestley, M.N. 2003. Performance-Based Seismic Response of Frame Structures Including Residual Deformations. Part II: Multi-Degree of Freedom Systems, Journal of Earthquake Engineering, 7(1): 119-147.

Perez, F., Pessiki, S., and Sause, R. 2004a. Seismic Design of Unbonded Post-Tensioned Precast Concrete Walls with Vertical Joint Connectors, PCI Journal, 49(1): 58-79.

Perez, F., Pessiki, S., and Sause, R. 2004b. Lateral Load Behavior of Unbonded Post-Tensioned Walls with Vertical Joints, PCI Journal, 49(2): 48-64.

Pollino, M. and Bruneau, M. 2005. Controlled Rocking Approach for the Seismic Resistance of Structures, Proceedings of the 2005 Annual Meeting of the Asian-Pacific Network of Centers for Earthquake Engineering Research, Jeju, Korea, November, 2005.

Popovics, S. 1973. A Numerical Approach to the Complete Stress-Strain Curves for Concrete, Cement and Concrete Research, 3(5): 583-599.

Porter, K.A. and Kiremidjian, A.S. 2001. Assembly-Based Vulnerability of Buildings and its Uses in Seismic Performance Evaluation and Risk Management Decision-Making, Blume Center Technical Report No. 139, John A. Blume Earthquake Engineering Center, Stanford University, Stanford, California.

Porter, K.A. 2003. An Overview of PEER's Performance-Based Earthquake Engineering Methodology, Proceedings of the 9th Conference on Applications of Statistics and Probability in Civil Engineering, San Francisco, July, 2003.

Priestley, M.J.N., and Park, R. 1987. Strength and Ductility of Concrete Bridge Columns Under Seismic Loading, ACI Structural Journal, 84(1): 61-76.

Priestley, M.J.N., Seible, F., and Calvi, G.M. 1996. Seismic Design and Retrofit of Bridges. New York, John Wiley and Sons, Inc.

Priestley, M.J.N., Sritharan, S., Conley, J. and Pampanin, S. 1999. Preliminary Results and Conclusions form the PRESSS Five-Story Precast Concrete Test Building, PCI Journal, 44(6): 42-67.

Priestley, M.J.N., and Tao, J. 1993. Seismic Response of Precast Prestressed Concrete Frames with Partially Debonded Tendons, PCI Journal, 38(1): 58-69.

R.S. Means, 2007. Means Assemblies Cost Data 32nd Edition, R.S. Means Company, Inc., Kingston, MA.

Richart, F., Brandtzaeg, A. and Brown, R. 1928. A Study of the Failure of Concrete Under Combined Compressive Stresses, Bulletin 185, University of Illinois Engineering Experimental Station, Champaign, Illinois.

Roder, C.W., Graff, R., Soderstrom, J.L., and Yoo, J.H. 2001. Seismic Performance of Pile-Wharf Connections, PEER Report 2002/07, Pacific Earthquake Engineering Research Center, University of California, Berkeley, California.

Rouse, J. 2004. Behavior of Bridge Piers with Ductile Fiber Reinforced Hinge Regions and Vertical Unbonded Post-Tensioning, *Ph.D. Dissertation*, Cornell University, Ithaca, New York.

Rouse, M. and Billington, S. 2003. Behavior of Bridge Piers with Ductile Fiber Reinforced Hinge Regions and Vertical, Unbonded Post-Tensioning, Proceedings of the FIB Symposium on Concrete Structures in Seismic Regions, Greece, May, 2003.

Ruiz-Garcia, J. and Miranda, E. 2005. Performance-Based Assessment of Existing Structures Accounting for Residual Displacements, Blume Center Technical Report No. 153, John A. Blume Earthquake Engineering Center, Stanford University, Stanford, California.

Sakai, J. and Mahin, S. 2003. Hysteretic Behavior and Dynamic Response of Re-Centering Reinforced Concrete Columns, Proceedings of the 6th Symposium on Seismic Design of Bridge Structures Based on the Ductility Design Method, Tokyo, Japan, January, 2003.

Sakai, J. and Mahin, S. 2004a. Mitigation of Residual Displacements of Circular Reinforced Concrete Bridge Columns, *Proceedings of the 13th World Conference on Earthquake Engineering*, Vancouver, Canada, August, 2004, Paper No. 1622.

Sakai, J., and Mahin, S. 2004b. Analytical Investigations of New Methods for Reducing Residual Displacements of Reinforced Concrete Bridge Columns, PEER Report 2004/02, Pacific Earthquake Engineering Research Center, University of California, Berkeley, California.

Sakai, J., Jeong, H., and Mahin, S. 2005. Earthquake Simulator Tests on the Mitigation of Residual Displacements of Reinforced Concrete Bridge Columns, *Proceedings of the 21st U.S.-Japan Bridge Engineering Workshop*, Japan, 2005.

Scott, B., R. Park, and M. Priestley, 1982. Stress-strain behavior of concrete confined by overlapping hoops at low and high strain rates, Journal of the American Concrete Institute 79 (1).

Scott, M. and Fenves, G. 2006. Plastic Hinge Integration Methods for Force-Based Beam-Column Elements, Journal of Structural Engineering, 132(2): 244-252.

Shiramama, H., Yamaguchi, T., and Ikeda, S. 1998. Seismic Response Behavior of Concrete Piers Prestressed in Axial Direction, Proceedings of the Japanese Concrete Institute, 20(3): 745-750.

Somerville, P. and Collins, N. 2002. Ground Motion Time Histories for the I880 Bridge – Oakland. PEER Technical Report.

Stanton, J. and McNiven, H. 1979. The Development of a Mathematical Model to Predict the Flexural Response of Reinforced Concrete Beams to Cyclic Loads, Using System Identification, Report No. EERC 79-02, Earthquake Engineering Research Center, University of California, Berkeley.

Stanton, J. 2005. Personal communication.

Structural Engineers Association of California. 1995. Vision 2000, Conceptual Framework for Performance-Based Seismic Design, Recommended Lateral Force Requirement and Commentary, 6th Edition, Sacramento, California.

Su, X. and Zhu, B. 1994. Algorithm for Hysteresis Analysis of Prestressed-Concrete Frames. *Journal of Structural Engineering*, 120(6): 1732-1744.

Tadros, M.K., Al-Omaishi, N., Seguirant, S., and Gallt, J.G. 2003. Prestress Losses in Pretensioned High-Strength Concrete Bridge Girders, National Cooperative Highway Research Program Report 496, , Transportation Research Board, Washington, D.C.

Taucer, F., E. Spacone, and F. Filippou, 1991. A fiber beam-column element for seismic response analysis of reinforced concrete structures, UCB/EERC Technical Report 91/17, Earthquake Engineering Research Center, University of California, Berkeley.

Tothong, P. and Cornell, C.A. 2006. An Empirical Ground Motion Attenuation Relation for Inelastic Spectral Displacement, Bulletin of the Seismological Society of America, 96(6): 2146-2164.

Tothong, P. 2006. Personal communication.

Tothong, P. 2007. Probabilistic Seismic Demand Analysis using Advanced Ground Motion Intensity Measure, Attenuation Relationships, and Near-Fault Effects, Ph.D. Dissertation, Department of Civil and Environmental, Stanford University, Stanford, CA.

Tsoukantas, S.G. and Tassios, T.P. 1989. Shear Resistance of Connections between Reinforced Concrete Linear Precast Elements, ACI Structural Journal, 86(3): 242-249.

Vamvatsikos, D. and Cornell, C. 2002. Incremental Dynamic Analysis, Earthquake Engineering and Structural Dynamics, 31(3): 491-512.

William, K. and Warnke, E. 1975. Constitutive Model for the Triaxial Behavior of Concrete, Proceedings of the International Association for Bridge and Structural Engineering, 19: 1-30.

Yazgan, U. and Dazio, A. 2006. Comparison of Different Finite-Element Modeling Approaches in Terms of Estimating the Residual Displacements of RC Structures, Proceedings of the 8th U.S. National Conference on Earthquake Engineering, San Francisco, California, April, 2006. Paper No. 309.

Yun, H., Kim, S., Jeon, E., and Park, W. 2005. Effects of Matrix Ductility on the Shear Performance of Precast Reinforced HPHFRCC Coupling Beams, Proceedings of the 2nd Korea-Japan International Joint Symposium on Manufacture/Construction/Structural Applications of High-Performance Fiber Reinforced Cementitious Composites, Daejon, Korea, October, 2005.

Zatar, M. and Mutsuyoshi, H. 2000. Reduced Residual Displacements of Partially Prestressed Concrete Bridge Piers, Proceedings of the 12th World Conference on Earthquake Engineering, Auckland, New Zealand, January-February, 2000.

Appendix A: Source Code for Constitutive Models

This appendix contains the source code written in C++ and developed for implementation in OpenSees for the following material models:

1. *Concrete01WithSITC*: Uniaxial material model for concrete that captures residual displacements (two files: **Concrete01WithSITC.h** and **Concrete01WithSITC.cpp**)
2. *ECC01:* Uniaxial material model for ECC based on the Han et al. (2003) model (two files: **ECC01.h** and **ECC01.cpp**)

File: Concrete01WithSITC.h

```
#ifndef Concrete01WithSITC_h
#define Concrete01WithSITC_h

// File: ~/material/Concrete01WithSITC.h
//
// Modified by: Won Lee
// Created: 10/3/05
// Modified from Concrete01.h (see details below)
// Desctiption: This file contains the class definition for Concrete01WithSITC
// Description: Concrete01 model modified to include SITC effect (ref. Prof.
// John Stanton of Univ. of Washington).  Use modified rules from his paper to include this
// effect (J.F. Stanton and H.D. McNiven, "The Development of a Mathematical
// Model to Predict the Flexural Response of Reinforced Concrete Beams to Cyclic
// Loads, Using System Identification", EERC Report Number 79/02, January 1979.

// BASED ON FILE:
// File: Concrete01.h
//
// Written: MHS
// Created: 06/99
// Revision: A
// Description: This file contains the class definition for
// Concrete01.h adapted from Concr1.f90 (Filippou)
//   - Modified Kent-Park envelope
//   - No tension
//   - Linear unloading/reloading

#include <UniaxialMaterial.h>

class Concrete01WithSITC : public UniaxialMaterial
```

```
{
 public:
  Concrete01WithSITC  (int  tag,  double  fpc,                    double eco, double fpcu, double ecu);
  Concrete01WithSITC ();
  ~Concrete01WithSITC();

      int setTrialStrain(double strain, double strainRate = 0.0);
      int setTrial (double strain, double &stress, double &tangent, double strainRate = 0.0);
      double getStrain(void);
      double getStress(void);
      double getTangent(void);
      double getInitialTangent(void) {return 2.0*fpc/epsc0;}

      int commitState(void);
      int revertToLastCommit(void);
      int revertToStart(void);

      UniaxialMaterial *getCopy(void);

      int sendSelf(int commitTag, Channel &theChannel);
      int recvSelf(int commitTag, Channel &theChannel,
         FEM_ObjectBroker &theBroker);

      void Print(OPS_Stream &s, int flag =0);

   protected:

   private:
      /*** Material Properties ***/
      double fpc;    // Compressive strength
      double epsc0;  // Strain at compressive strength
      double fpcu;   // Crushing strength
      double epscu;  // Strain at crushing strength

      /*** CONVERGED History Variables ***/
      double CminStrain;   // Smallest previous concrete strain (compression)
      double CunloadSlope; // Unloading (reloading) slope from CminStrain
      double CendStrain;   // Strain at the end of unloading from CminStrain
     double CmaxStrain;   // Largest previous concrete strain (tension)
     double CslopeSITC;
     double CendStrainSITC;
     int Cindex;
     int CsmallStrainIndex;

      /*** CONVERGED State Variables ***/
      double Cstrain;
      double Cstress;
      double Ctangent;  // Don't need Ctangent other than for revert and sendSelf/recvSelf

      /*** TRIAL History Variables ***/
      double TminStrain;
      double TunloadSlope;
      double TendStrain;
     double TmaxStrain;
     double TslopeSITC;
     double TendStrainSITC;
     int Tindex;
     int TsmallStrainIndex;

      /*** TRIAL State Variables ***/
```

```
    double Tstrain;
    double Tstress;
    double Ttangent; // Not really a state variable, but declared here for convenience

    void determineTrialState (double dStrain);

    void reload();
    void unload();
    void envelope();
    void getSITCslope();

};

#endif
```

File: Concrete01WithSITC.cpp

```
// File: ~/material/Concrete01WithSITC.C
//
// Modified by: Won Lee
// Created: 10/3/05
// Modified from Concrete01.C (see details below)
// Description: Concrete01 model modified to include SITC effect (ref. Prof.
// John Stanton of Univ. of Washington).  Use modified rules from his paper to include this
// effect (J.F. Stanton and H.D. McNiven, "The Development of a Mathematical
// Model to Predict the Flexural Response of Reinforced Concrete Beams to Cyclic
// Loads, Using System Identification", EERC Report Number 79/02, January 1979.

// FILE BASED ON:
// File: ~/material/Concrete01.C
//
// Written: MHS
// Created: 06/99
// Revision: A

#include <Concrete01WithSITC.h>
#include <Vector.h>
#include <Matrix.h>
#include <Channel.h>
#include <Information.h>
#include <math.h>
#include <float.h>

#define MAT_TAG_Concrete01WithSITC 100000

//int count = 0;

Concrete01WithSITC::Concrete01WithSITC
(int tag, double FPC, double EPSC0, double FPCU, double EPSCU)
  :UniaxialMaterial(tag, MAT_TAG_Concrete01WithSITC),
   fpc(FPC), epsc0(EPSC0), fpcu(FPCU), epscu(EPSCU),
   CminStrain(0.0), CendStrain(0.0),
   Cstrain(0.0), Cstress(0.0), CmaxStrain(0.0),
   CslopeSITC(0.0), CendStrainSITC(0.0), Cindex(0), CsmallStrainIndex(0)
{
  //count++;
   // Make all concrete parameters negative
   if (fpc > 0.0)
        fpc = -fpc;

   if (epsc0 > 0.0)
        epsc0 = -epsc0;

   if (fpcu > 0.0)
        fpcu = -fpcu;

   if (epscu > 0.0)
        epscu = -epscu;

   // Initial tangent
   double Ec0 = 2*fpc/epsc0;
   Ctangent = Ec0;
   CunloadSlope = Ec0;
   Ttangent = Ec0;
```

```
   // Set trial values
   this->revertToLastCommit();

}

Concrete01WithSITC::Concrete01WithSITC():UniaxialMaterial(0, MAT_TAG_Concrete01WithSITC),
 fpc(0.0), epsc0(0.0), fpcu(0.0), epscu(0.0),
 CminStrain(0.0), CunloadSlope(0.0), CendStrain(0.0),
 Cstrain(0.0), Cstress(0.0), CmaxStrain(0.0),
 CslopeSITC(0.0), CendStrainSITC(0.0), Cindex(0), CsmallStrainIndex(0)

{
   // Set trial values
   this->revertToLastCommit();
}

Concrete01WithSITC::~Concrete01WithSITC ()
{
    // Does nothing
}

int Concrete01WithSITC::setTrialStrain (double strain, double strainRate)
{

  // Set trial strain
  Tstrain = strain;

   TminStrain = CminStrain;
   //TmaxStrain = CmaxStrain;
   Tindex = Cindex;

  TslopeSITC = CslopeSITC;
  TendStrainSITC = CendStrainSITC;
  TunloadSlope = CunloadSlope;

  // Determine change in strain from last converged state
  double dStrain = Tstrain - Cstrain;

  if (fabs(dStrain) < DBL_EPSILON) {
    return 0;
  }

  if (Tstrain < 0.0) {  // compression
     if (Tstrain <= CminStrain) { // further on envelope curve
          TminStrain = Tstrain;
          envelope();
          unload();
          Tindex = 1;
     }
     else if (Tstrain >= TendStrainSITC) {
          Tstress = 0.0;
          Ttangent = 0.0;
          Tindex = 5;
     }
     else { // anywhere in compression greater than minimum strain
          if (dStrain <= 0.0) { //loading in compression
                  if (Cindex == 2 || Cindex == 1) {
                          Tstress = Cstress + TunloadSlope*dStrain;
                          Ttangent = TunloadSlope;
                          Tindex = 2;
```

```
			}
			else if (Cindex == 3) {
				Tstress = Cstress + TslopeSITC*dStrain;
				Ttangent = TslopeSITC;
				Tindex = 3;
			}
			else if (Cindex == 5) {
				if (Tstrain <= TendStrainSITC && Cstrain >= TendStrainSITC) {
					Ttangent = TslopeSITC;
					Tstress = TslopeSITC*(Tstrain-TendStrainSITC);
					Tindex = 3;
				}
				else if (Tstrain <= TendStrain) {
					Ttangent = TunloadSlope;
					Tstress = TunloadSlope*(Tstrain-TendStrain);
					Tindex = 2;
				}
				else {
					Ttangent = 0.0;
					Tstress = 0.0;
					Tindex = 5;
				}
			}
			else {

				opserr << "something in compression is wrong!! Cstrain " << endln;
			}
		}
		else { // unloading in compression
			if (Cindex == 1 || Cindex == 2) { //unloading on regular branch
				if (Tstrain >= TendStrain) {
					Tstress = 0.0;
					Ttangent = 0.0;
					Tindex = 5;
				}
				else {
					Tstress = Cstress + TunloadSlope*dStrain;
					Ttangent = TunloadSlope;
					Tindex = 2;
				}
			}
			else if (Cindex == 3) {
				Tstress = Cstress + TslopeSITC*dStrain;
				Ttangent = TslopeSITC;
			    Tindex = 3;
				if (Tstress > 0.0) {
					opserr << "PROBLEM IN UNLOADING IN COMPRESSION!!!" << endln;
				}
			}
			else if (Cindex == 5) { // index must be 5
				Tstress = 0.0;
				Ttangent = 0.0;
				Tindex = 5; // **************
			}
			else {
				opserr << "Something is wrong in tension!!!! Cindex is " << endln;
			}
		}
	}
}
```

```
  else { // TENSION
    Ttangent = 0.0;
    Tstress = 0.0;
    Tindex = 5;
  }
  return 0;
}

int
Concrete01WithSITC::setTrial (double strain, double &stress, double &tangent, double strainRate)
{
   TminStrain = CminStrain;
   //TmaxStrain = CmaxStrain;
   Tindex = Cindex;

  // Set trial strain
  Tstrain = strain;

  TslopeSITC = CslopeSITC;
  TendStrainSITC = CendStrainSITC;
  TunloadSlope = CunloadSlope;

  // Determine change in strain from last converged state
  double dStrain = Tstrain - Cstrain;

  if (fabs(dStrain) < DBL_EPSILON) {
    tangent = Ttangent;
    stress = Tstress;
    return 0;
  }

  TendStrainSITC = 0.03;

  if (Tstrain >=  TendStrainSITC ) {
    Ttangent = 0.0;
    Tstress = 0.0;
    Tindex = 5;
    tangent = Ttangent;
    stress = Tstress;
    return 0;
  }

  if (Tstrain < 0.0) {  // compression
    if (Tstrain <= CminStrain) { // further on envelope curve
         TminStrain = Tstrain;
         envelope();
         unload();
         Tindex = 1;
    }
    else if (Tstrain >= TendStrainSITC) {
         Tstress = 0.0;
         Ttangent = 0.0;
         Tindex = 5;
    }
    else { // anywhere in compression greater than minimum strain
         if (dStrain <= 0.0) { //loading in compression
                 if (Cindex == 2 || Cindex == 1) {
                         Tstress = Cstress + TunloadSlope*dStrain;
                         Ttangent = TunloadSlope;
                         Tindex = 2;  //
```

```
            }
            else if (Cindex == 3) {
                    Tstress = Cstress + TslopeSITC*dStrain;
                    Ttangent = TslopeSITC;
                    Tindex = 3;
            }
            else if (Cindex == 5) {
                    if (Tstrain <= TendStrainSITC && Cstrain >= TendStrainSITC) {
                            Ttangent = TslopeSITC;
                            Tstress = TslopeSITC*(Tstrain-TendStrainSITC);
                            Tindex = 3;
                    }
                    else if (Tstrain <= TendStrain) {
                            Ttangent = TunloadSlope;
                            Tstress = TunloadSlope*(Tstrain-TendStrain);
                            Tindex = 2;
                    }
                    else {
                            Ttangent = 0.0;
                            Tstress = 0.0;
                            Tindex = 5;
                    }
            }
            else {

                    opserr << "something in compression is wrong!! Cstrain " << endln;
            }
    }
    else { // unloading in compression
            if (Cindex == 1 || Cindex == 2) { //unloading on regular branch
                    if (Tstrain >= TendStrain) {
                            Tstress = 0.0;
                            Ttangent = 0.0;
                            Tindex = 5;
                    }
                    else {
                            Tstress = Cstress + TunloadSlope*dStrain;
                            Ttangent = TunloadSlope;
                            Tindex = 2;
                    }
            }
            else if (Cindex == 3) {
                    Tstress = Cstress + TslopeSITC*dStrain;
                    Ttangent = TslopeSITC;
                Tindex = 3;
                    if (Tstress > 0.0) {
                            opserr << "PROBLEM IN UNLOADING IN COMPRESSION!!!" << endln;
                    }
            }
            else if (Cindex == 5) { // index must be 5
                    Tstress = 0.0;
                    Ttangent = 0.0;
                    Tindex = 5; // **************
            }
            else {
                    opserr << "Something is wrong in tension!!!! Cindex is " << endln;
            }
    }
 }
}
```

```
  else { // TENSION

     if (dStrain > 0.0) { // going toward tension
          if (Cindex == 1 || Cindex == 2 || Cindex == 5 || Cindex == 0) {
                  Tstress = 0.0;
                  Ttangent = 0.0;
                  Tindex = 5;
          }
          else if (Cindex == 3) {
                  Tstress = Cstress + TslopeSITC*dStrain;
                  Ttangent = TslopeSITC;
                  Tindex = 3;
          }
          else {
                  opserr << " something is wrong in tension loading!!! Cindex " << endln;
          }
     }
     else {  // going toward compression
          if (Cindex == 5) {
                  if (Tstrain <= TendStrainSITC && Cstrain >= TendStrainSITC) {
                          Ttangent = TslopeSITC;
                          Tstress = TslopeSITC*(Tstrain-TendStrainSITC);
                          Tindex = 3;
                  }
                  else {
                          Ttangent = 0.0;
                          Tstress = 0.0;
                          Tindex = 5;
                  }
          }
          else if (Cindex == 3) {
                  Ttangent = TslopeSITC;
                  Tstress = Cstress + TslopeSITC*dStrain;
                  Tindex = 3;
          }
          else {
                  opserr << "something is wrong in tension going to compression " << endln;
          }
     }
  }
  stress = Tstress;
  tangent = Ttangent;
  return 0;
}

void Concrete01WithSITC::reload ()
{

   if (Tstrain <= TminStrain) {

        TminStrain = Tstrain;
        // Determine point on envelope
        envelope ();

        unload ();
   }
   else if (Tstrain <= TendStrain) {
        Ttangent = TunloadSlope;
        Tstress = Ttangent*(Tstrain-TendStrain);
   }
```

```
   else {
        Tstress = 0.0;
        Ttangent = 0.0;
   }

}

void Concrete01WithSITC::envelope ()
{
   if (Tstrain > epsc0) {
        double eta = Tstrain/epsc0;
        Tstress = fpc*(2*eta-eta*eta);
        double Ec0 = 2.0*fpc/epsc0;
        Ttangent = Ec0*(1.0-eta);
   }
   else if (Tstrain > epscu) {
        Ttangent = (fpc-fpcu)/(epsc0-epscu);
        Tstress = fpc + Ttangent*(Tstrain-epsc0);
   }
   else {
        Tstress = fpcu;
        Ttangent = 0.0;
   }
}

void Concrete01WithSITC::getSITCslope ()
{
   double tempStrain = Tstrain;
   double tempStress = Tstress;
   Tstrain = CminStrain;
   envelope();
   TslopeSITC = Tstress/(CminStrain-TendStrainSITC);
   Tstrain = tempStrain;
   Tstress = tempStress;
}

void Concrete01WithSITC::unload ()
{
   double tempStrain = TminStrain;

   if (tempStrain < epscu)
        tempStrain = epscu;

   double eta = tempStrain/epsc0;

   double ratio = 0.707*(eta-2.0) + 0.834;

   if (eta < 2.0)
        ratio = 0.145*eta*eta + 0.13*eta;

   TendStrain = ratio*epsc0;
   TslopeSITC = Tstress/(TminStrain - TendStrainSITC);

   double temp1 = TminStrain - TendStrain;

   double Ec0 = 2.0*fpc/epsc0;

   double temp2 = Tstress/Ec0;

   if (temp1 > -DBL_EPSILON) {   // temp1 should always be negative
```

```
        TunloadSlope = Ec0;
   }
   else if (temp1 <= temp2) {
        TendStrain = TminStrain - temp1;
        TunloadSlope = Tstress/temp1;
   }
   else {
        TendStrain = TminStrain - temp2;
        TunloadSlope = Ec0;
   }
}

double Concrete01WithSITC::getStress ()
{
   return Tstress;
}

double Concrete01WithSITC::getStrain ()
{
   return Tstrain;
}

double Concrete01WithSITC::getTangent ()
{
   return Ttangent;
}

void Concrete01WithSITC::determineTrialState (double dStrain)

{
   TminStrain = CminStrain;
   TendStrain = CendStrain;
   TunloadSlope = CunloadSlope;

   double tempStress = Cstress + TunloadSlope*dStrain;

   // Material goes further into compression
   if (dStrain <= 0.0) {

        reload ();

        if (tempStress > Tstress) {
                Tstress = tempStress;
                Ttangent = TunloadSlope;
        }
   }

   // Material goes TOWARD tension
   else if (tempStress <= 0.0) {
        Tstress = tempStress;
        Ttangent = TunloadSlope;
   }

   // Made it into tension
   else {
       Tstress = 0.0;
        Ttangent = 0.0;
   }
}
```

```
int Concrete01WithSITC::commitState ()
{
   // History variables
   CminStrain = TminStrain;
   CunloadSlope = TunloadSlope;
   CendStrain = TendStrain;
   CmaxStrain = TmaxStrain;
   CslopeSITC = TslopeSITC;
   CendStrainSITC = TendStrainSITC;
   Cindex = Tindex;
   CsmallStrainIndex = TsmallStrainIndex;

   // State variables
   Cstrain = Tstrain;
   Cstress = Tstress;
   Ctangent = Ttangent;

   return 0;
}

int Concrete01WithSITC::revertToLastCommit ()
{
   // Reset trial history variables to last committed state
   TminStrain = CminStrain;
   TendStrain = CendStrain;
   TunloadSlope = CunloadSlope;
   TmaxStrain = CmaxStrain;
   TslopeSITC = CslopeSITC;
   TendStrainSITC = CendStrainSITC;
   Tindex = Cindex;
   TsmallStrainIndex = CsmallStrainIndex;

   // Recompute trial stress and tangent
   Tstrain = Cstrain;
   Tstress = Cstress;
   Ttangent = Ctangent;

   return 0;
}

int Concrete01WithSITC::revertToStart ()
{
  double Ec0 = 2.0*fpc/epsc0;

   // History variables
   CminStrain = 0.0;
   CunloadSlope = Ec0;
   CendStrain = 0.0;
   CmaxStrain = 0.0;
   CslopeSITC = 0.0;
   CendStrainSITC = 0.0;
   Cindex = 0;
   CsmallStrainIndex = 0;

   // State variables
   Cstrain = 0.0;
   Cstress = 0.0;
   Ctangent = Ec0;

   // Reset trial variables and state
```

```
   this->revertToLastCommit();

   return 0;
}

UniaxialMaterial* Concrete01WithSITC::getCopy ()
{
   Concrete01WithSITC* theCopy = new Concrete01WithSITC(this->getTag(),
                                  fpc, epsc0, fpcu, epscu);

   // Converged history variables
   theCopy->CminStrain = CminStrain;
   theCopy->CunloadSlope = CunloadSlope;
   theCopy->CendStrain = CendStrain;
   theCopy->CmaxStrain = CmaxStrain;
   theCopy->CslopeSITC = CslopeSITC;
   theCopy->CendStrainSITC = CendStrainSITC;
   theCopy->Cindex = Cindex;
   theCopy->CsmallStrainIndex = CsmallStrainIndex;

   // Converged state variables
   theCopy->Cstrain = Cstrain;
   theCopy->Cstress = Cstress;
   theCopy->Ctangent = Ctangent;

   return theCopy;
}

int Concrete01WithSITC::sendSelf (int commitTag, Channel& theChannel)
{
   int res = 0;
   static Vector data(16);
   data(0) = this->getTag();

   // Material properties
   data(1) = fpc;
   data(2) = epsc0;
   data(3) = fpcu;
   data(4) = epscu;

   // History variables from last converged state
   data(5) = CminStrain;
   data(6) = CunloadSlope;
   data(7) = CendStrain;

   // State variables from last converged state
   data(8) = Cstrain;
   data(9) = Cstress;
   data(10) = Ctangent;

   // variables added by WL
   data(11) = CmaxStrain;
   data(12) = CslopeSITC;
   data(13) = CendStrainSITC;
   data(14) = Cindex;
   data(15) = CsmallStrainIndex;

   // Data is only sent after convergence, so no trial variables
   // need to be sent through data vector
```

```
   res = theChannel.sendVector(this->getDbTag(), commitTag, data);
   if (res < 0)
      opserr << "Concrete01WithSITC::sendSelf() - failed to send data\n";

   return res;
}

int Concrete01WithSITC::recvSelf (int commitTag, Channel& theChannel,
                                 FEM_ObjectBroker& theBroker)
{
   int res = 0;
   static Vector data(16);
   res = theChannel.recvVector(this->getDbTag(), commitTag, data);

   if (res < 0) {
      opserr << "Concrete01WithSITC::recvSelf() - failed to receive data\n";
      this->setTag(0);
   }
   else {
      this->setTag(int(data(0)));

      // Material properties
      fpc = data(1);
      epsc0 = data(2);
      fpcu = data(3);
      epscu = data(4);

      // History variables from last converged state
      CminStrain = data(5);
      CunloadSlope = data(6);
      CendStrain = data(7);

      // State variables from last converged state
      Cstrain = data(8);
      Cstress = data(9);
      Ctangent = data(10);

     // variables added by WL
     data(11) = CmaxStrain;
      data(12) = CslopeSITC;
      data(13) = CendStrainSITC;
     data(14) = Cindex;
     data(15) = CsmallStrainIndex;

      // Set trial state variables
      Tstrain = Cstrain;
      Tstress = Cstress;
      Ttangent = Ctangent;
   }

   return res;
}

void Concrete01WithSITC::Print (OPS_Stream& s, int flag)
{
   s << "Concrete01WithSITC, tag: " << this->getTag() << endln;
   s << "  fpc: " << fpc << endln;
   s << "  epsc0: " << epsc0 << endln;
   s << "  fpcu: " << fpcu << endln;
   s << "  epscu: " << epscu << endln;
```

File: ECC01.h

```
#ifndef ECC01_h
#define ECC01_h

// File: ECC01.h
//
// Written: Won Lee of Stanford University
// Created: 09/04
// Revision: A
//
// Description: This file contains the class definition for
// ECC01.h
//   - ECC model based on Han et al. model
//      (Han TS, Feenstra PH, Billington SL, ACI Structural Journal,
//              Nov-Dec 2003, "Simulation of Highly Ductile Fiber Reinforced
//              Cement-Based Composite Components Under Cyclic Loading")
//

#include <UniaxialMaterial.h>

class ECC01 : public UniaxialMaterial
{
 public:
  ECC01 (int tag, double SIGT0, double EPST0, double SIGT1, double EPST1, double EPST2, double SIGC0,
   double EPSC0, double EPSC1, double ALPHAT1, double ALPHAT2, double ALPHAC, double ALPHACU, double
   BETAT, double BETAC);
  ECC01 ();
  ~ECC01();

      int setTrialStrain(double strain, double strainRate = 0.0);
      int setTrial (double strain, double &stress, double &tangent, double strainRate = 0.0);
      double getStrain(void);
      double getStress(void);
      double getTangent(void);
      double getInitialTangent(void) {return sigc0/epsc0;}

      int commitState(void);
      int revertToLastCommit(void);
      int revertToStart(void);

      UniaxialMaterial *getCopy(void);

      int sendSelf(int commitTag, Channel &theChannel);
      int recvSelf(int commitTag, Channel &theChannel,
         FEM_ObjectBroker &theBroker);

      void Print(OPS_Stream &s, int flag =0);

   protected:

   private:
      /*** Material Properties ***/
      double sigt0;             // Tensile cracking stress
      double epst0;             // Strain at tensile cracking
      double sigt1;             // Peak tensile stress
      double epst1;             // Peak tensile strain
     double epst2;             // Ultimate tensile strain
     double sigc0;             // Peak compressive stress
    double epsc0;              //      Peak             compressive strain
```

```
    double epsc1;              // Ultimate compressive strain
    double alphaT1;            // Constant parameter for unloading equation in tensile strain-
                                  hardening region
    double alphaT2;            // Constant parameter for unloading equation in tensile
                                   softening region (=1 for linear unloading)
    double alphaC;             // Constant parameter for unloading equation in compressive
                                  softening region
    double alphaCU;            // Constant parameter for envelope compression softening
                                  equation
    double betaT;              // Constant parameter for permanent strain in tension
    double betaC;              // Constant parameter for permanent strain in compression

     /*** CONVERGED History Variables ***/
     double CminStrain;   // Smallest (most negative) previous concrete strain (compression)
     double CmaxStrain;   // Largest previous conrete strain (tension)
     double Cstmp;        // temporary stress value, used to compute stresses and
                              strains in re/unloading
     double Cetmp;        // temporary strain value, used to compute stresses and strains in
                             re/unloading
     int Cindex;          // Index that tells you where you are on the stress-strain curve

     /*** CONVERGED State Variables ***/
     double Cstrain;
     double Cstress;
     double Ctangent;  // Don't need Ctangent other than for revert and sendSelf/recvSelf

     /*** TRIAL History Variables ***/
     double TminStrain;
     double TmaxStrain;
     double Tstmp;
     double Tetmp;
     int Tindex;

     /*** TRIAL State Variables ***/
     double Tstrain;
     double Tstress;
     double Ttangent; // Not really a state variable, but declared here
                      // for convenience

     //void determineTrialState (double dStrain);

     void envelope();
     void ECCGetStressAndStiffness(int index, double sigmax, double epstul, double sigmin, double
  epscul);
};

#endif
```

File: ECC01.cpp

```
//
// Written by: Won Lee of Stanford University
// Created: 09/04

// Description: This file contains the class implementation for
// ECC01.
//   - ECC model based on Han et al. model
//      (Han TS, Feenstra PH, Billington SL, ACI Structural Journal,
//              Nov-Dec 2003, "Simulation of Highly Ductile Fiber Reinforced
//              Cement-Based Composite Components Under Cyclic Loading")
//

#include "ECC01.h"
#include <Vector.h>
#include <Matrix.h>
#include <Channel.h>
#include <Information.h>
#include <math.h>
#include <float.h>

#define MAT_TAG_ECC01 1000

ECC01::ECC01
(int tag, double SIGT0, double EPST0, double SIGT1, double EPST1, double EPST2, double SIGC0,
   double EPSC0, double EPSC1, double ALPHAT1, double ALPHAT2, double ALPHAC, double ALPHACU, double
   BETAT, double BETAC)
  :UniaxialMaterial(tag, MAT_TAG_ECC01),
   sigt0(SIGT0), epst0(EPST0), sigt1(SIGT1), epst1(EPST1),
   epst2(EPST2), sigc0(SIGC0), epsc0(EPSC0), epsc1(EPSC1),
   alphaT1(ALPHAT1), alphaT2(ALPHAT2), alphaC(ALPHAC), alphaCU(ALPHACU), betaT(BETAT), betaC(BETAC),
   CminStrain(0.0), CmaxStrain(0.0),
   Cstrain(0.0), Cstress(0.0),
   Cstmp(0.0), Cetmp(0.0), Cindex(0), TmaxStrain(0.0), TminStrain(0.0), Tindex(0)
{

   // Make all compressive parameters negative

   if (sigc0 > 0.0)
        sigc0 = -sigc0;

   if (epsc0 > 0.0)
        epsc0 = -epsc0;

   if (epsc1 > 0.0)
        epsc1 = -epsc1;

   // Initial tangent
   double Ec0 = sigc0/epsc0;
   Ctangent = Ec0;
   Ttangent = Ec0;

   // Set trial values
   this->revertToLastCommit();
}

ECC01::ECC01():UniaxialMaterial(0, MAT_TAG_ECC01),
 sigt0(0.0), epst0(0.0), sigt1(0.0), epst1(0.0),
 epst2(0.0),     sigc0(0.0),     epsc0(0.0),            epsc1(0.0),
```

```
 alphaT1(0.0), alphaT2(0.0), alphaC(0.0), alphaCU(0.0), betaT(0.0), betaC(0.0),
 CminStrain(0.0), CmaxStrain(0.0),
 Cstrain(0.0), Cstress(0.0),
 Cstmp(0.0), Cetmp(0.0), Cindex(0), TmaxStrain(0.0), TminStrain(0.0), Tindex(0)
{
  // Set trial values
  this->revertToLastCommit();
}

ECC01::~ECC01 ()
{
   // Does nothing
}

int ECC01::setTrialStrain (double strain, double strainRate)
{
  double sigmax =0.0, epstul =0.0, sigmin =0.0, epscul =0.0;

  // Set trial strain
  Tstrain = strain;

  // update max and min values
  if (Tstrain > TmaxStrain) {
    TmaxStrain = Tstrain;
  }
  if (Tstrain < TminStrain) {
    TminStrain = Tstrain;
  }

  double dStrain = Tstrain - Cstrain;

  if (fabs(dStrain) < DBL_EPSILON)
    return 0;

  // TENSION
  if (Tstrain > 0.0) {
    // loading  in tension
    if (TmaxStrain <= Tstrain) {
          if (Tstrain <= epst0) {
                  Tindex = 1;
          }
          else if (Tstrain <= epst1) {
                  Tindex = 2;
          }
          else if (Tstrain <= epst2) {
                  Tindex = 3;
          }
          else {
                  Tindex = 4;
          }
    }
    else {
          // unloading/reloading in tension (hardening, first branch)
          if (TmaxStrain <= epst0) {
                  Tindex = 1;
          }
          // unloading/reloading in tension (hardening, second branch)
          else if (TmaxStrain <= epst1) {
                  // unloading (tension:hardening second branch)
                  epstul = betaT*(TmaxStrain-epst0);
```

```
		sigmax = sigt0 + (sigt1-sigt0)*(TmaxStrain-epst0)/(epst1-epst0);
		if (Tstrain <= Cstrain) {
			if (Tstrain <= epstul) {
				Tindex = 9;
			}
			else {
			      if (Cindex == 2) {
				Tstmp = sigmax;
				Tetmp = TmaxStrain;
			      }
			      else if (Cindex == 7) {
				Tstmp = Cstress;
				Tetmp = Cstrain;
			      }
			      Tindex = 5;
			}
		}
		else {// reloading (tension:hardening second branch)
			if (Tstrain <= epstul) {
				Tindex = 9;
			}
			else {
				if (Cindex == 5) {
					Tstmp = Cstress;
					Tetmp = Cstrain;
				}
				else if ((Cindex == 9) || (Cindex <= -1)) {
					Tstmp = 0.0;
					Tetmp = epstul;
				}
				Tindex = 7;
			}
		}
	}
	//unloading/reloading in tension (softening region)
	else if (TmaxStrain <= epst2) {
		epstul = betaT*(epst1-epst0);
		sigmax = sigt1*(1.0-(TmaxStrain-epst1)/(epst2-epst1));
		//unloading (tension:softening)
		if (Tstrain <= Cstrain) {
			if (Tstrain <= epstul) {
				Tindex =9;
			}
			else {
				if (Cindex == 3) {
					Tstmp = sigmax;
					Tetmp = TmaxStrain;
				}
				else if (Cindex ==8) {
					Tstmp = Cstress;
					Tetmp = Cstrain;
				}
				Tindex = 6;
			}
		}
		// reloading (tension:softening)
		else {
			if (Tstrain <= epstul) {
				Tindex = 9;
			}
```

```
                        else {
                                if (Cindex == 6) {
                                        Tstmp = Cstress;
                                        Tetmp = Cstrain;
                                }
                                else if (Cindex == 9) {
                                        Tstmp = 0.0;
                                        Tetmp = epstul;
                                }
                                Tindex = 8;
                        }
                }
        }
        else {
                if (Tstrain <= epst2) {
                        Tindex = 9;
                }
                else {
                        Tindex = 4;
                }
        }
   }
}

else { // COMPRESSION
   //Loading in compression
   if (TminStrain >= Tstrain) {
        if (Tstrain >= epsc0) {
                Tindex = -1;
        }
        else if (Tstrain >= epsc1) {
                Tindex = -2;
        }
        else {
                Tindex = -3;
        }
   }
   else {
        //unloading/reloading in compression
        if (TminStrain >= epsc0) {
                // unloading/reloading in compression:pre-peak
                Tindex = -1;
        }
        else if (TminStrain >= epsc1) {
                //unloading compression:post-peak
                epscul = betaC*(TminStrain-epsc0);
                sigmin = sigc0*pow(((TminStrain-epsc1)/(epsc0-epsc1)),alphaCU);
                //
                if (Tstrain >= Cstrain) {
                        if (Tstrain >= epscul) {
                                Tindex = -6;
                        }
                        else {
                                if (Cindex == -2) {
                                        Tstmp = sigmin;
                                        Tetmp = TminStrain;
                                }
                                else if (Cindex == -5) {
                                        Tstmp = Cstress;
                                        Tetmp = Cstrain;
```

```
                                }
                                Tindex = -4;
                        }
                }
                // reloading compression:post-peak
                else {
                        if (Tstrain >= epscul) {
                                Tindex = -6;
                        }
                        else {
                                if (Cindex == -4) {
                                        Tstmp = Cstress;
                                        Tetmp = Cstrain;
                                }
                                else if ((Cindex == -6) || (Cindex >= 1)) {
                                        Tstmp = 0.0;
                                        Tetmp = epscul;
                                }
                                Tindex = -5;
                        }
                }
        }
        else  {
                if (Tstrain >= epsc1) {
                        Tindex = -6;
                }
                else {
                        Tindex = -3;
                }
        }
    }

  }

  ECCGetStressAndStiffness (Tindex, sigmax, epstul, sigmin, epscul);

  return 0;

}

int ECC01::setTrial (double strain, double &stress, double &tangent, double strainRate)
{
  double sigmax =0.0, epstul =0.0, sigmin =0.0, epscul =0.0;

  // Set trial strain
  Tstrain = strain;

  if (Tstrain > TmaxStrain) {
     TmaxStrain = Tstrain;
  }
  if (Tstrain < TminStrain) {
     TminStrain = Tstrain;
  }

  double dStrain = Tstrain - Cstrain;

  if (fabs(dStrain) < DBL_EPSILON) {
    tangent = Ttangent;
    stress = Tstress;
    return 0;
```

```
}

// TENSION
if (Tstrain > 0.0) {
   // loading  in tension
   if (TmaxStrain <= Tstrain) {
        if (Tstrain <= epst0) {
                Tindex = 1;
        }
        else if (Tstrain <= epst1) {
                Tindex = 2;
        }
        else if (Tstrain <= epst2) {
                Tindex = 3;
        }
        else {
                Tindex = 4;
        }
   }
   else {
        // unloading/reloading in tension (hardening, first branch)
        if (TmaxStrain <= epst0) {
                Tindex = 1;
        }
        // unloading/reloading in tension (hardening, second branch)
        else if (TmaxStrain <= epst1) {
                // unloading (tension:hardening second branch)
                epstul = betaT*(TmaxStrain-epst0);
                sigmax = sigt0 + (sigt1-sigt0)*(TmaxStrain-epst0)/(epst1-epst0);
                if (Tstrain <= Cstrain) {
                        if (Tstrain <= epstul) {
                                Tindex = 9;
                        }
                        else {
                              if (Cindex == 2) {
                                Tstmp = sigmax;
                                Tetmp = TmaxStrain;
                              }
                              else if (Cindex == 7) {
                                Tstmp = Cstress;
                                Tetmp = Cstrain;
                              }
                              Tindex = 5;
                        }
                }
                else {  // reloading (tension:hardening second branch)
                        if (Tstrain <= epstul) {
                                Tindex = 9;
                        }
                        else {
                                if (Cindex == 5) {
                                        Tstmp = Cstress;
                                        Tetmp = Cstrain;
                                }
                                else if ((Cindex == 9) || (Cindex <= -1)) {
                                        Tstmp = 0.0;
                                        Tetmp = epstul;
                                }
                                Tindex = 7;
                        }
```

```
                }
            }
            //unloading/reloading in tension (softening region)
            else if (TmaxStrain <= epst2) {
                epstul = betaT*(epst1-epst0);
                sigmax = sigt1*(1.0-(TmaxStrain-epst1)/(epst2-epst1));
                //unloading (tension:softening)
                if (Tstrain <= Cstrain) {
                    if (Tstrain <= epstul) {
                        Tindex =9;
                    }
                    else {
                        if (Cindex == 3) {
                            Tstmp = sigmax;
                            Tetmp = TmaxStrain;
                        }
                        else if (Cindex ==8) {
                            Tstmp = Cstress;
                            Tetmp = Cstrain;
                        }
                        Tindex = 6;
                    }
                }
                // reloading (tension:softening)
                else {
                    if (Tstrain <= epstul) {
                        Tindex = 9;
                    }
                    else {
                        if (Cindex == 6) {
                            Tstmp = Cstress;
                            Tetmp = Cstrain;
                        }
                        else if (Cindex == 9) {
                            Tstmp = 0.0;
                            Tetmp = epstul;
                        }
                        Tindex = 8;
                    }
                }
            }
            else {
                if (Tstrain <= epst2) {
                    Tindex = 9;
                }
                else {
                    Tindex = 4;
                }
            }
        }

    }

    else { // if it is compression
        //Loading in compression
        if (TminStrain >= Tstrain) {
            if (Tstrain >= epsc0) {
                Tindex = -1;
            }
            else if (Tstrain >= epsc1) {
```

```
				Tindex = -2;
			}
			else {
				Tindex = -3;
			}
		}
		else {
			//unloading/reloading in compression
			if (TminStrain >= epsc0) {
				// unloading/reloading in compression:pre-peak
				Tindex = -1;
			}
			else if (TminStrain >= epsc1) {
				//unloading compression:post-peak
				epscul = betaC*(TminStrain-epsc0);
				sigmin = sigc0*pow(((TminStrain-epsc1)/(epsc0-epsc1)),alphaCU);
				if (Tstrain >= Cstrain) {
					if (Tstrain >= epscul) {
						Tindex = -6;
					}
					else {
						if (Cindex == -2) {
							Tstmp = sigmin;
							Tetmp = TminStrain;
						}
						else if (Cindex == -5) {
							Tstmp = Cstress;
							Tetmp = Cstrain;
						}
						Tindex = -4;
					}
				}
				// reloading compression:post-peak
				else {
					if (Tstrain >= epscul) {
						Tindex = -6;
					}
					else {
						if (Cindex == -4) {
							Tstmp = Cstress;
							Tetmp = Cstrain;
						}
						else if ((Cindex == -6) || (Cindex >= 1)) {
							Tstmp = 0.0;
							Tetmp = epscul;
						}
						Tindex = -5;
					}
				}
			}
			else  {
				if (Tstrain >= epsc1) {
					Tindex = -6;
				}
				else {
					Tindex = -3;
				}
			}
		}
```

```
    //return 0;
  }

  ECCGetStressAndStiffness (Tindex, sigmax, epstul, sigmin, epscul);
  stress = Tstress;  //
  tangent = Ttangent;

  return 0;
}

void ECC01::ECCGetStressAndStiffness (int index, double sigmax, double epstul, double sigmin, double
   epscul)
{
   // anywhere on the envelope curve
   if ((Tindex >= -3) && (Tindex <= 4)) {
        envelope ();
   }
   // tension region
   else if (Tindex == 5) {

     if (Tetmp-epstul != 0.0) {
       Tstress = Tstmp*pow(((Tstrain-epstul)/(Tetmp-epstul)),alphaT1);
       Ttangent = alphaT1*Tstmp*pow(((Tstrain-epstul)/(Tetmp-epstul)),(alphaT1-1))*(1/(Tetmp-epstul));
     }

   }
   else if (Tindex== 6) {
     if (Tetmp-epstul != 0.0) {
        Tstress = Tstmp*pow(((Tstrain-epstul)/(Tetmp-epstul)),alphaT2);
        Ttangent = alphaT2*Tstmp*pow(((Tstrain-epstul)/(Tetmp-epstul)),(alphaT2-1))*(1/(Tetmp-epstul));
     }
   }
   else if (Tindex== 7) {
     if (TmaxStrain-Tetmp != 0.0) {
        Tstress = Tstmp + (sigmax-Tstmp)*(Tstrain-Tetmp)/(TmaxStrain-Tetmp);
        Ttangent = (sigmax-Tstmp)/(TmaxStrain-Tetmp);
     }
   }
   else if (Tindex== 8) {
     if (TmaxStrain-Tetmp != 0.0) {
        Tstress = Tstmp + (sigmax-Tstmp)*(Tstrain-Tetmp)/(TmaxStrain-Tetmp);
        Ttangent = (sigmax-Tstmp)/(TmaxStrain-Tetmp);
     }
   }
   else if (Tindex== 9) {
        Tstress = 0.0;
        Ttangent = 0.0;
   }
   // compression region
   else if (Tindex== -4) {
     if (Tetmp-epscul != 0.0) {
        Tstress = Tstmp*pow(((Tstrain-epscul)/(Tetmp-epscul)),alphaC);
        Ttangent = alphaC*Tstmp*pow(((Tstrain-epscul)/(Tetmp-epscul)),(alphaC-1))*(1/(Tetmp-epscul));
     }
   }
   else if (Tindex== -5) {
     if (TminStrain-Tetmp != 0.0) {
        Tstress = Tstmp + (sigmin-Tstmp)*(Tstrain-Tetmp)/(TminStrain-Tetmp);
        Ttangent = (sigmin-Tstmp)/(TminStrain-Tetmp);
     }
```

```
   }
   else if (Tindex== -6) {
         Tstress = 0.0;
         Ttangent = 0.0;
   }
}

void ECC01::envelope ()
{
   double initialSlope = sigt0/epst0;
   double Ec0 = sigc0/epsc0;

   if (Tstrain > 0) { //WL: if in tension
         if (Tstrain < epst0) {
                 Tstress = initialSlope*Tstrain;
                 Ttangent = initialSlope;
         }
         else if (Tstrain < epst1) {
                 Ttangent = (sigt1-sigt0)/(epst1-epst0);
                 Tstress = sigt0 + Ttangent*(Tstrain-epst0);
         }
         else if (Tstrain < epst2) {
                 Ttangent = (-sigt1)/(epst2-epst1);
                 Tstress = sigt1 + Ttangent*(Tstrain-epst1);
         }
         else {
                 Tstress = 0.0;
                 Ttangent = 0.0;
         }
   }
   else { // WL: if in compression
         if (Tstrain > epsc0) {
                 // for now hardcode in the r coefficient = 5
                 Tstress = sigc0*5*(Tstrain/epsc0)*(1/(5-1+pow(Tstrain/epsc0,5)));
                 //Ttangent                                  =                                  (1/pow(5-
   1+pow(Tstrain/epsc0,5),2))*((Tstrain/epsc0)*((1/epsc0)*5*pow(Tstrain/epsc0,5-1)       )-(1/epsc0)*(5-
   1+pow(Tstrain/epsc0,5)));
                 //Tstress = Ec0*Tstrain;
                 Ttangent = Ec0;
         }
         else if (Tstrain > epsc1) {
                 Ttangent   =   alphaCU*sigc0*pow(((Tstrain-epsc1)/(epsc0-epsc1)),(alphaCU-1))*(1/(epsc0-
   epsc1));
                 Tstress = sigc0*pow(((Tstrain-epsc1)/(epsc0-epsc1)),alphaCU);
         }
         else {
                 Tstress = 0.0;
                 Ttangent = 0.0;
         }
   }
}

double ECC01::getStress ()
{
   return Tstress;
}

double ECC01::getStrain ()
{
   return Tstrain;
```

```
}

double ECC01::getTangent ()
{
   return Ttangent;
}

int ECC01::commitState ()
{
   // History variables
   CminStrain = TminStrain;
   CmaxStrain = TmaxStrain;
   Cstmp = Tstmp;
   Cetmp = Tetmp;
   Cindex = Tindex;

   // State variables
   Cstrain = Tstrain;
   Cstress = Tstress;
   Ctangent = Ttangent;

   return 0;
}

int ECC01::revertToLastCommit ()
{
   // Reset trial history variables to last committed state
   TminStrain = CminStrain;
   TmaxStrain = CmaxStrain;
   Tstmp = Cstmp;
   Tetmp = Cetmp;
   Tindex = Cindex;

   // Recompute trial stress and tangent
   Tstrain = Cstrain;
   Tstress = Cstress;
   Ttangent = Ctangent;

   return 0;
}

int ECC01::revertToStart ()
{
  double Ec0 = sigc0/epsc0;

   // History variables
   CminStrain = 0.0;
   CmaxStrain = 0.0;
   Cstmp = 0.0;
   Cetmp = 0.0;
   Cindex = 0;

   // State variables
   Cstrain = 0.0;
   Cstress = 0.0;
   Ctangent = Ec0;

   // Reset trial variables and state
   this->revertToLastCommit();
```

```
   return 0;
}

UniaxialMaterial* ECC01::getCopy ()
{
   ECC01* theCopy = new ECC01(this->getTag(),
                              sigt0, epst0, sigt1, epst1, epst2, sigc0, epsc0, epsc1,
                              alphaT1, alphaT2, alphaC, alphaCU, betaT, betaC);

   // Converged history variables
   theCopy->CminStrain = CminStrain;
   theCopy->CmaxStrain = CmaxStrain;
   theCopy->Cstmp = Cstmp;
   theCopy->Cetmp = Cetmp;
   theCopy->Cindex = Cindex;

   // Converged state variables
   theCopy->Cstrain = Cstrain;
   theCopy->Cstress = Cstress;
   theCopy->Ctangent = Ctangent;

   return theCopy;
}

 int ECC01::sendSelf (int commitTag, Channel& theChannel)
{
   int res = 0;
   //static Vector data(11);
   static Vector data(23);
   data(0) = this->getTag();

   // Material properties
   data(1) = sigt0;
   data(2) = epst0;
   data(3) = sigt1;
   data(4) = epst1;
   data(5) = epst2;
   data(6) = sigc0;
   data(7) = epsc0;
   data(8) = epsc1;
   data(9) = alphaT1;
   data(10) = alphaT2;
   data(11) = alphaC;
   data(12) = alphaCU;
   data(13) = betaT;
   data(14) = betaC;

   // History variables from last converged state
   data(15) = CminStrain;
   data(16) = CmaxStrain;
   data(17) = Cstmp;
   data(18) = Cetmp;
   data(19) = Cindex;

   // State variables from last converged state
   data(20) = Cstrain;
   data(21) = Cstress;
   data(22) = Ctangent;

   res = theChannel.sendVector(this->getDbTag(), commitTag, data);
```

```
   if (res < 0)
      opserr << "ECC01::sendSelf() - failed to send data\n";

   return res;
}

int ECC01::recvSelf (int commitTag, Channel& theChannel,
                                 FEM_ObjectBroker& theBroker)
{
   int res = 0;
   static Vector data(23);
   res = theChannel.recvVector(this->getDbTag(), commitTag, data);

   if (res < 0) {
      opserr << "ECC01::recvSelf() - failed to receive data\n";
      this->setTag(0);
   }
   else {
      this->setTag(int(data(0)));

      // Material properties
     sigt0 = data(1);
     epst0 = data(2);
     sigt1 = data(3);
     epst1 = data(4);
     epst2 = data(5);
     sigc0 = data(6);
     epsc0 = data(7);
     epsc1 = data(8);
     alphaT1 = data(9);
     alphaT2 = data(10);
     alphaC = data(11);
     alphaCU = data(12);
     betaT = data(13);
     betaC = data(14);

      // History variables from last converged state
     CminStrain = data(15);
     CmaxStrain = data(16);
     Cstmp = data(17);
     Cetmp = data(18);
     Cindex = data(19);

      // State variables from last converged state
      Cstrain = data(20);
      Cstress = data(21);
      Ctangent = data(22);

      // Set trial state variables
      Tstrain = Cstrain;
      Tstress = Cstress;
      Ttangent = Ctangent;
   }

   return res;
}

void ECC01::Print (OPS_Stream& s, int flag)
{
   s << "ECC01, tag: " << this->getTag() << endln;
```

```
   s << "  sigt0: " << sigt0 << endln;
   s << "  epst0: " << epst0 << endln;
   s << "  sigt1: " << sigt1 << endln;
   s << "  epst1: " << epst1 << endln;
   s << "  epst2: " << epst2 << endln;
   s << "  sigc0: " << sigc0 << endln;
   s << "  epsc0: " << epsc0 << endln;
   s << "  epsc1: " << epsc1 << endln;
   s << "  alphaT1: " << alphaT1 << endln;
   s << "  alphaT2: " << alphaT2 << endln;
   s << "  alphaC: " << alphaC << endln;
   s << "  alphaCU: " << alphaCU << endln;
   s << "  betaT: " << betaT << endln;
   s << "  betaC: " << betaC << endln;
}
```

Appendix B: Comparison of Bridges with Different Column Heights

The PEER PBEE analysis reported in Chapter 5 was repeated for an alternative baseline bridge (Type 1 from Ketchum et al. 2004). This bridge has the same span lengths, deck width, and deck depth as the baseline bridge from Chapter 5 but with columns that were 22′ tall rather than 50′ tall. The columns were 4′ in diameter with 42 #10 bars (in bundles of 2 bars) in the longitudinal direction and #8 spirals at a spacing of 3.5 in.

The design for the UBPT columns for the 22′ column bridge was also created in a similar manner as those for the baseline 50′ column bridge wherein the amount of bonded longitudinal reinforcement was reduced and UBPT was added to achieve self-centering behavior. Also, the amount of transverse reinforcement was again increased to accommodate the additional axial load from the post-tensioning. The final design used a PT tendon with an area of 22 in.^{2} and stressed to 100 ksi, and bonded reinforcement consisted of 16 #10 bars in the longitudinal direction with #8 spirals at a spacing of 1.25 in. All models and assumptions used for the PBEE analysis were the same for the 22′ column bridges as they were for the baseline 50′ column bridges, and are summarized in Section 5.7.1.

The results from the four steps of the PEER analysis (hazard, structural, damage, and loss analyses) using the baseline assumptions outlined in Section 5.7.1 were combined using the framing integral (Eq. 2.1) to generate repair cost and downtime hazard curves. The repair cost for damage associated with peak drifts achieved, namely bar buckling and concrete spalling for both bridge types and column heights are shown in Figure B.1. These estimates were made using the procedure described in Section 5.5. The repair cost hazard curve for damage related to residual displacement is shown in Figure B.2. Repair costs for residual displacements were calculated assuming that if the bridge is in the excessive residual displacement damage state, it has to be demolished and replaced. The replacement cost for the bridge is taken as $1,344,000 and the standard deviation is taken as $621,000. Finally, the downtime hazard curve for these bridges is shown in Figure B.3 and is calculated as described in Section 5.6.

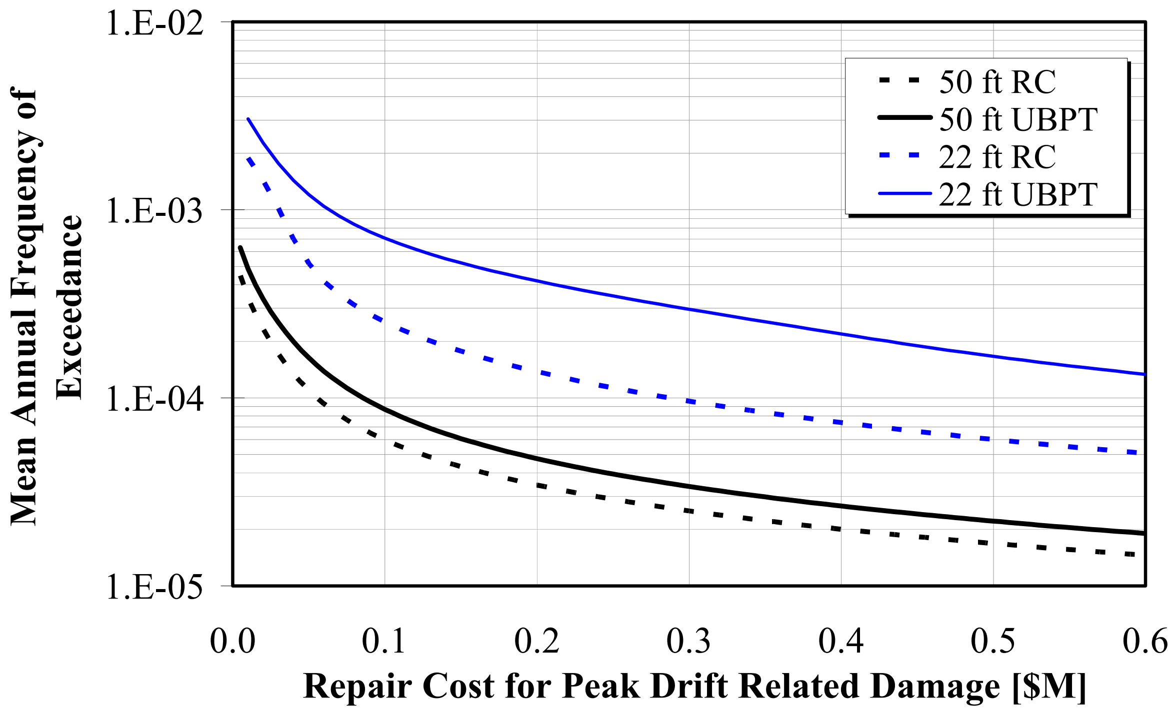

Fig. B.1 Repair cost hazard curves for spalling and buckling damage for the RC and UBPT bridges with 50′ and 22′ columns.

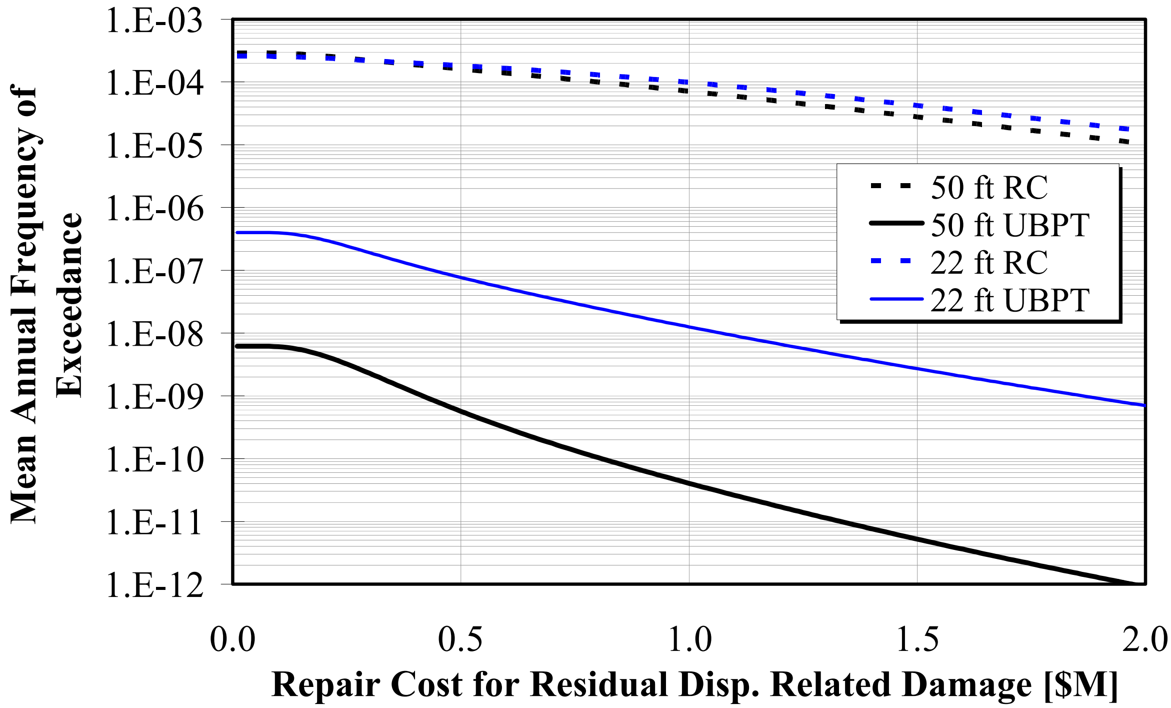

Fig. B.2 Repair cost hazard curves for residual displacement-related damage for the RC and UBPT bridges with 50′ and 22′ columns.

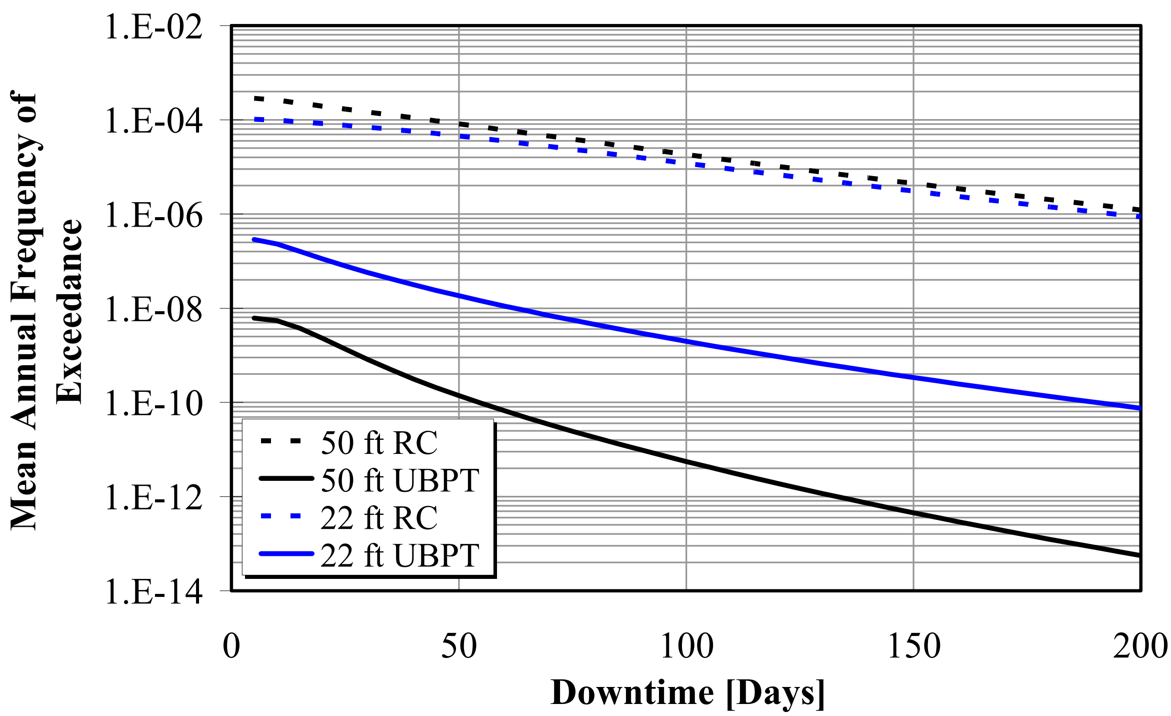

Fig. B.3 Downtime hazard curves for the RC and UBPT bridges with 50′ and 22′ columns.

The repair cost hazard curves for peak-drift induced damage (buckling, spalling; Fig. B.1) show that more damage is sustained in the bridges with shorter columns. For a given mean annual frequency of exceedance, the difference in repair costs for the UBPT bridge going from a 50′ column to a 22′ column is considerably greater than the increase in expected repair cost for a bridge with shorter RC columns. The larger increase in cost for the UBPT bridge with 22′ columns reflects the fact that more peak drift damage is expected in the shorter columns. The fragility curves for damage states related to cost are functions of column height, and the drift at which damage occurs is lower for shorter columns than longer columns.

The repair cost hazard curves for residual drift induced damage (Fig. B.2) shows very little difference in expected costs for the RC bridge regardless of column height because of the similarly low values of residual drifts sustained by both column types and because the residual drift fragility curve is not a function of column height. For the UBPT bridges, the difference was greater, which is attributed to the greater residual drifts sustained by the shorter columns. The large difference in mean annual frequency of exceedance for a given repair cost between the RC and UBPT bridges was therefore less pronounced for the bridges with shorter columns.

The downtime hazard curves showed similar trends to the residual-displacement-induced repair cost curves because downtime is also a function of residual displacement in this analysis. For a given value of downtime, there was a slightly lower mean annual frequency of occurrence for the RC bridge with 22′ columns relative to the RC bridge with 50′ columns. With the UBPT bridges, the mean annual frequency of occurrence increased when the shorter columns replaced the 50′ ones. While the difference between the RC and UBPT bridges is less pronounced with the 22′ columns, it remains none-the-less significant. For example, for a downtime of 30 days, the RC system has a mean annual frequency of exceedance of approximately 7.0E-5, which corresponds to a probability of 0.35 percent in 50 years. In comparison, for a downtime of 30 days, the UBPT system has a mean annual frequency of exceedance of approximately 5.7E-8, which corresponds to a probability of only 0.00029 percent in 50 years. With increasing values of downtime, the difference between the two systems increases.

Based on these analyses, the UBPT system will perform better than the RC system in this baseline bridge with tall columns rather than short ones.

Appendix C: Correlation between Peak and Residual Drifts in RC Bridge Columns

An additional study was carried out to investigate the correlation between the simulated residual displacements and peak displacements of the four 22′ RC columns used in the Type 1 bridge described in Appendix B and subjected to ground motions. An incremental dynamic analysis using the 17 earthquake motions with 7 intensity levels, described in Section 5.4, was performed giving 119 sets of peak and residual displacements for each column. This work was carried out by graduate researcher Yuka Nishikawa.

The data for each column were plotted and compared with a model proposed by MacRae and Kawashima (1997) for single-degree-of-freedom bilinear oscillators to estimate residual displacements for design. The model requires input of (1) predicted yield displacement, (2) an estimate of the peak displacement, and (3) the initial stiffness and the post-yield stiffness of the oscillators.

For the comparisons made here, it was assumed that the four columns of the bridge could be modeled as single-degree-of-freedom bilinear oscillators in the direction transverse to the length of the bridge. Pushover analyses were performed in the transverse direction on the columns in the bridge model, rather than on single, isolated columns.[1] From these pushover analyses, the yield displacement, the initial stiffness, and the post-yield stiffness of the columns were estimated. The peak transverse displacements were computed from the dynamic analyses. Together these values were used to estimate residual displacements.

---

[1] While performing the analysis on the columns within the bridge model was not explicitly stated in MacRae and Kawashima (1997), the example in their work described a full bridge model. Furthermore, results using only single-column pushover curves were evaluated, and gave considerably unrealistic predictions.

The initial and post-elastic stiffness for each column for the model was obtained from the slope of the force-displacement curve from pushover analyses. In all cases, the pushover curves had a positive stiffness ratio, r, as defined by MacRae and Kawashima (1997) where r is the ratio of the post-yield stiffness to the initial elastic stiffness. In determining these stiffnesses, "best-fit lines" in the initial elastic and post-elastic regions were taken but could vary greatly depending on the judgment of what a "best fit" is. It was found for the bridge studied here that the impact of small changes in judgment of a "best fit" significantly affected the resulting regression curve predicting the relationship between peak and residual displacements. Therefore a reasonable maximum and minimum value for each of the initial and post-elastic stiffnesses was taken, and regression curves were constructed with both results to give boundaries for the predictive model.

The results of the OpenSees incremental dynamic analyses and the MacRae and Kawashima predictions with the maximum and minimum pushover stiffness assumption for each column are shown in Figures C.1–C.4. In each plot, the predictions using the MacRae and Kawashima model are shown in blue for when minimum values for the initial and post-yield column stiffness are assumed and in red when the maximum values of these stiffnesses are assumed. The points on the plots represent the results of the 119 dynamic analyses on the bridge model.

The MacRae and Kawashima model fits the analytical data somewhat for columns 1 and 4, those closest to the abutments. These columns have a higher stiffness in the pushover analysis (due to the proximity of the abutments and the constraint the abutments provide) than columns 2 and 3. The predictions for columns 2 and 3 do not provide a reasonable match to the dynamic analyses. No clear relationship was found between the outliers for each column other than that several of the points with high residual drift (>2 in.) but low peak drift (<3 in.) were from the Tottori earthquake motion. Overall, the predictions were not very good. However it is recognized that the columns for this bridge subjected to earthquake motions do not act as true single-degree-of-freedom bilinear oscillators as is the case for the studies used to develop the predictive method. Improved methods for predicting the relationship between the peak and residual displacement of columns in a bridge system are needed.

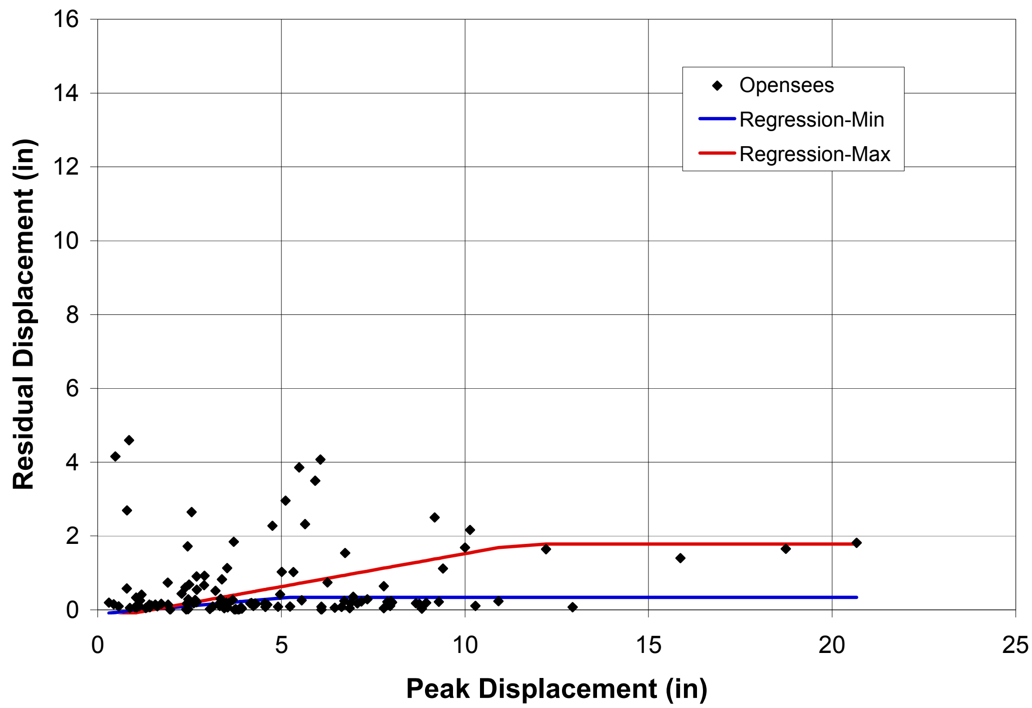

Fig. C.1 Peak vs. residual drift for column 1.

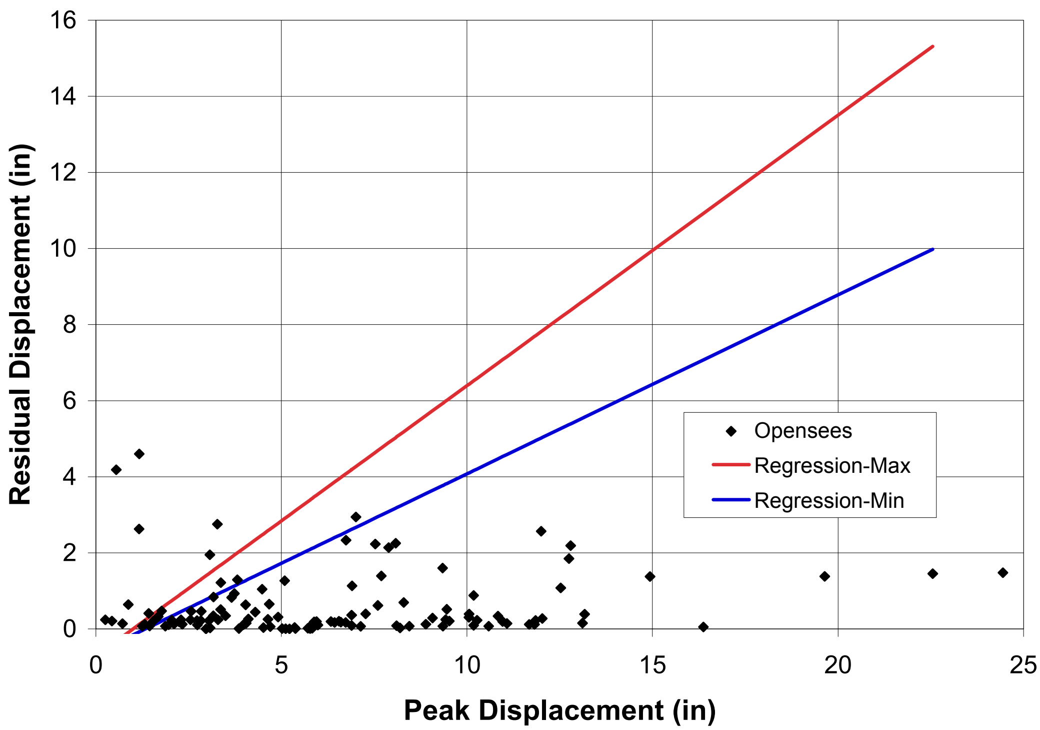

Fig. C.2 Peak vs. residual drift for column 2.

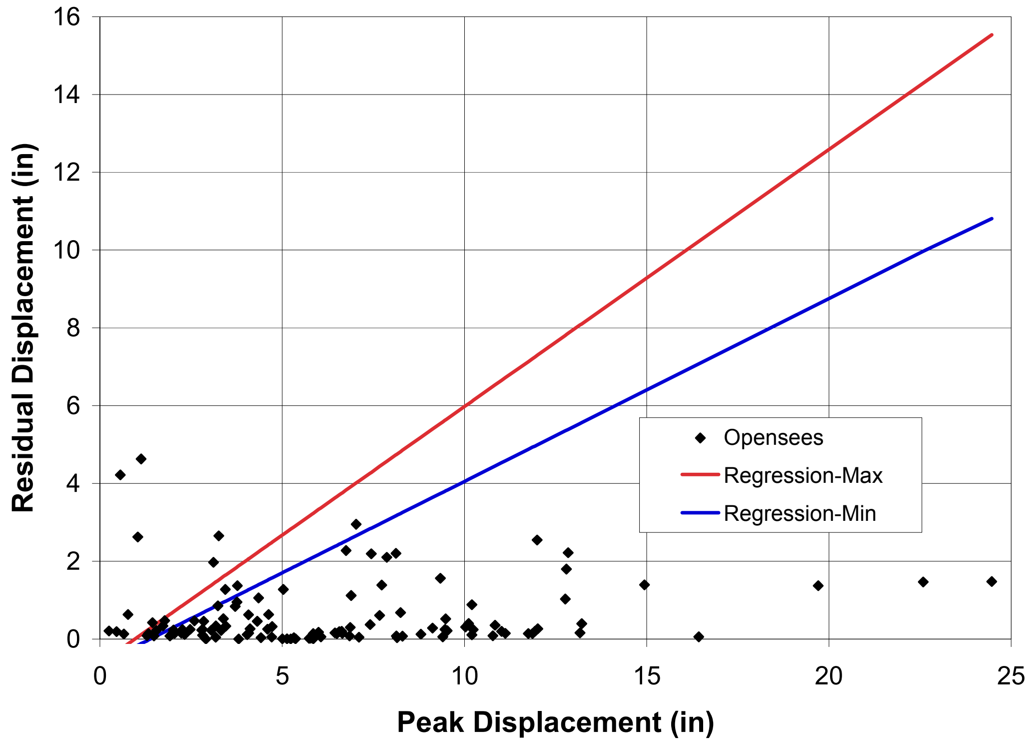

Fig. C.3 Peak vs. residual drift for column 3.

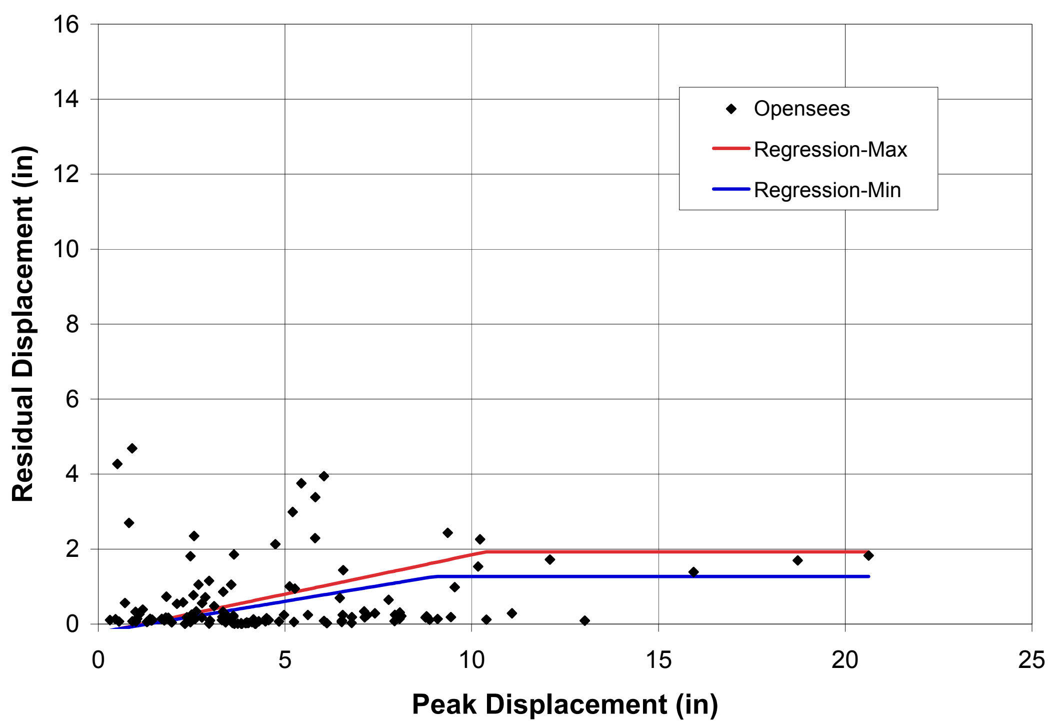

Fig. C.4 Peak vs. residual drift for column 4.

PEER REPORTS

PEER reports are available individually or by yearly subscription. PEER reports can be ordered at http://peer.berkeley.edu/publications/peer_reports.html or by contacting the Pacific Earthquake Engineering Research Center, 1301 South 46th Street, Richmond, CA 94804-4698. Tel.: (510) 665-3448; Fax: (510) 665-3456; Email: peer_editor@berkeley.edu

PEER 2009/03 *The Integration of Experimental and Simulation Data in the Study of Reinforced Concrete Bridge Systems Including Soil-Foundation-Structure Interaction.* Matthew Dryden and Gregory L. Fenves. November 2009.

PEER 2009/02 *Improving Earthquake Mitigation through Innovations and Applications in Seismic Science, Engineering, Communication, and Response. Proceedings of a U.S.-Iran Seismic Workshop.* October 2009.

PEER 2009/01 *Evaluation of Ground Motion Selection and Modification Methods: Predicting Median Interstory Drift Response of Buildings.* Curt B. Haselton, Ed. June 2009.

PEER 2008/10 *Technical Manual for Strata.* Albert R. Kottke and Ellen M. Rathje. February 2009.

PEER 2008/09 *NGA Model for Average Horizontal Component of Peak Ground Motion and Response Spectra.* Brian S.-J. Chiou and Robert R. Youngs. November 2008.

PEER 2008/08 *Toward Earthquake-Resistant Design of Concentrically Braced Steel Structures.* Patxi Uriz and Stephen A. Mahin. November 2008.

PEER 2008/07 *Using OpenSees for Performance-Based Evaluation of Bridges on Liquefiable Soils.* Stephen L. Kramer, Pedro Arduino, and HyungSuk Shin. November 2008.

PEER 2008/06 *Shaking Table Tests and Numerical Investigation of Self-Centering Reinforced Concrete Bridge Columns.* Hyung IL Jeong, Junichi Sakai, and Stephen A. Mahin. September 2008.

PEER 2008/05 *Performance-Based Earthquake Engineering Design Evaluation Procedure for Bridge Foundations Undergoing Liquefaction-Induced Lateral Ground Displacement.* Christian A. Ledezma and Jonathan D. Bray. August 2008.

PEER 2008/04 *Benchmarking of Nonlinear Geotechnical Ground Response Analysis Procedures.* Jonathan P. Stewart, Annie On-Lei Kwok, Yousseff M. A. Hashash, Neven Matasovic, Robert Pyke, Zhiliang Wang, and Zhaohui Yang. August 2008.

PEER 2008/03 *Guidelines for Nonlinear Analysis of Bridge Structures in California.* Ady Aviram, Kevin R. Mackie, and Božidar Stojadinović. August 2008.

PEER 2008/02 *Treatment of Uncertainties in Seismic-Risk Analysis of Transportation Systems.* Evangelos Stergiou and Anne S. Kiremidjian. July 2008.

PEER 2008/01 *Seismic Performance Objectives for Tall Buildings.* William T. Holmes, Charles Kircher, William Petak, and Nabih Youssef. August 2008.

PEER 2007/12 *An Assessment to Benchmark the Seismic Performance of a Code-Conforming Reinforced Concrete Moment-Frame Building.* Curt Haselton, Christine A. Goulet, Judith Mitrani-Reiser, James L. Beck, Gregory G. Deierlein, Keith A. Porter, Jonathan P. Stewart, and Ertugrul Taciroglu. August 2008.

PEER 2007/11 *Bar Buckling in Reinforced Concrete Bridge Columns.* Wayne A. Brown, Dawn E. Lehman, and John F. Stanton. February 2008.

PEER 2007/10 *Computational Modeling of Progressive Collapse in Reinforced Concrete Frame Structures.* Mohamed M. Talaat and Khalid M. Mosalam. May 2008.

PEER 2007/09 *Integrated Probabilistic Performance-Based Evaluation of Benchmark Reinforced Concrete Bridges.* Kevin R. Mackie, John-Michael Wong, and Božidar Stojadinović. January 2008.

PEER 2007/08 *Assessing Seismic Collapse Safety of Modern Reinforced Concrete Moment-Frame Buildings.* Curt B. Haselton and Gregory G. Deierlein. February 2008.

PEER 2007/07 *Performance Modeling Strategies for Modern Reinforced Concrete Bridge Columns.* Michael P. Berry and Marc O. Eberhard. April 2008.

PEER 2007/06 *Development of Improved Procedures for Seismic Design of Buried and Partially Buried Structures.* Linda Al Atik and Nicholas Sitar. June 2007.

PEER 2007/05 *Uncertainty and Correlation in Seismic Risk Assessment of Transportation Systems.* Renee G. Lee and Anne S. Kiremidjian. July 2007.

PEER 2007/04 *Numerical Models for Analysis and Performance-Based Design of Shallow Foundations Subjected to Seismic Loading.* Sivapalan Gajan, Tara C. Hutchinson, Bruce L. Kutter, Prishati Raychowdhury, José A. Ugalde, and Jonathan P. Stewart. May 2008.

PEER 2007/03 *Beam-Column Element Model Calibrated for Predicting Flexural Response Leading to Global Collapse of RC Frame Buildings.* Curt B. Haselton, Abbie B. Liel, Sarah Taylor Lange, and Gregory G. Deierlein. May 2008.

PEER 2007/02 *Campbell-Bozorgnia NGA Ground Motion Relations for the Geometric Mean Horizontal Component of Peak and Spectral Ground Motion Parameters.* Kenneth W. Campbell and Yousef Bozorgnia. May 2007.

PEER 2007/01 *Boore-Atkinson NGA Ground Motion Relations for the Geometric Mean Horizontal Component of Peak and Spectral Ground Motion Parameters.* David M. Boore and Gail M. Atkinson. May. May 2007.

PEER 2006/12 *Societal Implications of Performance-Based Earthquake Engineering.* Peter J. May. May 2007.

PEER 2006/11 *Probabilistic Seismic Demand Analysis Using Advanced Ground Motion Intensity Measures, Attenuation Relationships, and Near-Fault Effects.* Polsak Tothong and C. Allin Cornell. March 2007.

PEER 2006/10 *Application of the PEER PBEE Methodology to the I-880 Viaduct.* Sashi Kunnath. February 2007.

PEER 2006/09 *Quantifying Economic Losses from Travel Forgone Following a Large Metropolitan Earthquake.* James Moore, Sungbin Cho, Yue Yue Fan, and Stuart Werner. November 2006.

PEER 2006/08 *Vector-Valued Ground Motion Intensity Measures for Probabilistic Seismic Demand Analysis*. Jack W. Baker and C. Allin Cornell. October 2006.

PEER 2006/07 *Analytical Modeling of Reinforced Concrete Walls for Predicting Flexural and Coupled–Shear-Flexural Responses*. Kutay Orakcal, Leonardo M. Massone, and John W. Wallace. October 2006.

PEER 2006/06 *Nonlinear Analysis of a Soil-Drilled Pier System under Static and Dynamic Axial Loading.* Gang Wang and Nicholas Sitar. November 2006.

PEER 2006/05 *Advanced Seismic Assessment Guidelines.* Paolo Bazzurro, C. Allin Cornell, Charles Menun, Maziar Motahari, and Nicolas Luco. September 2006.

PEER 2006/04 *Probabilistic Seismic Evaluation of Reinforced Concrete Structural Components and Systems.* Tae Hyung Lee and Khalid M. Mosalam. August 2006.

PEER 2006/03 *Performance of Lifelines Subjected to Lateral Spreading.* Scott A. Ashford and Teerawut Juirnarongrit. July 2006.

PEER 2006/02 *Pacific Earthquake Engineering Research Center Highway Demonstration Project.* Anne Kiremidjian, James Moore, Yue Yue Fan, Nesrin Basoz, Ozgur Yazali, and Meredith Williams. April 2006.

PEER 2006/01 *Bracing Berkeley. A Guide to Seismic Safety on the UC Berkeley Campus.* Mary C. Comerio, Stephen Tobriner, and Ariane Fehrenkamp. January 2006.

PEER 2005/16 *Seismic Response and Reliability of Electrical Substation Equipment and Systems*. Junho Song, Armen Der Kiureghian, and Jerome L. Sackman. April 2006.

PEER 2005/15 *CPT-Based Probabilistic Assessment of Seismic Soil Liquefaction Initiation.* R. E. S. Moss, R. B. Seed, R. E. Kayen, J. P. Stewart, and A. Der Kiureghian. April 2006.

PEER 2005/14 *Workshop on Modeling of Nonlinear Cyclic Load-Deformation Behavior of Shallow Foundations.* Bruce L. Kutter, Geoffrey Martin, Tara Hutchinson, Chad Harden, Sivapalan Gajan, and Justin Phalen. March 2006.

PEER 2005/13 *Stochastic Characterization and Decision Bases under Time-Dependent Aftershock Risk in Performance-Based Earthquake Engineering.* Gee Liek Yeo and C. Allin Cornell. July 2005.

PEER 2005/12 *PEER Testbed Study on a Laboratory Building: Exercising Seismic Performance Assessment.* Mary C. Comerio, editor. November 2005.

PEER 2005/11 *Van Nuys Hotel Building Testbed Report: Exercising Seismic Performance Assessment.* Helmut Krawinkler, editor. October 2005.

PEER 2005/10 *First NEES/E-Defense Workshop on Collapse Simulation of Reinforced Concrete Building Structures.* September 2005.

PEER 2005/09 *Test Applications of Advanced Seismic Assessment Guidelines.* Joe Maffei, Karl Telleen, Danya Mohr, William Holmes, and Yuki Nakayama. August 2006.

PEER 2005/08 *Damage Accumulation in Lightly Confined Reinforced Concrete Bridge Columns.* R. Tyler Ranf, Jared M. Nelson, Zach Price, Marc O. Eberhard, and John F. Stanton. April 2006.

PEER 2005/07 *Experimental and Analytical Studies on the Seismic Response of Freestanding and Anchored Laboratory Equipment.* Dimitrios Konstantinidis and Nicos Makris. January 2005.

PEER 2005/06 *Global Collapse of Frame Structures under Seismic Excitations*. Luis F. Ibarra and Helmut Krawinkler. September 2005.

PEER 2005//05 *Performance Characterization of Bench- and Shelf-Mounted Equipment.* Samit Ray Chaudhuri and Tara C. Hutchinson. May 2006.

PEER 2005/04 *Numerical Modeling of the Nonlinear Cyclic Response of Shallow Foundations.* Chad Harden, Tara Hutchinson, Geoffrey R. Martin, and Bruce L. Kutter. August 2005.

PEER 2005/03 *A Taxonomy of Building Components for Performance-Based Earthquake Engineering.* Keith A. Porter. September 2005.

PEER 2005/02 *Fragility Basis for California Highway Overpass Bridge Seismic Decision Making*. Kevin R. Mackie and Božidar Stojadinović. June 2005.

PEER 2005/01 *Empirical Characterization of Site Conditions on Strong Ground Motion.* Jonathan P. Stewart, Yoojoong Choi, and Robert W. Graves. June 2005.

PEER 2004/09 *Electrical Substation Equipment Interaction: Experimental Rigid Conductor Studies.* Christopher Stearns and André Filiatrault. February 2005.

PEER 2004/08 *Seismic Qualification and Fragility Testing of Line Break 550-kV Disconnect Switches.* Shakhzod M. Takhirov, Gregory L. Fenves, and Eric Fujisaki. January 2005.

PEER 2004/07 *Ground Motions for Earthquake Simulator Qualification of Electrical Substation Equipment.* Shakhzod M. Takhirov, Gregory L. Fenves, Eric Fujisaki, and Don Clyde. January 2005.

PEER 2004/06 *Performance-Based Regulation and Regulatory Regimes.* Peter J. May and Chris Koski. September 2004.

PEER 2004/05 *Performance-Based Seismic Design Concepts and Implementation: Proceedings of an International Workshop.* Peter Fajfar and Helmut Krawinkler, editors. September 2004.

PEER 2004/04 *Seismic Performance of an Instrumented Tilt-up Wall Building.* James C. Anderson and Vitelmo V. Bertero. July 2004.

PEER 2004/03 *Evaluation and Application of Concrete Tilt-up Assessment Methodologies.* Timothy Graf and James O. Malley. October 2004.

PEER 2004/02 *Analytical Investigations of New Methods for Reducing Residual Displacements of Reinforced Concrete Bridge Columns.* Junichi Sakai and Stephen A. Mahin. August 2004.

PEER 2004/01 *Seismic Performance of Masonry Buildings and Design Implications.* Kerri Anne Taeko Tokoro, James C. Anderson, and Vitelmo V. Bertero. February 2004.

PEER 2003/18 *Performance Models for Flexural Damage in Reinforced Concrete Columns.* Michael Berry and Marc Eberhard. August 2003.

PEER 2003/17 *Predicting Earthquake Damage in Older Reinforced Concrete Beam-Column Joints.* Catherine Pagni and Laura Lowes. October 2004.

PEER 2003/16 *Seismic Demands for Performance-Based Design of Bridges.* Kevin Mackie and Božidar Stojadinović. August 2003.

PEER 2003/15 *Seismic Demands for Nondeteriorating Frame Structures and Their Dependence on Ground Motions.* Ricardo Antonio Medina and Helmut Krawinkler. May 2004.

PEER 2003/14 *Finite Element Reliability and Sensitivity Methods for Performance-Based Earthquake Engineering.* Terje Haukaas and Armen Der Kiureghian. April 2004.

PEER 2003/13 *Effects of Connection Hysteretic Degradation on the Seismic Behavior of Steel Moment-Resisting Frames.* Janise E. Rodgers and Stephen A. Mahin. March 2004.

PEER 2003/12 *Implementation Manual for the Seismic Protection of Laboratory Contents: Format and Case Studies.* William T. Holmes and Mary C. Comerio. October 2003.

PEER 2003/11 *Fifth U.S.-Japan Workshop on Performance-Based Earthquake Engineering Methodology for Reinforced Concrete Building Structures.* February 2004.

PEER 2003/10 *A Beam-Column Joint Model for Simulating the Earthquake Response of Reinforced Concrete Frames.* Laura N. Lowes, Nilanjan Mitra, and Arash Altoontash. February 2004.

PEER 2003/09 *Sequencing Repairs after an Earthquake: An Economic Approach.* Marco Casari and Simon J. Wilkie. April 2004.

PEER 2003/08 *A Technical Framework for Probability-Based Demand and Capacity Factor Design (DCFD) Seismic Formats*. Fatemeh Jalayer and C. Allin Cornell. November 2003.

PEER 2003/07 *Uncertainty Specification and Propagation for Loss Estimation Using FOSM Methods.* Jack W. Baker and C. Allin Cornell. September 2003.

PEER 2003/06 *Performance of Circular Reinforced Concrete Bridge Columns under Bidirectional Earthquake Loading*. Mahmoud M. Hachem, Stephen A. Mahin, and Jack P. Moehle. February 2003.

PEER 2003/05 *Response Assessment for Building-Specific Loss Estimation.* Eduardo Miranda and Shahram Taghavi. September 2003.

PEER 2003/04 *Experimental Assessment of Columns with Short Lap Splices Subjected to Cyclic Loads*. Murat Melek, John W. Wallace, and Joel Conte. April 2003.

PEER 2003/03 *Probabilistic Response Assessment for Building-Specific Loss Estimation.* Eduardo Miranda and Hesameddin Aslani. September 2003.

PEER 2003/02 *Software Framework for Collaborative Development of Nonlinear Dynamic Analysis Program.* Jun Peng and Kincho H. Law. September 2003.

PEER 2003/01 *Shake Table Tests and Analytical Studies on the Gravity Load Collapse of Reinforced Concrete Frames.* Kenneth John Elwood and Jack P. Moehle. November 2003.

PEER 2002/24 *Performance of Beam to Column Bridge Joints Subjected to a Large Velocity Pulse.* Natalie Gibson, André Filiatrault, and Scott A. Ashford. April 2002.

PEER 2002/23 *Effects of Large Velocity Pulses on Reinforced Concrete Bridge Columns.* Greg L. Orozco and Scott A. Ashford. April 2002.

PEER 2002/22 *Characterization of Large Velocity Pulses for Laboratory Testing.* Kenneth E. Cox and Scott A. Ashford. April 2002.

PEER 2002/21 *Fourth U.S.-Japan Workshop on Performance-Based Earthquake Engineering Methodology for Reinforced Concrete Building Structures*. December 2002.

PEER 2002/20 *Barriers to Adoption and Implementation of PBEE Innovations.* Peter J. May. August 2002.

PEER 2002/19 *Economic-Engineered Integrated Models for Earthquakes: Socioeconomic Impacts.* Peter Gordon, James E. Moore II, and Harry W. Richardson. July 2002.

PEER 2002/18 *Assessment of Reinforced Concrete Building Exterior Joints with Substandard Details.* Chris P. Pantelides, Jon Hansen, Justin Nadauld, and Lawrence D. Reaveley. May 2002.

PEER 2002/17 *Structural Characterization and Seismic Response Analysis of a Highway Overcrossing Equipped with Elastomeric Bearings and Fluid Dampers: A Case Study.* Nicos Makris and Jian Zhang. November 2002.

PEER 2002/16 *Estimation of Uncertainty in Geotechnical Properties for Performance-Based Earthquake Engineering.* Allen L. Jones, Steven L. Kramer, and Pedro Arduino. December 2002.

PEER 2002/15 *Seismic Behavior of Bridge Columns Subjected to Various Loading Patterns.* Asadollah Esmaeily-Gh. and Yan Xiao. December 2002.

PEER 2002/14 *Inelastic Seismic Response of Extended Pile Shaft Supported Bridge Structures.* T.C. Hutchinson, R.W. Boulanger, Y.H. Chai, and I.M. Idriss. December 2002.

PEER 2002/13 *Probabilistic Models and Fragility Estimates for Bridge Components and Systems.* Paolo Gardoni, Armen Der Kiureghian, and Khalid M. Mosalam. June 2002.

PEER 2002/12 *Effects of Fault Dip and Slip Rake on Near-Source Ground Motions: Why Chi-Chi Was a Relatively Mild M7.6 Earthquake.* Brad T. Aagaard, John F. Hall, and Thomas H. Heaton. December 2002.

PEER 2002/11 *Analytical and Experimental Study of Fiber-Reinforced Strip Isolators*. James M. Kelly and Shakhzod M. Takhirov. September 2002.

PEER 2002/10 *Centrifuge Modeling of Settlement and Lateral Spreading with Comparisons to Numerical Analyses***.** Sivapalan Gajan and Bruce L. Kutter. January 2003.

PEER 2002/09 *Documentation and Analysis of Field Case Histories of Seismic Compression during the 1994 Northridge, California, Earthquake.* Jonathan P. Stewart, Patrick M. Smith, Daniel H. Whang, and Jonathan D. Bray. October 2002.

PEER 2002/08 *Component Testing, Stability Analysis and Characterization of Buckling-Restrained Unbonded Braces™.* Cameron Black, Nicos Makris, and Ian Aiken. September 2002.

PEER 2002/07 *Seismic Performance of Pile-Wharf Connections.* Charles W. Roeder, Robert Graff, Jennifer Soderstrom, and Jun Han Yoo. December 2001.

PEER 2002/06 *The Use of Benefit-Cost Analysis for Evaluation of Performance-Based Earthquake Engineering Decisions.* Richard O. Zerbe and Anthony Falit-Baiamonte. September 2001.

PEER 2002/05 *Guidelines, Specifications, and Seismic Performance Characterization of Nonstructural Building Components and Equipment*. André Filiatrault, Constantin Christopoulos, and Christopher Stearns. September 2001.

PEER 2002/04 *Consortium of Organizations for Strong-Motion Observation Systems and the Pacific Earthquake Engineering Research Center Lifelines Program: Invited Workshop on Archiving and Web Dissemination of Geotechnical Data, 4–5 October 2001*. September 2002.

PEER 2002/03 *Investigation of Sensitivity of Building Loss Estimates to Major Uncertain Variables for the Van Nuys Testbed.* Keith A. Porter, James L. Beck, and Rustem V. Shaikhutdinov. August 2002.

PEER 2002/02 *The Third U.S.-Japan Workshop on Performance-Based Earthquake Engineering Methodology for Reinforced Concrete Building Structures*. July 2002.

PEER 2002/01 *Nonstructural Loss Estimation: The UC Berkeley Case Study.* Mary C. Comerio and John C. Stallmeyer. December 2001.

PEER 2001/16 *Statistics of SDF-System Estimate of Roof Displacement for Pushover Analysis of Buildings.* Anil K. Chopra, Rakesh K. Goel, and Chatpan Chintanapakdee. December 2001.

PEER 2001/15 *Damage to Bridges during the 2001 Nisqually Earthquake.* R. Tyler Ranf, Marc O. Eberhard, and Michael P. Berry. November 2001.

PEER 2001/14 *Rocking Response of Equipment Anchored to a Base Foundation.* Nicos Makris and Cameron J. Black. September 2001.

PEER 2001/13 *Modeling Soil Liquefaction Hazards for Performance-Based Earthquake Engineering.* Steven L. Kramer and Ahmed-W. Elgamal. February 2001.

PEER 2001/12 *Development of Geotechnical Capabilities in OpenSees.* Boris Jeremi . September 2001.

PEER 2001/11 *Analytical and Experimental Study of Fiber-Reinforced Elastomeric Isolators*. James M. Kelly and Shakhzod M. Takhirov. September 2001.

PEER 2001/10 *Amplification Factors for Spectral Acceleration in Active Regions.* Jonathan P. Stewart, Andrew H. Liu, Yoojoong Choi, and Mehmet B. Baturay. December 2001.

PEER 2001/09 *Ground Motion Evaluation Procedures for Performance-Based Design.* Jonathan P. Stewart, Shyh-Jeng Chiou, Jonathan D. Bray, Robert W. Graves, Paul G. Somerville, and Norman A. Abrahamson. September 2001.

PEER 2001/08 *Experimental and Computational Evaluation of Reinforced Concrete Bridge Beam-Column Connections for Seismic Performance*. Clay J. Naito, Jack P. Moehle, and Khalid M. Mosalam. November 2001.

PEER 2001/07 *The Rocking Spectrum and the Shortcomings of Design Guidelines.* Nicos Makris and Dimitrios Konstantinidis. August 2001.

PEER 2001/06 *Development of an Electrical Substation Equipment Performance Database for Evaluation of Equipment Fragilities*. Thalia Agnanos. April 1999.

PEER 2001/05 *Stiffness Analysis of Fiber-Reinforced Elastomeric Isolators.* Hsiang-Chuan Tsai and James M. Kelly. May 2001.

PEER 2001/04 *Organizational and Societal Considerations for Performance-Based Earthquake Engineering.* Peter J. May. April 2001.

PEER 2001/03 *A Modal Pushover Analysis Procedure to Estimate Seismic Demands for Buildings: Theory and Preliminary Evaluation.* Anil K. Chopra and Rakesh K. Goel. January 2001.

PEER 2001/02 *Seismic Response Analysis of Highway Overcrossings Including Soil-Structure Interaction.* Jian Zhang and Nicos Makris. March 2001.

PEER 2001/01 *Experimental Study of Large Seismic Steel Beam-to-Column Connections.* Egor P. Popov and Shakhzod M. Takhirov. November 2000.

PEER 2000/10 *The Second U.S.-Japan Workshop on Performance-Based Earthquake Engineering Methodology for Reinforced Concrete Building Structures.* March 2000.

PEER 2000/09 *Structural Engineering Reconnaissance of the August 17, 1999 Earthquake: Kocaeli (Izmit), Turkey.* Halil Sezen, Kenneth J. Elwood, Andrew S. Whittaker, Khalid Mosalam, John J. Wallace, and John F. Stanton. December 2000.

PEER 2000/08 *Behavior of Reinforced Concrete Bridge Columns Having Varying Aspect Ratios and Varying Lengths of Confinement.* Anthony J. Calderone, Dawn E. Lehman, and Jack P. Moehle. January 2001.

PEER 2000/07 *Cover-Plate and Flange-Plate Reinforced Steel Moment-Resisting Connections.* Taejin Kim, Andrew S. Whittaker, Amir S. Gilani, Vitelmo V. Bertero, and Shakhzod M. Takhirov. September 2000.

PEER 2000/06 *Seismic Evaluation and Analysis of 230-kV Disconnect Switches.* Amir S. J. Gilani, Andrew S. Whittaker, Gregory L. Fenves, Chun-Hao Chen, Henry Ho, and Eric Fujisaki. July 2000.

PEER 2000/05 *Performance-Based Evaluation of Exterior Reinforced Concrete Building Joints for Seismic Excitation.* Chandra Clyde, Chris P. Pantelides, and Lawrence D. Reaveley. July 2000.

PEER 2000/04 *An Evaluation of Seismic Energy Demand: An Attenuation Approach.* Chung-Che Chou and Chia-Ming Uang. July 1999.

PEER 2000/03 *Framing Earthquake Retrofitting Decisions: The Case of Hillside Homes in Los Angeles.* Detlof von Winterfeldt, Nels Roselund, and Alicia Kitsuse. March 2000.

PEER 2000/02 *U.S.-Japan Workshop on the Effects of Near-Field Earthquake Shaking.* Andrew Whittaker, ed. July 2000.

PEER 2000/01 *Further Studies on Seismic Interaction in Interconnected Electrical Substation Equipment.* Armen Der Kiureghian, Kee-Jeung Hong, and Jerome L. Sackman. November 1999.

PEER 1999/14 *Seismic Evaluation and Retrofit of 230-kV Porcelain Transformer Bushings*. Amir S. Gilani, Andrew S. Whittaker, Gregory L. Fenves, and Eric Fujisaki. December 1999.

PEER 1999/13 *Building Vulnerability Studies: Modeling and Evaluation of Tilt-up and Steel Reinforced Concrete Buildings.* John W. Wallace, Jonathan P. Stewart, and Andrew S. Whittaker, editors. December 1999.

PEER 1999/12 *Rehabilitation of Nonductile RC Frame Building Using Encasement Plates and Energy-Dissipating Devices.* Mehrdad Sasani, Vitelmo V. Bertero, James C. Anderson. December 1999.

PEER 1999/11 *Performance Evaluation Database for Concrete Bridge Components and Systems under Simulated Seismic Loads.* Yael D. Hose and Frieder Seible. November 1999.

PEER 1999/10 *U.S.-Japan Workshop on Performance-Based Earthquake Engineering Methodology for Reinforced Concrete Building Structures.* December 1999.

PEER 1999/09 *Performance Improvement of Long Period Building Structures Subjected to Severe Pulse-Type Ground Motions*. James C. Anderson, Vitelmo V. Bertero, and Raul Bertero. October 1999.

PEER 1999/08 *Envelopes for Seismic Response Vectors.* Charles Menun and Armen Der Kiureghian. July 1999.

PEER 1999/07 *Documentation of Strengths and Weaknesses of Current Computer Analysis Methods for Seismic Performance of Reinforced Concrete Members.* William F. Cofer. November 1999.

PEER 1999/06 *Rocking Response and Overturning of Anchored Equipment under Seismic Excitations.* Nicos Makris and Jian Zhang. November 1999.

PEER 1999/05 *Seismic Evaluation of 550 kV Porcelain Transformer Bushings.* Amir S. Gilani, Andrew S. Whittaker, Gregory L. Fenves, and Eric Fujisaki. October 1999.

PEER 1999/04 *Adoption and Enforcement of Earthquake Risk-Reduction Measures.* Peter J. May, Raymond J. Burby, T. Jens Feeley, and Robert Wood.

PEER 1999/03 *Task 3 Characterization of Site Response General Site Categories*. Adrian Rodriguez-Marek, Jonathan D. Bray, and Norman Abrahamson. February 1999.

PEER 1999/02 *Capacity-Demand-Diagram Methods for Estimating Seismic Deformation of Inelastic Structures: SDF Systems*. Anil K. Chopra and Rakesh Goel. April 1999.

PEER 1999/01 *Interaction in Interconnected Electrical Substation Equipment Subjected to Earthquake Ground Motions.* Armen Der Kiureghian, Jerome L. Sackman, and Kee-Jeung Hong. February 1999.

PEER 1998/08 *Behavior and Failure Analysis of a Multiple-Frame Highway Bridge in the 1994 Northridge Earthquake.* Gregory L. Fenves and Michael Ellery. December 1998.

PEER 1998/07 *Empirical Evaluation of Inertial Soil-Structure Interaction Effects.* Jonathan P. Stewart, Raymond B. Seed, and Gregory L. Fenves. November 1998.

PEER 1998/06 *Effect of Damping Mechanisms on the Response of Seismic Isolated Structures.* Nicos Makris and Shih-Po Chang. November 1998.

PEER 1998/05 *Rocking Response and Overturning of Equipment under Horizontal Pulse-Type Motions.* Nicos Makris and Yiannis Roussos. October 1998.

PEER 1998/04 *Pacific Earthquake Engineering Research Invitational Workshop Proceedings, May 14–15, 1998: Defining the Links between Planning, Policy Analysis, Economics and Earthquake Engineering.* Mary Comerio and Peter Gordon. September 1998.

PEER 1998/03 *Repair/Upgrade Procedures for Welded Beam to Column Connections.* James C. Anderson and Xiaojing Duan. May 1998.

PEER 1998/02 *Seismic Evaluation of 196 kV Porcelain Transformer Bushings.* Amir S. Gilani, Juan W. Chavez, Gregory L. Fenves, and Andrew S. Whittaker. May 1998.

PEER 1998/01 *Seismic Performance of Well-Confined Concrete Bridge Columns.* Dawn E. Lehman and Jack P. Moehle. December 2000.

ONLINE REPORTS

The following PEER reports are available by Internet only at http://peer.berkeley.edu/publications/peer_reports.html

PEER 2009/109 *Simulation and Performance-Based Earthquake Engineering Assessment of Self-Centering Post-Tensioned Concrete Bridge Systems.* Won K. Lee and Sarah L. Billington. December 2009.

PEER 2009/107 *Experimental and Computational Evaluation of Current and Innovative In-Span Hinge Details in Reinforced Concrete Box-Girder Bridges: Part 2: Post-Test Analysis and Design Recommendations.* Matias A. Hube and Khalid M. Mosalam. December 2009.

PEER 2009/106 *Shear Strength Models of Exterior Beam-Column Joints without Transverse Reinforcement.* Sangjoon Park and Khalid M. Mosalam. November 2009.

PEER 2009/105 *Reduced Uncertainty of Ground Motion Prediction Equations through Bayesian Variance Analysis.* Robb Eric S. Moss. November 2009.

PEER 2009/104 *Advanced Implementation of Hybrid Simulation.* Andreas H. Schellenberg, Stephen A. Mahin, Gregory L. Fenves. November 2009.

PEER 2009/103 *Performance Evaluation of Innovative Steel Braced Frames.* T. Y. Yang, Jack P. Moehle, and Božidar Stojadinović. August 2009.

PEER 2009/102 *Reinvestigation of Liquefaction and Nonliquefaction Case Histories from the 1976 Tangshan Earthquake.* Robb Eric Moss, Robert E. Kayen, Liyuan Tong, Songyu Liu, Guojun Cai, and Jiaer Wu. August 2009.

PEER 2009/101 *Report of the First Joint Planning Meeting for the Second Phase of NEES/E-Defense Collaborative Research on Earthquake Engineering.* Stephen A. Mahin et al. July 2009.

PEER 2008/104 *Experimental and Analytical Study of the Seismic Performance of Retaining Structures.* Linda Al Atik and Nicholas Sitar. January 2009.

PEER 2008/103 *Experimental and Computational Evaluation of Current and Innovative In-Span Hinge Details in Reinforced Concrete Box-Girder Bridges. Part 1: Experimental Findings and Pre-Test Analysis.* Matias A. Hube and Khalid M. Mosalam. January 2009.

PEER 2008/102 *Modeling of Unreinforced Masonry Infill Walls Considering In-Plane and Out-of-Plane Interaction.* Stephen Kadysiewski and Khalid M. Mosalam. January 2009.

PEER 2008/101 *Seismic Performance Objectives for Tall Buildings.* William T. Holmes, Charles Kircher, William Petak, and Nabih Youssef. August 2008.

PEER 2007/101 *Generalized Hybrid Simulation Framework for Structural Systems Subjected to Seismic Loading.* Tarek Elkhoraibi and Khalid M. Mosalam. July 2007.

PEER 2007/100 *Seismic Evaluation of Reinforced Concrete Buildings Including Effects of Masonry Infill Walls.* Alidad Hashemi and Khalid M. Mosalam. July 2007.